Vitantonio Roma

Soil Properties and Site Characterization by means of Rayleigh Waves

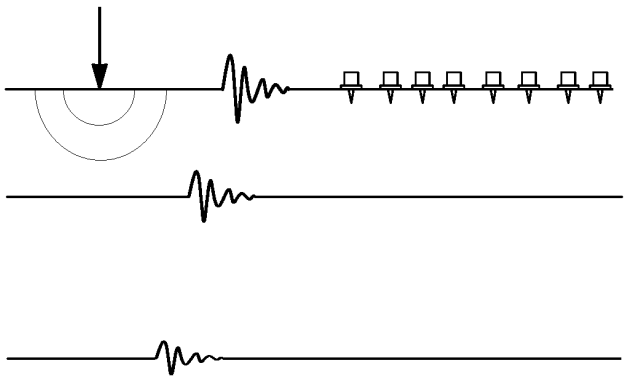

Geotechnical Engineering PhD Programme

Politecnico di Torino Politecnico di Milano
Università di Genova Università di Padova

Department of Structural and Geotechnical Engineering

Technical University of Turin (Politecnico)

Soil Properties and Site Characterization by means of Rayleigh Waves

By

Vitantonio Roma

Approved:

Advisor:

Prof. Renato Lancellotta

Head of the PhD Programme in Geotechnical Engineering:

Prof. Renato Lancellotta

November 2001

A Miriam,
goccia nel deserto.
(To Miriam,
drop in the desert)

Acknowledgments

A PhD program does not reveal its essence, if not at its end. I must consider lucky my self and I am grateful to my Master Prof. Renato Lancellotta. Since the preparation to the access examination for the PhD, he has been transmitting to me the love for the Geotechnics. He has always been an example of how a magister should reach his alumni. What he has taught to me goes beyond research itself and cannot be expressed in words. There are values in life that come before everything else.
My thanks go to Prof. Glenn Rix of the Georgia Institute of Technology of Atlanta. At first glance you can see at the same time his quietness and his passion for his job. Thanks to his guidance I have learnt so much about my research. Particularly I like the way he leads his co-workers, trusting them and always offering his critical suggestions.
A third figure has continuously stimulated my curiosity for the search of the physical truth. Prof. Michele Jamiolkowski is an example of the scientist in my mind. There is always something relevant to learn from his words and from the simplicity by which he explains the most complicate ideas.
Other persons have allowed for this thesis to be made. Prof. Diego Lo Presti, Prof. Alessandro De Stefano, Prof. Giovanni Barla, Prof. Carlos Santamarina, Prof. Daniele Costanzo, Dr Carlo Lai, Dr Michele Iovieno, Mr. Gregory Hebeler have spent some of their time discussing with me about different aspects of my research.
I cannot forget all the friends I have shared with part of my life during my PhD: Guido Musso, Roberto Maniscalco, Renzo Pallara, Sebastiano Foti, Rosario Ceravolo, Gaetano Amatruda, Florian Herzog, Peter Dijk, Claudio Genovese, Marco Barla, Laura Tonni, Riccardo Castellanza, Claudio Genovese, Renzo Pallara, Giuseppe Scarmozzino, SungSoo.
Particular thanks to the people of the West Merrits community in Atlanta such as Matt Bandy, Garrett Jones, Andrea Thomas, Adria Williams. They represent the most important experience in USA.

Introduction

Geotechnical Engineering is a quite young branch of the science, if compared to other disciplines, such as Structural or Mechanical Engineering. In fact it was Terzaghi in 1933 who proposed a rigorous and organized approach for understanding the behavior of the soil in the applications of Civil Engineering. Since then the Geotechnique has developed enormously, involving the study of more and more phenomena related to soils.

When dealing with a real application, the main purpose of a geotechnical engineer is to comprehend which is the physical behavior of the global soil-structure system and to find out the optimal solution in terms of safety and costs. In any design it becomes important the choice of those properties of the system that will be used for modeling the physical reality and for predicting the system behavior, under the action of the internal and external forces. In a general philosophy of designing, some basics are followed: resistance, deformations, durability , environmental impact and cost.

Classically resistance and deformations are the first aspects in the designing process for the engineer, because they respectively refer to the safety from collapse and to the serviceability of the soil-structure system.

As a consequence main relevance has always been given to the geotechnical parameters and to the methods used for their evaluation. In this work the attention has been put on two properties of the soil, i.e. the stiffness and the damping. Actually the aims of this research go beyond, since the more general goal of site characterization is sought. This implies not only the determination of the stiffness and damping profiles, but also the geometry of the site and the presence of the water table.

In this regard non-invasive surface waves represent a valid alternative both to laboratory tests, when dealing with hard-to-sample soils and to in situ invasive tests, that give only localized information and are expensive, since require the use of boreholes.

In the geophysical field the use of surface waves is not new, in fact seismic reflection and refraction methods are well established, but in the geotechnical scale the SASW (Spectral Analysis of Surface Waves) method has been used only recently worldwide. This technique consists of generating a perturbation at a point on the free surface of the site and then the traveling disturbance is measured at several stations on the same free surface. The speed of the surface waves depends on the geometry of the site as well as the stiffness of the soil. In addition the attenuation of the registered signal with distance from the source is due to both the geometrical spreading and the material damping. In this thesis major attention is focused on the dispersion and the attenuation of Rayleigh waves,

which represent the predominant components of motion of the surface waves in the far field.
The site characterization by means of Rayleigh waves can be achieved performing three fundamental steps:
1) *experimental test* in which the real system is excited and the traveling perturbation is measured at the several stations, for calculating the experimental system response.
2) *theoretical simulation* of the wave propagation phenomenon through an ideal layered site, in order to evaluate the theoretical system response, which must be consistent with the experimental response as much as possible.
3) *inversion problem*, in which the system parameters are perturbed until the distance between the experimental and the theoretical system responses is minimized. This task is achieved by means of an optimization algorithm.

In this thesis we search a new theoretical procedure, that be consistent with the experimental multistation SASW method, and a valid inversion algorithm, that allows for the investigation of systems with both regular (normally dispersive) and irregular (inversely dispersive) stiffness profiles. In order to achieve this purpose, the relative importance of all the Rayleigh modes needs to be understood during propagation in a layered medium.
The multistation SASW method manifests advantages and limitations respect to other techniques, in fact it has to be considered only one complementary tool for soil investigation. One drawback could be the complexity associated to the inversion problem, that could give rise to the non-uniqueness of the solution. Another limitation is that the stiffness and the damping of soils are concerned with very small deformations. Nevertheless the multistation SASW method provides the most reliable values of the stiffness and damping for soil-structure dynamical interaction, since the in situ real scale is involved.
The potentialities of the multistation SASW method show up in a wide variety of geotechnical applications, such as pavement system identification, offshore characterization, soil improvement tests, obstacle detection.

Thesis Outline

Except for the introductory parts of the Chapters 1, 2 and 4, the rest of the thesis represents an original contribution to the research on Rayleigh waves propagation through layered media and geotechnical soil characterization by means of multistation SASW method.

In **Chapter 1**, after a brief summary of the basic concepts of the wave propagation in linear elastic, mono-phase, isotropic media, the attention is focused on generalized modes of Rayleigh waves through a layered half-space and their numerical search. Some numerical problems in searching the Rayleigh modes have been pointed out and solved.

Chapter 2 is addressed to the soil characterization by means of surface waves from the early methods in the 60's and 80's until nowadays. Both geophysical and geotechnical techniques are reminded and a new approach is proposed, for obtaining the theoretical response of the system. As innovative contribution of this research the relative importance of Rayleigh waves generated at the free surface of a layered medium is explained in the frequency-wave number domain and the frequencies and wave numbers of resonance are recognized. This two aspects constitute an original contribution to the knowledge of the influence of higher modes of Rayleigh waves for geotechnical soil characterization and surface wave motion. The Chapter ends with a new formula for frequencies and wave numbers of resonance valid for a single layer over an infinite half-space. This formula is a very useful result, because puts in evidence the effects of surface Rayleigh waves in soil-structure dynamic interactions.

In **Chapter 3** the new method for the theoretical simulation of the system response is inserted into an inversion procedure, which identifies either the shear waves velocities or the thickness profiles with depth by means of a non-linear constrained optimization algorithm. The algorithm used for minimizing the distance between the theoretical and the experimental system responses is the Davidon-Fletcher-Powell (DFP), that belongs to the class of Quasi-Newton algorithms. As system response the geometrical dispersion relation of Rayleigh waves is adopted. The optimization algorithm is based on the new approach presented by the author in Chapter 2 and it is part of the code developed by the author for solving the Rayleigh inversion problem.

In **Chapter 4** the theory of visco-elasticity is utilized for determining the damping ratio profile. By using the correspondence principle of visco-elasticity the complex eigenvalue Rayleigh problem is solved and both the coupled and the uncoupled inversion procedures are presented. The attenuation relation of Rayleigh waves is added to the geometrical

dispersion relation as system response. The effort is made for considering al the Rayleigh modes in the Geometric spreading of the perturbation, instead of the simplified geometrical attenuation law for homogeneous half-space. The original idea of a hybrid approach is presented, which combines coupled measurements and uncoupled inversion of the dispersion and the attenuation relations.

Chapter 5 is devoted to the experimental results, that represent a fundamental aspect of the research. The experiments have the meaningful role of validating or rejecting the theoretical interpretation of the real phenomena. A theoretical model can be accepted for simulation and prediction of real phenomena, only if it is supported by a good agreement with experimental observations and no contradictions exist in any particular manifestations. In this Chapter both the uncoupled and the coupled procedures are employed for the characterization of real sites and a hybrid approach is also proposed.

Some issues have been confined into the Appendices, nevertheless they have relevant importance for the development of the ideas contained in this thesis.

In **Appendix A** the equivalence of any type of surface point source in evaluating the geometrical dispersion relation of Rayleigh waves is affirmed. For the first time both theoretical demonstration and experimental evidence are provided for such a statement. This result reveals to be a key element in the theoretical simulation of the dispersion relation of Rayleigh waves, because it says that it is not necessary to characterize the source for the simulation. In fact the theoretical Rayleigh dispersion relation is evaluated, by using the Transfer function of the system, obtained by knowing the system response to a time harmonic source. Instead the experimental dispersion relation is calculated, by using the measurements obtained by means of either an impulsive or a harmonic source.

In **Appendix B** the interesting concept of the equivalence, under precise circumstances, of the energy speed and the group velocity associated to a traveling perturbation is reminded. In addition the new concept of an apparent group velocity is underlined. The idea of an apparent group velocity is supported by the observation of a wave train, that spreads away from the source. Into the wave train different modes are contained, each one of them traveling at their own phase and group velocities. Nevertheless if the several components are thought to be combined together to form a whole complicate disturbance, when the dispersion phenomenon has not completely occurred yet, it can be assumed that the energy of the whole perturbation propagates at a sort of an equivalent speed, i.e. the apparent group velocity. Indeed the apparent group velocity is the velocity of the whole disturbance as it is measured in the experiments. For the apparent group velocity an analytical expression has been derived.

In **Appendix C** the stiffness matrix method is followed for the explicit evaluation of the geometrical Rayeligh dispersion relation in the case of a single layer over an infinite half-space. Just in this simple case the difficulties of an analytical approach are evident.
The thesis ends up with the Conclusions, in which the efforts, the ideas and the limitations of this research are reminded.

Contents

Chapter1

Wave propagation in elastic solids

Introduction

In this chapter we present the propagation of waves in an unbounded region, through an interface, in a homogeneous and in a layered half-space. This will enable us to introduce several types of waves: reflected and transmitted, body waves and interface waves. Among them the Rayleigh waves and their geometrical dispersion relation will be treated in detail into a layered half-space.

1.1 Unbounded region

In the sequel we will assume that the medium is homogeneous, isotropic, linear elastic. We will model the medium as an equivalent continuum, in which the stress and the strain tensors σ and ε can be mathematically defined as continuous and derivable functions inside the region of interest. In particular the strain tensor can be expressed in terms of the derivatives of the displacements, under the hypothesis of small strain, as:

$$\varepsilon_{ij} = \frac{1}{2}(u_{i,j} + u_{j,i}) \tag{1.1}$$

The rotation tensor can also be introduced as:

$$\vartheta_{ij} = \frac{1}{2}(u_{i,j} - u_{j,i}) \tag{1.2}$$

The stress tensor can be used in order to evaluate the traction t by means of the Cauchy's stress formula:

$$t_l = \sigma_{kl} n_k \tag{1.3}$$

where k denotes the direction of the unit vector n perpendicular to the surface element and l indicates the direction of the traction on the surface element.

By the balance of momentum of momentum it can be easily shown that the stress tensor is symmetric, being the medium non polar, that is:

$$\sigma_{ij} = \sigma_{ji} \tag{1.4}$$

Thanks to the hypothesis of linear elasticity it is possible to express the constitutive law, that correlates the state of the stress to the stress of the strain, with a 4-th order tensor C_{ijkl} :

$$\sigma_{ij} = C_{ijkl}\varepsilon_{kl} \tag{1.5}$$

where $C_{ijkl} = C_{jikl} = C_{klij} = C_{ijlk}$, since both the stress and the strain tensors are symmetric.
Under the assumptions of homogeneity and isotropy the 21 independent elastic constants reduce to only 2, so that we can write the Hooke's law as:

$$\sigma_{ij} = \lambda\varepsilon_{kk}\delta_{ij} + 2\mu\varepsilon_{ij} \tag{1.6}$$

where λ and μ are the Lame's elastic constants and δ_{ij} is the Kronecker delta.
It is useful to define the stress and the strain deviators *s* and *e* as:

$$s_{ij} = \sigma_{ij} - \frac{1}{3}\sigma_{kk}\delta_{ij} \tag{1.7a}$$

$$e_{ij} = \varepsilon_{ij} - \frac{1}{3}\varepsilon_{kk}\delta_{ij} \tag{1.7b}$$

As it can be seen each of them is obtained substructing from either the stress or the strain tensor a spherical tensor. It can be proved that the following relationships hold between the deviatoric stress and strain tensors:

$$s_{ij} = 2\mu \cdot e_{ij} \tag{1.8a}$$

$$\sigma_{kk} = 3B \cdot \varepsilon_{kk} \tag{1.8b}$$

where μ and

$$B = \lambda + \frac{2}{3}\mu \tag{1.9}$$

are the shear and the bulk moduli.

Other two elastic constants, which are commonly used, are the Young's modulus E and the Poisson's ratio ν. The links among all the elastic constants introduced up to now are illustrated in the table below:

	E, ν	μ	λ, μ
λ	$\frac{E\nu}{(1+\nu)(1-2\nu)}$	$\frac{\mu(E-2\mu)}{3\mu-E}$	λ
μ	$\frac{E}{2(1+\nu)}$	μ	μ
E	E	E	$\frac{\mu(3\lambda+2\mu)}{\lambda+\mu}$
B	$\frac{E}{3(1-2\nu)}$	$\frac{\mu E}{3(3\mu-E)}$	$\lambda+\frac{2}{3}\mu$
ν	ν	$\frac{E-2\mu}{2\mu}$	$\frac{\lambda}{2(\lambda+\mu)}$

Table 1.1: Relationships among isotropic elastic constants (Achenbach, 1999).

According to the principle of balance of linear momentum, the instantaneous rate of change of the linear momentum of a body is equal to the resultant external force acting on the body at the particular instant of time. As a consequence the Cauchy's first law of motion holds:

$$\sigma_{kl,k} + \rho f_l = \rho \ddot{u}_l \qquad (1.10)$$

where ρ is the mass density, f_l is the component of the body force per unit mass in the direction l, $\ddot{u}_l$ is the component of the acceleration along l.

The equations (1.1), (1.6), (1.10) enable one to write the equations of motion in terms of displacements:

$$\mu u_{i,jj} + (\lambda+\mu) u_{j,ji} + \rho f_i = \rho \ddot{u}_i \qquad \text{i=1, 2, 3} \qquad (1.11)$$

In order to completely define the elasto-dynamic problem, both boundary conditions and initial conditions must be specified. The boundary conditions can be expressed in terms of displacements or tractions, the initial

conditions are usually explicited at time t=0 for displacements and velocities.
In vector notation the (1.11) can be rewritten as:

$$\mu\nabla^2\underline{u} + (\lambda+\mu)\nabla\nabla\cdot\underline{u} = \rho\ddot{\underline{u}} \tag{1.12}$$

where ∇ and ∇^2 are the nabla and the Laplacian operators.
If we decompose the displacements in terms of the scalar potential φ and the vector potential $\underline{\psi}$:

$$\underline{u} = \nabla\varphi + \nabla\wedge\underline{\psi} \tag{1.13}$$

$$\underline{\psi} = (\psi_1, \psi_2, \psi_3) \tag{1.14}$$

substituting (1.13) into (1.12), we have:

$$\nabla[(\lambda+2\mu)\nabla^2\varphi - \rho\ddot{\varphi}] + \nabla\wedge[\mu\nabla^2\underline{\psi} - \rho\ddot{\underline{\psi}}] = 0 \tag{1.15}$$

from which the two equations of motion follow:

$$\nabla^2\varphi = \frac{1}{c_P^2}\ddot{\varphi} \tag{1.16a}$$

$$\nabla^2\underline{\psi} = \frac{1}{c_S^2}\ddot{\underline{\psi}} \tag{1.16b}$$

where $c_P^2 = \dfrac{\lambda+2\mu}{\rho}$ and $c_S^2 = \dfrac{\mu}{\rho}$ (1.17a, 1.17b)

The use of potentials to decompose the displacement field allows for the coupled equations of motion (1.12) with the 3 components of the displacements to be uncoupled into longitudinal and shear patterns of motion. Nevertheless a coupling still exists when trying to satisfy the boundary conditions.
From (1.16a) and (1.16b) it can be seen that in an unbounded medium two different kinds of waves can propagate. The first one is named compression wave P. The particle motion is in the same direction as the wave travels along with a speed c_P and no distortion occurs. The second wave is the distortional or shear wave S, that is slower than the P wave, since $c_S<c_P$. The particles oscillate around their equilibrium position perpendicularly to the

direction of propagation without changes of volume. It is worthy to note that the speeds of P and S waves depend on the elastic properties of the. This is a fundamental feature, because the shear modulus G and the bulk modulus B can be easily evaluated, by measuring the velocities of P and S waves.

1.1.1 Shapes of the wave fronts

Up to now we know that in an unbounded medium two kinds of waves, say P and S waves, can propagate, but we have not specified yet which shape their wave fronts have. First of all it is necessary to properly define the concept of a wave front. To a perturbation we can associate a phase and an amplitude. The phase gives an idea of the periodicity in time and space of the motion, the amplitude is strictly correlated to the energy transported by the perturbation. The wave front of the wave can either refer to the phase or to the amplitude of the wave and in a three dimensional space it separates the region that has just experienced the perturbation from the region that is still at rest and has not been perturbed yet. Actually many geometric shapes may exist, but the simplest are of three types: plane, spherical and cylindrical.
Plane waves are characterised by plane wave fronts upon which the amplitude of the perturbation remains constant, so that no geometrical attenuation shows up. This is why people at the extremes of a very long corridor can clearly hear each other when speaking. In spherical waves the total energy of the perturbation spreads out from the source with spherical wave fronts, so that the energy density decreases with a factor of $\frac{1}{r^2}$ at a distance r from the source. There are several examples in nature of spherical waves, such as the light coming from the sun or the sound produced by an explosion in a point of the sky. Finally cylindrical waves propagate along cylindrical wave fronts and the geometrical attenuation of the energy density is governed by a factor of $\frac{1}{r}$. A typical example is given by the perturbation that travels on the surface of a lake after a stone has fallen into it.

1.1.2 Progressive and standing waves

Another important distinction among all the possible perturbations is between standing waves and progressive waves. Standing waves are characterised by the appearance of stationary points of zero phase, called nodes. They appear always the same in time and space and are likely to be found in bodies of finite dimensions. Progressive waves travel through the body with nodes that move.

For example the displacement due to a plane wave propagating with phase velocity c in the direction of the unit propagation vector $\hat{p}$ can be written as:

$$\underline{u}(\underline{x},t) = f(\underline{x} \cdot \hat{p} - ct)\hat{d} \tag{1.18}$$

in which $\underline{x}$ is the position vector, t is the time and $\hat{d}$ is the unit vector indicating the direction of the particle motion.
The wave fronts of the phase are expressed by:

$$\underline{x} \cdot \hat{p} = cons\tan t \tag{1.19}$$

and they travel perpendicularly to the propagation vector $\hat{p}$ with a speed equal to c.
A particular case of wave is the steady-state disturbance, since the quantities of interest can be mathematically described in the form:

$$\underline{u}(\underline{x},t) = A(\underline{x}) \cdot e^{i\omega t} \tag{1.20}$$

where ω is the circular frequency and there is a separation of the spatial and temporal variables, since the amplitude A depends only on the position vector $\underline{x}$ and the time t appears only in the phase term.
This solution is expected when the source is time harmonic and the advantages is that every solution generated by any complicate external force can be represented as a proper combination of a finite or infinite number of steady-state solutions if the superposition principle holds.

1.2 Plane interface between two half-spaces

In the following we will deal with steady-state plane waves if not differently specified and it will be shown what happens when an incident wave encounters a plane interface between two half-spaces with different mechanical properties (fig.1.1). The first half-space is beneath the interface and its properties are λ, μ, and ρ, the second half-space is above the interface and its properties are indicated by the index B.

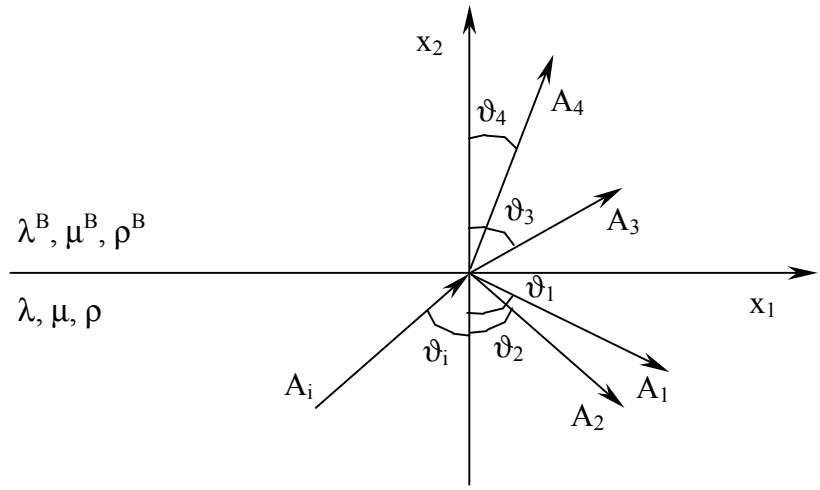

Figure 1.1: Incident wave A_i, reflected A_1, A_2 and transmitted A_3, A_4 in-plane waves at a plane interface between two different half-spaces.

Let us consider the in-plane motion, so that only P and SV waves are concerned. In general an incident P or SV wave coming from the first half-space generates both P and SV reflected waves in the same half-space and P and SV transmitted waves in the second half-space. Under particular conditions waves propagating along the interface can be generated, that, when no one of the two half-spaces is air, are called Stoneley waves. In all cases the principle of causality must be respected, so that all the waves produced by the incident wave at the interface must propagate away from the interface (Achenbach, 1999). The principle of causality is one of the postulates of the theory of relativity and it states that in any real phenomenon in which it is possible to recognise the cause and the related effects, the cause always precedes the effects. About this issue several researches have been conducted nowadays and it has been recently published a paper on Nature (Wang, L. J. Et al., 2000) in which the Authors claim to have experimentally shown how it is apparently possible to measure the output signal from a properly made system (the effects) before the input pulse (the cause). Actually as output quantity they have measured the signal travelling at the phase velocity, that does not transfer the energy associated to the signal.

1.2.1 *Incident P wave*

Let write the incident P wave in terms of displacements as:

$$\underline{u}_i = A_i^P e^{i(k_i x_1 sin\vartheta_i + k_i x_2 \cos\vartheta_i - \omega t)} \tag{1.21}$$

Assume the same form for the reflected P (indicated by the index 1) and SV (indicated by the index 2) waves in the first half-space:

$$\underline{u}_1 = A_1 e^{i(k_1 x_1 sin\vartheta_1 - k_1 x_2 \cos\vartheta_1 - \omega t)} \tag{1.22a}$$

$$\underline{u}_2 = A_2 e^{i(k_2 x_1 sin\vartheta_2 - k_2 x_2 \cos\vartheta_2 - \omega t)} \tag{1.22b}$$

and the transmitted P (indicated by the index 3) and SV (indicated by the index 4) waves in the second half-space:

$$\underline{u}_3 = A_3 e^{i(k_3 x_1 sin\vartheta_3 + k_3 x_2 \cos\vartheta_3 - \omega t)} \tag{1.23a}$$

$$\underline{u}_4 = A_4 e^{i(k_4 x_1 sin\vartheta_4 - k_4 x_2 \cos\vartheta_4 - \omega t)} \tag{1.23b}$$

In formulas (1.21, 1.22a, 1.22b, 1.23a, 1.23b)

$$k_i = \frac{\omega}{c_P} = \frac{2\pi}{\lambda_P} \qquad k_1 = \frac{\omega}{c_P} \qquad \text{(1.24a, 1.24b)}$$

$$k_2 = \frac{\omega}{c_S} \qquad k_3 = \frac{\omega}{c_P^B} \qquad k_4 = \frac{\omega}{c_S^B} \qquad \text{(1.24a, 1.24b, 1.24c)}$$

are the wave numbers associated to the incident, reflected and transmitted waves, ϑ_i , ϑ_1 , ϑ_2 , ϑ_3 , ϑ_4 are the angles formed by the waves with the x_2 axe as shown in fig.1.1.
Assuming that a perfect contact exists at the interface, the continuity of displacements and the stresses must be imposed:

$$\underline{u}_i + \underline{u}_1 + \underline{u}_2 = \underline{u}_3 + \underline{u}_4 \qquad \text{at } x_2 = 0 \tag{1.25a}$$

$$\underline{\sigma}_i + \underline{\sigma}_1 + \underline{\sigma}_2 = \underline{\sigma}_3 + \underline{\sigma}_4 \qquad \text{at } x_2 = 0 \tag{1.25b}$$

All the components must have the same exponential term, so it comes out that:

$$k_i c_P = k_1 c_P = k_2 c_S = k_3 c_P^B = k_4 c_S^B = k \tag{1.26a}$$

$$k_i sin\,\vartheta_i = k_1 sin\,\vartheta_{1i} = k_2 sin\,\vartheta_2 = k_3 sin\,\vartheta_3 = k_4 sin\,\vartheta_4 \tag{1.26b}$$

Some considerations can just be done concerning the phases of all the involved waves. First of all the waves have the same apparent wave numbers k and hence the same apparent phase velocity c, that is the component parallel to the interface of each wave travels along the interface with the same phase velocity. Secondly the reflected P wave in the first half-space is reflected at the same angle of the incident P wave, since:

$$k_i = k_1 \Longrightarrow \qquad \vartheta_i = \vartheta_1 \tag{1.27}$$

Finally both reflected and transmitted P waves are more inclined respect to the vertical than the correspondent reflected and transmitted SV waves, since the Snell's law holds:

$$\frac{sin\,\vartheta_1}{c_P} = \frac{sin\,\vartheta_2}{c_S} = \frac{sin\,\vartheta_3}{c_P^B} = \frac{sin\,\vartheta_4}{c_S^B} \tag{1.28}$$

Equations (1.25a, 1.25b) allow to determine the amplitudes of the generated waves as the unknowns of a linear system:

$$[M]\cdot\begin{pmatrix} A_1 \\ A_2 \\ A_3 \\ A_4 \end{pmatrix} = A_i\{N\} \tag{1.29}$$

in which [M] is a matrix 4x4 and N is a column vector 4x1, whose elements are functions of all the properties of the two half-spaces and of the angles ϑ, but not of the circular frequency ω.The expressions of the amplitudes and the matrix [M] and the vector (N) can be found in the book by (Achenbach, 1999) and (Ewing et al., 1957).
For incident SV waves again both SV and P waves can be generated at an interface according to the Snellius law (1.28), instead for incident SH waves only SH waves can be reflected and transmitted, since under the assumptions of isotropy the horizontal motion is uncoupled from the vertical motion.

1.2.2 Stoneley waves

If we want to investigate the existence of waves travelling along the interface of separation between two half-spaces we should suppose displacements of the form:

$$u_1 = (D_3 e^{b_3 x_2} + D_4 e^{b_4 x_2}) e^{ik(x_1 - ct)} \qquad \text{for } x_2 < 0 \qquad (1.30a)$$

$$u_2 = (\frac{b_3}{ik} D_3 e^{b_3 x_2} - \frac{ik}{b_4} D_4 e^{b_4 x_2}) e^{ik(x_1 - ct)} \qquad \text{for } x_2 < 0 \qquad (1.30b)$$

in the half-space $x_2 < 0$ (see fig.1.1) and:

$$u_1 = (D_1 e^{-b_1 x_2} + D_2 e^{-b_2 x_2}) e^{ik(x_1 - ct)} \qquad \text{for } x_2 > 0 \qquad (1.31a)$$

$$u_2 = (-\frac{b_1}{ik} D_1 e^{-b_1 x_2} + \frac{ik}{b_2} D_2 e^{-b_2 x_2}) e^{ik(x_1 - ct)} \text{ for } x_2 > 0 \qquad (1.31b)$$

in the half-space $x_2 > 0$, in which D_1, D_2, D_3, D_4 are constants to be determined, whereas:

$$b_1 = k \cdot \left[1 - \left(\frac{c}{c_P} \right)^2 \right]^{\frac{1}{2}} \qquad b_2 = k \cdot \left[1 - \left(\frac{c}{c_S} \right)^2 \right]^{\frac{1}{2}} \qquad (1.32a, b)$$

$$b_3 = k \cdot \left[1 - \left(\frac{c}{c_P^B} \right)^2 \right]^{\frac{1}{2}} \qquad b_4 = k \cdot \left[1 - \left(\frac{c}{c_S^B} \right)^2 \right]^{\frac{1}{2}} \qquad (1.32c, d)$$

are taken as positive values, with *k* wave number and *c* phase velocity of the surface wave. In the above formulas the subscripts 1, 2 refer to the components of motion perpendicular and parallel to the interface respectively. The superscript B in formulas (1.32) refers to the second half-space (x_2>0).

From (1.30a, b) and (1.31a, b) we can see that the form chosen for the displacements is such that they exponentially decay along x_2 going away from the interface, instead they can propagate along x_1.
By imposing the continuity of stresses and displacements at the interface a homogeneous system of four equations with the unknowns D_1, D_2, D_3, D_4 is obtained and in order to have non trivial solutions, the determinant of the coefficients must be set equal to zero.

$$\det\begin{bmatrix} 1 & 1 & -1 & -1 \\ \frac{b_1}{k} & \frac{k}{b_2} & \frac{b_3}{k} & \frac{k}{b_2} \\ 2\frac{b_1}{k} & \left(2-\frac{c^2}{c_S^2}\right)\frac{k}{b_2} & 2\frac{\mu^B}{\mu}\frac{b_3}{k} & \frac{\mu^B}{\mu}\left[2-\left(\frac{c}{c_S^B}\right)^2\right]\frac{k}{b_4} \\ 2-\frac{c^2}{c_S^2} & 2 & -\frac{\mu^B}{\mu}\left[2-\left(\frac{c}{c_S^B}\right)^2\right] & -2\frac{\mu^B}{\mu} \end{bmatrix}=0 \qquad (1.33)$$

It is known (Achenbach, 1999) that real and positive values of the phase velocity *c* that satisfy the above condition (1.33) are found only over a certain range of the ratios ρ^B/ρ and μ^B/μ.
From a look at the matrix of the coefficients in (1.33) the reader can note that even in this case the elements of this matrix do not depend on the wave number *k*, but only on the characteristics of the two half-spaces, that means that Stoneley waves are not dispersive.

1.3 Infinite homogeneous half-space

When one of the two half-spaces separated by an interface, say the upper one, is air it can be assumed that there are not transmitted waves and in general only reflected waves exist. It can be proven that for a homogeneous half-space, besides the body P and S waves as just seen in an unbounded region, a new kind of wave exists, called Rayleigh wave from Lord Rayleigh who first investigated it.

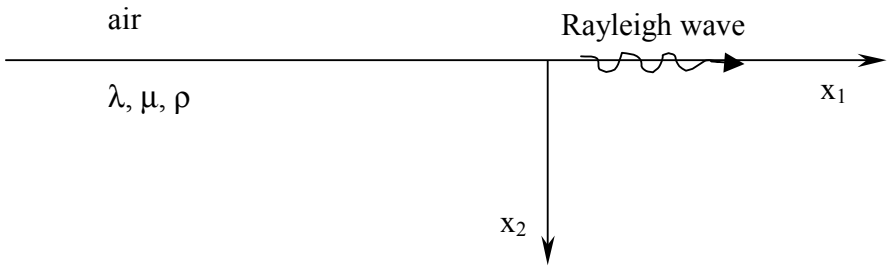

Figure 1.2: Rayleigh waves in a homogeneous half-space

With the aim of establishing the existence of the Rayleigh wave we want to know if a perturbation of the type:

$$u_1 = Ae^{-bx_2}e^{ik(x_1-ct)} \tag{1.34a}$$

$$u_2 = Be^{-bx_2}e^{ik(x_1-ct)} \tag{1.34b}$$

can satisfy the stress-free boundary condition at the free surface of the half-space, when no other kinds of wave are present.
In (1.34a, b) A, B and b are constants to be determined, with the constraint of a positive value for b, so that an exponential decay occurs going away from the free surface. Substituting the solutions (1.34a, b) into the equations of motion (1.12) two values of b are obtained for non trivial solutions of A and B:

$$b_1 = k \cdot \left[1 - \left(\frac{c}{c_P}\right)^2\right]^{\frac{1}{2}} \qquad b_2 = k \cdot \left[1 - \left(\frac{c}{c_S}\right)^2\right]^{\frac{1}{2}} \tag{1.35a, b}$$

that are positive only if :

$$c < c_S < c_P \tag{1.36}$$

This means that if Rayleigh wave exists it must propagate with a speed c slower than S and P waves. A more general expression can be used for the displacements (1.34a, b), by means of the (1.35a, b):

$$u_1 = \left[A_1 e^{-b_1 x_2} + A_2 e^{-b_2 x_2}\right] e^{ik(x_1 - ct)} \tag{1.37a}$$

$$u_2 = \left[-\frac{b_1}{ik} A_1 e^{-b_1 x_2} + \frac{ik}{b_2} A_2 e^{-b_2 x_2}\right] e^{ik(x_1 - ct)} \tag{1.37b}$$

By imposing the stress-free boundary condition and looking for non trivial solutions of A_1 and A_2 the following Rayleigh equation is reached:

$$\left(2 - \frac{c^2}{c_S^2}\right)^2 - 4\left(1 - \frac{c^2}{c_P^2}\right)^{\frac{1}{2}}\left(1 - \frac{c^2}{c_S^2}\right)^{\frac{1}{2}} = 0 \tag{1.38}$$

or in another form, introducing the concept of slowness s as the inverse of the phase velocity for surface, P and S waves respectively:

$$s = \frac{1}{c} \qquad s_P = \frac{1}{c_P} \qquad s_S = \frac{1}{c_S} \tag{1.39a, b, c}$$

$$R(s) = (2s^2 - s_S^2)^2 + 4s^2(s_P^2 - s^2)^{\frac{1}{2}}(s_P^2 - s^2)^{\frac{1}{2}} = 0 \tag{1.40}$$

It is well established that (1.38) admits only one real and positive root $c=c_R<c_S$, that varies monotonically from $0.862 \cdot c_S$ to $0.955 \cdot c_S$ as the Poisson ratio increases from 0 to 0.5 according to the approximate formula (Achenbach, 1999):

$$c_R = \frac{0.862 + 1.14\nu}{1 + \nu} \cdot c_S \tag{1.41}$$

Since the wave number k does not appear in (1.38) Rayleigh waves in a homogeneous half-space are not dispersive.
Coming back to the displacements for Rayleigh waves, we can observe from fig.1.3 that the horizontal and the vertical components are 90° out of phase, so that during the propagation they generate an ellipse. The major axe of the

ellipse is parallel to the free surface down to a depth of about 0.2λ, where the horizontal displacement changes its sign and the orientation of the axes and the sense of going around of the ellipse are reversed. It can also be realized how the displacements drop down with increasing depth, so that the motion, due to Rayleigh wave, is confined in the upper side of the half-space, inside a length of about 1.5 wavelengths λ (see fig.1.4).

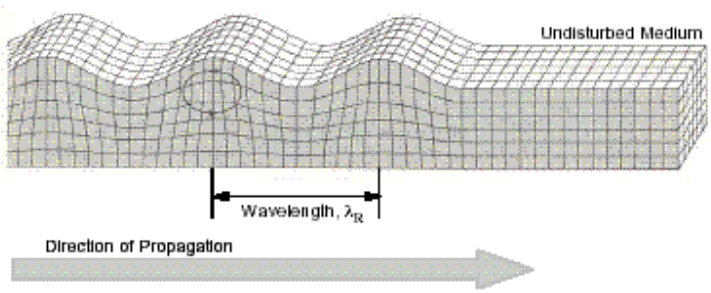

Figure 1.3: Rayleigh disturbance on the free surface of a homogeneous half-space (Bolt, B.A., 1976).

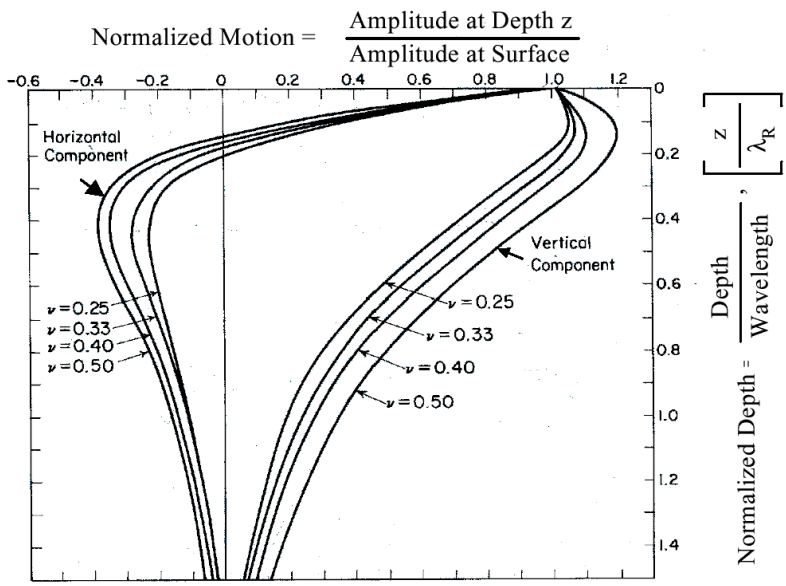

Figure 1.4: Variation of horizontal and vertical normalized components of displacements induced by Rayleigh waves with normalized depth in a homogeneous isotropic, elastic half-space (Richart et al.,1970).

1.4 Layered half-space

In the previous sections we have seen which types of waves can propagate into an unbounded region, i.e. P, SV, SH waves and in a homogeneous half-space, i.e. P, SV, SH and Rayleigh waves . We have also studied what happens at an interface between two half-spaces with different characteristics: mode conversion, Stoneley waves. We know that when a P or S wave encounters an interface, several kinds of waves can be generated, depending upon the properties of the two half-spaces. In a general situation part of the energy carried by the incident wave is reflected back and the remaining part passes through the interface, sometimes another part travels in the vicinity of the interface, that behaves like a store of energy. Anyway when a layered half-spaced is considered, with *n* infinitely horizontal, homogeneous, linear elastic layers overlying an infinite half-space, it can be imagined how complicate it becomes to account for all the possible waves (see fig.1.5).

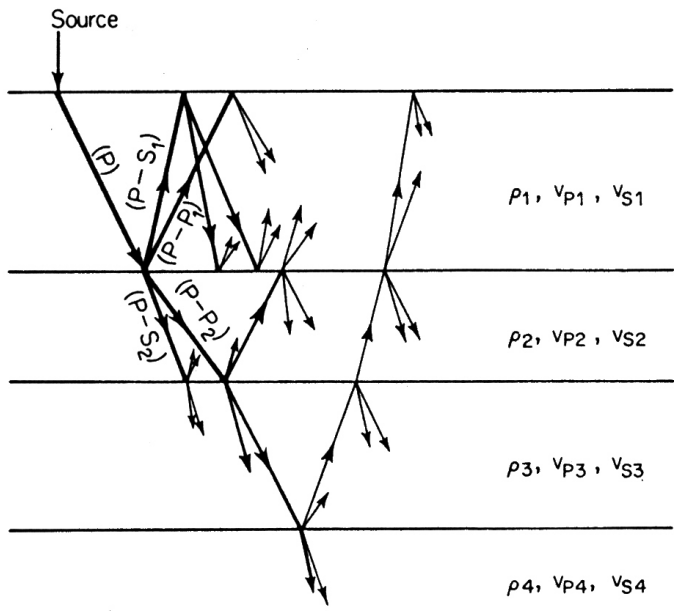

Figure 1.5: Multiple interaction among incident, reflected and transmitted waves in a layered half-space: mode conversion phenomenon (from Richart et al.,1970).

What happens is an interaction among all the incident, reflected and transmitted waves inside each i-th layer, that combine together canceling or reinforcing each other, giving raise to destructive or constructive interference.
In order to explain this concept, look at the fig.1.6

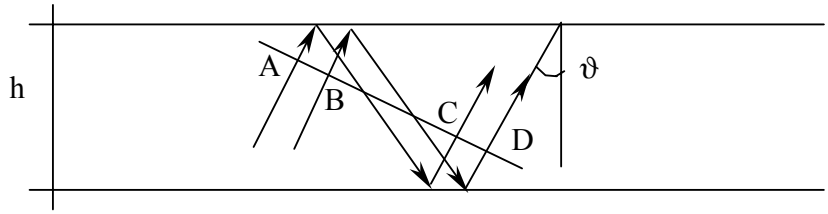

Figure 1.6: Constructive interference of reflected rays in a wave-guide (Tolstoy, 1973, Ewing et al, 1957).

If we consider a plane wave reflected back and forth inside a layer, after n reflections any pair of neighboring elements of a wave-front will remain in phase, that is:

Path A to C = path B to D = $n\lambda$

in which λ is the wavelength of the wave.

Rigorously speaking the equations of motion must be written for each i-th layer using the mechanical properties of the layer. Also the continuity of displacements and stresses at the interfaces must be imposed. For each layer 4 independent constants have been adopted: shear wave velocity V_{Si}, thickness h_i, Poisson's ratio ν_i and mass density ρ_i (see fig.1.7). The radiation condition is also assumed (that is the perturbation disappears at infinite depth), in addition to the stress-free condition on the free surface (if no external loads are applied) and the boundary-initial conditions (that need to be specified for each situation).

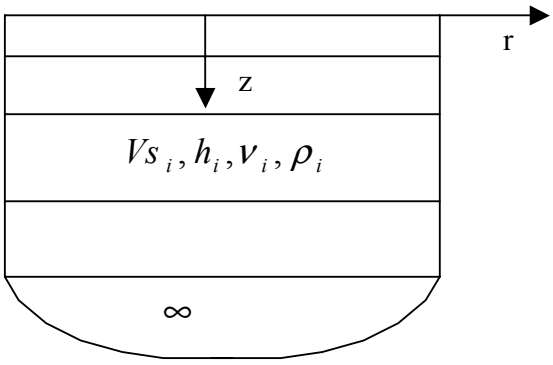

Figure 1.7: Model of the layered half-space

1.4.1 Love waves

Before going on with the analysis of the Rayleigh waves and the other types of surface waves in the vertical plane, Love waves deserve to be mentioned. Love waves are horizontally polarized waves that propagate near the free surface of a layered half-space (see fig.1.8).

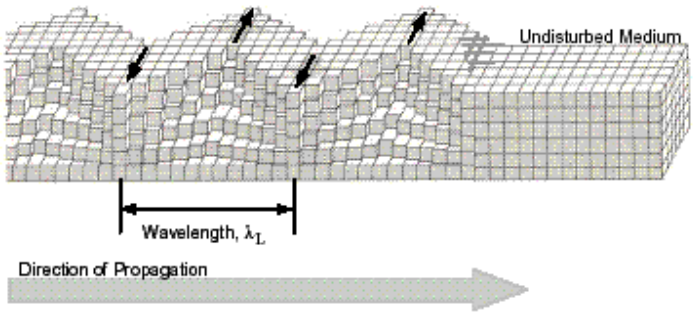

Figure 1.8: Love wave on the top of a layered half-space (Bolt, 1976).

In fact it can be proved that this type of wave cannot exist in an infinite homogeneous half-space (Aki and Richards, 1980, Pujol, 2002), and at least one layer is necessary for their existence. The reason is that Love waves are the result of the constructive interference among incident and multiple reflected SH waves. It is interesting to notice that, under the hypothesis of linear elasticity in an isotropic medium, an incident SH wave generates only reflected and transmitted SH waves and mode conversion does not occur, for the

equation of motion for horizontal displacement is uncoupled. This aspect could be properly used in soil characterization, since during the experiments, only horizontally polarized motion should be measured, if a perfect horizontal source is employed. Even if it will not be shown herein, it is reminded that Love waves are dispersive, that is the phase velocity depends on the frequency associated to the wave, how it will be better explained in the next section 1.4.3.

1.4.2 Head waves

Head waves are also referred as "refraction arrivals" or "Lateral waves" and the "seismic refraction" method for determining the thickness and the body velocities of a layered half-space are based on these types of waves. When an incident wave impacts an interface between two layers with different velocities at the total internal reflection angle δ (see fig.1.9), a disturbance is generated, that travels along the interface with the velocity $v_2 > v_1$ of the lower layer.

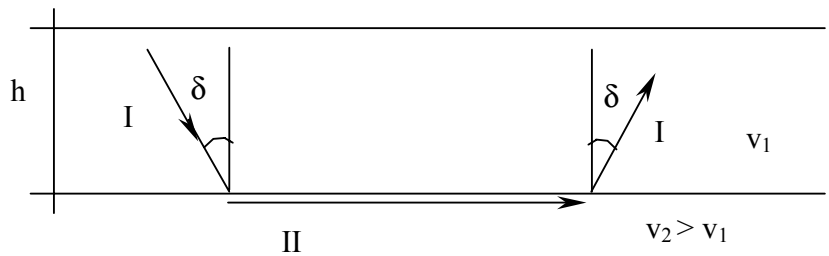

Figure 1.9: Head wave generated at an interface

On the interface the disturbance produces a new wave, that arises from the interface at the same angle δ and has got an amplitude proportional to the amplitude of the incident wave (Brekhovoskikh, 1960).

1.4.3 Rayleigh waves and geometrical dispersion relation

Our interest will be on Rayleigh waves in a layered half-space, since, as it will be shown, the geometrical dispersion of these waves in such a system constitutes a powerful tool for determining the geometrical and mechanical properties of the site (Rix, 2000, Lai, 1998, Foti, 2000). We want to investigate whether in a layered half-space, as previously described (see fig.1.7), Rayleigh waves can exist in absence of any external loads. Several ways have been followed by researchers in the past, for answering this question, but the most

common methods are the *propagator matrix methods* (Kennett, 1983, Aki and Richards, 1980) and the *method of reflection and transmission coefficients* (Kennet, 1974, Aki and Richards, 1980). The *transfer matrix methods* (Thomson, 1950, Haskell, 1953) and the dynamic stiffness matrix method (Kausel and Roesset, 1981) belong to the first class of methods. In the *transfer matrix method*, without loss of generality, a plane time harmonic perturbation is assumed as solution for the equations of motion in the vertical plane that are written for each layer. Successively by imposing the continuity of the velocities and the stresses at the interface between the n-th layer and the (n-1)-th layer, enables one to write a recursive formula that correlates stresses and displacements in one layer. The matrix that allows for such a correspondence is the transfer matrix of the layer. The quantities of the first layer and of the half-space can be related, by means of the continuity of displacements and stresses at the interfaces. If the amplitude of the perturbation is made exponentially decay to zero at infinite depth (radiation condition) and the stresses at the free surface of the layered half-space are set equal to zero, a system of equations is obtained. In order to have non trivial solutions, the determinant of the matrix of the coefficients of this system, the so called global transfer matrix, must vanish. In this way the Rayleigh secular function (1.45) is originated. The Rayleigh secular function is an implicit relationship among the geometrical-mechanical properties of the layered half-space and the frequency f and the wave number k of the possible perturbations, that we want to find into the system under the above specified conditions:

$$R(Vs_i, h_i, \nu_i, \rho_i, k, f) = 0 \qquad i = 1 \div n+1 \tag{1.42}$$

The *stiffness matrix method* is conceptually the same as the transfer matrix method, but it offers the advantages given by the use of the tools of the structural analysis.

By using the transfer matrix of the generic i-th layer, the equilibrium of the force acting on the i-th layer is assured and the stiffness matrix of the layer is defined as the link between the forces and the displacements at the two interfaces of the i-th layer. Then, using the rules of the structural analysis, the stiffness matrices of all the layers and the half-space are combined together at the nodal interfaces, to get the dynamic equilibrium of the whole system:

$$\overline{F} = [S] \cdot \overline{X} \tag{1.43}$$

in which $\overline{F}$ and $\overline{X}$ represent the external loads and the displacements at the interfaces of the layers. Even in this method in-plane time-harmonic solution has been assumed, so that the stiffness matrix S includes both inertial and elastic contributions expressed in terms of the geometrical and mechanical properties of the system V_{Si}, h_i, ν_i, ρ_i (i=1÷n+1) and of the circular frequency ω and the wave number *k*.
Since we are interested in studying the free vibrations of the system, the external loads vector is set equal to zero:

$$\overline{F} = 0 \tag{1.44a}$$

and the resulting homogeneous eigenvalue problem is considered:

$$0 = [S] \cdot \overline{X} \tag{1.44b}$$

In order to look for non trivial solutions, the determinant of the stiffness matrix S must vanish:

$$\det[S] = 0 \tag{1.45}$$

In this way the Rayleigh geometrical dispersion relation is again reached in implicit form (1.42). In Appendix C the explicit analytical expression of the Rayleigh dispersion relation will be evaluated for the case of a single layer over an infinite half-space. In chapter 2 this simple system will be analyzed more in detail.
Now we will focus on the roots of the Rayleigh dispersion relation (1.42), also called period equation of Rayleigh. Generally the roots are searched by numerical techniques, fixing a value of frequency f_0 and looking for the wave numbers that satisfy (1.42). The Rayleigh dispersion relation is a multi-valued function, so for a fixed frequency several wave numbers may exist that solve (1.42). Each solution is an eigenvalue and physically represents a simple wave, called Rayleigh mode, that can propagate in the system under all the conditions that have been previously specified. For a fixed circular frequency ω_0 the first mode corresponds to the greatest wave number k_1 and it is the fundamental Rayleigh mode. The other wave numbers define the higher Rayleigh modes and are characterized by smaller wave numbers. For a better comprehension of these concepts an example (case A) will be introduced.
Consider the system whose characteristics are reported in the table 1.2 below:

Layer	Thickness h(m)	Vp (m/s)	Vs (m/s)	Mass density (Kg/m^3)
1	5	600	350	1800
2	10	700	400	1800
Half-space	∞	800	450	1800

Table 1.2: Characteristics of the system for Case A

If we plot the Rayleigh dispersion relation in the frequency- wave number domain (see fig.1.10), we observe that for very low frequencies at least one root or wave number k exists.

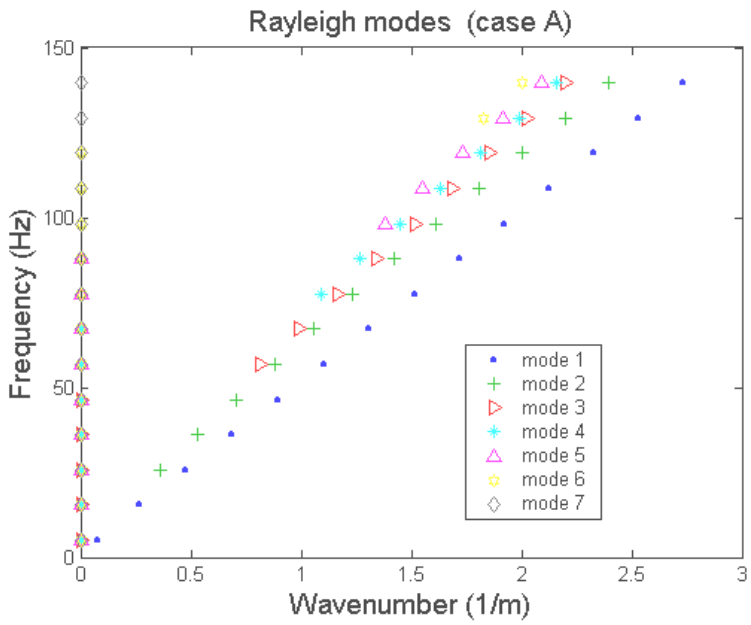

Figure 1.10: Dispersion Relation and Rayleigh modes for Case A.

It corresponds to the first or fundamental mode and in fig.1.10 is represented by blue dots.
For frequencies greater than about 25 Hz a second root is found, that is the second mode (green plus) and so on for the other higher modes. It is evident that each higher mode appears above a certain frequency called *cut-off frequency*. The cut-off frequency increases as the mode number increases too and the mode cannot propagate below this critical frequency, since it does not

carry energy at all. It is important to underline that we have introduced the concept of Rayleigh modes as the roots of the dispersion relation (1.42), so instead of fixing a value of frequency and looking for the wave numbers that satisfy (1.42), we can also hold a fixed wave number and search all the frequencies that solve (1.42).
This idea is easy to understand if in the fig.1.10 we enter with a particular wave number, say k=1/m and intersect the first three modal curves, to which three different frequencies correspond. It should be noted that the 7-th mode has got a cut-off frequency of about 150 Hz, hence it is not visible on the graph.
For each mode we can define modal quantities, that refer to phase velocity, group velocity, displacement and energy. If we imagine to keep constant a value of frequency f_0, each mode is individuated by its wave number and the modal phase velocity becomes:

$$c_j = \frac{\omega_0}{k_j} = \frac{2\pi f_0}{k_j} \tag{1.46}$$

Another quantity needs to be introduced, that is the group velocity defined as:

$$\frac{\partial \omega}{\partial k} = c + k\frac{\partial c}{\partial k} \tag{1.47}$$

For a fixed value of frequency the group velocity is:

$$U_j = \frac{\partial \omega_0}{\partial k_j} \tag{1.48}$$

Looking at the fig.1.11 the geometrical meaning of both phase and group velocities is presented. At a point P on a generic j-th modal curve the phase velocity is the tangent of the angle δ, instead the group velocity is the tangent of the angle β made by the tangent to the modal curve in P and the horizontal line.
The physical meaning of these two velocities is explained in Appendix B, here we only say that the phase velocity describes how fast the surface of constant phase, associated to the perturbation, is moving. The group velocity has got a cinematic and an energetic definitions, so it may represent either the speed of a group of waves travelling together or the velocity of the energy carried by the disturbance.

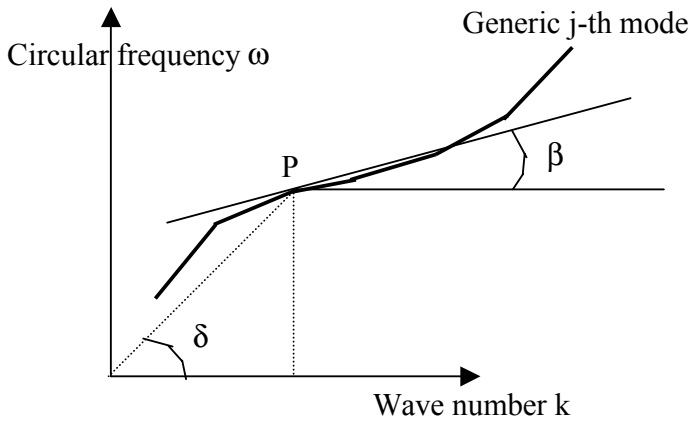

Figure 1.11: Geometric explanation of phase and group velocities in the frequency-wave number domain.

Now that the significance of phase velocity has been clarified, it is possible to show the Rayleigh dispersion relation for the same case A in the phase velocity-frequency domain (fig.1.12):

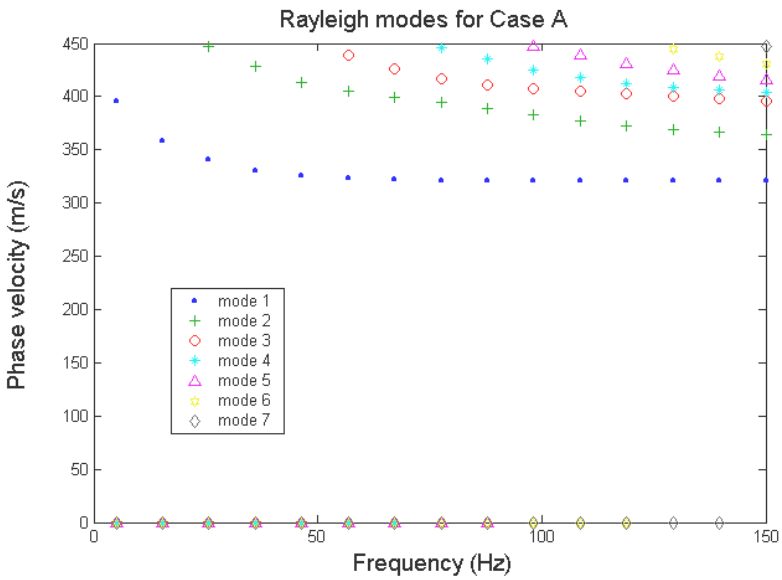

Figure 1.12: Rayleigh modes for case A.

In this representation some interesting aspects can be underlined. First of all for a given frequency each mode is characterized by its own velocity and this is why we talk of dispersion. Actually the dispersion of waves is always present in a system when waves of different wavelengths travel with different speeds. So if the phase velocity is a non constant function of the frequency, then dispersion exists and, as a consequence, group and phase velocities are different.
In fig.1.12 the cut-off frequencies for the higher modes are again visible. It can also be observed that, at the cut-off frequency, all the modes have got a phase velocity equal to the shear wave velocity of the half-space $V_{S\infty}$=450 m/s. The reason is that at the cut-off frequency the generic j-th mode has got its greatest wavelength λ_{max} according to the relationship between spatial and temporal scales:

$$c = \lambda \cdot f \tag{1.49}$$

For the second mode of the case A the maximum wavelength is:

$$\lambda_{\max} = \frac{c}{f_{cut-off}} \cong \frac{450 m/s}{25.7 Hz} = 17.5 m \tag{1.50}$$

Since Rayleigh waves travel on the surface inside a belt of about 1-2 wavelengths, the disturbance with a great wavelength is mainly travelling through the deepest layer. On the other hand for very high frequencies the wavelength is so small, that it is as if the disturbance does not feel the presence of the deeper layers and travels through the surface layer with the same phase velocity that it would have in a homogeneous half-space with the same characteristics of the first layer. In fact as the frequency increases to infinity, all the modal phase velocities tend to the value given by (1.41), where c_S =V_{S1}=350m/s and ν=0.24:

$$c = \frac{0.862 + 1.14 \cdot 0.24}{1 + 0.24} \cdot 350 m/s = 320 m/s$$

The figure 1.13 well illustrates the physical insight behind these observations:

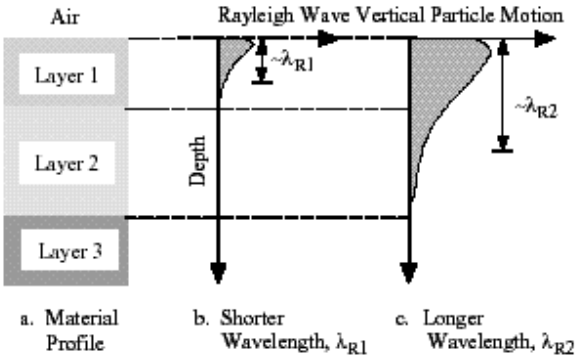

Figure 1.13: Depth sampled by Rayleigh waves with different wavelengths (Stokoe II and Santamarina, 2000)

Waves with different wavelengths give information on the medium by sampling its characteristics at different depths. Of course a medium-size wavelength, that involves all the layers, informs about averaged properties. This feature constitutes the basis for soil characterization in practice.

1.4.3.1 ***Some aspects about the search of the Rayleigh modes***

The code used for solving the eigenvalue problem (1.45) and finding the roots of the geometrical dispersion relation (1.42), is based on the *method of Reflection and Transmission coefficients* and it has been first implemented by (Kennet, 1974) and successively modified by several researchers (Luco and Apsel, 1983, Apsel and Luco, 1983, Chen, 1993, Lai 1998) and finally properly improved by the Author. The Rayleigh dispersion relation is obtained setting a complex function equal to zero. In order to find the zeros of this complex function, the frequency is kept constant and the wave numbers, that make the absolute value |R| of this complex function equal to zero, are searched

$$| R(Vs_i, h_i, \nu_i, \rho_i, k, f) | = 0 \qquad i = 1 \div n+1 \tag{1.51}$$

Actually the code fails in finding the roots in some particular conditions for certain frequencies. As a consequence Rayleigh modes appear to be discontinuous, as documented and justified by (Lai, 1998). This mistake

causes a wrong evaluation of all the modal quantities, hence the code does not work correctly in these cases and the results are not faithful. The jumps in modal curves usually happen when the medium is characterized by an irregular stiffness profile, that is the stiffness does not increase monotonically with depth, but there is at least one softer layer trapped between two stiffer ones.
Consider for example the system indicated as case B, which is described in table 1.3:

Layer	Thickness h(m)	Vp (m/s)	Vs (m/s)	Mass density (Kg/m^3)
1	5	400	700	1800
2	3	300	500	1800
Half-space	∞	450	800	1800

Table 1.3: Characteristics of the system for the case B.

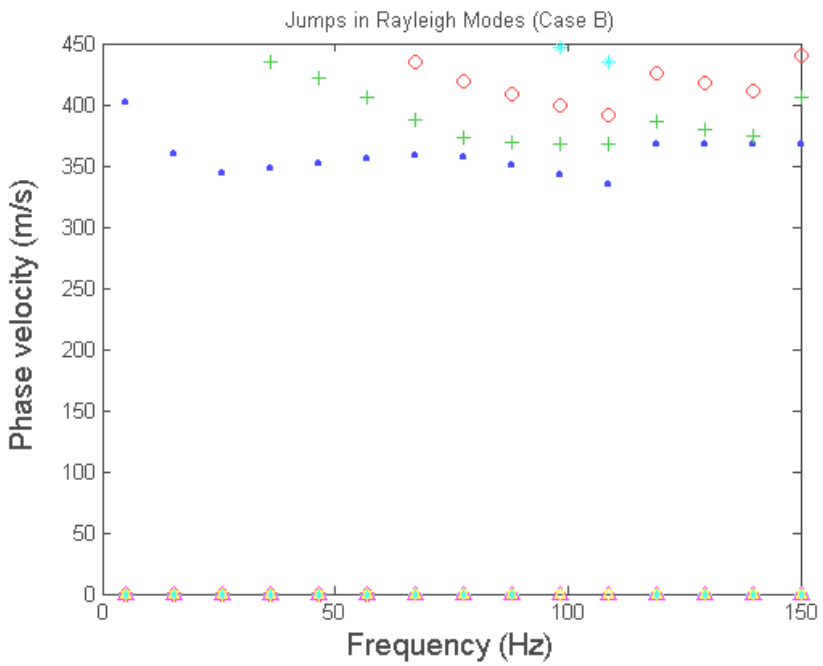

Figure 1.14: Failure of the original code in finding Rayleigh modes

The code fails in searching the modes, since the phase velocity of the 1st mode is not found for frequencies greater than f =103Hz and its value is taken equal

to the phase velocity of the 2nd mode, so that a jump or sharp discontinuity exists, which is transferred to all the higher modes (fig.1.14).
This problem exists even at higher frequencies. This is due to the particular shape of |R|. Looking at the fig.1.15 there are three wave numbers for which |R|=0 at the frequency f =103 Hz: k_4=1.46 1/m, k_3=1.63 1/m, k_2=1.75 1/m. In correspondence of all these zeros |R| is not a regular function, in fact these are spire points. It is not said that the function |R| has got a regular tendency inside the ranges delimitated by its zeros, in fact between k_3=1,6 1/m and k_2=1,75 1/m |R| has another spire point on its relative maximum. The most interesting aspect is that the function |R| has got a discontinuity at k_1=1,9 1/m (fig.1.15), that seems to be a vertical asymptote (fig.1.16), , despite it is derivable and concave and appears regular for k>k_2.

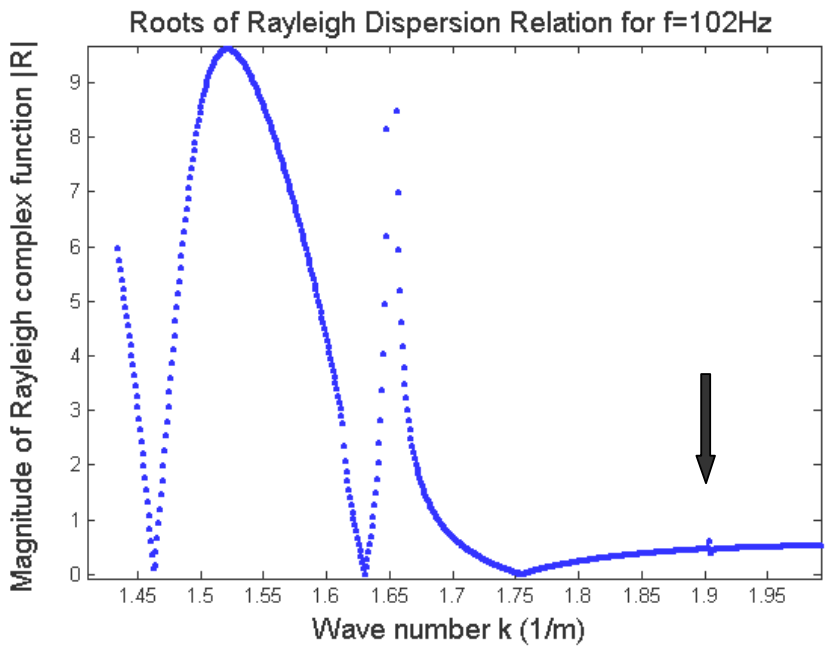

Figure 1.15: Roots of Rayleigh dispersion Relation for f=102Hz (case B)

As the wave number approaches the value k_1=1,9 1/m, the function |R| shows two branches: the one on the right respect to k_1 goes to zero, the one on the left side goes to a great value, probably to infinity.

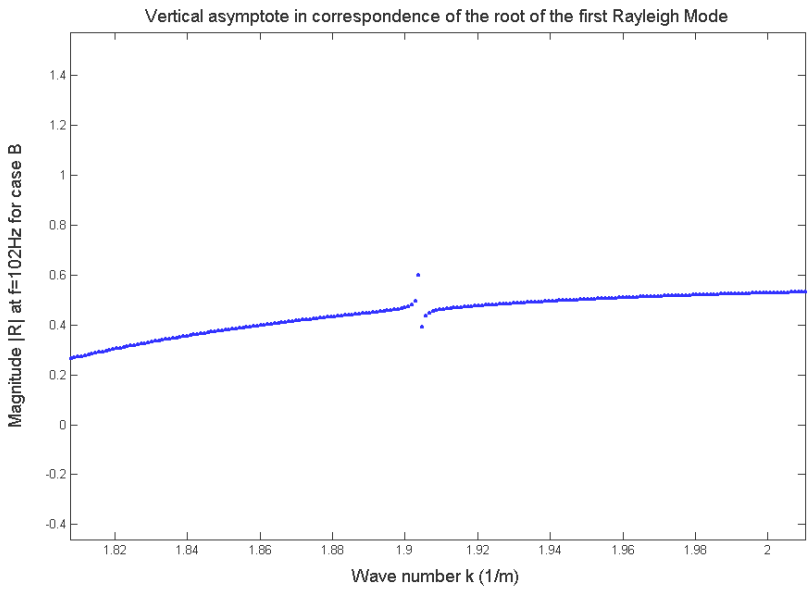

Figure 1.16: Vertical asymptote in correspondence of the fundamental root of the Rayleigh Dispersion Relation at a frequency f=102Hz.

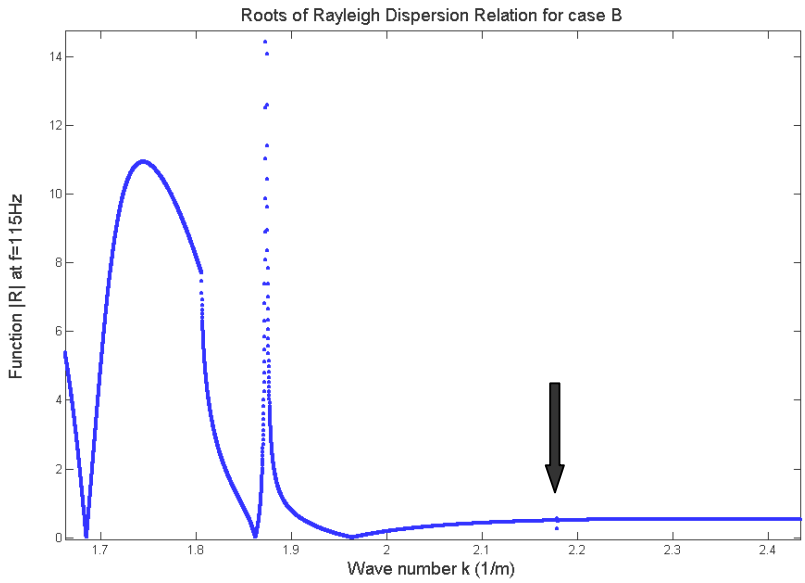

Figure 1.17: Absolute value of the Rayleigh Dispersion Relation at the frequency f=115Hz for case B

It is worthy to observe that at the frequency f=103 Hz the root k_1=1,9 1/m is still found, but at greater frequencies, for example at f=115 Hz, the subinterval Δk used for the search is not sufficiently small to find that zero. To solve this problem we need to reduce the subinterval Δk so that the discontinuity will be found (fig.1.17). With a zoom around the discontinuity, it can be realized (fig.1.18) that the discontinuity is again characterized by a vertical asymptote with two different branches around it.

We want to give an idea how much the subinterval Δk needs to be reduced to find all the zeros. The initial number of points used to obtain Δk is NUM=200, with $\Delta k=(k_{max}-k_{min})/NUM$. With NUM=$10^3$ at f=134 Hz the discontinuity is not visible yet. Only by both increasing NUM=10^4 and reducing Δk to $\Delta k'=(2,7-2,6)/10^4 = 10^{-5}$1/m, it is possible to see the discontinuity.

After studying several systems for different frequencies, it can be said that as frequency increases, |R| has got more than one zero characterized by a discontinuity and it does not seem possible at the moment to establish a priori which zero needs a smaller subinterval Δk to be found. In fact it might happen that the 1st and 3rd modes jump at some frequencies for a fixed Δk, but the 2nd and higher modes do not, instead the 2nd mode might have a discontinuity stronger than the 3rd mode at different frequencies.

In other words the discontinuity of the generic mode jth is more or less sharp compared to that one of the other modes, depending upon the frequency.

To solve the problem of mode-jumps we need to find out the discontinuity near the root. At the moment a well known strategy of establishing the order of appearance of such discontinuities is not available, nevertheless an automatic procedure to correctly find the roots has been developed.

The code has got some disadvantages as it needs large time to exactly find all the roots for every kind of medium. It is important to underline that the wave number root of the Rayleigh Dispersion Relation must be found with high accuracy ($\Delta k=10^{12}$ 1/m), otherwise at frequencies sufficiently high, modal quantities like group velocity and displacement amplitude show an irregular and not reliable tendency due to any numerical instability. In fact the group velocity is evaluated by calculation of energy integrals, that are of the order of 10^{-12} for certain frequencies, hence a small inaccuracy in the wave number causes the group velocity to considerably change. Because the group velocity appears at the denominator of the displacements the mistake is transferred as a consequence. After solving the problem of the jumps, the real modal curves can be plotted. For the case B the Rayleigh modes are reported in fig.1.19. It is clear that the behavior of the modal curves are now reliable and continuous.

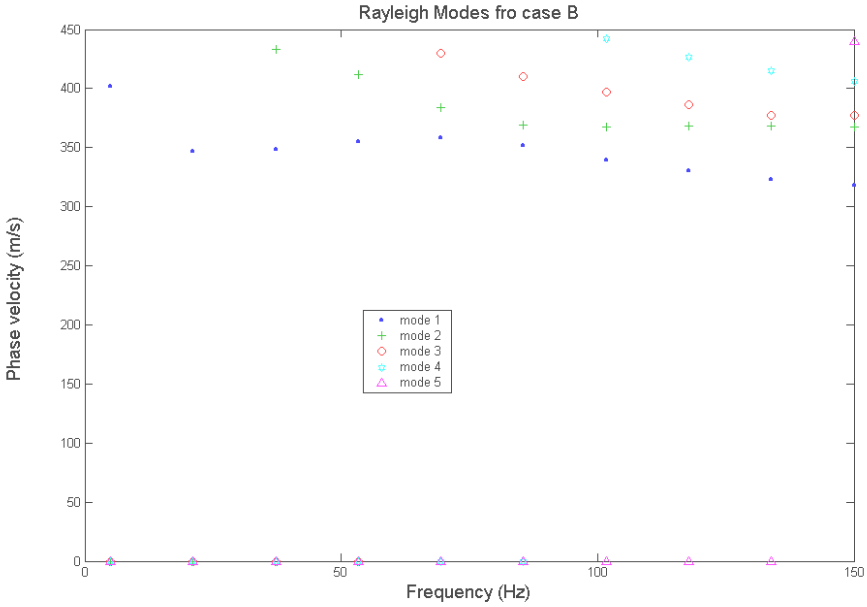

Figure 1.18: Two branches of the Rayleigh Dispersion Relation at the frequency f=115Hz in correspondence of the 1st root.

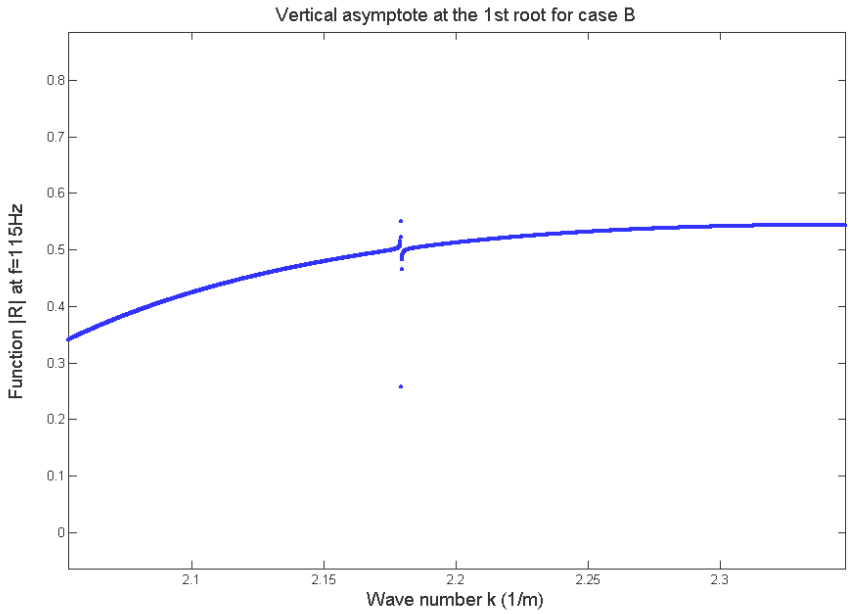

Figure 1.19: Correct Rayleigh Modes for case B.

Before concluding this paragraph the author wants to make some considerations about the existence of the jumps in the function absolute value of the complex Rayleigh dispersion relation |R|. Even if, neither a mathematical explanation nor a physical sense have be given yet, in the opinion of the author the discontinuities are not purely due to the way the Rayleigh dispersion function has been built. Evaluating the same function |R| by means of the Stiffness Matrix method, similar results have been found, since the function |R| shows an infinite value for certain frequencies. It seems that the same problem has been encountered by other researchers, who have not reached yet an agreement about the meaning of such behavior (H.R. Hermann, 2000).

1.5 Waves generated by a vertical point source on the free surface

Up to now we have not specified how the several types of waves had been generated and we have limited the discussion to time harmonic plane waves. In fact the treatment of the Rayleigh waves has been conducted under the hypothesis that no external forces had been applied on the system.
Now we want to know what happens when an external load, say a vertical point source, is applied on the free surface of the half-space. About this issue a huge number of references can be found in literature (Lamb, 1904, Ewing et al, 1957, Achenbach, 1999, Richart et al, 1970), so we will give a brief remind of the basic concepts.
Consider as first case a time harmonic vertical load acting on a circular footing on the free surface of a homogeneous linear elastic, isotropic half-space (see fig.1.20).

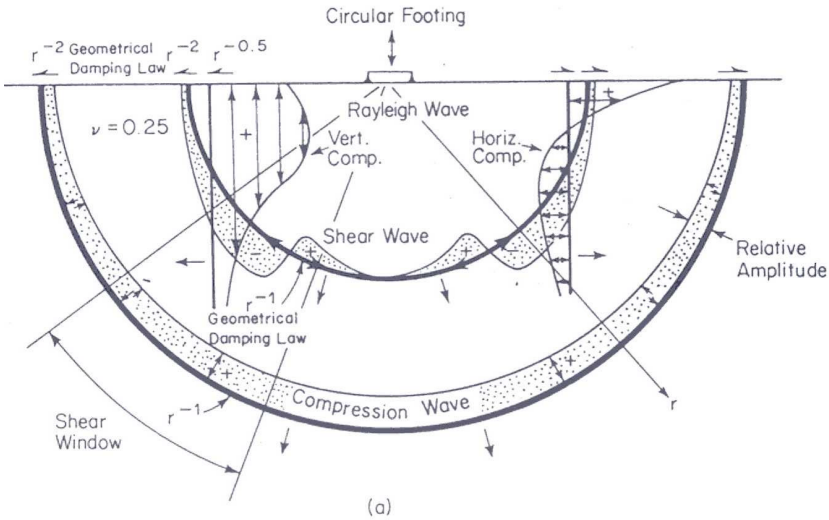

Wave Type	Per Cent of Total Energy
Rayleigh	67
Shear	26
Compression	7

Figure 1.20: Waves generated by a vertical time harmonic load on a circular footing on the free surface of a homogeneous half-space(a) and energy distribution among them(b) for a Poisson ratio ν=0.25.(Richart et al., 1970).

As it can be seen from the figure, spherical P and S waves spread out from the point source, followed by Rayleigh waves, that propagate along cylindrical wave-fronts. The different shape of the wave-fronts causes a different geometrical attenuation of the amplitudes associated to body and Rayleigh waves. In fact the energy density e is proportional to the amplitude square:

$$e \propto A^2 \tag{1.51}$$

and if no material dissipation exists, the amplitude of Rayleigh waves decays as $\frac{1}{\sqrt{r}}$, instead body waves attenuate as $\frac{1}{r}$, where r is the distance from the source. Also the distribution of the energy input by the external load is not equal among P, S and Rayleigh waves, but Rayleigh waves take about one third of the total energy depending on the Poisson ratio.
These are the reasons for which in the far field the main contribution to the displacement field on the free surface is given by Rayleigh waves and the effects of body waves can be neglected. This is one of the reasons for which only the contribution of the Rayleigh waves is considered in theinversion procedure proposed in this research.

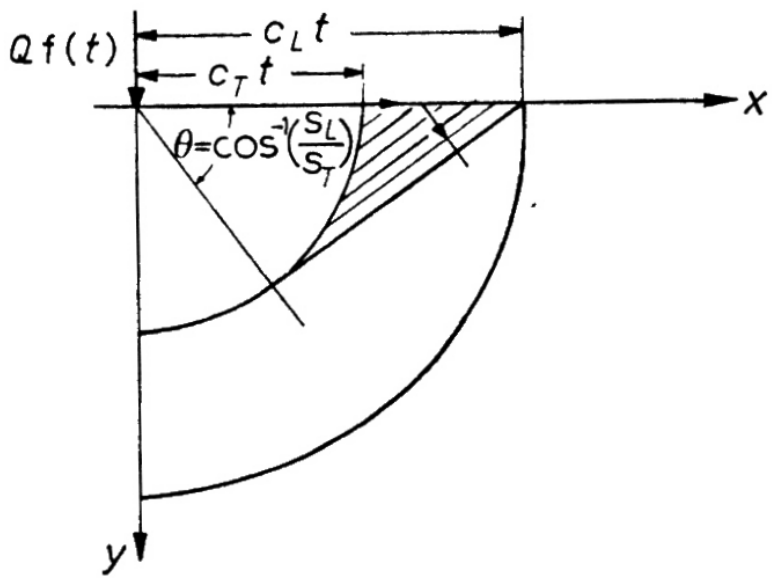

Figure 1.21: Head Waves between P and S wave fronts.

Since an external load is applied, the mathematical problem associated to the physics of the system is not any more a homogeneous eigenvalue

problem and it can be demonstrated that the total displacement field due to Rayleigh waves can be expressed in terms of a proper combination of all the Rayleigh modes of vibration, found in the previous section (Aki and Richards, 1980).

Actually the elasto-dynamic theory, in the case of a transient vertical line load, predicts the existence of head waves on the free surface of a homogeneous half-space, so that P waves can satisfy the stress free boundary conditions. As shown in fig.1.21, head waves are comprised between the wave-fronts of P and S waves (Achenbach, 1999).

If an impulsive point load is considered, under the assumption that the super position principle holds, it can be decomposed into its harmonic components and the final response can be obtained by means of the Fourier's theorem.

In the case in which the half-space is not homogeneous, but it presents a stack of horizontal layers, all the complications due to multiple reflections and refraction and mode conversions arise. We only anticipate that, under suitable conditions, concerning the stratigraphy and the position of the table water, refracted or head waves and, with more difficulty, reflected waves can be discerned and usefully utilized in seismic reflection and refraction methods to infer information about the site properties. To this issue is dedicated the Chapter 2.

Chapter 2

Soil Characterization using Surface Waves

Introduction

This Chapter starts with a short remind of the seismic methods widely used in geophysical field for soil characterization. Then a historically ordered perspective about the surface wave techniques, used in the geotechnical scale, will precede the more advanced procedures, developed nowadays for the evaluation of both the experimental and the theoretical dispersion relation of Rayleigh waves. After comparing the different techniques, the f-k method, based on a multi-sensors array, will be discussed as tool for determining the dynamic soil properties Vs and Ds. At the end a new procedure will be proposed, for computing the theoretical apparent dispersion relation. The new method is consistent with the experimental f-k technique, used to determine the experimental dispersion relation, and offers some advantages for an automatic inversion procedure, that will be presented in the next Chapter 3. The last part of the Chapter 2 is devoted to the frequencies and the wave numbers of resonance of a layered half-space for travelling Rayleigh waves. In particular a sensitivity analysis has been conducted for the case of a single layer resting on the half-space and a simple formula has been found, that correlates the frequencies and the wave numbers of resonance to geometrical and mechanical properties of the system.

2.1 Seismic Reflection and Refraction methods

In Chapter 1 we have said that the existence of the interfaces into a layered half-space is the cause of reflections and refractions of incoming waves. For this reason all the possible contributions to the displacement field generated by an impulsive vertical surface source are found on the free surface in the time-space domain. Two techniques, that are well known to geophysicists, are the *seismic reflection and refraction methods*.

The refraction method consists of recognizing the first arrivals of both the direct waves and the refracted waves. The basic assumption is that the

second layer has got a wave velocity greater than the first one, so that after a certain time (or distance x_c) the refracted waves, that travel through the second layer, anticipate the direct waves (fig.2.1):

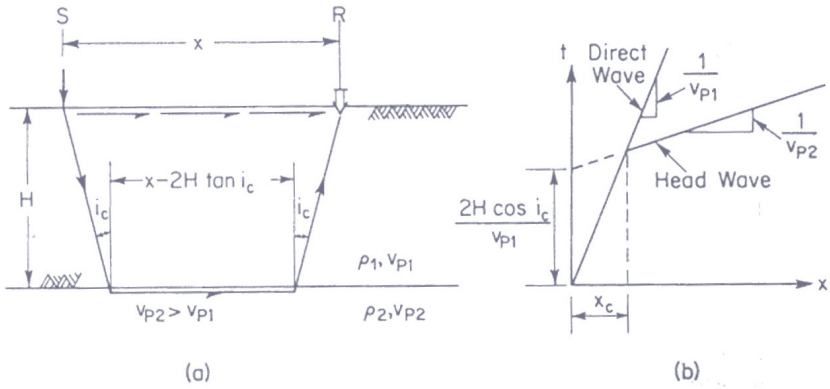

Figure 2.1: Seismic Refraction method: refracted P wave detected at the free surface(a) and time-space representation of the first arrivals (b).(Richart et al, 1970).

It is straightforward to evaluate the thickness H and the velocities V_1 and V_2 from the slope of the two curves in fig.2.1b, once direct and head waves have been clearly individuated in the time-space representation. This kind of test can be performed using either P or SH waves, and there are some limitations, due to the presence of a stiffer layer or if a thin layer overlies a very stiff layer. In the case a stiffer layer exists, no information can be get from layers deeper than that, because refracted waves below the stiff layer travel more slowly than the waves through the stiff layer. When a thin soft layer overlies a very stiff layer, it may happen that the refracted waves from the stiffer layer anticipate the refracted waves travelling through the soft layer, so that the last one is hidden. When working with P waves an additional limitation is represented by the position of the water table. The water table does not allow to measure the so called 2nd P wave velocity, associated to the skeleton as predicted by (Biot, 1956), if the 2nd P wave velocity is less than the velocity of the 1st P wave into the water. Hence the 1st P wave is the only one revealed at a depth greater than the water table (see fig.2.2). In fact the 2nd P wave travels through the skeleton at a lower speed and arrives after the 1st P wave, that travels through the fluid and covers the first arrivals of the 2nd P wave. This limitation on the other hand allows for recognizing the existence and the position of the water table. Obviously these circumstances are true only if the skeleton is less compressible than the fluid, as it is the case in most of the soils.

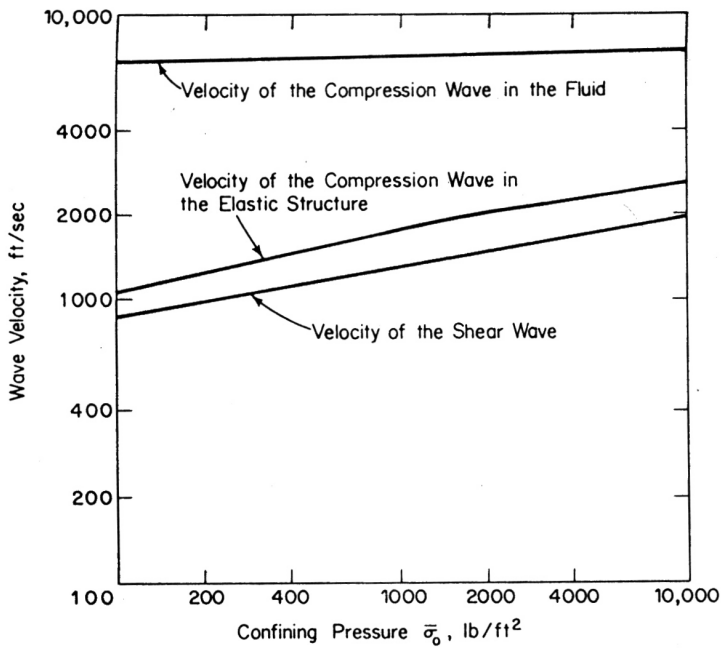

Figure 2.2: Body wave velocities in saturated soils: P waves of the first and second kind and S wave. (Richart et al., 1970).

Nevertheless it may happen that the 1st P wave through the fluid be slower than the 2nd P wave through the skeleton, as it occurs for some rocks. In this case the presence of the water table does not represent an obstacle for soil characterization, provided that no softer layers are between the water table and the bedrock.

The reflection method is based on the measurement of the first arrivals of the reflected waves. Usually the reflected waves have an hyperbolic path in the time-space domain (see fig.2.3), but they are not easily recognizable among the contributions of all the other kinds of waves and they are never the first arrivals at the receivers. In fig.2.4 an example of displacement field is presented, caused by an out-plane SH source. All direct and reflected and refracted waves are present, included Love waves.(Rix, 2000-a)

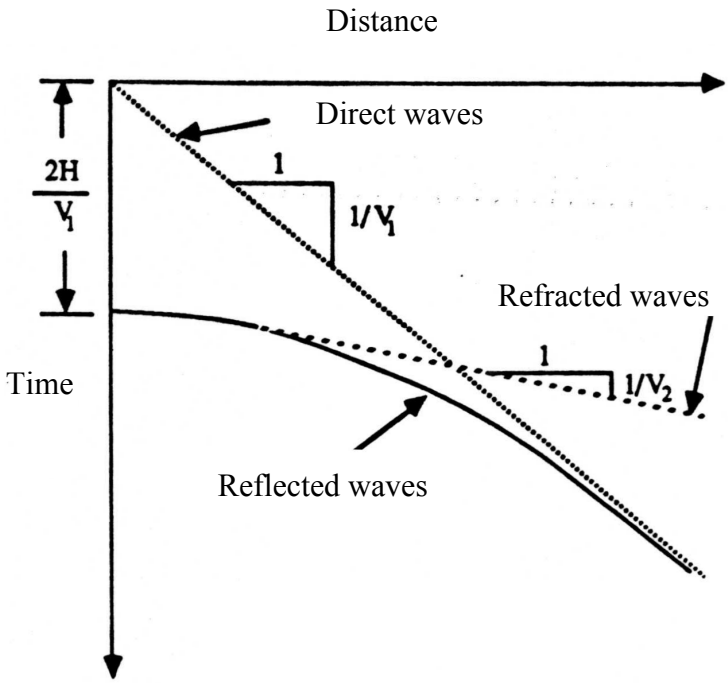

Figure 2.3: Direct, reflected and refracted waves in time-space domain (Rix, 2000-a).

In the following the interest will be concentrated on the possibilities that Rayleigh waves offer, to overcome some of the difficulties and the limitations of seismic refraction and reflection methods, as a complementary non-invasive tool for soil characterization.

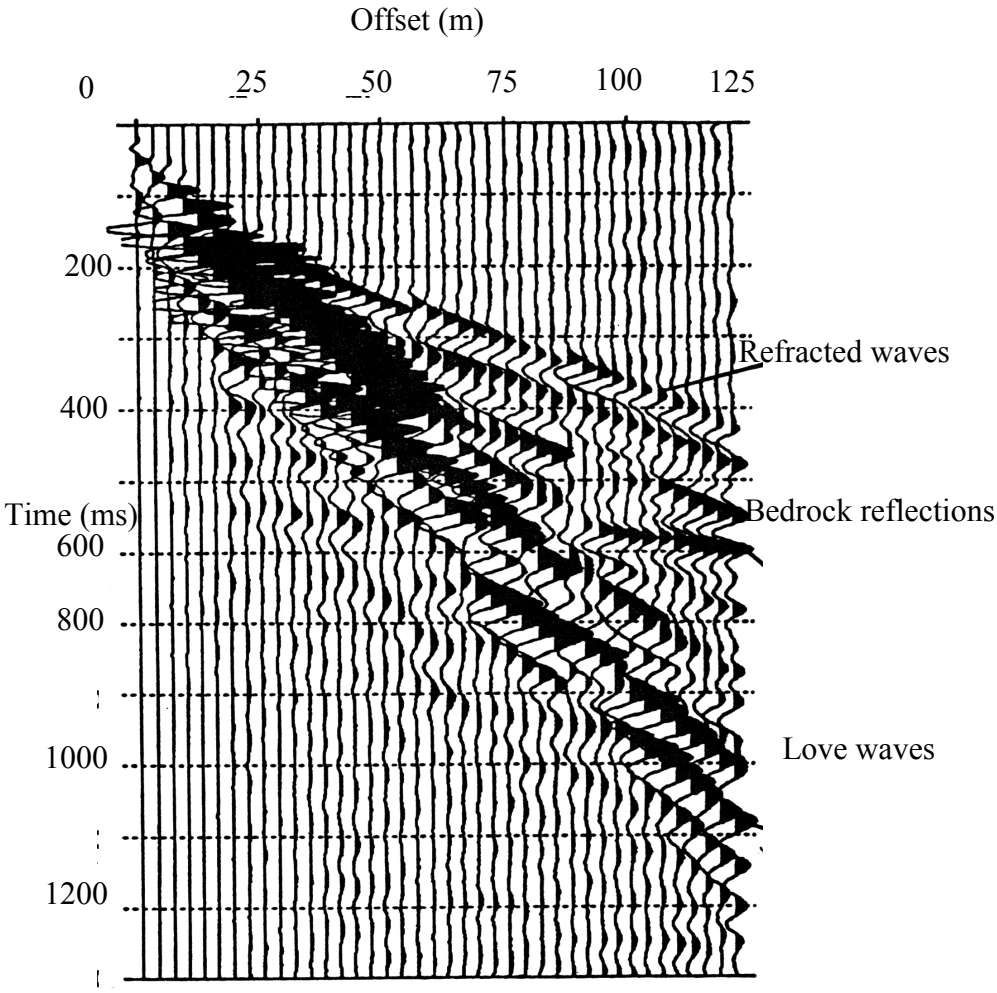

Figure 2.4: Displacements field on the free surface generated by a horizontally source on the free surface. Refracted and reflected as well as Love waves can be recognized (Rix, 2000-a).

2.2 Historical Review of SASW procedures

The interest towards surface waves for the determination of dynamic soil properties dates back to the attempts made by Jones in 1950's (Jones, 1962) and Ballard (Ballard, 1964). Jones developed the so called Steady-State Vibration method, but it was onerous and prohibitive in terms of time. Only in the earlier 1980's some researchers of the Texas Department of Transportation suggested the Spectral Analysis of Surface Waves (SASW) method, (Heisey et al. 1982, Nazarian and Stokoe, 1984) that has been

continuously improved, due to the attracting advantages and business purposes in engineering applications of this non-invasive method.

2.3 Steady-State Vibration Technique

The Steady-State Vibration method is based on the use of a time harmonic source, that is put on the free surface of the site under investigation.

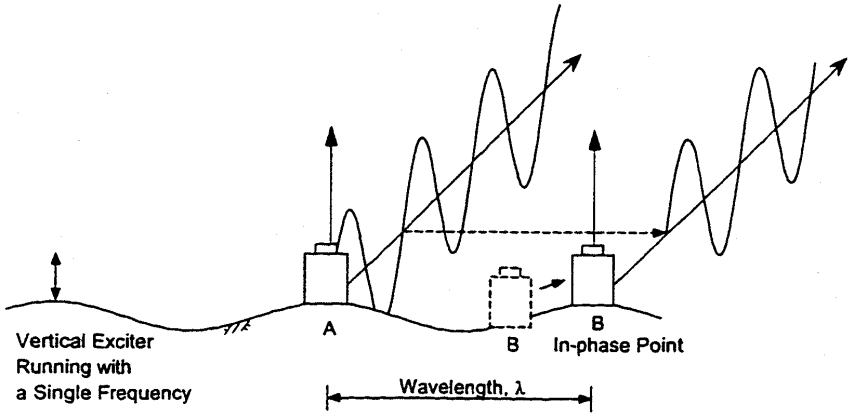

Figure 2.5: Steady-State Method for the experimental evaluation of the dispersion relation (Hebeler, 2001, Joh, 1996).

The goal is to move two displacements sensors on the free surface until the signals detected at the two sensors are in phase. As it is illustrated in fig.2.5, one sensor is held fixed and the second one is moved along the surface to find the in-phase points.
The idea behind this procedure is that the distance between two in-phase points corresponds to the wavelength of the signal at the frequency of excitation, so that the experimental phase velocity can be easily evaluated by using the formula:

$$c = \lambda \cdot f \tag{2.1}$$

It is implicitly assumed that for each frequency of excitation the system responds with a harmonic perturbation characterized by only a wavelength, that is the one experimentally measured. Actually in Chapter 1 it was shown that several modes can propagate through the system for the same frequency. It means that the wavelength experimentally calculated can either coincide with one mode or more probably to a combination of all the modes

together. This aspect will be considered afterwards more deeply, since it represents a key aspect in the inversion procedure.
By measuring all the in-phase points at different frequencies a graph can be plotted, that enables one to accurately evaluate the wavelength (fig.2.6a). Once the *apparent* wavelength has been measured, the experimental *apparent* dispersion relation can be represented in terms of the phase velocity varying with the wavelength (fig.2.6b). In the represented case the phase velocity always increases with the wavelength, hence the correspondent site is normally dispersive, in the sense explained in section 2.4.1. The final step of the method consists of determining the shear wave velocity profile by means of the phase velocity profile. An empirical rule is adopted, that associates a shear wave velocity to a phase velocity:

$$Vs \cong 1.1 \cdot c_R \qquad (2.2.a)$$

where c_R is the experimentally measured Rayleigh phase velocity. The depth z, corresponding to the shear wave velocity, is evaluated from the wavelength λ of the phase velocity c_R:

$$z = (1.5 \div 2) \cdot \lambda \qquad (2.2.b)$$

In this way a direct correspondence is created from the dispersion profile (fig.2.6b) and the shear wave velocity profile (fig.2.6c).
It has been shown that this approximation holds very well for homogeneous sites and when the stiffness gradually increases with depth (Ballard, 1964), but when these conditions do not exist the method gives unreliable results (Rix, 1988).

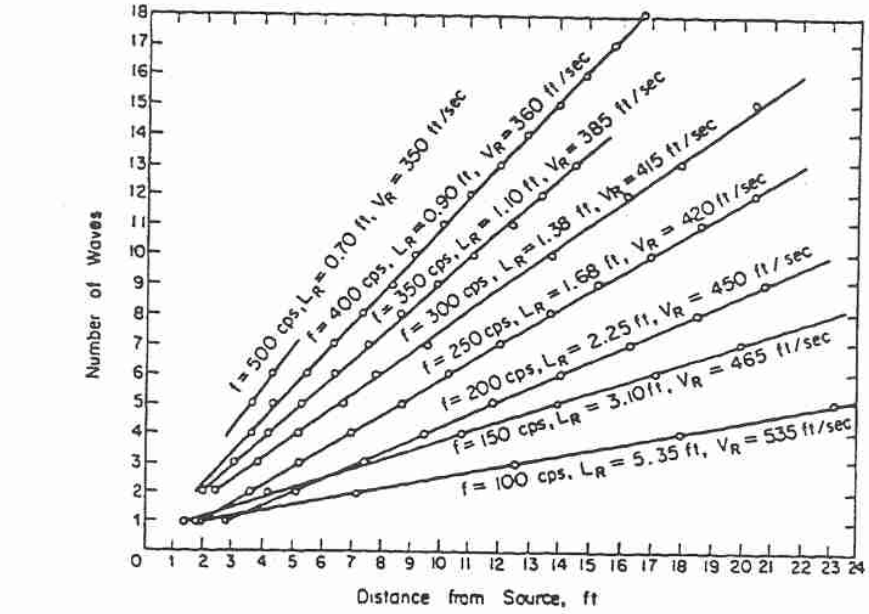

(a) Determination of Average Wavelength of Rayleigh Wave (Richart *et al.*, 1970)

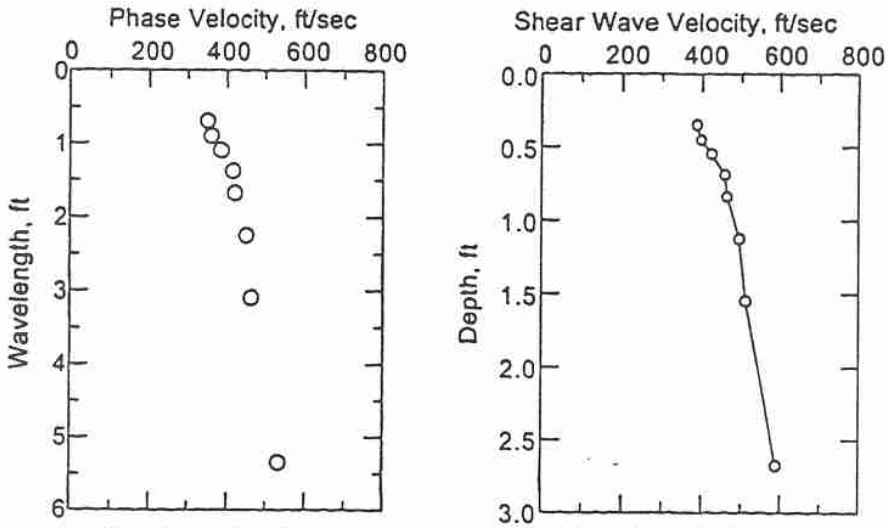

(b) Dispersion Curve (c) Shear Wave Velocity Profile

Figures 2.6a, b, c: Determination of the experimental wavelength (a), phase velocity (b) and shear wave velocity profile (Hebeler, 2001, Joh, 1996).

The reason why this method fails with irregular stiffness profiles is that the modal shape of the displacements, associated to the first Rayleigh mode for such cases, is not the same as in normally dispersvie profiles, but changes

with frequency. As it will be explained in the sequel, the higher modes become important in different ranges of frequency, so that the first mode is not always predominant for all the frequencies and a simple correspondence between the two graphs in fig.2.6b and fig.2.6c is not valid anymore.

2.4 Spectral Analysis of Surface Waves Method

In 1980's a great impulse has been given to the future use of the surface waves for geotechnical tests by Stokoe and his co-workers (Heisey et al, 1982, Stokoe II et al, 1988, Nazarian and Stokoe II, 1984, Nazarian, 1984, Sànchez-Salinero, I., 1987). They tried to overcome the disadvantages presented by the Steady-State vibration method by means of the more powerful devices for signal analysis and the use of the Fourier Transformation. A huge gain in terms of time can be reached by using an impulsive source, that generates several frequencies at the same time. Then, thanks to the Fourier Transformation of the signal, information can be obtain about the frequencies contained by the travelling disturbance. The idea is to detect the perturbation at two stations on the free surface and then to calculate the phase shift between the signals $y_1(t)$ and $y_2(t)$, measured at the two receivers, to be used for experimental phase velocity evaluation. Initially an impulsive source was used to generate the perturbation and a couple of receivers to detect it, collocated according to two different schemes . The first one is the Common Source array (see fig.2.7), instead the second one is the Common Receiver Midpoint array (see fig.2.8).
It has been experimentally proven (Sanchez-Salinero, 1986) that by assuming the same distance between the first receiver and the source and the two receivers, i.e. $d_1=d_2$, the phase velocity shows a smoother behavior, without fluctuations, typically found with other configurations.
The Common Receiver Midpoint fig.2.8 array is usually preferred, because the position of the source respect to the receivers is reversed and it is believed that the disturbing effects due to horizontal irregularities and bending inclination can be mitigated.

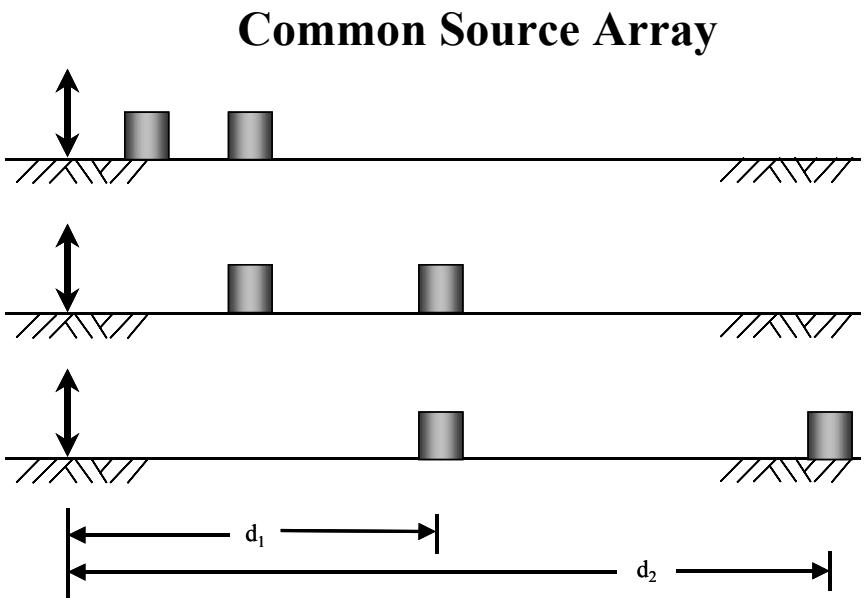

Figure 2.7: Common Source array in the SASW test (Hebeler, 2001).

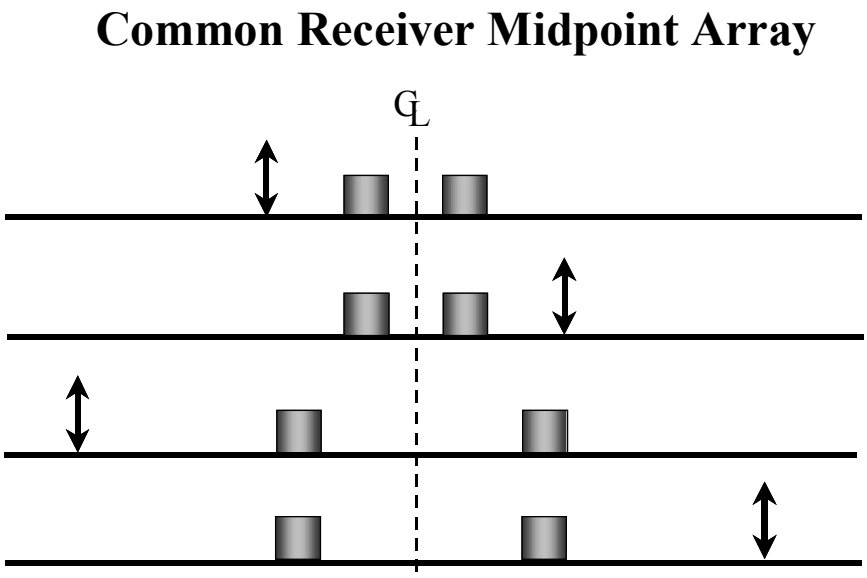

Figure 2.8: Common Receiver Midpoint configuration with source reversed in SASW test (Hebeler, 2001).

From the recorded signals $y_1(t)$ and $y_2(t)$ at the two receivers the following quantities can be calculated:

$$Y_1(f) = FFT[y_1(t)] \tag{2.3a}$$

$$Y_2(f) = FFT[y_2(t)] \tag{2.3b}$$

which are the Fast Fourier Transformed of the signals in time domain, then the Auto Power Spectra:

$$G_{11} = Y_1(f) \cdot Y_1^*(f) \tag{2.4a}$$

$$G_{22} = Y_2(f) \cdot Y_2^*(f) \tag{2.4b}$$

and the Cross Power Spectrum (2.5) and the Coherence function (2.6)

$$G_{12} = Y_1(f) \cdot Y_2^*(f) \tag{2.5}$$

$$\gamma_{12}^2 = \frac{|G_{12}|^2}{G_{11} \cdot G_{22}} \tag{2.6}$$

The Auto Power Spectra give an estimate of the energy contained into the signals taken independently, the Coherence measures the existing correlation between two different signals and indicates the goodness of the signal to noise ratio. The Coherence varies from 0 to 1, depending on the quality of the detected signals. If the Coherence is near 1 it means that the measured signals are very well correlated, but several factors, as body wave interference, noise, spatial variability may cause the value of the Coherence be sensibly lower than 1. Finally the phase of the Cross Power Spectrum

$$\Delta\Phi = \tan^{-1}\left(\frac{\mathrm{Im}(G_{12})}{\mathrm{Re}(G_{12})}\right) \tag{2.7}$$

represents the phase shift between the signals at the two stations and it is used to calculate the phase velocity as:

$$c(f) = \frac{2\pi f \cdot \Delta x}{\Delta \Phi} \tag{2.8}$$

where Δx is the distance between the two receivers and f is the frequency at which the phase velocity is calculated.
In fig.2.9 a view of all the quantities above defined is given for the real site Shelby Forest in USA (G. Hebeler, 2001).
The assumption behind this procedure is the same used in the Steady-State Vibration method, i.e. the disturbance measured between the two stations is assumed to be characterized by a constant *apparent* wavelength, so that the same simple harmonic form can be associated to the two signals recorded at the two stations. In reality this is not completely true, since a wave train with different wavelengths is generated at the time the impulsive source impacts. As a consequence waves with different wavelengths can be found between the two stations, depending on the distance between the two receivers and the distance from the source.

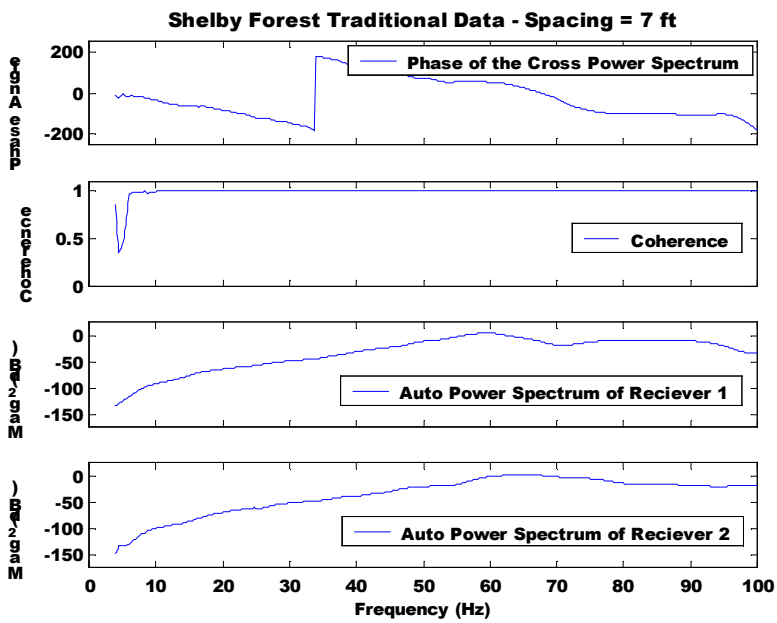

Figure 2.9: Phase of the Cross Power Spectrum, Coherence function and Auto Power Spectra at Shelby Forest for a spacing of 7ft between the receivers (Hebeler, 2001).

What happens is that the measured wavelength and hence the calculated phase velocity depends on the position of the two receivers and only a part of the whole frequency range 1Hz-100Hz can be explored for an assigned configuration. This means that, in order to have an experimental phase velocity in a wide range of frequencies, more configurations must be chosen, accordingly with different types of source. It is well known in fact that hammers generate perturbations relatively rich of high frequencies (i.e. short wavelengths) and big weights produce disturbances with small frequencies (i.e. long wavelengths). The results of such a phenomenon are clearly reported in fig. 2.10, where several estimations of the phase velocities have been plotted for different distances between the receivers.
The next step is to average the several pieces of experimental curves at those frequencies where they overlap, in order to get only one averaged experimental dispersion curve. In fig.2.11 the *composite* curve is represented made by means of all the pieces of dispersion curve, obtained with different configurations and the *averaged* experimental curve is also shown. Finally a reduced number of experimental points must be selected, to be used in the computationally expensive inversion process. This operation does not influence much the accuracy of the inversion process, since it has been proved (Yuan and Nazarian, 1993) that, increasing the number of points beyond approximately (0.5 - 1.0)N, where N is the number of the unknowns, only increases the computational cost of the inversion, without adding information to the dispersive characteristics of the medium.

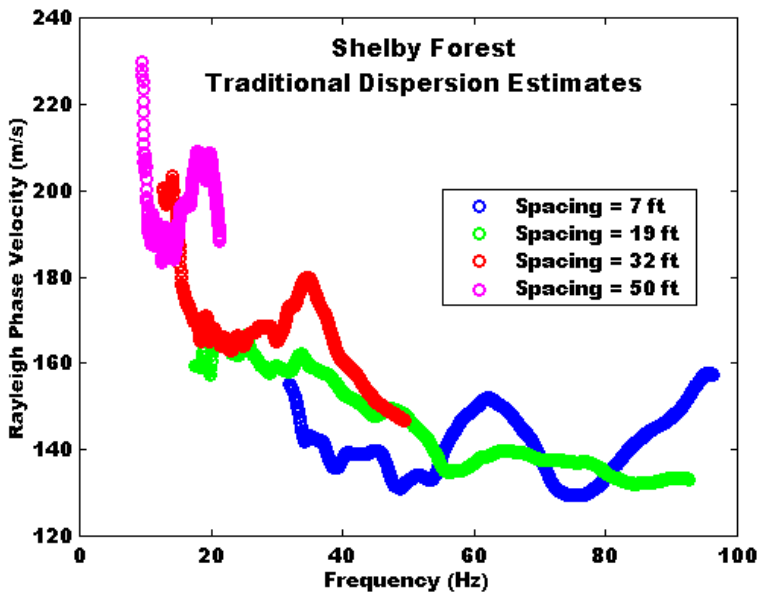

Figure 2.10: Standard SASW method: pieces of dispersion curve for different configurations at Shelby Forest site (Hebeler, 2001)

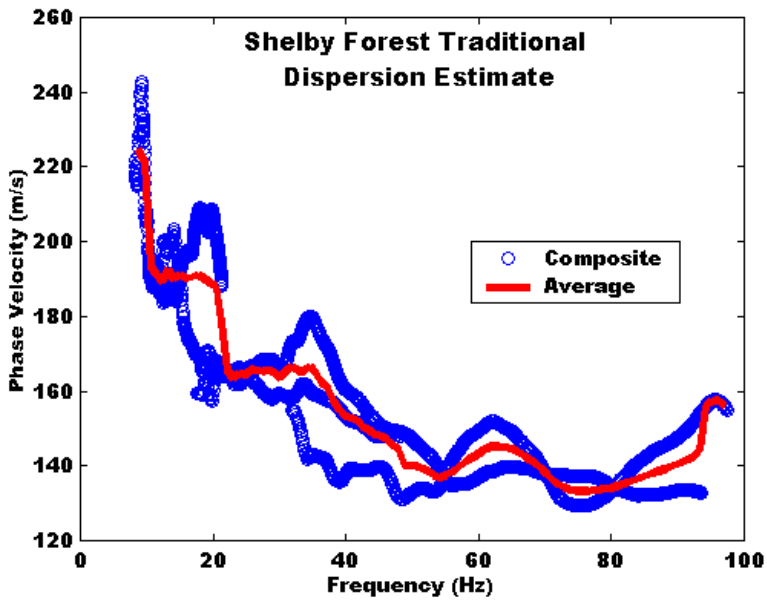

Figure 2.11: Composite and Averaged experimental dispersion curves (G. Hebeler, 2001)

It is evident that the averaged dispersion curve represents an improvement respect to the original pieces, but it is still rough and it is anyway the result of an averaging process. This means that in the inversion procedure this arbitrary averaging process will increase the non-uniqueness of the stratigraphy, since detailed information is lost.
The standard SASW test as described above shows some drawbacks such as: goodness and quality of the measurements need to be established looking at the coherence function; unwrapping of the phase of the Cross Power Spectrum; limited number of stations for measurement; need of averaging process; a quite rough final experimental dispersion curve.
In order to overcome these disadvantages, other techniques have been improved, such as the active and the passive f-k methods, just well known to geophysical researchers and based on multi-channel gathering of data.
Before introducing the f-k methods, a section will be dedicated to explain the distinction between normal dispersion and inverse dispersion, that has important consequences in the inversion problem of the dynamic soil characteristics.

2.4.1 Normally and Inversely dispersive systems

In Chapter 1 we have defined both the phase velocity and the group velocity. When a system is dispersive, that is the phase velocity is a non constant function of the frequency, then the phase velocity and the group velocity are not equal. If the phase velocity is greater than the group velocity, the system is said normally dispersive. Instead, if inside any range of frequency the phase velocity is less than the group velocity, the system is called inversely dispersive. For example, the waves travelling on the surface of the water are subjected to normal dispersion. In fact the ripples propagate quickly, with a speed equal to the phase velocity and pass through the big beats of waves, that travel more slowly with the group velocity. The fig.2.12a and fig.2.12b clearly put in evidence the two situations, in which the system is normally or inversely dispersive.
In the first case (fig.2.12a) the phase velocity is greater than the group velocity, hence the wavelets inside the groups propagate through the groups, passing in front of them. In the inversely dispersive case (fig.2.12b) the wave-packets are faster than the wavelets, that are left back by the wave-packets. As a result, after the same amount of time, in the normally dispersive case the space covered by the crest is greater than the distance covered by the peak of the wave-packet. In the inversely dispersive case the situation is reversed.

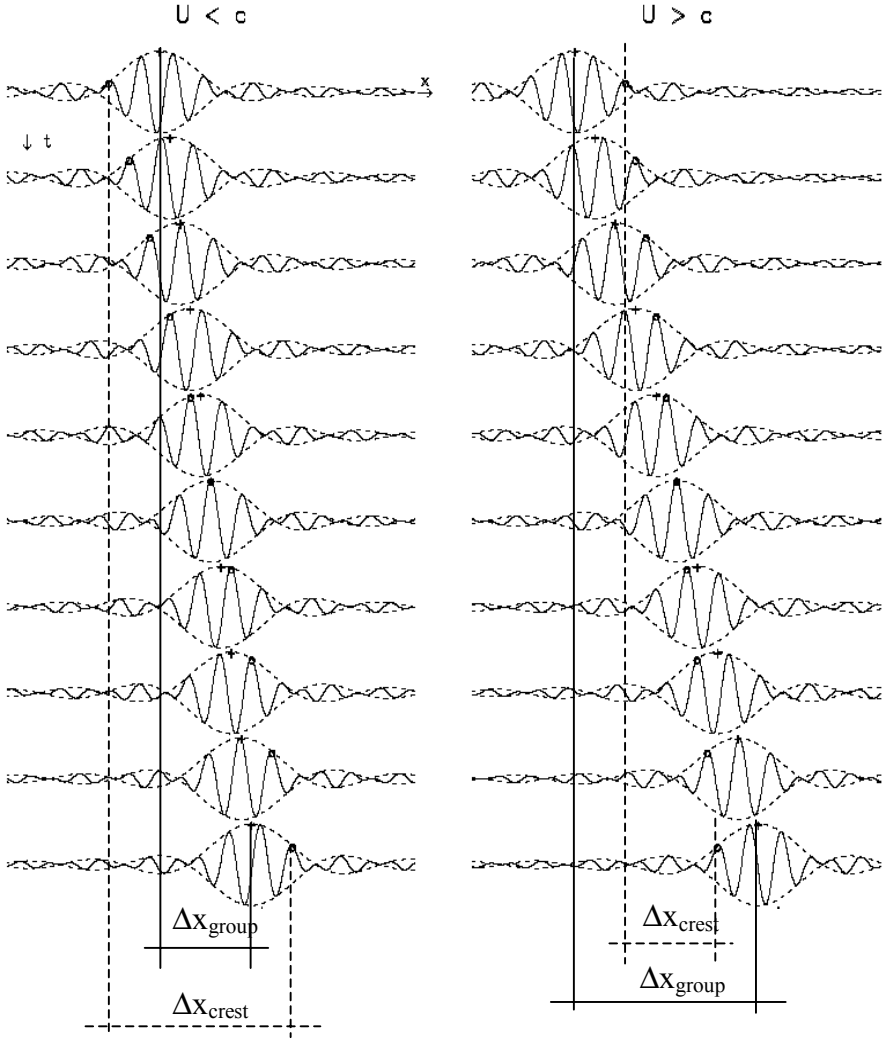

Figures 2.12a, b: Normal and Inverse Dispersion Phenomenon (Pojul, 2000).

As it has been showed at the beginning of this chapter, it is possible to evaluate an experimental dispersion relation associated to a site, by means of the motion of the particles, measured on the free surface of the site. In particular different procedures have been reminded for the experimental calculation of the dispersion relation, for example in terms of the phase velocity.

For a layered half-space either normal or inverse dispersion may occur, depending on the stiffness variation with depth. When the stiffness

gradually increases with depth the system is normally dispersive and the experimentally measured phase velocity always decreases with frequency (i.e. increases with the wavelength, fig.2.13a). When the stiffness varies irregularly with depth, i.e. softer layers trapped between stiffer ones or vice versa stiffer layers trapped between softer ones, then the system shows an inversely dispersive behavior and the experimental phase velocity changes as shown in fig.2.13b(Rix, 2000-a).

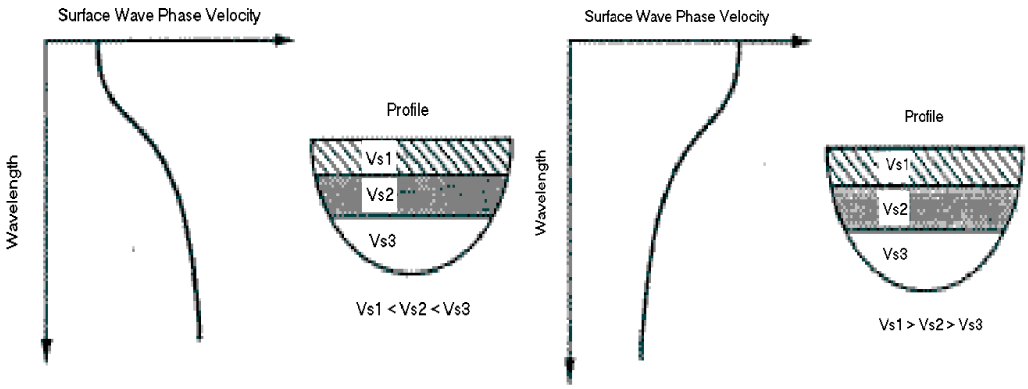

Figures 2.13a, b: Normally and inversely dispersive layered half-spaces (Rix, 2000-a).

Now an essential aspect that needs to be underlined is that only one dispersion relation can be obtained by means of experimental measurements, instead we have seen in Chapter 1 that from the theory of wave propagation several modes of Rayleigh may exist. Actually it will be shown in the following that sometimes more than one experimental curve can be extracted from measured data, under proper conditions. Anyway the real core of the inversion procedure for determining the dynamic soil properties is the way the theoretical *apparent* or *effective* dispersion curve is evaluated. The reason is that the usually employed technique, followed to infer the characteristics of the site is to vary the properties of the system, starting from an initial guess and trying to minimize the distance between the experimental and the theoretical response functions of the system. The choice of the response function is fundamental, but once it is done and before running the optimization procedure, the main role is played by the forward simulation, that gives the theoretical *apparent* curve. The terms *apparent* or *effective* comes out from the fact that the experimental dispersion relation is what we can see from real experiments (Gucunski and Woods R.D., 1991-a, Gucunski and Woods, 1991-b, Gucunski and Woods, 1992, Tokimatsu, 1995), because of several factors: the number of receivers

and their spacing; the total distance investigated by the array of receivers, the properties of the site. Therefore one open issue remains how either to generate a theoretical *apparent* curve or to experimentally measure well separated Rayleigh modes. About the separation of Rayleigh modes during the propagation, more details will be given in Appendix B.
At a geotechnical scale of interest it is very difficult to have a separation of the Rayleigh modes, since a quite detailed stratigraphy in the upper 30m-50m is desired and hence the maximum covered distance on the free surface is always less than 50m and only exceptionally reaches 100m. So the only way to account for all the modes of Rayleigh, given the limited number of receivers, is to generate an *apparent* dispersion relation. Until now two main classes of strategies have been followed. The first one is the so called 2-D method, where only the fundamental mode of Rayleigh is considered and all the higher modes are ignored. The second one is named the 3-D method and it completely simulates the SASW test previously described, taking into account all types of waves generated on the free surface by a point impulsive source (Ganji et al., 1998, Joh. 1996).
The 2-D method is by far the simplest one and it allows to save a lot of time, but it gives good results only for normally dispersive sites, because without doubts it fails when dealing with inversely dispersive systems (Tokimatsu et al., 1992-a). The 3-D method is obviously more rigorous, since it considers both all the higher modes of Rayleigh and body and head waves on the free surface. Actually the 3-D method enables one to theoretically evaluate the displacements at the two receivers of the SASW configuration and to repeat all the steps followed in the experimental test. Of course this means a huge amount of time needed and it is too expensive in terms of time in view of an inversion procedure. As a consequence a lot of efforts have been done to overcome the problems of the 2-D method, keeping at the same time the advantages offered by the 3-D method. An interesting solution has been recently proposed by Lai (Lai, 1998, Lai and Rix,1998), that provides an *apparent* or *effective* theoretical phase velocity.

2.5 Effective Phase Velocity

As just said in section 2.1 (it will be further explained in section 2.6) when a vertical impulsive point source is applied on the free surface of a layered half space, in general several types of waves are generated. First of all P and S waves spread away from the source with spherical wave-fronts , followed by Rayleigh waves along cylindrical wave-fronts, together with head waves and reflected waves. Assume for the moment to have been able to experimentally isolate Rayleigh waves from all the other waves (in a certain manner this is provided by field transformations and separation of

different events as explained later in section 2.6). Now it is a fact that a global displacement field results from the contributions of all the Rayleigh modes of propagation and in the simple case of time harmonic source we can write (Aki and Richards, 1980, Lai, 1998):

$$u_\beta(x,z,\omega,t) = \sum_{j=1}^{M} \left[A_\beta(x,z,\omega) \right]_j \cdot e^{i\left(\omega \cdot t - k_j \cdot x + \varphi_\beta\right)} \tag{2.9}$$

$$\left[A_\beta(x,z,\omega)\right]_j = \begin{bmatrix} A_r(x,z,\omega) \\ A_y(x,z,\omega) \end{bmatrix}_j = \frac{F_0 \cdot r_2(z_S, k_j, \omega)}{4 v_j \cdot U_j \cdot I_j \cdot \sqrt{2\pi x \cdot k_j}} \cdot \begin{bmatrix} r_1(z,k_j,\omega) \\ r_2(z,k_j,\omega) \end{bmatrix} \tag{2.10}$$

$$I_j(z,k_j,\omega) = \frac{1}{2}\int_0^\infty \rho(z)\left[r_1^2(z,k_j,\omega) + r_2^2(z,k_j,\omega)\right]dz \tag{2.11}$$

in which β indicates either the vertical or the horizontal component of motion, j denotes the generic j-th mode, M is the total number of modes, k_j is the wave number corresponding to the j-th mode for the given frequency of excitation ω, z_s is the source depth, φ_β is a phase shift equal to $\pm\pi/4$ according to β, A_j is the modal amplitude of the modal displacement, v_j and U_j are the modal phase and group velocities, F_0 is the amplitude of the vertical harmonic force, I_j is the first energy integral and r_1, r_2 are the eigenvectors as they are defined in (Lai, 1998).

This is true if the superposition principle holds, as it is the case, since we assume an elastic behaviour of the material, because of the small range of deformations we deal with.

Each modal component independently satisfies the equations of motion, so each mode can represent an independent simple wave, that travels independently from the other modes, with its own phase and group velocities. As it has been explained in Appendix B, the energy associated with the generic mode propagates with the group velocity, instead the modal phase advances with the phase velocity.

Lai and Rix (1998) had the brilliant idea to think of all the modes as a global disturbance, characterised by an *effective* phase velocity. If we take the imaginary part of the complex displacement (2.9)(we could have taken even the real part without any substantial change in the results), we have (Lai, 1998):

$$\mathrm{Im}\left[u_\beta(x,z,\omega,t)\right] = C_\beta(r,z,\omega) \cdot sin\left[\omega t - \Psi_\beta(r,z,\omega)\right] \tag{2.12}$$

in which the amplitude and the spatial part of the phase are written below:

$$C_\beta(r,z,\omega)=\sqrt{\sum_i^M\sum_j^M\left[A_\beta(r,z,\omega)\right]_i\cdot\left[A_\beta(r,z,\omega)\right]_j\cdot\cos\left[r(k_i-k_j)\right]} \tag{2.13}$$

$$\Psi_\beta(r,z,\omega)=\tan^{-1}\left\{\frac{\sum_i^M\left[A_\beta(r,z,\omega)\right]_i\cdot sin\left[rk_i+\varphi_\beta)\right]}{\sum_j^M\left[A_\beta(r,z,\omega)\right]_j\cdot\cos\left[rk_j+\varphi_\beta)\right]}\right\} \tag{2.14}$$

If we want to consider the locus of all the points that have constant phase, we must set the total phase equal to a constant:

$$\left[\omega t-\Psi_\beta(r,z,\omega)\right]=\text{constant} \tag{2.15}$$

Then if Ψ_β is smooth enough to admit partial derivatives, we can differentiate respect to time and obtain:

$$\omega-\frac{\partial\Psi_\beta}{\partial r}\frac{dr}{dt}+\frac{\partial\Psi_\beta}{\partial z}\frac{dz}{dt}+\frac{\partial\Psi_\beta}{\partial\omega}\frac{d\omega}{dt}=0 \tag{2.16}$$

Now if we observe that the frequency of excitation ω does not vary with time and we assume that the propagation occurs along r only, not along z, then we have:

$$\frac{dr}{dt}=c(r,z,\omega)=-\frac{\omega}{\frac{\partial\Psi_\beta}{\partial r}} \tag{2.17}$$

that is the so called *effective* or *apparent* phase velocity. For an explicit expression the reader is referred to (Lai, 1998).
The result just obtained needs some comments. Above all the physical picture to keep in mind is made of several simple waves, that coincide with the Rayleigh modes in the case of time harmonic source. All the modes spread away from the point source with cylindrical wave-fronts at different speeds. Precisely their amplitudes propagate with the modal group velocities, instead their phases with the modal phase velocities. As the time passes, the disturbance separates out into a longer and longer train, made of

independent waves with different wave numbers. Before the separation of the Rayleigh modes, they are still together and a simpler way to look at them is to consider an equivalent complicate wave, whose *effective* or *apparent* phase velocity is given by (2.17). It should be more meaningful to obtain the expression of the *apparent* group velocity associated to the global perturbation. This quantity should give an estimate of the speed at which the perturbation travels, when considered as an whole. Of course this picture holds, if the dispersion has not significantly occurred yet, otherwise it would be more appropriate to consider the modes independent and separated.
As a consequence of this dispersion phenomenon the *effective* or *apparent* phase velocity depends on the distance r covered by the disturbance. Again this is reasonable, if we think that during the propagation the different modal components travel at different velocities inside the wave train, that gradually expands and moves with a speed that varies in space and time. In the opinion of the author the *apparent* phase or *apparent* group velocities do have physical meaning, because they represent an equivalent manner to look at the travelling disturbance, just as it appears time after time along its path.
The new concept of the *apparent* phase velocity offers the advantages of the 3-D methods, because all the higher Rayleigh modes are taken into account. The *effective* phase velocity can also be entirely evaluated from the homogeneous eigenvalue problem presented in Chapter 1 and finally analytical expressions of the partial derivatives of the effective phase velocity respect to the properties of the system have been found by Lai and Rix (1998). The availability of the partial derivatives is very useful in the inversion procedure, since it allows for time saving and more stability respect to the partial derivatives numerically calculated.
Another aspect, that deserves to be mentioned, is that the effective phase velocity described by formula (2.17) defines a surface in the frequency-space domain, so it is more correct to speak in terms of dispersion surface, rather than in terms of dispersion curve. On the other hand this feature represents a problem, because an arbitrary averaging process among all the receivers is necessary, in order to obtain a dispersion curve.
In this research a different approach has been chosen, based on the frequency-wave number analysis, just widely used in geophysical field and introduced in recent years for geotechnical investigation by some researchers (Foti, 2000, Tokimatzu, 1995, Hebeler, 2001, Zywicky, 1999).

2.6 F-K Method

Consider the global wave field generated on the free surface of a site by a point source, applied on the same free surface. As just said at the end of the Chapter 1 and in section 2.1 about seismic methods, several types of waves

can be found on the free surface. This aspect really constitutes a problem for the discernment of reflected and refracted waves for the application of the corresponding techniques. For this reason in geophysical applications it is necessary to filter the total wave field from disturbing scattered waves, guided waves, Rayleigh waves, that are called *ground roll*. In order to solve this problem several strategies have been developed, mostly based on the wave field transformation.

The f-k method consists of transforming the measured wave field from the time-space domain of acquisition to the frequency-wave number domain. This double transformation can be performed by means of a 2D Fourier transformation, one from time to frequency and the other from space to wave number. The reason of such a transformation in analysing the measurements, collected on the free surface of a site, is that in the transformed domain it is easier to discern all kinds of waves and separate the so called *ground roll* from noise or from reflected and refracted waves.

In fact a separation of the different events exists in the frequency-wave number domain, as it is explained in fig.2.14, where the reflected waves are found near the frequency axis, instead the ground roll is close to the wave number axis.

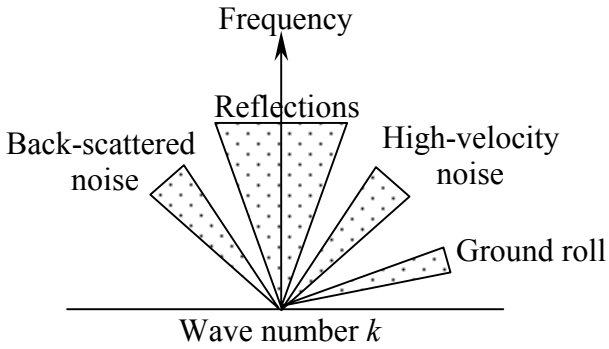

Figure 2.14: Separation of different events in the frequency-wave number domain (Doyle, 1995).

Now the interesting feature is that the *ground roll* is mainly constituted by Rayleigh waves, hence the f-k method represents a powerful tool to isolate the Rayleigh waves from the global wave field and it can be successfully used to experimentally estimate the Rayleigh dispersion relation (Foti, 2000, Zywicki, 1999, Gabriels et al., 1987). Let now briefly explain the basic concepts behind this method.
Consider the wave field generated on the free surface of a site expressed in the time-space domain as (McMechan and Yedlin, 1981):

$$u(x,t) = \iint \frac{N(k,\omega)}{R(k,\omega)} \cdot e^{i(kx-\omega t)} \cdot d\omega \cdot dk \tag{2.18}$$

where $N(k,\omega)$ is a function of the exciting source and $R(k,\omega)$ is the Rayleigh dispersion relation discussed in Chapter 1. In Appendix C the term $R(k,\omega)$ has been explicitly written for the particular case of an impulsive point source, applied on the free surface of a layer resting over a half-space.
By applying a 2-D Fourier transformation from time to frequency and from space to wave number the frequency-wave number representation of the wave field is obtained:

$$\overline{\overline{u}}(k,\omega) = \iint u(x,t) \cdot e^{i\omega t} \cdot e^{-ikx} d\omega \cdot dk = \frac{N(k,\omega)}{R(k,\omega)} \tag{2.19}$$

From (2.19) it is immediate to realize that the relative maxima in the amplitude of the spectrally decomposed wave field are reached for those pairs of frequencies and wave numbers, that make the Rayleigh secular function equal to zero:

$$R(k,\omega) = 0 \tag{2.20}$$

This is the Rayleigh geometrical dispersion relation and its solutions have just been discussed in Chapter 1.
In the paper by McMechan and Yedlin (1981) a similar observation has been made on the transformed wave field from time-space domain to slowness-frequency domain, but it must be underlined that when $R(k,\omega)=0$, it is not said that the wave field goes to infinity as they have assessed. There is no justification for an infinite value of the wave field, because even in absence of material dissipation of energy, the spreading of the energy and its transmission towards deeper layers assure finite peaks in the spectrum. A mathematical explanation is that the numerator $N(k,\omega)$ also approaches to zero in correspondence of the Rayleigh modes, so that the wave field remains of finite amplitude. In fact experimental and numerical simulations support this consideration (see fig.2.29).
It is necessary to clarify some aspects about the f-k method. In the formula (2.18) the wave field should rigorously be expressed in terms of the displacements, since as it is shown in Appendix C the peaks in the spectrum of the displacements give the Rayleigh dispersion relation. Nevertheless, by means of some assumptions, it can be easily demonstrated that, the way the peaks in the spectrum are searched, the dispersion curve does not vary, if the spectra of the energy or displacements or velocities or accelerations are used.
In the frequency-wave number domain the magnitude of the energy spectrum $E(k,\omega)$ can be correlated in a simplified manner to the magnitude of the displacement spectrum $S(k,\omega)$ as:

$$|E(k,\omega)| \propto |S(k,\omega)|^2 \tag{2.21}$$

If at each fixed frequency ω_0 we look for the wave number, at which the energy spectrum is maximum, the following condition for the existence of any stationary points must be imposed:

$$\frac{\partial |\mathrm{E}(\mathrm{k},\omega_0)|}{\partial k} = 0 \text{, that is} \tag{2.22}$$

$$\frac{\partial \mid \mathrm{E}(\mathrm{k},\omega_0)\mid}{\partial k} \propto \mid \mathrm{S}(\mathrm{k},\omega_0)\mid \frac{\partial \mid \mathrm{S}(\mathrm{k},\omega_0)\mid}{\partial k} = 0 \tag{2.23}$$

From (2.23) it can be seen that the maxima and the minima in the wave number domain are the same in the spectra of the displacements and the energy.
If we assume that the following relationships hold in the frequency-wave number domain among the spectra of the displacements $S(k,\omega)$, the velocities $V(k,\omega)$ and the accelerations $A(k,\omega)$:

Physical quantity	$\lvert S(k,\omega)\rvert$	$\lvert V(k,\omega)\rvert$	$\lvert A(k,\omega)\rvert$
$\lvert S(k,\omega)\rvert$	-	$\lvert V(k,\omega)\rvert \cdot \omega$	$\lvert A(k,\omega)\rvert\ \omega^2$
$\lvert V(k,\omega)\rvert$	$\lvert S(k,\omega)\rvert/\omega$	-	$\lvert A(k,\omega)\rvert\ \omega$
$\lvert A(k,\omega)\rvert$	$\lvert S(k,\omega)\rvert/\omega^2$	$\lvert V(k,\omega)\rvert/\omega$	-

Table 2.1: Relationships among the magnitude of the spectra for the measured signals.

Then it becomes easy to realize that the wave numbers, that define the dispersion curve and correspond to the peaks in the spectra are the same:

$$\frac{\partial \mid \mathrm{S}(\mathrm{k},\omega_0)\mid}{\partial k} = \frac{1}{\omega_0}\cdot\frac{\partial \mid \mathrm{V}(\mathrm{k},\omega_0)\mid}{\partial k} = \frac{1}{\omega_0^2}\cdot\frac{\partial \mid \mathrm{A}(\mathrm{k},\omega_0)\mid}{\partial k} = 0 \tag{2.24}$$

The key aspect is that in the spectra only the position of the peaks in the wave number domain are needed to calculate the dispersion curve and not the amplitude of the spectrum. Instead, when calculating the damping ratio, the amplitude of the spectrum and the measured quantity play a main role, because the attenuation of the amplitude with the distance is considered.
The above considerations explain why using the signal measured with either geophones or accelerometers gives the same experimental dispersion curve.
Another point, that needs to be underlined, is that in the experiments a discrete representation of the phenomenon is available. This means that the discrete nature of the measured signals obligates to operate with discrete variables as well as transformations instead of continuous ones. Hence the Fourier pair in (2.18) and (2.19) have to be replaced by:

$$\overline{\overline{u}}_{q,r} = \sum_{l=0}^{N-1}\left[\sum_{m=0}^{M-1} u_{l,m}\cdot e^{-i(r\frac{2\pi}{M}m)}\right]\cdot e^{-i(q\frac{2\pi}{N}l)} \tag{2.25}$$

$$u_{l,m} = \frac{1}{M \cdot N} \sum_{q=0}^{N-1} \left[\sum_{r=0}^{M-1} \overline{\overline{u}}_{l,m} \cdot e^{-i(r\frac{2\pi}{M}m)} \right] \cdot e^{-i(q\frac{2\pi}{N}l)} \tag{2.26}$$

where M and N are the temporal and spatial samples and Δt and Δx are the temporal and spatial sampling intervals. As a consequence care must be taken in choosing Δt and Δx to avoid *aliasing* and *leakage* when processing the gathered signals, as it will be illustrated in the next sections 2.6.1.1 and 2.6.1.2.

Other methods exist that are based on a double transformation of the wave field from time-space domain to either frequency-slowness or frequency-wave number domains. Anyway by means of the Fourier Slice Theorem (Santamarina and Fratta, 1998, Foti, 2000) it can be proved that an equivalence among them can be established.
Regardless of the 2-D transformation used, several researchers (Gabriels et al., 1987, Tselentis and Delis, 1998, Foti 2000, Zywicki, 1999, Hebeler, 2001, Nolet and Panza, 1976) have been able to calculate the experimental Rayleigh dispersion relation for real sites.
Actually some of them have been able to estimate not only the fundamental mode, but also the higher modes (Gabriels et al., 1987). This has been possible because of the long distances covered in geophysical tests, since in such a big spatial scale the dispersion phenomenon takes place and it becomes easier to measure the separated Rayleigh modes. In the geotechnical scale it is almost impossible to distinguish the Rayleigh modes, because the distances involved in the experiments are not enough for mode dispersion. As a consequence only an *apparent* or *effective* dispersion curve can be measured. In the sequel we will focus our attention on the *apparent* or *effective* dispersion relation. It will be shown that in certain cases more than one experimental curve can be obtained from the f-k spectrum of the measured wave field (see fig.2.23).

2.6.1 Experimental Apparent Dispersion curve

A primary feature, that has not been said yet, is that in the f-k method more than two receivers are used. Usually at least 12 receivers are needed for an acceptable f-k representation of the wave field and the more the number of receivers, the better the calculation of the experimental dispersion relation. In this research up to 24 receivers have been employed for the acquisition of the experimental data. The typical setup of the experiment consists of a linear array of surface receivers, that are expected to measure the perturbation produced either by an impulsive or a time harmonic source, vertically applied on a point of the free surface (see fig.2.15).

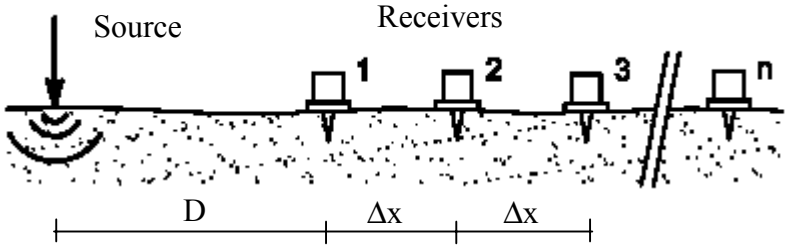

Figure 2.15: Experimental setup for multi-station f-k method (Foti, 2000, Zywicki, 1999, Hebeler, 2001).

More details about the receivers, that have been used in the experiments as well as the kind of sources, will be given in Chapter 5, devoted to the experimental results.
The number N of receivers, the distance D source-first receiver and the spacing Δx between two consecutive receivers control the resolution in the wave number domain and the maximum wave number that can be resolved without the *aliasing* phenomenon. The *aliasing* is an effect due to the discrete nature of the gathered signal in the experimental test, by which all the harmonic components above the Nyquest wave number are lost:

$$k_{Nyquist} = \frac{2\pi}{2\Delta x_{\min}} \tag{2.27}$$

where Δx_{min} is the minimum spatial sampling interval between any two receivers.
This means that a small distance between two consecutive receivers allows to get reliable information into a large range of wave numbers. Unfortunately a small Δx also influences the resolution in wave number domain, as for definition the resolution in wave number is given by:

$$\Delta k = \frac{2\pi}{L} \tag{2.28}$$

$$L = (N-1)\cdot \Delta x + D \tag{2.29}$$

where L is the total distance between the source and the last receiver, N is the number of receivers. If D=Δx, then (2.23) simplifies to:

$$\Delta k = \frac{2\pi}{N \cdot \Delta x} \tag{2.30}$$

As the resolution in space Δx decreases the resolution in wave number increases, as a consequence of the Heisenberg uncertainty principle (Santamarina and Fratta, 1998). It states that for a fixed number of receivers N, an improvement in space resolution is gained at expenses of resolution in wave number. This problem can be solved by using a variable Δx along the array of receivers.

Another compromise, to be reached in choosing the space interval Δx, is that, for a given number of receivers N, a too small Δx causes a too short wave train with all types of waves combined together in the disturbance, hence near field effects must be considered. Instead, if a too great Δx is chosen, the advantages of being in the far field, with a dispersed train of waves, can be lost because of aliasing phenomenon.

Of course a critical parameter is the number N of receivers, in fact a greater number of receivers allows for a better resolution in both space and wave number. The improvement in wave number resolution assumes a main role in determining the experimental dispersion relation. In fact with a sufficient number of receivers it would be possible to experimentally distinguish the higher Rayleigh modes.

One trick to improve the resolution in wave number, without reducing the resolution in space Δx consists in zero-padding the collected signal, but care must be taken with this strategy, that could introduce *leakage*. *Leakage* usually happens when a Discrete Fourier Transform is applied to a discrete signal. The DFT introduces high artificial frequencies, because of the supposed periodicity of the analyzed signal, hence altering the frequency content of the signal itself. In order to mitigate the leakage, a windowing process is recommended (Santamarina and Fratta, 1998).

What has been said about the transformation of a discrete signal from space to wave number domain, is also valid when passing from time to frequency. So we can define a Nyquist frequency:

$$f_{Nyquist} = \frac{1}{2\Delta t} \tag{2.31}$$

and a frequency resolution:

$$\Delta f = \frac{1}{M \cdot \Delta t} \tag{2.32}$$

in which Δt is the sampling interval in time or time resolution and M is the total number of times at which the signal is measured.

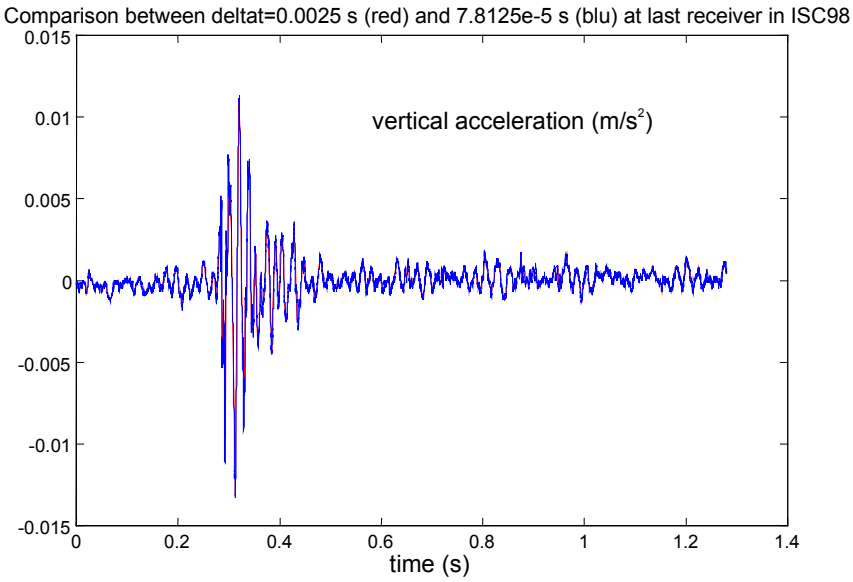

Figure 2.16: Impulsive source: hammer. Particle acceleration at the last receiver (number 16) located at x=32m.

Even in this case the resolution in frequency is controlled by the total duration of the travelling perturbation. Beside there are no limitations in the number M of times that can be measured, unfortunately in the case of transient disturbances the total signal is contained in a very short time, about 0.3s÷0.5s, depending on the characteristics of the site (see fig.2.16).

2.6.1.1 Impulsive Source

One important factor, that controls the way the experimental apparent dispersion curve is evaluated, is the kind of source. In this research we deal with a vertical point source rather than horizontal one and all the collected data refer to the vertical component of motion. This choice arises from the

observation that either vertical or horizontal components of motion independently give the same information for the evaluation of the dispersion relation, if an isotropic behavior of the material is assumed.
Essentially two types of source can be used: an impulsive one or a time harmonic one.
The impulsive source can be represented by a heavy or slight hammer or by a weight drop or a heavy metallic bucket, depending on the depth one wants to investigate. In fact the impulsive source offers the advantage of generating at the same time several simple waves with different wavelengths. Now the less heavy and small is the source, the higher frequencies are produced. A slight hammer generates a disturbance characterized by energy at high frequencies, that generally means short wavelengths (see formula (A.1)), that sample the very surface part of the site. This allows for building up the dispersion curve at high frequencies (see fig.2.17).

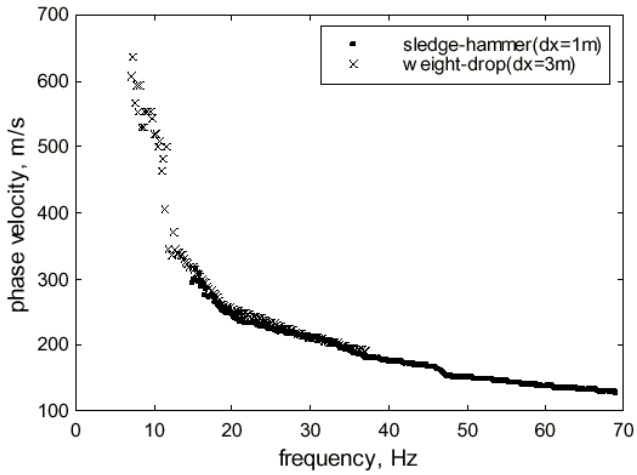

Fig.2.17: Experimental dispersion curve obtained by using a sledge-hammer (dots) and a weight drop (croxes).(Foti, 2000).

A heavy weight drop, that falls down from a certain height, furnishes a disturbance rich with low frequencies, hence long wavelengths, that interest deeper layers of the site and help to construct the dispersion curve in the low frequency range (see fig.2.17).
The range of frequencies of interest in geotechnical and earthquake engineering applications varies from 0Hz to a maximum of 100Hz, hence we will mainly focus the attention on this interval of frequencies.
For the conduction of the experiments either 16 or 24 vertical receivers have been used, that allow for a reliable gathering at frequencies greater than the resonant frequency of the sensors (1Hz for accelerometers, 4.5Hz for geophones, see Chapter 5). The sampling temporal interval is taken as:

$\Delta t = 2 \cdot 10^{-3} s$ and as total duration $T = 2048 \cdot \Delta t = 4096 \cdot 10^{-3} s$, adding zeros before and after the real disturbance, to allow for a better resolution in frequency:

$$\Delta f = \frac{1}{M \cdot \Delta t} = \frac{1}{2048 \cdot 2 \cdot 10^{-3} s} = 0.244 Hz \tag{2.33}$$

The Nyquest frequency is:

$$f_{Nyquist} = \frac{1}{2\Delta t} = \frac{1}{2 \cdot 2 \cdot 10^{-3}} = 250 Hz \tag{2.34}$$

that is sufficiently high for the range of frequency of interest.
For what it concerns the wave number domain, more than one choice can be done. If a slight source is used, a shorter total length is covered on the free surface, due to a space resolution of either Δx=1.5m or Δx=2.0m. Instead with a heavy source, smaller frequencies are desired (i.e. waves with great wavelengths, that can penetrate more deeply in the system), hence a Δx=3.0m is adopted. The total covered length, the Nyquest wave number and the wave number resolution Δk, corresponding to the above space samplings and to a zero-padding of 1024-24=1000 additional points in space are reported in the table 2.2 below:

	Δx=1.0m	Δx=1.5m	Δx=2.0m
Total length (m)	24	36	48
$K_{Nyquest}$(1/m)	3.1	2.1	1.6
Δk (1/m)	0.06	0.04	0.03

Table 2.2: Usual choices for the spatial array of the receivers in the f-k method with impulsive source.

It can be realized that a small Δx allows for a greater range of wave numbers to be investigated, but a worse resolution in wave number domain. This aspect becomes important if the system is inversely dispersive and the separated modes of Rayleigh want to be experimentally determined. Unfortunately a small Δx does not allow the dispersion phenomenon to separate the several wavelengths of the travelling perturbation. On the opposite, a greater Δx covers a great distance, offers a better resolution in wave number, but a lower Nyquest wave number. The traces of the velocities obtained in Tuscany (Italy) during a survey for a seismic mapping of the region are plotted below (fig.2.18.b). They have been properly scaled,

multiplying by the square of the distance the amplitudes, to account for the geometrical attenuation.
Despite the total length is 24 meters, it is not enough to have a complete dispersion of the several components of the perturbation, at least three different groups can be observed at the last receiver, that travel with different group velocities (fig.2.18.a). It is important to notice that it is not said, probably it is not, that the three groups represent three different modes of Rayleigh. In fact, assuming that the near field effects can be ignored at 24m apart from the source, each Rayleigh mode is made by different waves, that travel with different velocities. As it is explained in Appendix B, there is a double multiplicity to be considered. On one side several Rayleigh modes exist in the frequency-wave number spectrum of the system, on the other hand each mode (i.e. each branch of the dispersion relation) is characterized by waves with different group velocities at different frequencies. This means that when an impulsive source is used, each mode is excited at the same time at different frequencies and the energy associated to the simple harmonics of the same mode, corresponding to these frequencies, propagate with different group velocities.

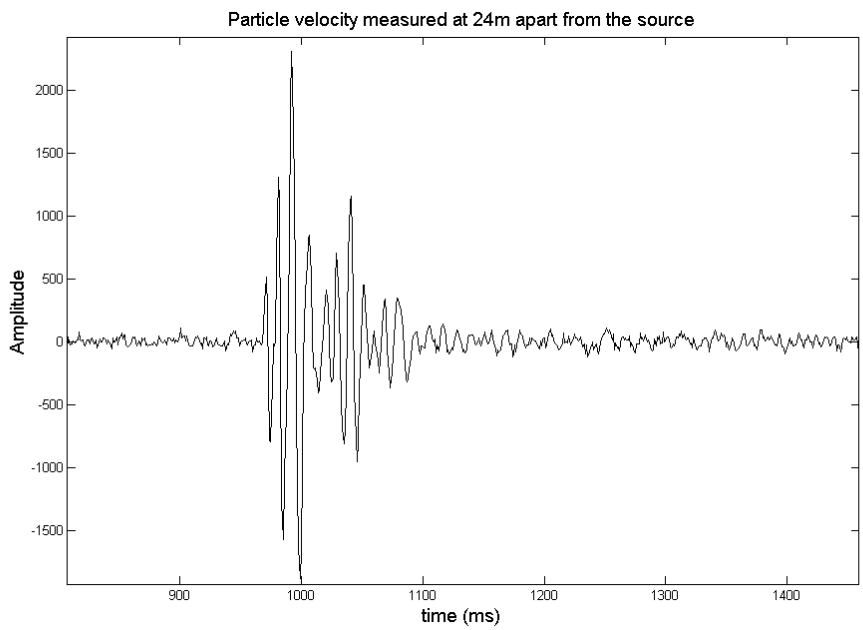

Figure 2.18.a: Dispersion phenomenon observed at the last receiver at 24m away from the source.

The f-k spectrum of the velocities corresponding to these data is represented in fig.2.19 and 2.20. It can be observed a representation of the global signal with all types of waves, measured on the free surface. Of course the part of interest of the signal needs to be properly extracted, so that only Rayleigh waves be considered. This process is accomplished by means of separation of events in the f-k spectrum and with the help of the frequency-phase velocity representation.

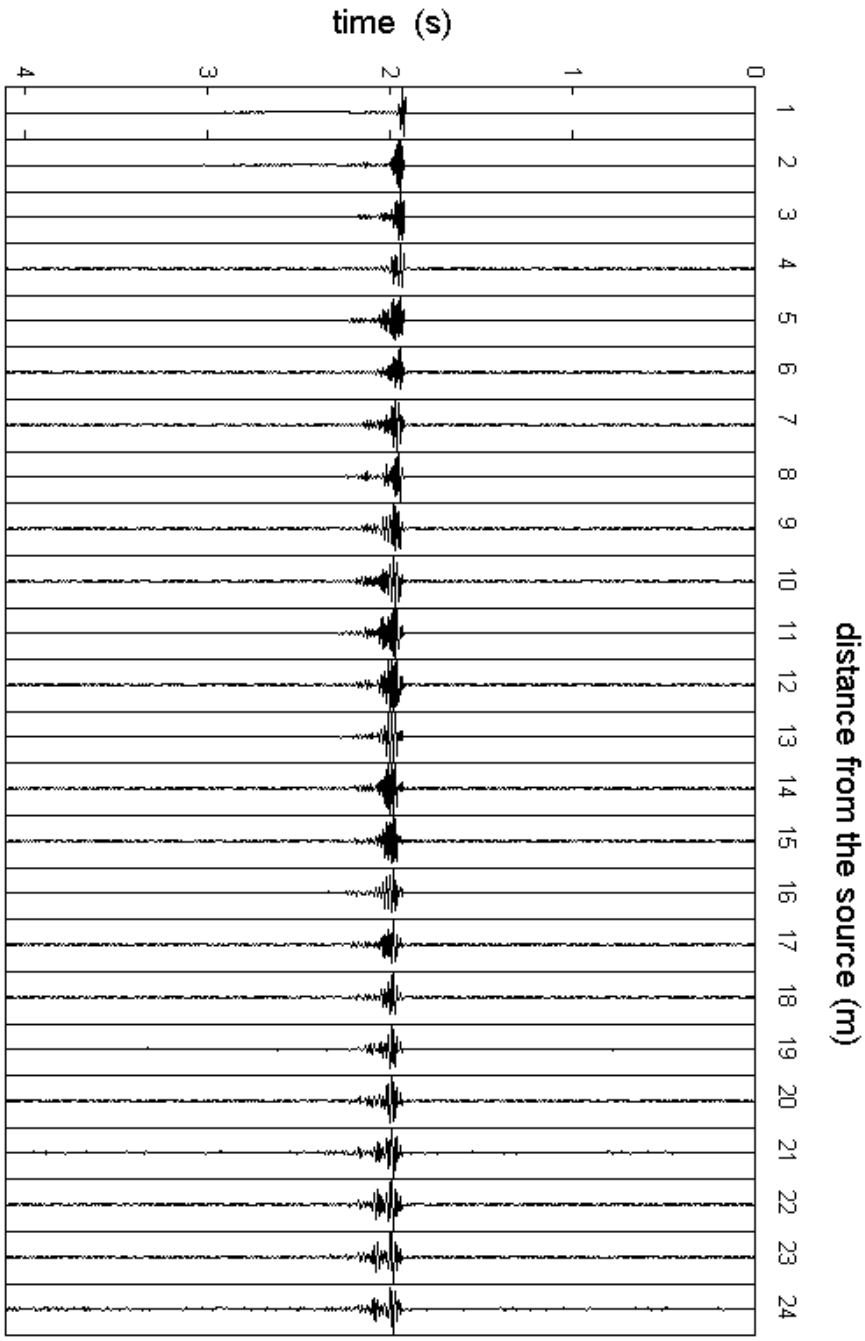

Figure 2.18.b: Traces at Bocce site in Tuscany (Italy): the wave train is not so much dispersed after 24m.

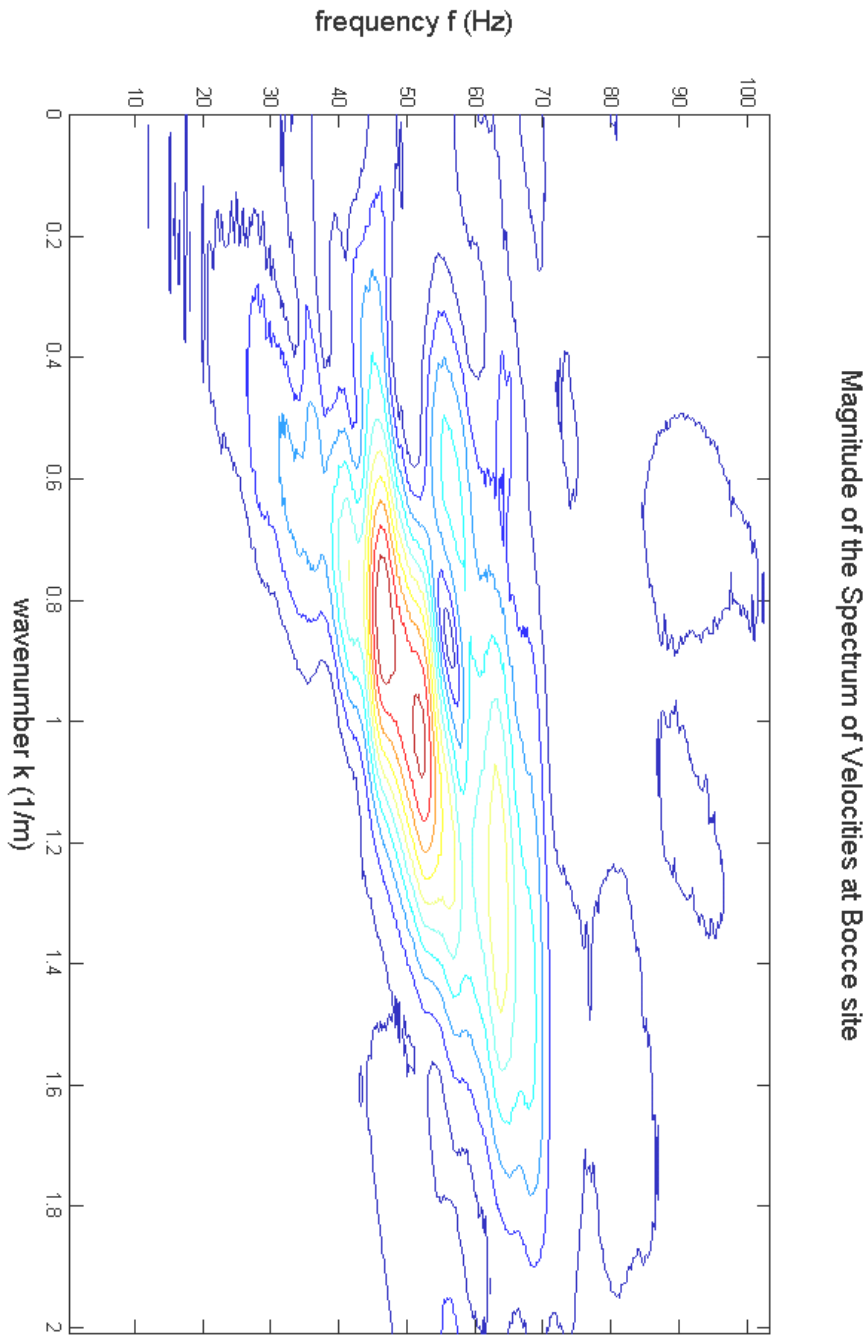

Figure 2.19: Contour plot of the Spectrum of the particle velocities measured on the free surface at Bocce site.

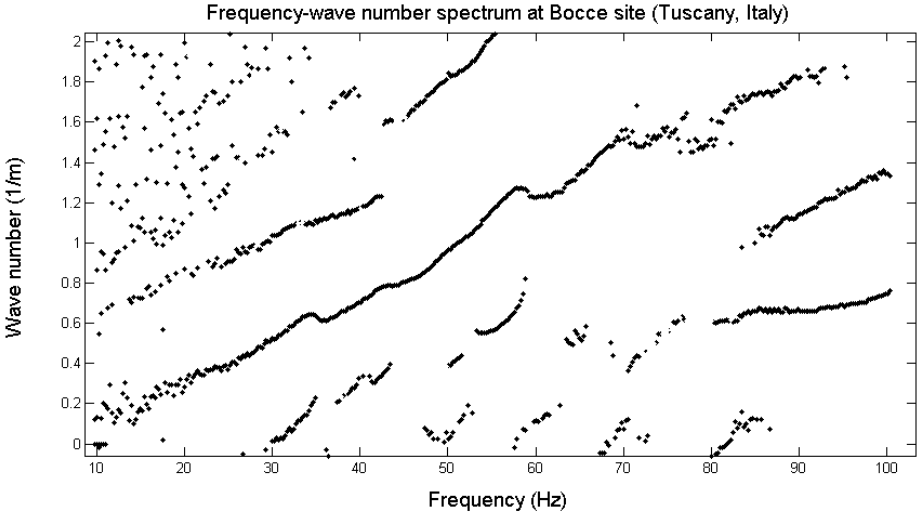

Figure 2.20: Frequency-wave number spectrum of the global field of vertical velocities on the free surface.

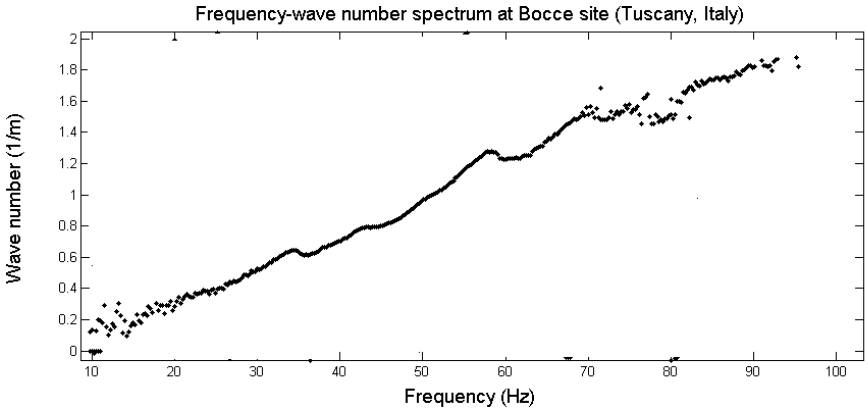

Figure 2.21.a: Experimental Rayleigh apparent dispersion relation at Bocce site (Tuscany, Italy) after a cleaning process.

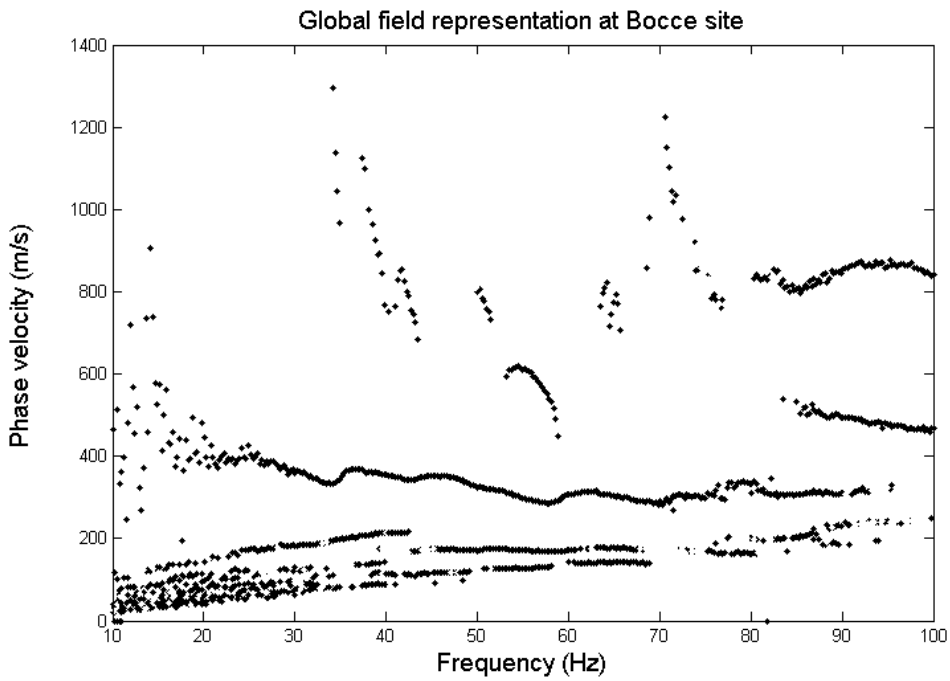

Figure 2.21.b: Representation of the global field in the frequency-phase velocity plane.

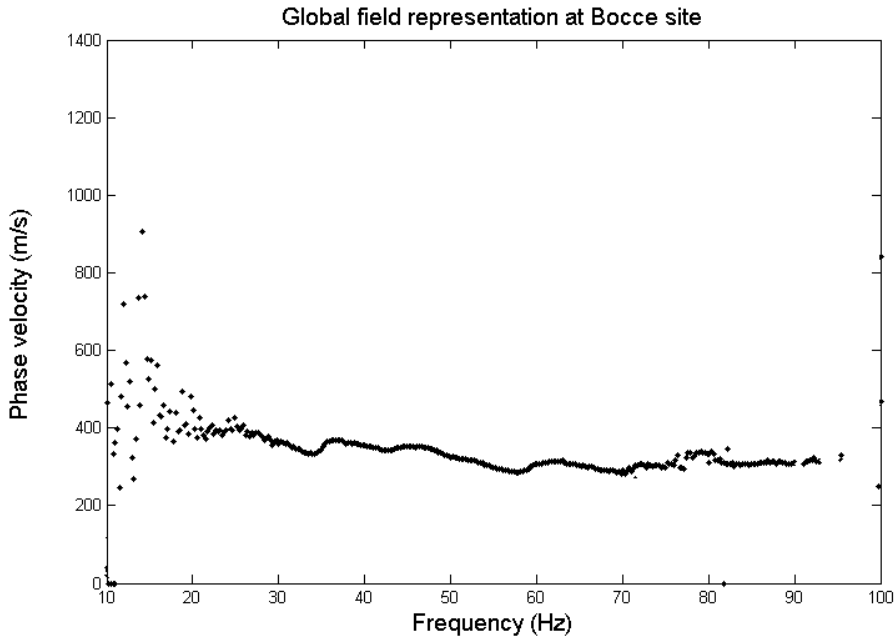

Figure 2.22: Final experimental apparent or effective dispersion curve at Bocce site in terms of phase velocity.

Since a sledge hammer has been used as source, the information below 25Hz is very poor and a heavier source, such as a weight drop is necessary to get the dispersion curve at lower frequencies. A valid alternative is represented by the use of an electro-mechanical vibratory shaker, that is able to generate a harmonic source. This allows for a better signal to noise ratio, hence for a more accurate evaluation of the experimental apparent dispersion relation, even at very low frequencies.

Before describing the procedure used to calculate the experimental dispersion curve in the case of a harmonic source, some aspects concerning the f-k method deserve to be mentioned.

In evaluating the experimental dispersion curves shown in fig.2.17 and fig.2.22 only the absolute maximum in the spectrum has been selected for each frequency. This kind of procedure is in agreement with the theoretical considerations explained at the beginning of this chapter, but more information could be obtained looking for all the relative maxima, that exist at each frequency. So for example at Parco Giochi site in Tuscany, when all the relative maxima are considered a more complete picture of the events is available(fig.2.23).

The two *apparent* curves have been obtained from the spectrum of the displacements, taking all the relative maxima at each fixed frequency.

What happens is that the absolute maximum (squares) switches from the lower curve to the upper one, so that it seems as if the apparent dispersion curve shows a discontinuity. This feature would create ambiguity in choosing the right curve to be used for the inversion process. In reality two experimental apparent curves can be extracted from the spectrum, by considering that all the relative maxima (dots, circles, crosses) make at least two crests in the spectrum. Now the question to answer is what these two curves represent. They are the result of the interaction between the physical properties of the system (i.e. Rayleigh modes) and the geometrical configuration of the receivers, used to detect the disturbance. In other words the phenomenon, that we investigate, appears as it is, depending on the tools that we use to observe it. The scheme in fig.2.25 explains this concept.

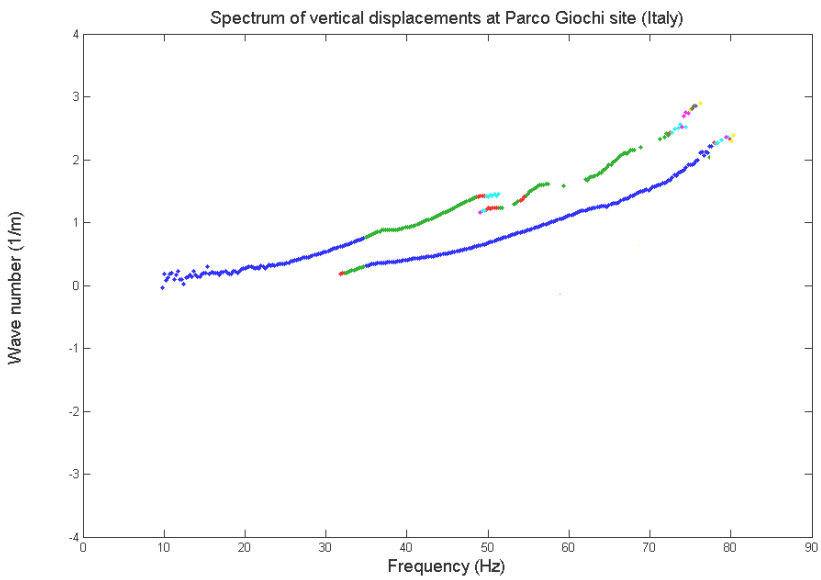

Figure 2.23: Two apparent dispersion curves at Parco Giochi site (Italy).

The same dispersion relation can be seen in the frequency-phase velocity plane (fig.2.24):

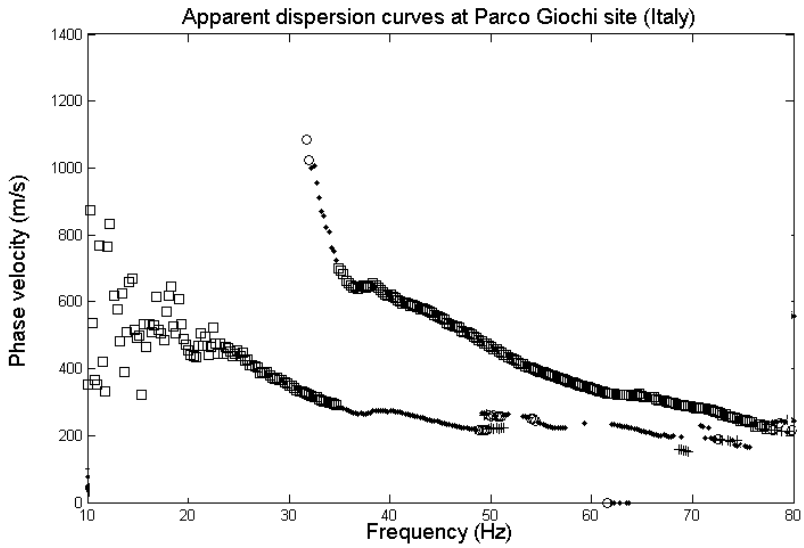

Figure 2.24: Two apparent dispersion curves at Parco Giochi site.

Even if it is very simplified, it helps to understand why the apparent curves are not only the combination of the Rayleigh modes, but they are also influenced by the array of the receivers. A more detailed explanation can be found in the section 2.6.2.a .

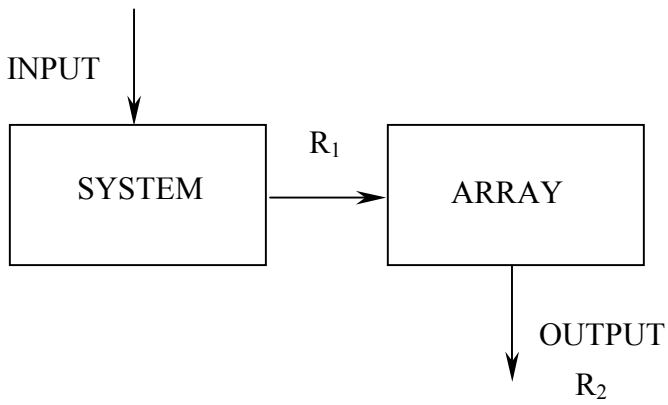

Figure 2.25: Schematic illustration of the interaction between the system and the geometrical array of the receivers used to measure the disturbance.

It must be said that, in the inversion process it is not excluded that the coupled response of system and array may be used, even if it is preferred to deal with quantities, that physically represent the system under investigation and efforts should be done to filter the properties of the system from other disturbances,. In fact, in the ideal noiseless conditions, if the configuration of receivers is held the same in the experimental test and during the theoretical simulation, the only remaining factor influencing the measured response is given by the properties of the system.
This subject will be further analyzed in the section 2.6.2.a.

2.6.1.2 Harmonic Source

Many advantages can be offered by using a harmonic source, rather than an impulsive one, even if the last one permits to measure a transient disturbance, that can be analyzed in the time-frequency domain. It comes out that a better signal to noise ratio can be obtained with the harmonic source, that is generated by means of an electromagnetic machine (see Chapter 5). At each fixed frequency the disturbance is acquired, after the source has been run a sufficient time, so that the transient be finished and the response of the system can be considered time harmonic. Generally a sampling interval Δt=0.002 s is assumed, since there is no interest in the energy content, if any, at frequencies higher than

$$f_{Nyquist} = \frac{1}{2\Delta t} = \frac{1}{2 \cdot 0.002s} = 250Hz \tag{2.35}$$

As in the case of an impulsive source, even in the case of harmonic source, the response of the system is searched in the frequency-wave number domain by means of a 2-D Fourier transformation of the data gathered in time-space. The following procedure is more deeply described in (Hebeler, 2001).
The first step consists of evaluating the Spatio-spectral Matrix R at each frequency of excitation (Hebeler, 2001).
The system is loaded at a fixed frequency f and M samples in time domain are acquired at each sensor simultaneously. Then the total length of the signal L at each sensor is divided into B=L/M blocks and a 1-D Fourier transformation is applied to each block and an averaging process is performed. This operation should eliminate the effects of random noise.
Successively the Cross Spectral Density CSD between each receiver pair is calculated and only one value is chosen among all the frequencies, that come out from the Fourier transformation of the data at a fixed frequency.
The mathematical expression of the R matrix is the following:

$$R(f) = \begin{bmatrix} R_{1,1}(f) & R_{1,2}(f) & \dots & R_{1,N}(f) \\ R_{2,1}(f) & R_{2,2}(f) & \dots & R_{2,N}(f) \\ \vdots & \vdots & \ddots & \vdots \\ R_{N,1}(f) & R_{N,2}(f) & \dots & R_{N,N}(f) \end{bmatrix} \tag{2.36}$$

where each term is represented by:

$$R_{i,j}(f) = \frac{1}{B}\sum_{n=1}^{B} S_{i,n}(\omega) S_{j,n}^{*}(\omega) \tag{2.37}$$

in which * indicates complex conjugation, ω the is the circular frequency, f is the source frequency and N (or n) is the total number of receivers. The term S(ω) is the Fourier transformed response of each sensor:

$$S(\omega) = \sum_{t=0}^{M-1} s(t) \cdot \exp\left(\frac{-i2\pi\omega t}{M}\right) \tag{2.38}$$

If no noise were present, the transformed representation of the perturbation, obtained at the fixed frequency, would show only one peak at about the

frequency of excitation. Because of other undesired sources, the signal is characterized by other peaks in the frequency domain, so that it is necessary to select the peak over a band-limited range around the frequency of excitation (see fig.2.26). In this way only one R(f) matrix is defined at each frequency of loading.

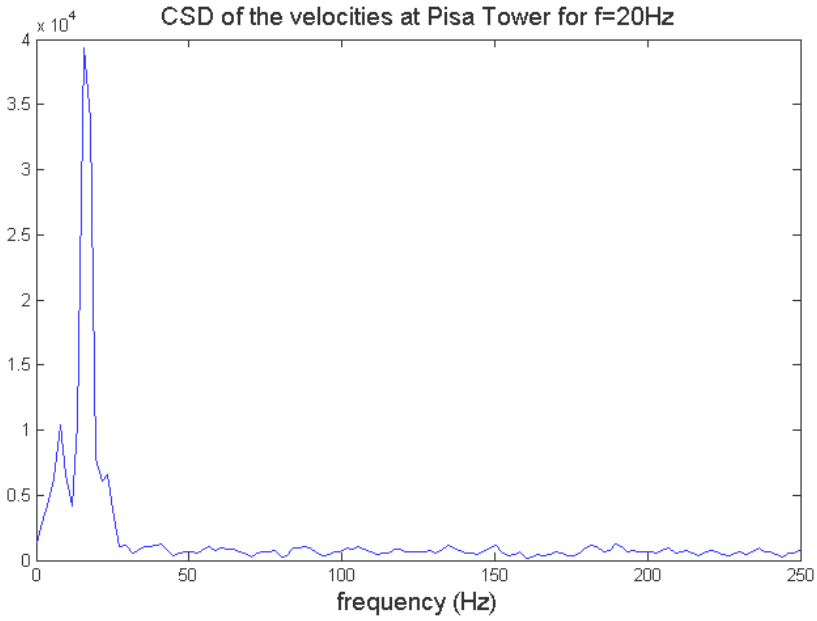

Figure 2.26: Cross Spectral Density of the measured particle velocities at the last geophone for a frequency of excitation f=20Hz.

The next step concerns the Fourier transformation from the space domain to the wave number domain. This task is accomplished by means of the Frequency Domain Beamformer (FDBF) analysis. A steering vector

$$e(k) = \left[e^{-ik \cdot x_1} \;\; e^{-ik \cdot x_2} \;\; \cdots \; e^{-ik \cdot x_N} \right]^T \tag{2.39}$$

is defined, that contains all the information about the geometric configuration of the receivers. A weighting matrix W(f) is also introduced, that allows for a certain variability of the method. W(f) can be chosen as the identity matrix or as:

$$W(f) = \sqrt{\hat{x}} \sqrt{\hat{x}^T} \tag{2.40}$$

where the vector $\hat{x}$ specifies the configuration of the receivers, to account for geometric spreading of Rayleigh waves with distance from the source. Finally the Power spectrum can be defined as:

$$P(f,k) = e(k)W^T(f)R(f)W(f)e^H(k) \tag{2.41}$$

where H denotes the Hermitian transposition (i.e. the transpose of the complex conjugate). Once the Power Spectrum has been evaluated, it is straightforward to calculate the apparent dispersion curve, by picking the peaks of the spectrum at the several frequencies, as it has been shown for the case of impulsive source. The method has been applied to the site at the Leaning Tower of Pisa and in fig.2.27 and fig.2.28 the normalized spectrum of velocities at f=20Hz and the resulting experimental dispersion curve can be seen.

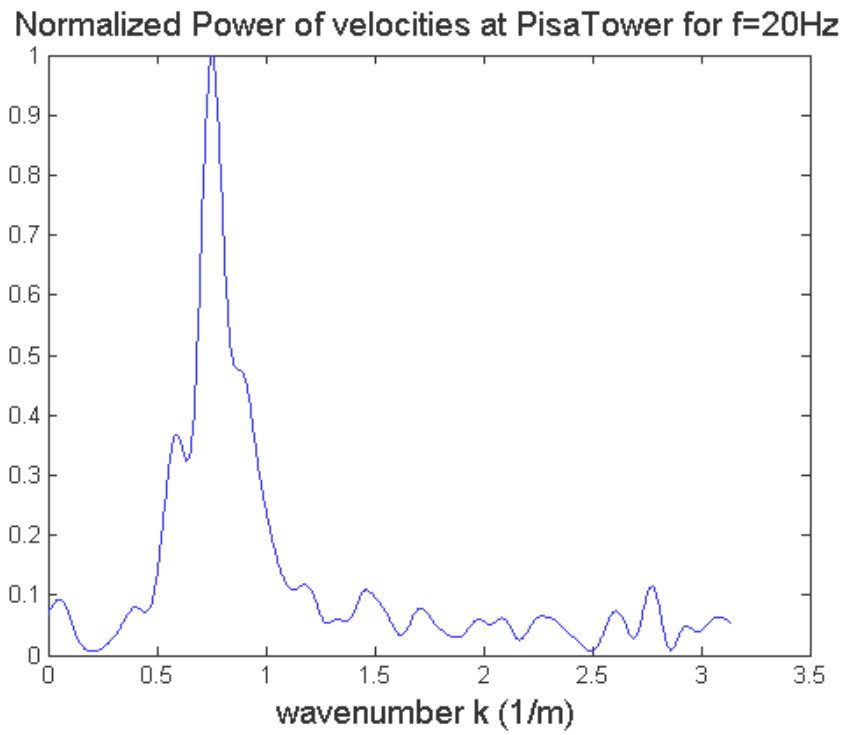

Figure 2.27: Normalized Power Spectrum of velocities at Pisa Tower for f=20Hz. The peak in the Spectrum individutes the wave number used to calculate the apparent dispersion curve.

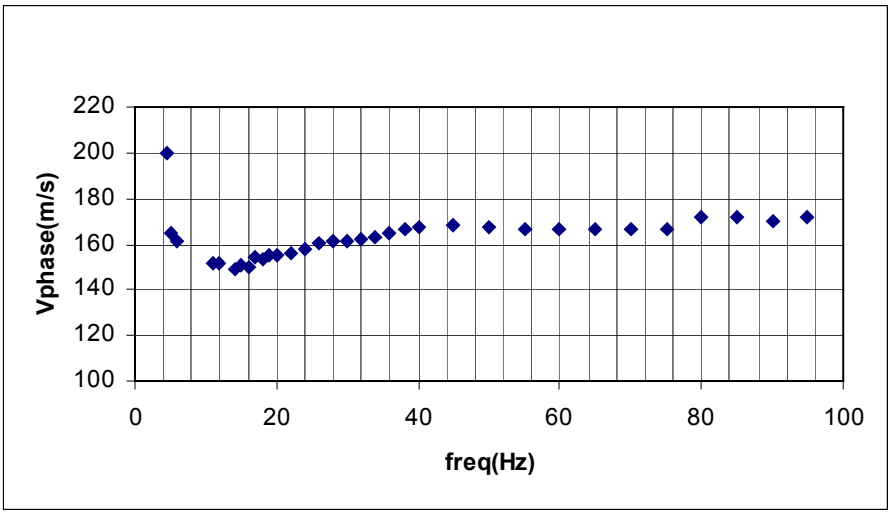

Figure 2.28: Experimental Apparent Dispersion curve at Pisa Tower, obtained by means of the FDBF analysis. Harmonic source and velocities measured by 24 geophones.

It is useful to remember that either accelerations or velocities or displacements can be used in evaluating the Rayleigh dispersion curve, as it has been explained at the beginning of the section 2.6.

2.6.2 Theoretical Apparent Dispersion curve: New Proposed Method

In the previous section the procedure to calculate the experimental dispersion curve has been described in both cases of impulsive and harmonic source.
One of the merit of this research is to propose a new method for evaluating the theoretical dispersion curve, that is consistent with the experimental procedure (Roma, 2001, Roma et al., 2001).
If one wanted to theoretically simulate the experimental test it should be necessary to assume the same spatial array of the sensors, the same temporal parameters and the source should be characterized. In this way the spatio-temporal response of the system at the receivers would be available and the same signal processing technique, to treat the data, could be used, as in the experimental procedure. Although this method is the most rigorous, it is also time expensive, especially in the view of an iterative procedure, inside an optimization algorithm. In order to overcome this drawback, the first step is to use the analytical expression of the displacements in the frequency-space domain and transform directly to the frequency-wave number domain, without passing through to the time-space domain. At this point one issue would be the need of characterizing the source in the frequency-wave number domain. In Appendix A it has been demonstrated that, under the assumptions of linearity of the phenomenon and if a point source is used, it is not necessary to characterize the source to evaluate the theoretical apparent dispersion curve. The small level of deformation (less than $10^{-4} \div 10^{-6}$ % depending on the soil) justifies the assumption of the linear elastic theory, to model the behavior of the soil as an equivalent continuum. The first hypothesis of linearity of the phenomenon has just been implicitly assumed, when dealing with a system of linear differential equations that constitute the eigenvalue problem of Rayleigh waves. The linearity allows for the super position principle to hold and for the use of the Fourier transforms. The second assumption of point source is also valid, since the distances that are involved in the experiment, are large enough to neglect the dimensions of the source. As it is explained in the Appendix A, the maximum wave number of interest is rarely greater than 3 rad/m and the types of source do not have a size, that corresponds to wave numbers lower than 12 rad/m. As a consequence the source can be represented in the frequency domain only, but, as it is shown in Appendix A, there is no need to characterize the source, since the position of the peaks of the spectrum in the wave number domain does not depend on the frequency content of the source. Instead the kind of source influences the range of frequencies, where the apparent dispersion curve is visible, so that different types of source, with different frequency content, make it possible to calculate parts of the same apparent dispersion curve, that should overlap (see fig.2.17, fig.2.A).

Hence, to consistently evaluate the apparent dispersion curve, it is only sufficient to have the response of the system due to a time harmonic point source and to simulate the same configuration of sensors, that has been adopted in the experimental test. The same signal processing procedure must be applied, with specific reference to the zero padding.
Another relevant aspect is that, by knowing the response of the system to a time harmonic source, the Transfer Function or Green Function of the system is available. This is useful not only for evaluating the response of the system to any type of loading, but also for determining the natural frequencies and the natural wave numbers of the system. An interesting operation consists of considering each modal response, independently from the others, and evaluating the spectrum of the displacements referred to each mode, following its modal path in the frequency-wave number plane. In this way it is possible to understand the meaning of the *apparent* dispersion curve as a proper combination of the generalized Rayleigh modes. It can also be explained how the predominance passes from one mode to another in the inversely dispersive systems.
Consider for example the system illustrated in the table 2.2:

Layer	**Thickness h(m)**	**Vp (m/s)**	**Vs (m/s)**	**Mass density (Kg/m^3)**
1	5	750	500	1800
2	10	600	400	1800
3	10	750	500	1800
Half-space	∞	900	600	1800

Table 2.2: Inversely dispersive site from Lai, 1998: Case 3.

For this system the Rayleigh modes and the theoretical apparent dispersion curve are plotted in the phase velocity-frequency domain in fig.2.29. The spatial array consists of 24 sensors with a sampling Δx=1.5m. As it can be seen, the apparent dispersion curve jumps from the first mode to the higher modes as the frequency increases. The explanation can be found looking at the normalized spectrum of the modal displacements in fig.2.30.

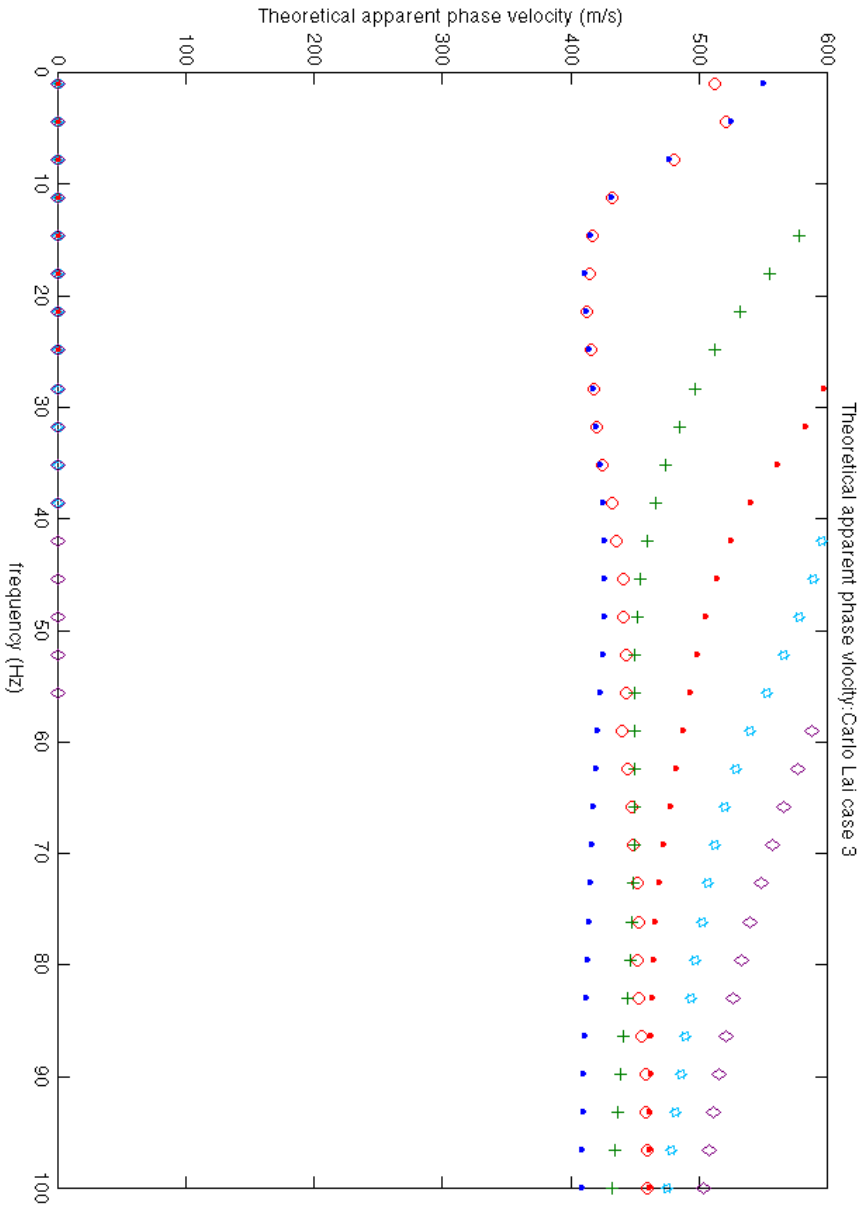

Figure 2.29: Rayleigh modes and theoretical apparent dispersion curve (red circles) for Lai Case3

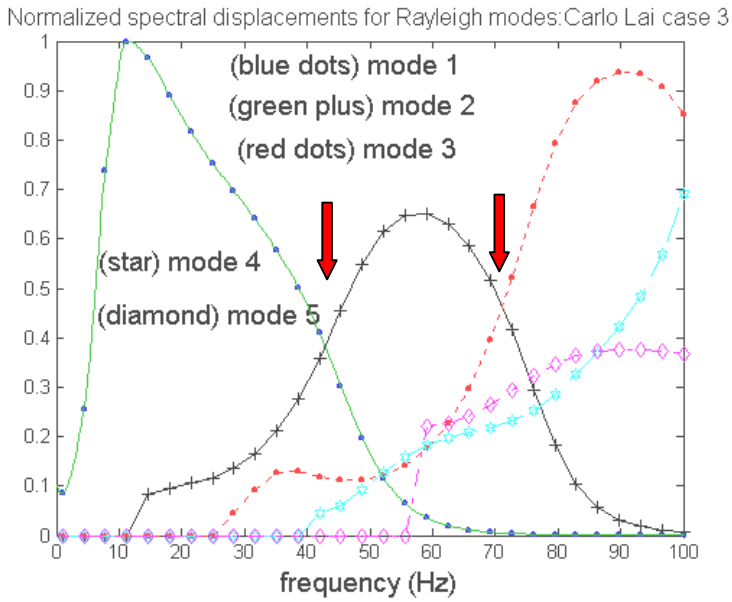

Figure 2.30: Relative importance of Rayleigh modes and natural frequencies.

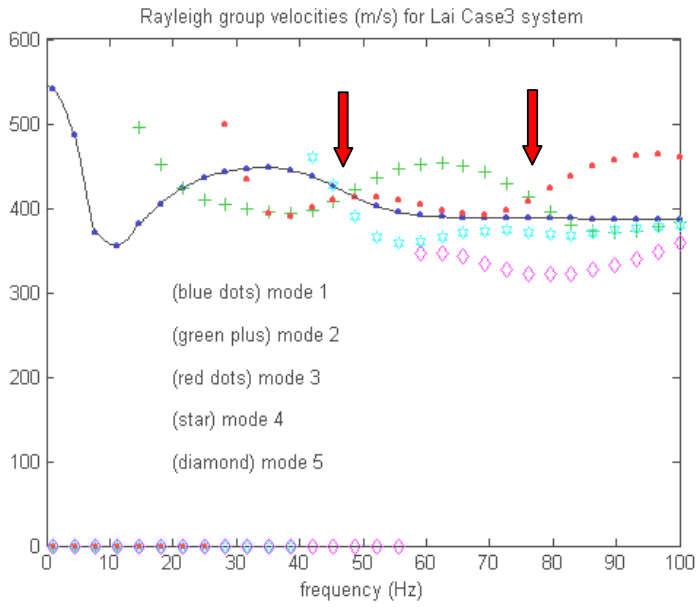

Figure 2.31: Modal group velocities for Lai Case3.

The transition of predominance from the ith mode to the jth mode occurs in a range of frequencies, where the energy of the ith mode drops down and the energy of the jth mode grows up. The reason why such a transition exists from one mode to another is not completely understood yet. It seems as if the frequencies of transition of predominance from the ith mode to the jth mode coincides with the zones where the curvature of the dispersion curve is stationary in the phase velocity-frequency representation (fig.2.29), as just evidenced by some authors (Gucunski and Woods, 1991).
The energy of the ith mode decreases at about the same frequency at which its group velocity becomes definitely lower than the group velocity of the new predominant j^{th} mode, without hope of overcoming it again at higher frequencies. This happens if the ith mode will never become predominant again at higher frequencies. In the meantime the energy of the new predominant j^{th} mode grows up. It seems as if the predominant mode be characterized by the fact that it will reach the maximum flux of energy, before losing its predominance. Remember that the group velocity represents the velocity at which the energy associated to the wave travels. The main energy is carried by the mode that will carry it at the maximum speed. Anyway in the opinion of the Author the Rayleigh dispersion relation contains all the information, that is necessary to predict how the influence of the several modes varies in the f-k representation. For the example Lai Case3 the transition from the 1st mode to the 2nd mode happens between 40Hz and 50Hz and from the 2nd mode to the 3rd mode between 70Hz and 80Hz.

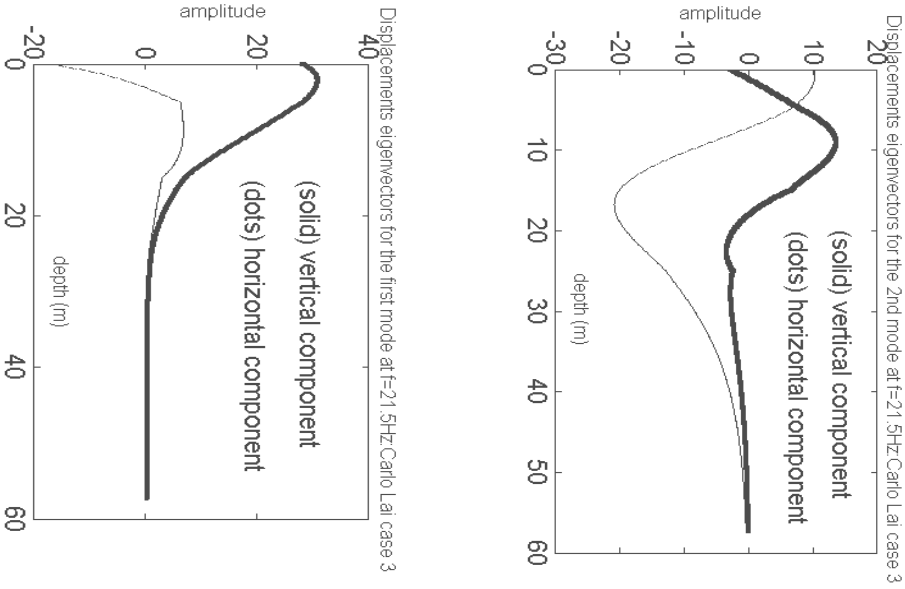

Figures 2.32a, b: Vertical (solid) and horizontal (dots) displacements eigenvectors for the 1st mode (a) and the 2nd mode (b) at the frequency f=21Hz for Lai Case3.

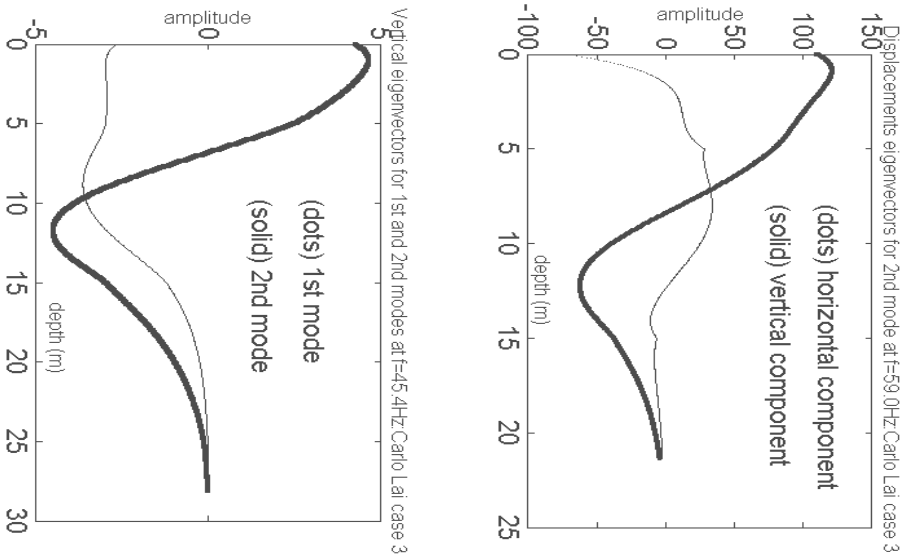

Figures 2.33a, b: Displacement eigenvectors for the 1st mode (dots) and the 2nd mode (solid) at f=45Hz (a) and vertical (solid) and horizontal (dots) components of the 2nd mode at f=60Hz (b).

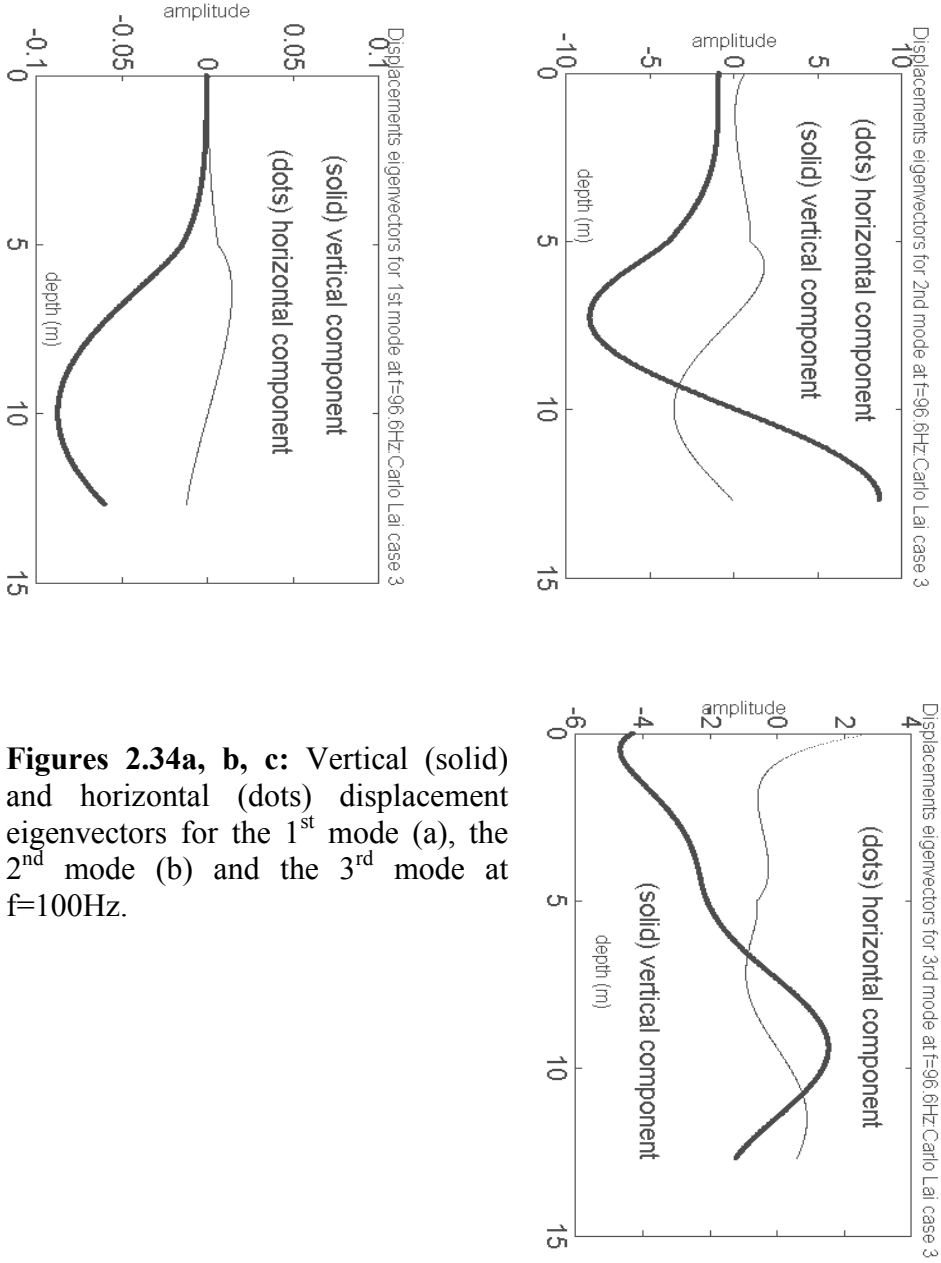

Figures 2.34a, b, c: Vertical (solid) and horizontal (dots) displacement eigenvectors for the 1st mode (a), the 2nd mode (b) and the 3rd mode at f=100Hz.

It is interesting to investigate the shapes of the displacement eigenvectors at different frequencies for the several modes. As it is expected at low frequencies (i.e.21Hz) the 1st mode is predominant, hence its modal shape follows the same trend with depth of the displacements in a homogeneous

half-space (fig.2.32a). The 2nd mode reaches a greater depth than the 1st mode, but it does not give any significant contribute on the surface (fig.2.32b). At higher frequencies (i.e.45Hz and 60Hz) the 2nd mode is predominant (fig.2.33a, b) on the free surface and its shape is again similar to that one in a homogeneous half-space, except that two changes in the sign of the curvature exist rather than one. The same behavior is observed for the 3rd mode with three changes in the sign of the curvature at the frequency of 100Hz (fig.2.34c), where the 1st and the 2nd modes can be neglected on the free surface (fig.2.34a, b).
An interesting observation is that the maximum depth at which information is available is 20m and it is reached by different modes at different frequencies. At f=21Hz by the 1st mode and the 2nd mode, but only the 1st mode is significant on the free surface, at f=45Hz and 60Hz only by the 2nd mode and at f=100Hz the maximum depth of 12m is achieved by the 2nd mode, but it cannot be observed on the free surface, where its amplitude is very small.

2.6.2.1 Influence of the spatial configuration of the receivers on the theoretical apparent dispersion curve

The importance of using the same spatial array of the receivers is due to the fact that the apparent dispersion curve is the result of an interaction of both the system and the spatial array (see section 2.6.1.1) and does not represent only the response of the system. The main reason is to be searched in the Discrete Fourier transform applied to the data, that are finite in time and space. This makes the Rayleigh modes appear as dispersed lobes rather than spikes in the spectrum at each fixed frequency, with secondary side-lobes that may interfere each other when two or more higher modes are pretty close at a certain frequency (see fig.2.37). This means that with the same system, changes in the spatial array of the sensors can cause variations in the apparent dispersion curve. As an example consider the system described in the table 2.3 (caseH):

Layer	Thickness h(m)	Vp (m/s)	Vs (m/s)	Mass density (Kg/m^3)
1	2	750	500	1900
2	10	300	200	1900
Half-space	∞	900	600	1900

Table 2.3: Site H: inversely dispersive site.

For this system a varying number n of receivers has been used to evaluate the theoretical dispersion curve with different inter-sensors spatial sampling Δx (see table 2.4).

	S(m)	Δx(m)	Sensors number	k_{Ny}	Total length
Case A	1.5	1.5	24	2	36
Case B	1.5	1.2	18	1.5	36
Case C	1.5	2.0	30	3	36
Case D	2.0	3.4	24	1	80

Table 2.4: Different spatial configuration of the receivers for the system H.

The dispersion curve does not change sensibly for the cases A, B and C.
As it can be seen in fig.2.35 and fig.2.36 the apparent dispersion curve varies at the frequency of about 75Hz for the case D. Up to the 6th mode, at a frequency of 70Hz, the theoretical apparent dispersion curve is the same for all the cases. In the cases A, B, C the theoretical dispersion curve passes from the 6th mode to the 9th mode, instead in the case D even the 8th mode becomes predominant between 70Hz and 80Hz.
As just said before, the reason is that the side-lobes generated by the different spatial arrays have different size and, when more modes are close in the wave number domain at a certain frequency, as a result of interference it is not possible any more to distinguish the peaks associated to the modes, but only one common and large peak appears. In the cases A, B, C in fig.2.37 we can observe the spectrum of displacements at the frequency of 75Hz. Only three peaks are visible, that represent all the existing Rayleigh modes at that frequency.

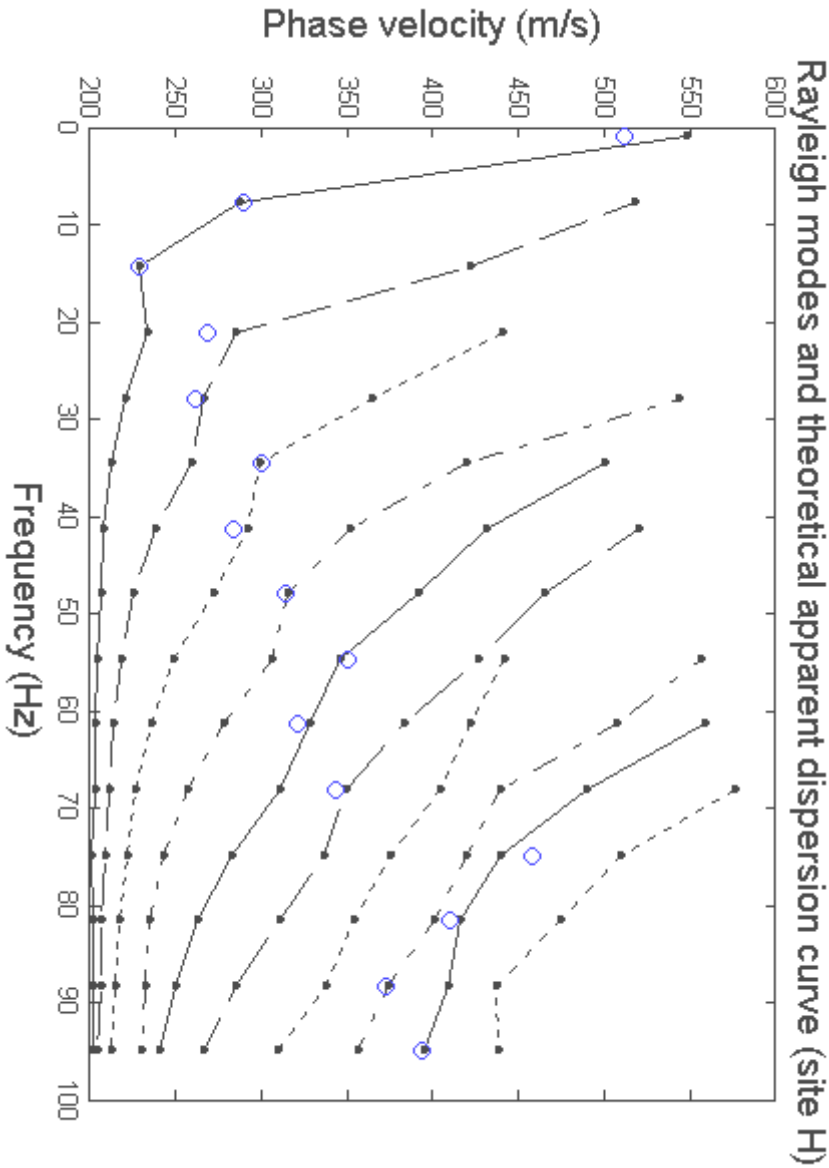

Figure 2.35: Rayleigh modes and theoretical apparent dispersion curve (o) for cases A, B, C.

Actually the main energy associated to the perturbation at that frequency is only carried by the 7th, 9th and the 6th modes (see fig.2.38), but the secondary left-lobe of the 7th mode interferes constructively with the peak of the 9th mode, more than the secondary right-lobe of the 9th does with the peak of the 7th mode, so that, when all of them are considered together (fig.2.37), the apparent maximum peak coincides with the first peak from the left, that is nearest to the 9th mode. As a consequence the apparent theoretical dispersion curve jumps from the 6th mode at f=69Hz to the 9th mode at f=75Hz.

In the case D (fig.2.36) another kind of interaction exists, so that at 75Hz the 7th mode is predominant, as it should be by looking at the fig.2.38, where the spectrum of all the modes considered independently has been reported. The meaning of such a plot is relevant, since it allows to identify the natural frequencies of the system as the frequencies at which the response is maximized. On this topic the whole end of the chapter is focused, due to its importance for dynamic soil-structure interaction applications. It is remarkable that in all the considered cases A, B, C, D the natural frequencies at which the system reaches the resonance, are the same. This means that the natural frequencies of the system are found without dependence on the particular spatial array of receivers that is used.

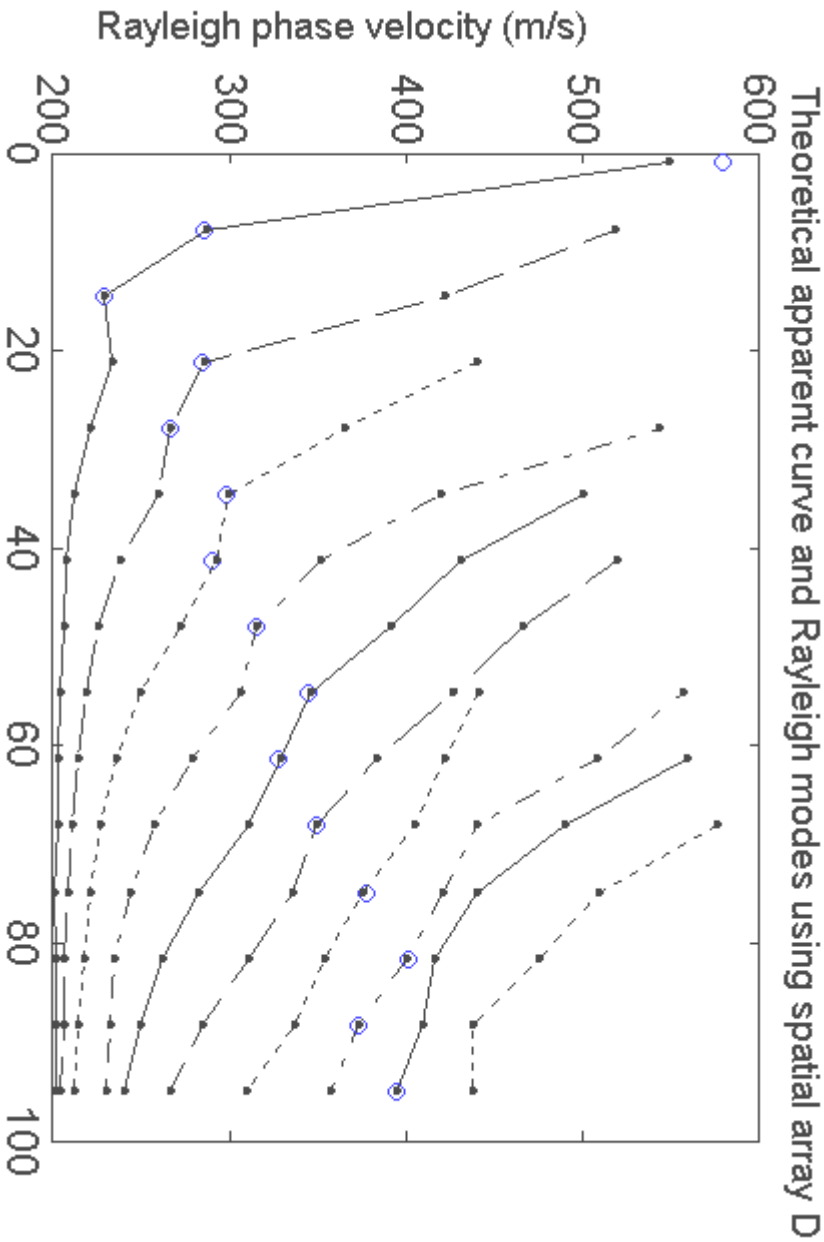

Figure 2.36: Rayleigh modes and theoretical apparent dispersion curve (o) for case D.

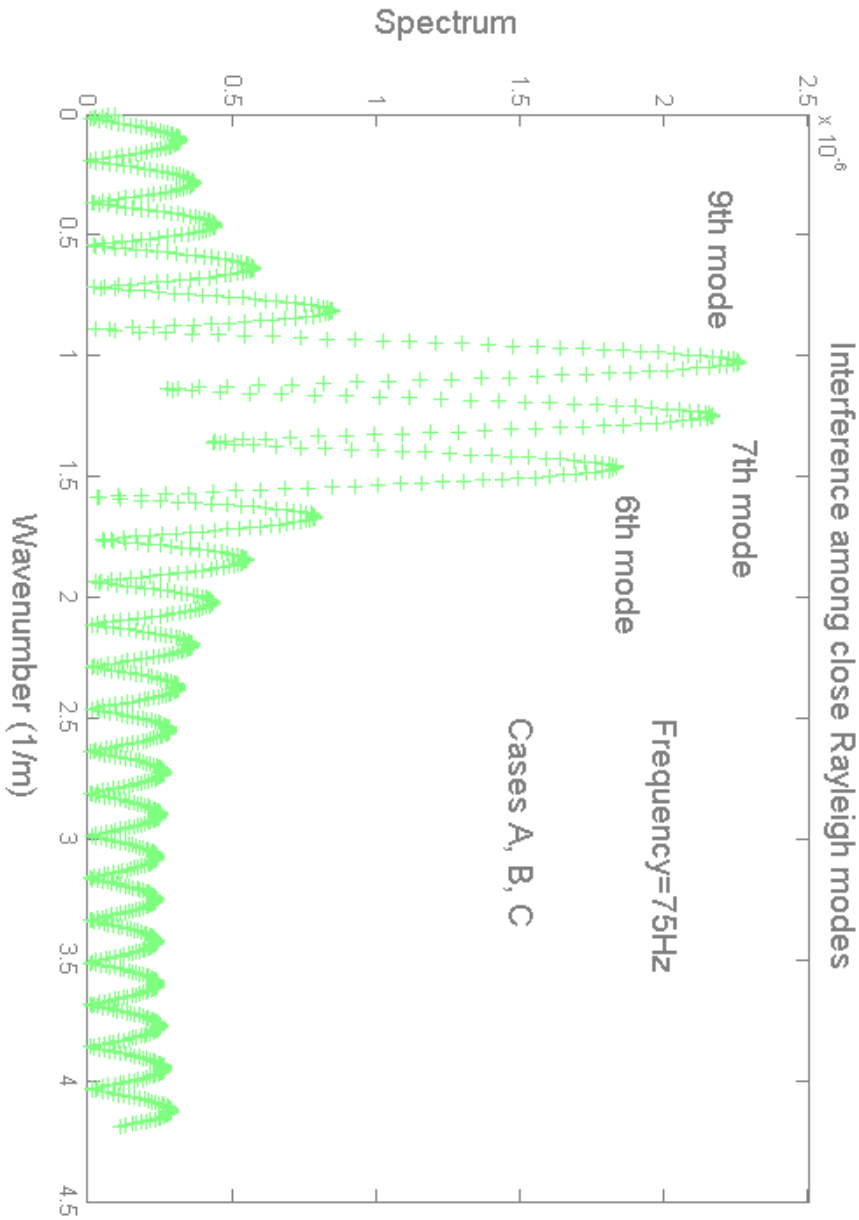

Figure 2.37: Spectrum of the vertical displacements at the frequency of 75Hz in the cases A, B, C. Interaction between the system and the spatial configuration of the receivers.

An interesting aspect is that the peaks in the modal spectrum of each mode are not modified, if the displacements are multiplied by a geometric factor $1/\sqrt{r}$, to account for the geometric attenuation of Rayleigh waves with distance r from the source. The same consideration has been made by (Tselentis and Delis, 1998) for the evaluation of the dispersion curve. The fig.2.39 shows the modal normalized spectra in the case D, after each modal component of the displacements has been amplified by the geometric factor $1/\sqrt{r}$.

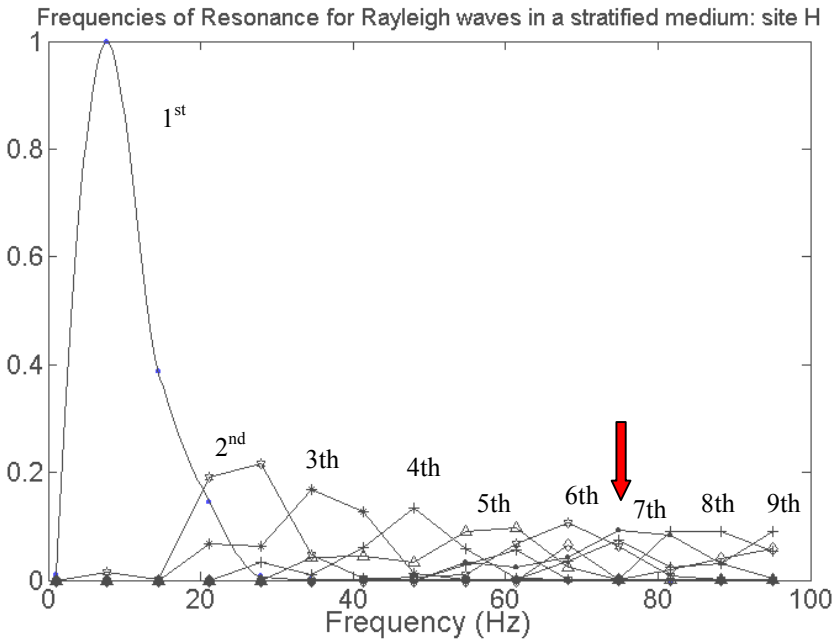

Figure 2.38: Normalized spectrum of the modal vertical displacements considered independently from each other (all the cases A, B, C, D). The relative importance of the higher modes of Rayleigh can be seen at different frequencies with the natural frequencies of the system H.

If the same configuration of receivers is adopted, a guarantee of consistency between the experimental and theoretical procedures can be established. This expedient assures that in ideal noiseless conditions the apparent dispersion curve only depends on the properties of the system, once the spatial array of sensors has been fixed.
In this section 2.6.2 it has been said that the apparent theoretical dispersion curve can be evaluated by means of only 1D Fourier transformation from the frequency-space domain to the frequency-wave number domain, instead of a 2D Fourier transformation from time-space to frequency-wave number. This is true under some hypotheses, which have been previously listed, and

it has been theoretically demonstrated and experimentally verified (see Appendix A). The two main advantages are that there is no need for the source characterization and the time saving in calculating the theoretical simulation. The reader should notice that it was not obvious affirming the equivalence among any kinds of sources in evaluating the theoretical response of the system.

In the next Chapter 3 it will be possible to implement an *Inversion algorithm* for determining the dynamic stiffness profile, thanks to this new method of evaluating the theoretical dispersion curve.

In the next section a comparison among the three methods will be presented for evaluating the theoretical apparent dispersion curve. The standard SASW with only two sensors, the effective phase-velocity method and the new proposed f-k theoretical method will be applied to both normally and inversely dispersive examples and the validity of the f-k theoretical method will be confirmed.

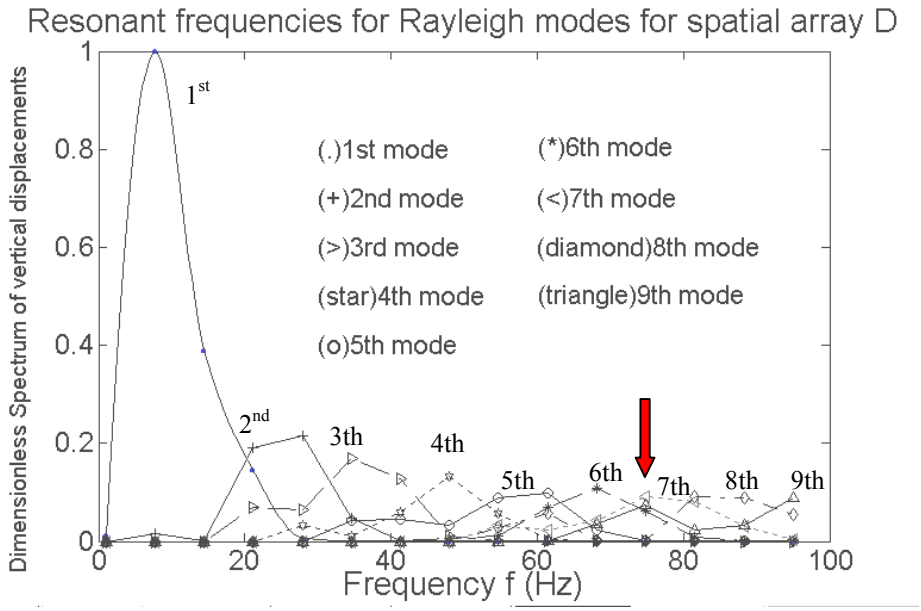

Figure 2.39: Influence of the geometric spreading factor 1/√r on the natural frequencies of the system and the theoretical apparent dispersion curve.

2.7 Comparison among SASW, Effective phase velocity and f-k methods

In this section some representative examples, both normally and inversely dispersive systems, will be studied in order to make a comparison among different methods for evaluating the theoretical apparent dispersion curve. As first case A a normally dispersive system is considered, whose characteristics are illustrated in the table 2.5 below:

Layer	Thickness h(m)	Vp (m/s)	Vs (m/s)	Mass density (Kg/m^3)
1	5	600	350	1800
2	10	700	400	1800
Half-space	∞	800	450	1800

Table 2.5: System A normally dispersive site.

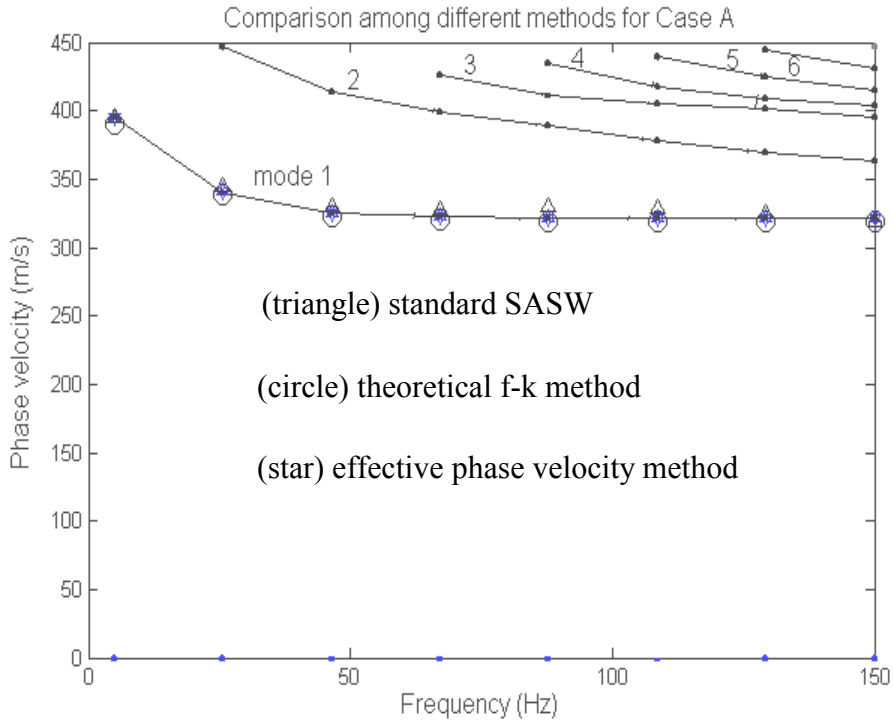

Figure 2.40: Comparison among different methods for evaluating the theoretical apparent dispersion curve for case A.

As it is expected, the fundamental Rayleigh mode is predominant at all the frequencies, since the system A is normally dispersive and the higher modes can be ignored in determining the theoretical dispersion curve, to be compared with the experimental curve.

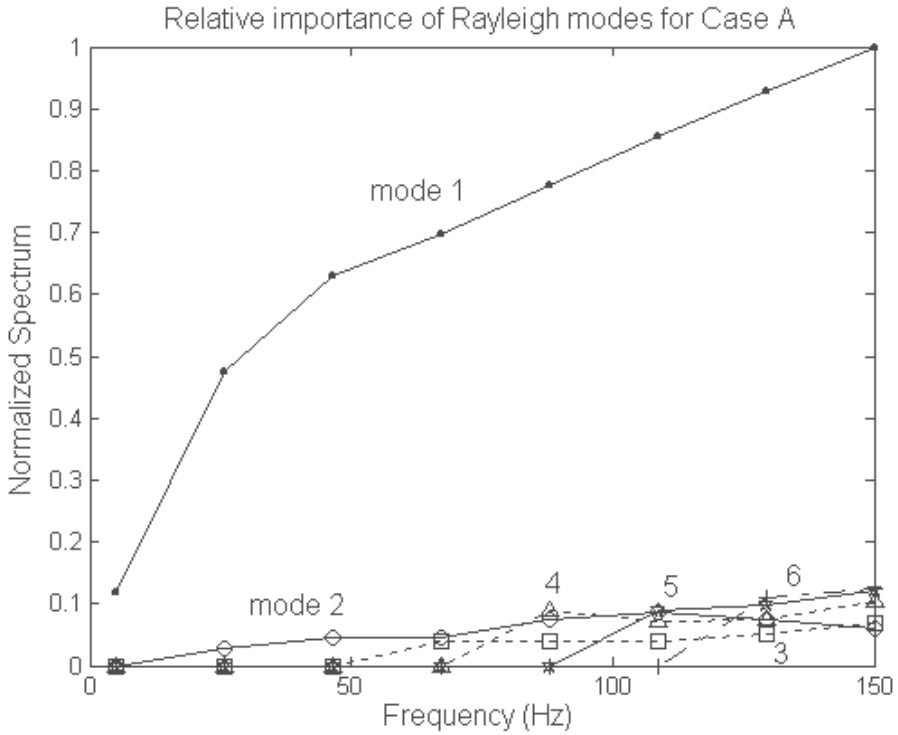

Figure 2.41: Relative importance of Rayleigh modes for case A

In fig.2.40 the Rayleigh modes are plotted in terms of the phase velocity, together with the apparent theoretical dispersion curves, evaluated by means of three different methods. The results of the standard SASW (triangles), of the effective phase velocity method (stars) and the theoretical f-k method (circles) match very well, perfectly fitting the fundamental mode of Rayleigh.

This result is clearly understood, if we observe the normalized spectrum of surface vertical displacements associated to each Rayleigh mode of vibration (fig.2.41). The first mode is always predominant over the higher modes, that increase and decrease with the frequency with an alternation of importance. So the transition of a sort of secondary predominance concerns the higher modes, that remain always negligible compared to the fundamental mode.

As second example an inversely dispersive system B has been taken, that is described in table 2.6.

Layer	Thickness h(m)	Vp (m/s)	Vs (m/s)	Mass density (Kg/m^3)
1	5	700	400	1800
2	3	500	300	1800
Half-space	∞	800	450	1800

Table 2.6: System B inversely dispersive: softer layer trapped between two stiffer ones

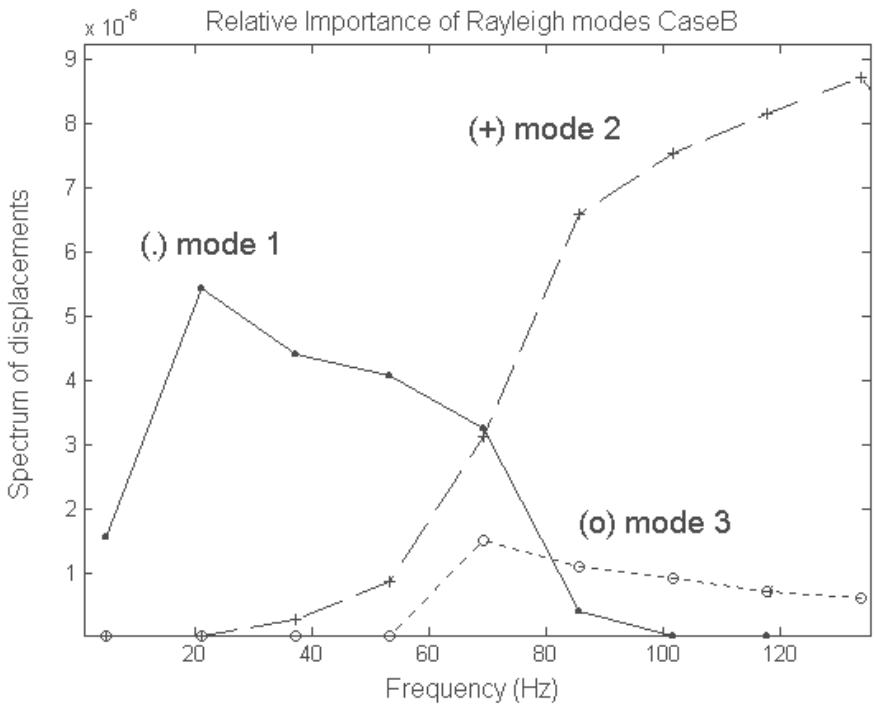

Figure 2.42: Relative importance of Rayleigh modes for case B

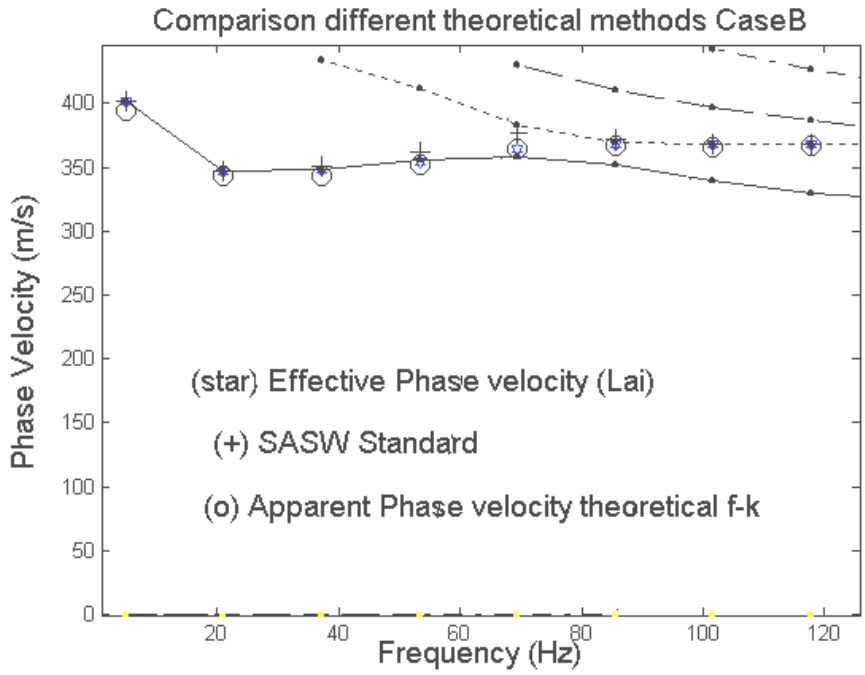

Figure 2.43: Theoretical apparent dispersion curve for Case B.

This case has just been encountered in Chapter 1, when describing the problem of the jumps in the Rayleigh dispersion relation. It represents a system with a soft layer trapped between two stiffer ones and, as shown in fig.2.42, the fundamental mode is the most important up to a frequency of about 70Hz, then the 2nd mode becomes predominant. Again the agreement among the theoretically dispersion curves, evaluated by means of different methods is excellent (fig.2.43).

An aspect, that needs to be mentioned about the effective phase velocity method by Lai, is that the effective phase velocity, as evaluated by means of (2.17), is a function of frequency and distance from the source. Hence for each frequency, n values of phase velocity are available, where n is the number of the sensors on the free surface (fig.2.44). This means that an averaging process is needed to obtain only one theoretical dispersion curve, to be compared to the experimental curve. Now an issue arises about the best criterion to be followed, to average the phase velocities at the several locations. It turns out that, by taking the mean value, satisfactory results are obtained (fig.2.43), even if, rigorously speaking, there is no reason for its validity, since the experimental dispersion curve is calculated in a different manner. It is this lack of consistency between the experimental f-k method and the theoretical effective phase velocity method (Foti, 2000), that has

motivated the search of a more consistent procedure, for evaluating the theoretical dispersion curve, as previously proposed in this Chapter (see section 2.6.2).

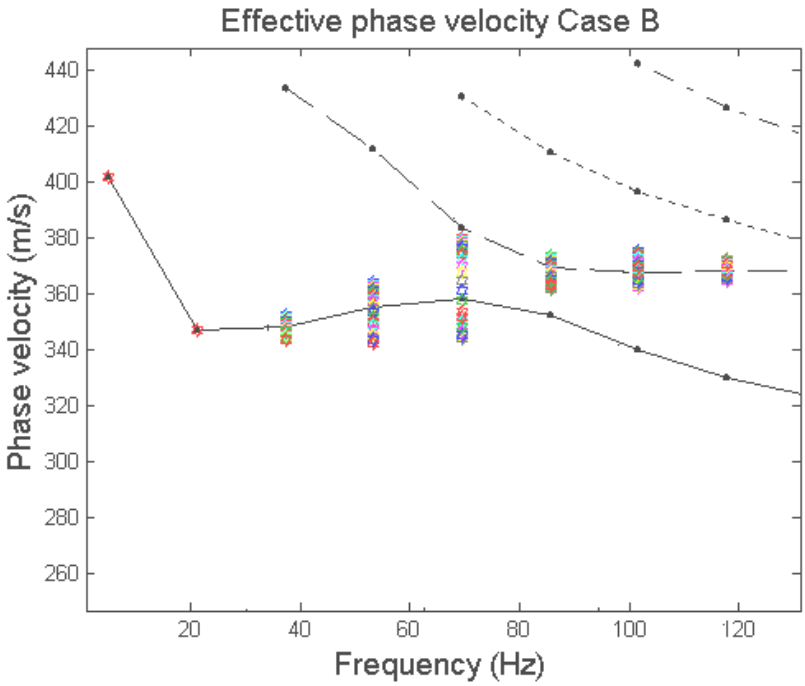

Figure 2.44: Effective Phase Velocities calculated at all the receivers location for each frequency.

As third example an inversely dispersive system has been chosen, that can be representative of a profile with a stiff layer on the top.

Layer	Thickness h(m)	Vp (m/s)	Vs (m/s)	Mass density (Kg/m^3)
1	10	1500	1000	1900
2	10	750	500	1900
Half-space	∞	1500	1000	1900

Table 2.7: System C inversely dispersive: stiff surface layer.

This case is similar to case B, except that a far more contrast exists between the stiffnesses of the surface layer and the second layer.

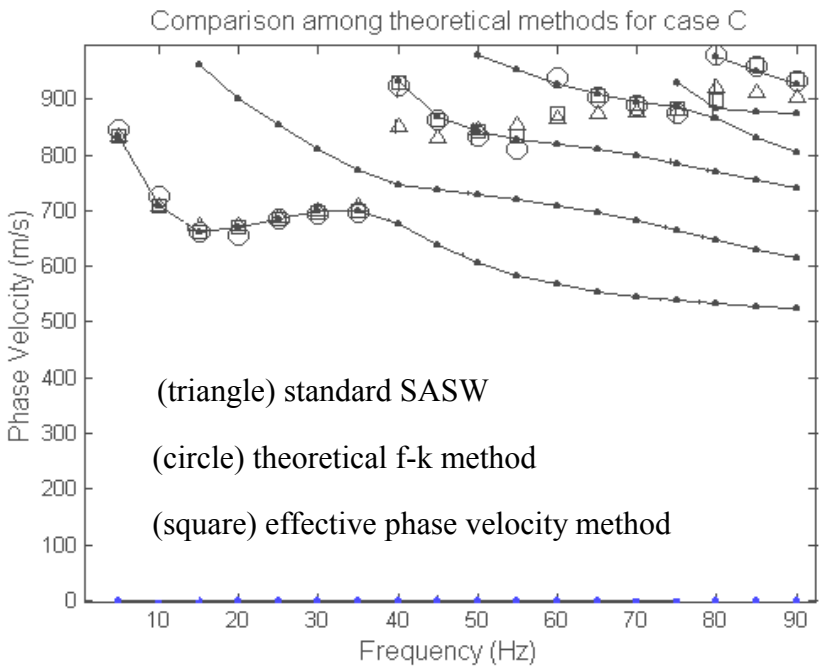

Figure 2.45: Theoretical Dispersion curves for Case C.

For this case it is quite evident that, at the cut-off frequency, each mode has a phase velocity value equal to the shear wave velocity 1000 m/s of the deepest layer, that is the half-space. Also all the Rayleigh modes tends to the asymptotic value equal to the shear wave velocity 500 m/s of the softer layer at high frequencies. Again in fig.2.45 and fig.2.46 the comparison among different procedures and the relative importance of Rayleigh modes are reported. The f-k method allows for a theoretical dispersion curve, that further considers the relative importance of Rayleigh modes. In fact the 2nd mode is never predominant (fig.2.46) and consequently the apparent dispersion curve never coincides with this mode (fig.2.45).

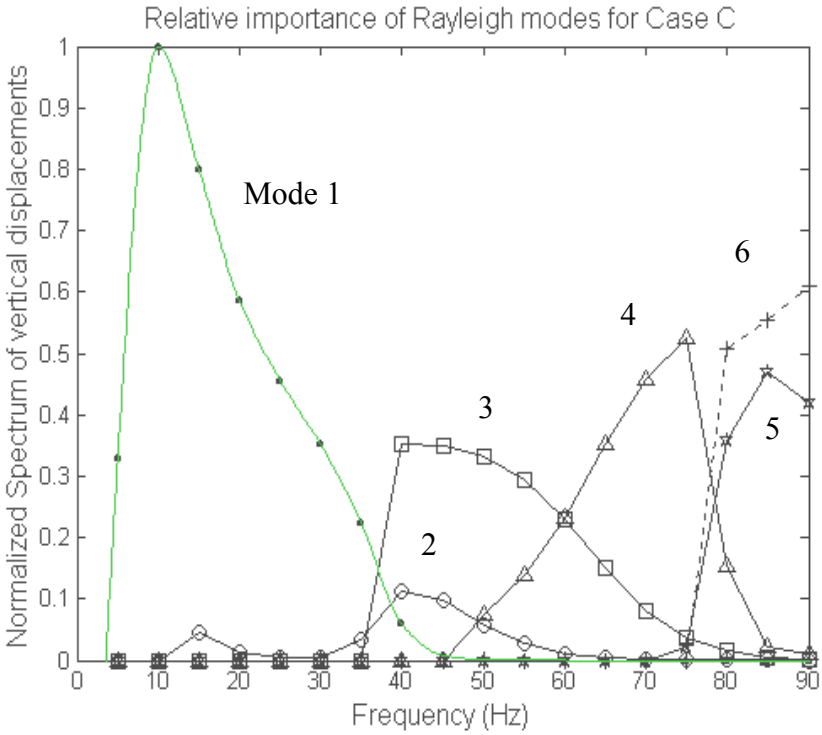

Figure 2.46: Relative importance of Rayleigh modes for Case C.

As last example another inversely dispersive system has been taken from the paper by (Gucunski and Woods, 1991), except that here any dissipation of energy has been neglected. This system represents a case where a stiffer layer is trapped between two softer ones.

Layer	Thickness h(m)	Vp (m/s)	Vs (m/s)	Mass density (Kg/m^3)
1	20	1200	600	1800
2	20	2000	1000	1800
3	80	1200	600	1800
Half-space	∞	2000	1000	1800

Table 2.8: System by Gucunski inversely dispersive: stiff layer trapped between two softer layers.

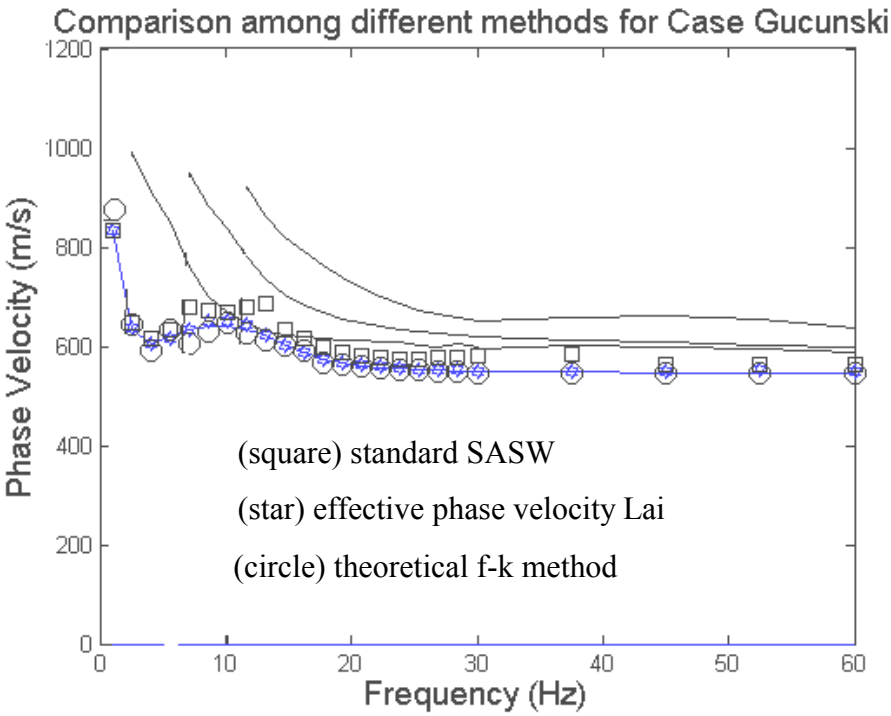

Figure 2.47: Rayleigh modes and apparent dispersion curves for case from Gucunski.

The fact that no layers exist, that are stiffer than the half-space, assures the existence of propagating Rayleigh waves at any frequency.
In fig.2.47 only the first four Rayleigh modes have been plotted together with the theoretically simulated apparent dispersion curves. The agreement among the several methods is satisfactory even in this types of systems, in which the fundamental mode is predominant at almost all the frequencies, except in a narrow range, between 5Hz and 10Hz in this case, where the system response coincides with the second mode. A more insightful picture of the relative importance of Rayleigh modes is offered in fig.2.48 by the projection on the frequency domain of the normalized spectrum of vertical displacements of each mode, along their path in the frequency-wave number domain. In fig.2.48 only the first three Rayleigh modes have been reported, since the higher modes are not relevant.

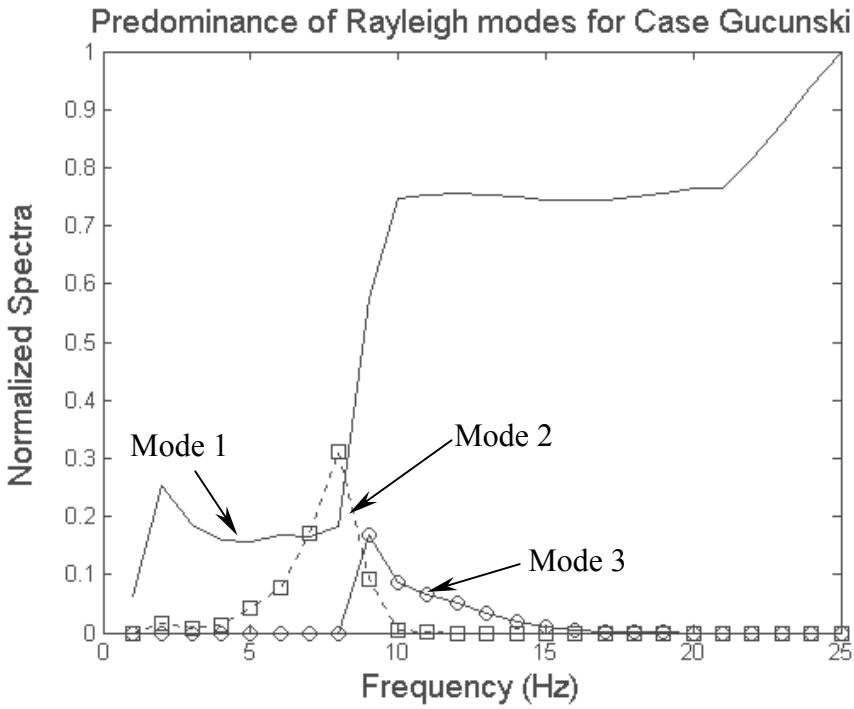

Figure 2.48: Case from (Gucunski and Woods, 1991). Projection on the frequency domain of the normalized spectrum of vertical displacements of each Rayleigh mode, following their path in the frequency-wave number domain.

2.8 Relative Importance of Generalized Rayleigh Modes of Propagation

As just previously underlined, the kind of representation in fig.2.48 enables one to discern the relative influence of each Rayleigh mode at a particular frequency of excitation. It also gives a clear identification of the system in terms of frequencies and wave numbers of resonance, where the system response is maximized. Look for example at the fig.2.29 case 3 from (Lai, 1998). It can be easily recognized that the peaks in the spectrum of the Rayleigh modes furnish the frequencies 10Hz, 60Hz, 90Hz where the system response reaches a maximum. The knowledge of the frequencies and the wave numbers of resonance for a given system is a precious information in several engineering applications, such as site local amplification, soil-structure dynamic interaction, control of vibrations produced by shallow machines or subways. Once the geometrical-mechanical properties of a layered half-space are given, it is possible to predict in which manner a known input source will be amplified by the system. The end of this Chapter will focus on this subject and the particular case of a single layer over a half-space will be studied, in order to correlate the frequencies and the wave numbers of resonance to the geometrical-mechanical properties of the system.

Hereafter a detailed explanation of the procedure followed to get the modal spectrum is described (Roma et al., 2001). Consider the jth modal component of the vertical displacements on the free surface of a layered half-space, due to a harmonic point source applied on the free surface as illustrated in fig.2.52 (see formula 2.9):

$$u_j\left(x,z,\omega,t\right)=A_j\left(x,z,\omega\right)\cdot e^{i\left(\omega\cdot t-k_j\cdot x+\frac{\pi}{4}\right)} \tag{2.42}$$

As it is explained in Appendix A, the modal Green Function or modal contribution to the space-frequency response of the system can be written from (2.42) as:

$$\bar{u}_j\left(x,z,\omega\right)=A_j\left(x,z,\omega\right)\cdot e^{i\left(-k_j\cdot x+\frac{\pi}{4}\right)} \tag{2.43}$$

which gives the vertical displacement in the frequency-space domain, due to the jth Rayleigh mode. By means of a Fourier Transformation the modal spectrum of the vertical displacements can be obtained in the frequency-wave number domain:

$$\bar{\bar{u}}_j(k,\omega) = e^{i\frac{\pi}{4}} \cdot \int A_j(x,z,\omega) \cdot e^{i\left(k-k_j\right)\cdot x} \cdot dk \qquad (2.44)$$

It is important now to think about the meaning of such a modal spectrum. In fact it says how the jth mode behaves along its modal dispersion path in the frequency-wave number domain. It is true that, by definition, the whole modal curve represents the locus of points, that define the natural modes of the system, but along the modal path in the frequency-wave number domain, some peaks are reached where the modal response is maximized.
So for example consider the system below:

Layer	**Thickness h(m)**	**Vp (m/s)**	**Vs (m/s)**	**Mass density (Kg/m^3)**
1	5	1500	1000	1800
2	5	750	500	1800
Half-space	∞	1500	1000	1800

Table 2.9: Inversely despersive system E.

The Rayleigh dispersion relation associated to this system is represented in the frequency-wave number domain in fig.2.49 and frequency-phase velocity in fig.2.50, instead the projection of the normalized spectrum of each mode (2.44) on the amplitude-frequency plane is plotted in fig.2.51.
A general observation is that higher modes reach at least a relative peak of resonance at higher frequencies than the lower modes.

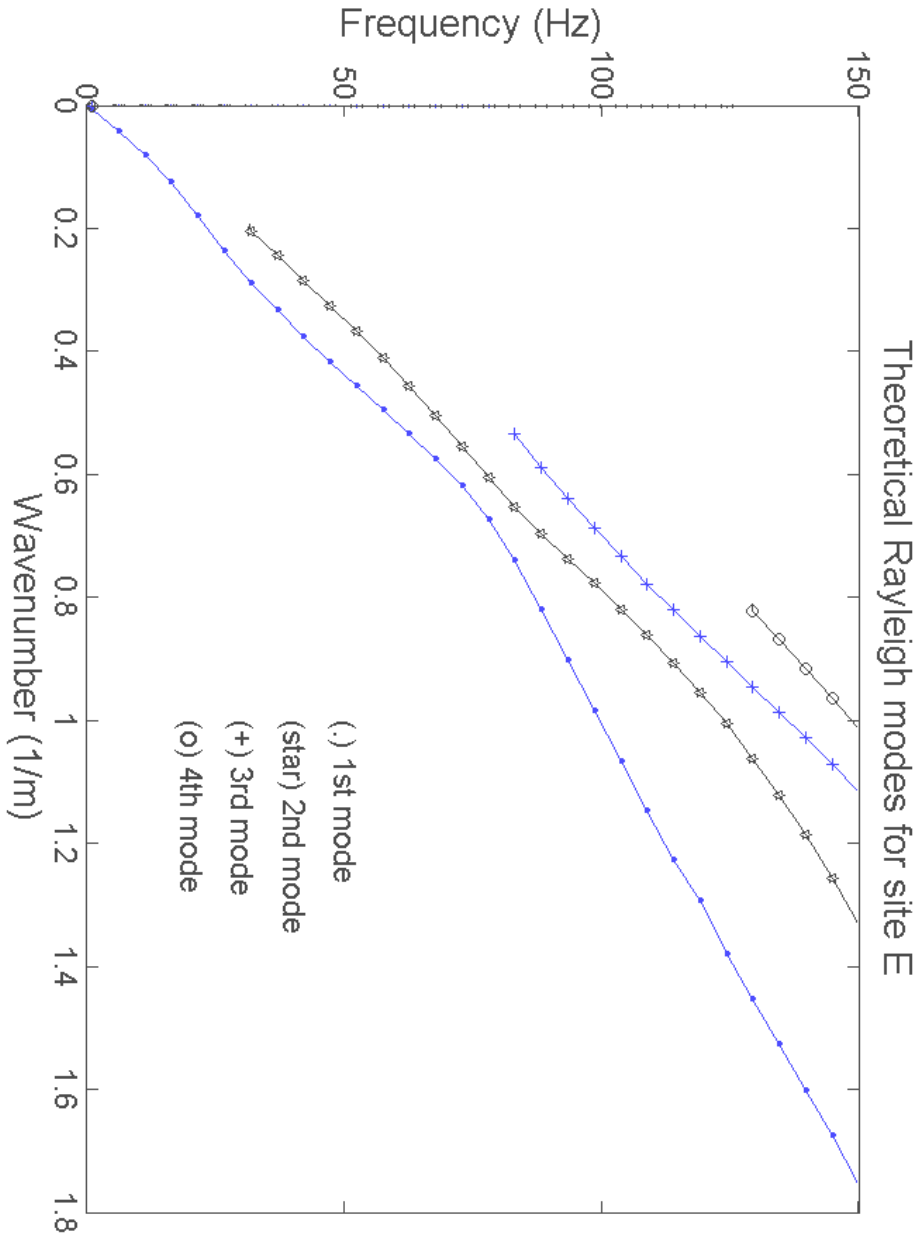

Figure 2.49: Rayleigh dispersion relation in f-k domain for the system E in table 2.9

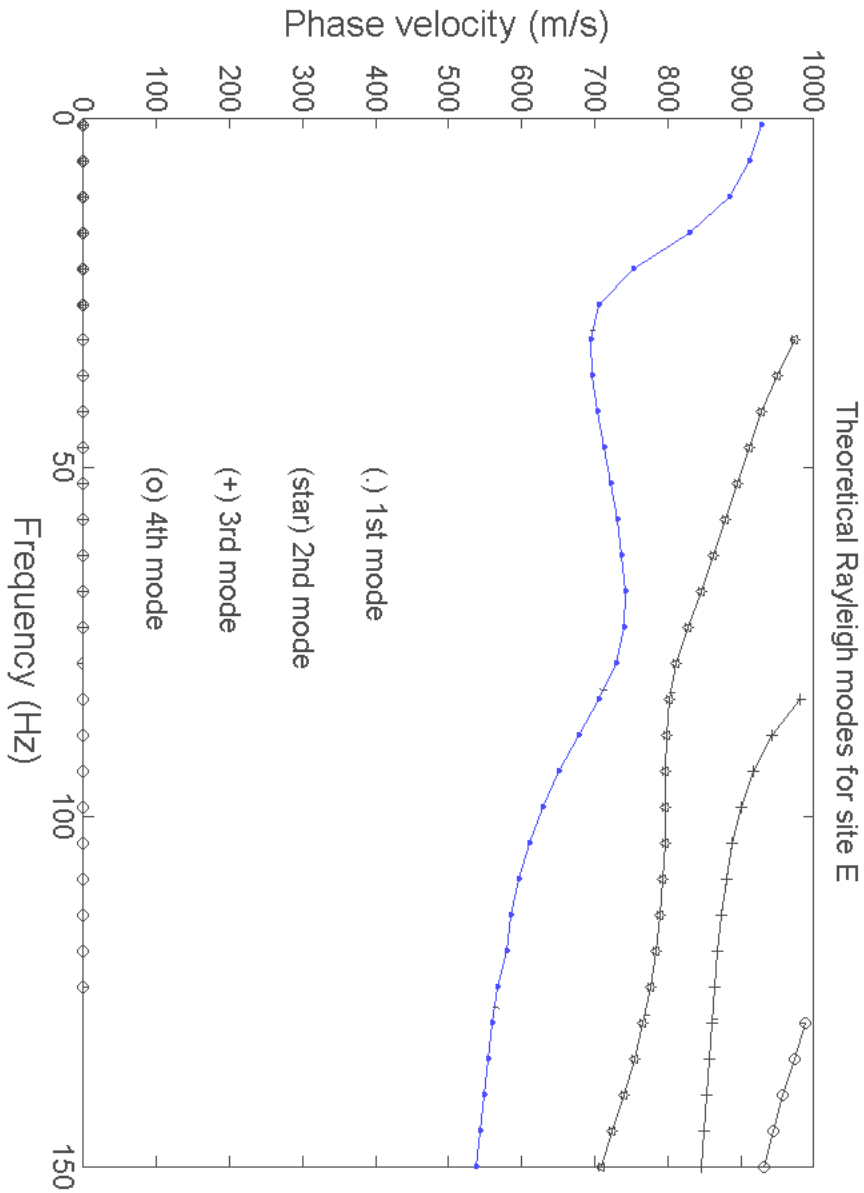

Figure 2.50: Rayleigh dispersion relation in f-Vphase domain for the system E in table 2.9.

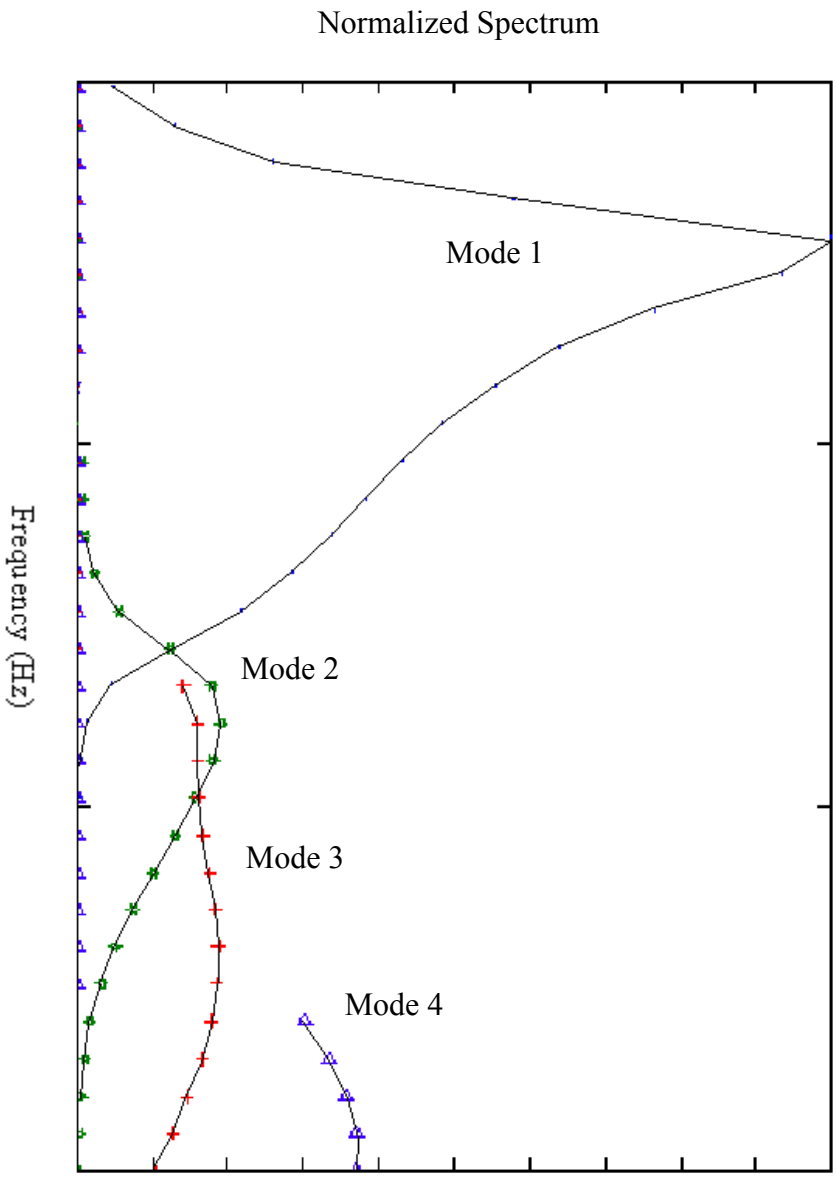

Figure .51: Projection of the normalized spectra of Rayleigh modes for the system E in table 2.9.

2.8.1 One layer over a Half-space

As it is expected, the Green Function of a system depends on its geometrical-mechanical characteristics, but very often it is not possible to find a simple correlation among the properties of the system and its natural frequencies and wave numbers. This is the case of a layered half-space, where neither the natural modes (given by the Rayleigh dispersion relation) are available in analytical form, nor the frequencies and the wave numbers of resonance. To have an idea of the analytical complexity of the problem in Appendix C the Rayleigh dispersion relation is reported for the simple case of a single layer over a half-space. Even in this simplified case, in order to study the influence of the system properties on the position of the peaks in the f-k spectrum of the displacements, associated to each Rayleigh mode, the only practicable way seemed a sensitivity analysis, to be held numerically by means of a code, properly implemented by the Author.
The schematic of the system is illustrated in fig.2.52 with its properties: thickness h_1 of the layer, shear wave velocities Vs_1 and Vs_∞, Poisson ratios ν_1 and ν_∞, mass densities ρ_1 and ρ_∞ of the layer (sub-index 1) and the half-space (sub-index ∞):

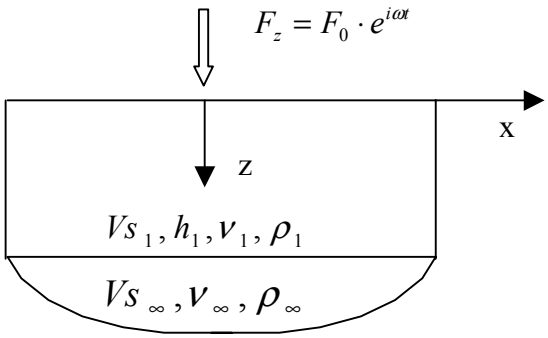

Figure 2.52: Mechanical System: a single layer over an infinite half-space. No dissipation is included in the model.

The strategy, that has been adopted, is to hold all the parameters constant except the one of interest, so that its influence on the position of the peaks can be easily put in evidence.

2.8.1.1 Dependence from the generic Rayleigh Mode

The first variable, that has been investigated, is the number j of the Rayleigh mode of vibration. In the fig.2.53 the dependence of the frequency of resonance f_R upon the jth mode has been represented for a set of constant properties.
In this study only the first five modes have been taken into account, since higher modes are not relevant in engineering applications. As it can be seen from fig.2.53 a linear relationship exists between the frequency of resonance f_R and the jth mode, i.e. the higher the mode the greater the frequency f_R. It should be observed that this excellent agreement has been found to hold for different sets of parameters.

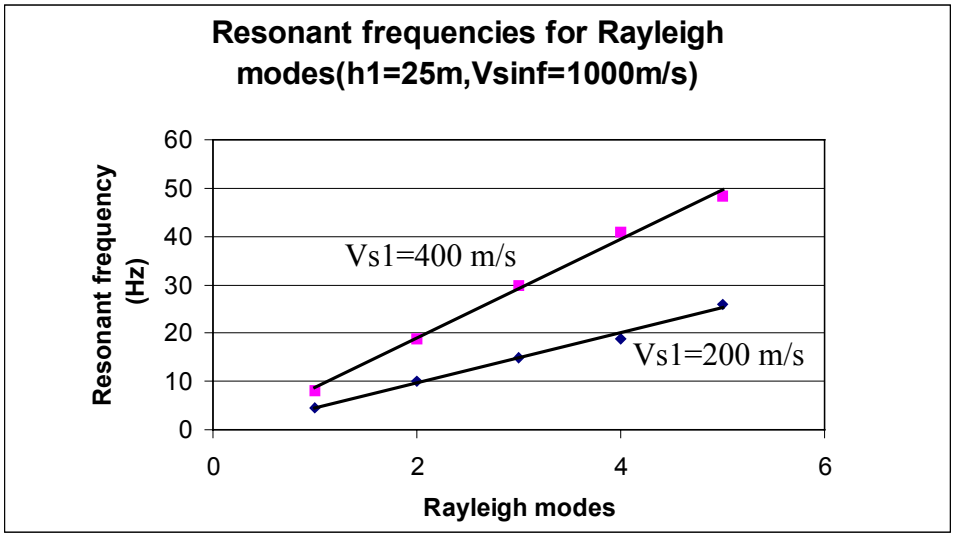

Figure 2.53: Influence of the j-th Rayleigh mode on the frequency of resonance

2.8.1.2 Influence of the Thickness

The next variable is the thickness h_1 of the layer, that is reported on the x axe(see fig.2.54). On the y axe a dimensionless quantity is put, that is given by:

$$y = \frac{f_R \cdot h_1}{Vs_\infty} \tag{2.45}$$

In this way it is more clear that an inversely proportionality ties the thickness h_1 and the resonant frequency f_R, in fact for all the modes the chosen dimensionless quantity y remains constant. Of course this is true for whatever choice of the constant properties the simulation is run. It is worthy to note that the relationship holds for a wide range of thickness i.e from 2m up to 25m at least.

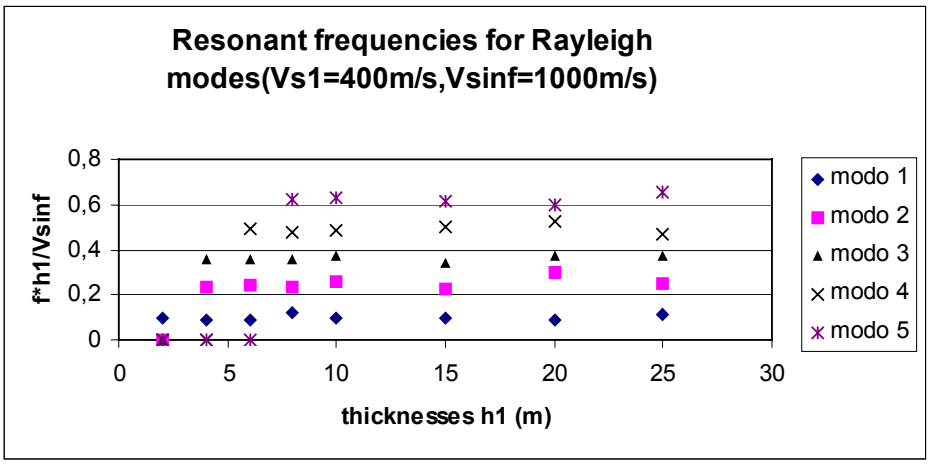

Figure 2.54: Variation of the resonant frequency f_R with the thickness h_1 of the layer.

2.8.1.3 Variation with Shear Wave Velocities of both the layer and the half-space

Successively the influence of the shear wave velocities of the layer Vs_1 (fig.2.55) and the half-space Vs_∞ (fig.2.56) has been studied and from fig.2.55 it can be inferred that again a linear link correlates Vs_1 to f_R, instead it seems that f_R does not depend on the stiffness of the half-space.

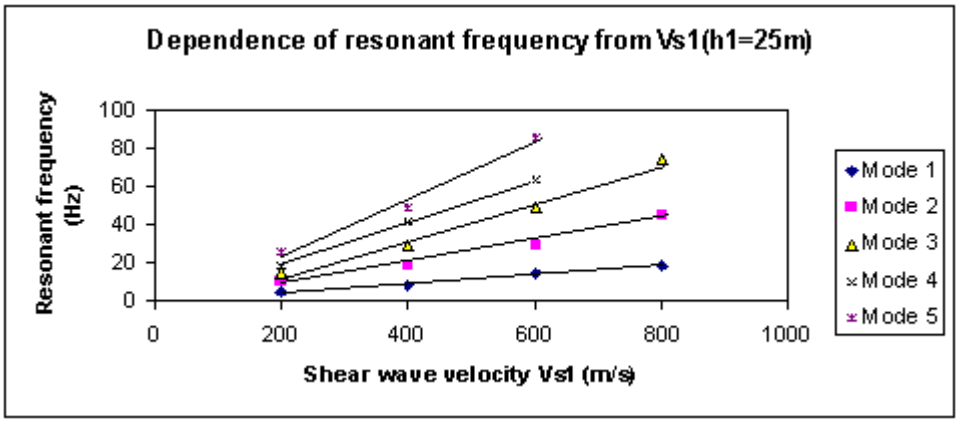

Figure 2.55: Frequency of resonance f_R as a function of the shear wave velocity Vs_1 for several modes.

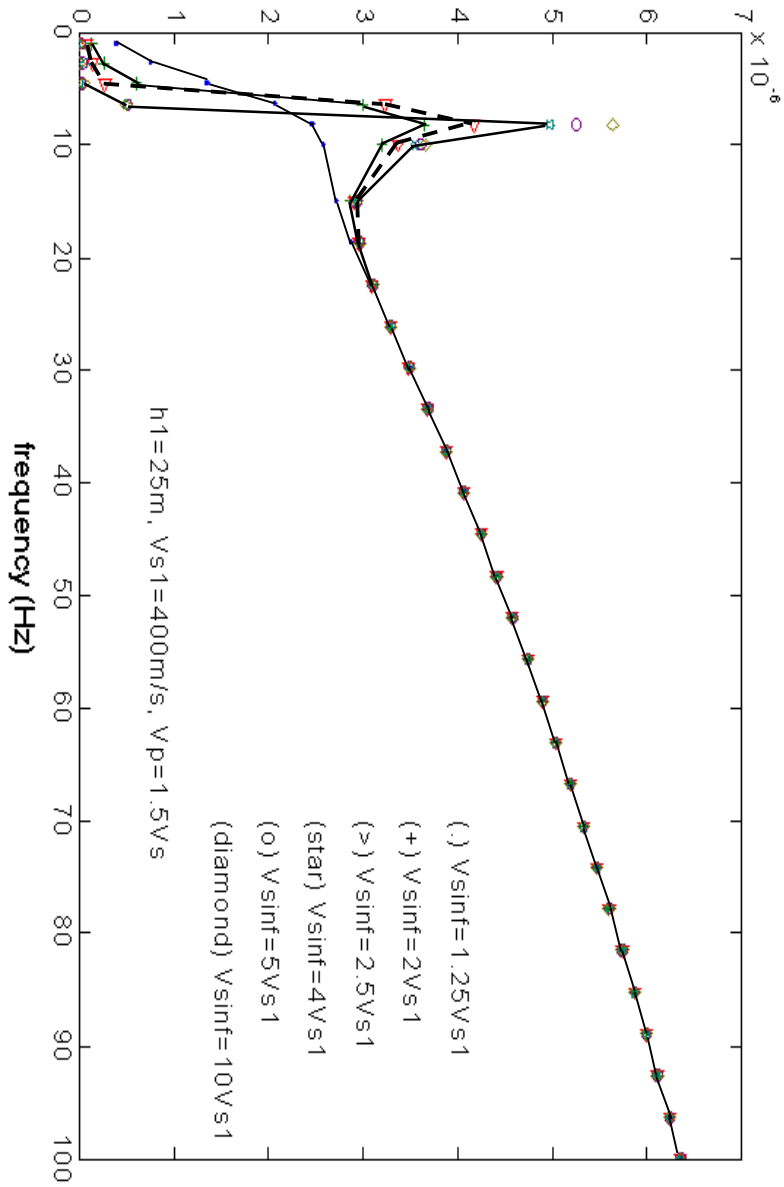

Figure 2.56: Spectrum of the vertical displacement (fundamental mode only) for different values of shear wave velocity Vs_{∞} of the half-space.

What it can be said is that, if the shear wave velocity Vs_{∞} (fig.2.56) of the half-space varies, the frequency at which the spectrum shows its peak does not change significantly, but only the magnitude of the peak is strongly influenced by the stiffness ratio between the half-space and the layer. Precisely as the contrast between the stiffness increases, the peak becomes sharper as it is expected. Indeed in the extreme case of infinitely rigid half-space, all the energy carried by an incident wave, coming from the upper layer on the interface is reflected back into the layer and no radiation of energy occurs. Actually a very slight variation of the frequency of resonance happens, since the whole system varies its stiffness, but this change can be neglected without any appreciable error. Even if not reported, such a behaviour has also been observed for higher modes.

2.8.1.4 Effects of the Poisson Ratio

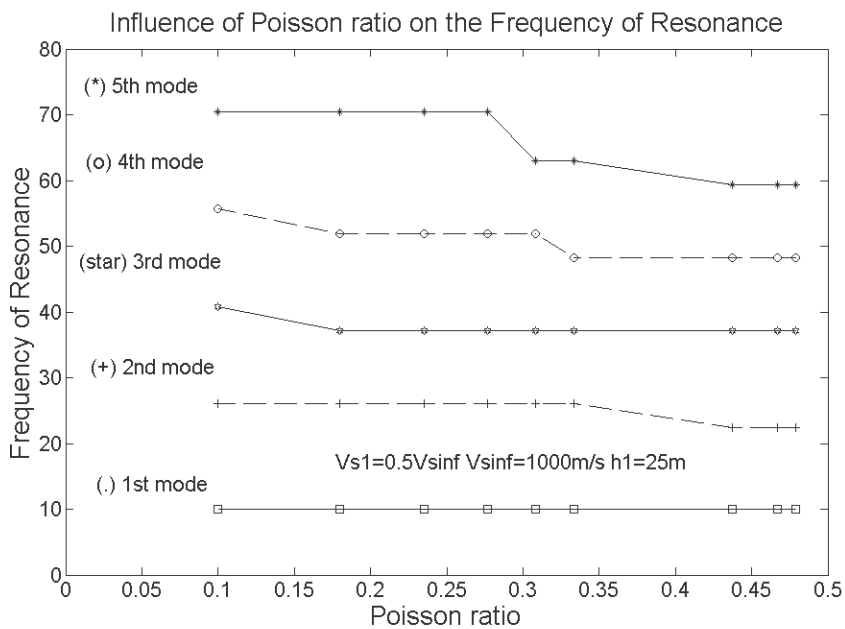

Figure 2.57: Influence of the Poisson ratios on the resonance of the Rayleigh modes. The same Poisson ratio $\nu_1 = \nu_{\infty}$ has been kept for the simulations.

The last parameters that have been analysed are the Poisson ratios, whose results seem to show that the frequency of resonance f_R is practically independent from them in a wide range of variation, even if a more detailed

investigation is suggested for confirmation. In fig.2.57 the frequencies of resonance for Rayleigh modes have been drawn, taking the same Poisson ratio for both the layer and the half-space. For the fundamental mode no variations exist by changing the Poisson ratios, instead the higher modes seem to have a weak dependence on them. In fig.2.58 the 3rd modal spectrum of the system specified in the figure has been plotted for three different values of the Poisson ratios. As it can be observed the position of the peak slightly varies.

By summarising all the results obtained herein an approximate relationship can be written among the parameters of the system under consideration and the frequency of resonance f_R for the generic j-th Rayleigh mode:

$$f_R(j) \cong (A + Bj)\frac{Vs_1}{h_1} \tag{2.46}$$

in which the two constants A and B have been determined as follows.

Plotting all the simulations, that have been performed, in terms of the dimensionless variable

$$\bar{y} = \frac{f_R \cdot h_1}{Vs_1} \tag{2.47}$$

as a function of the generic j-th Rayleigh mode a line can be drawn from which the two constants A and B that appear in (2.46) has been evaluated (fig.2.59).

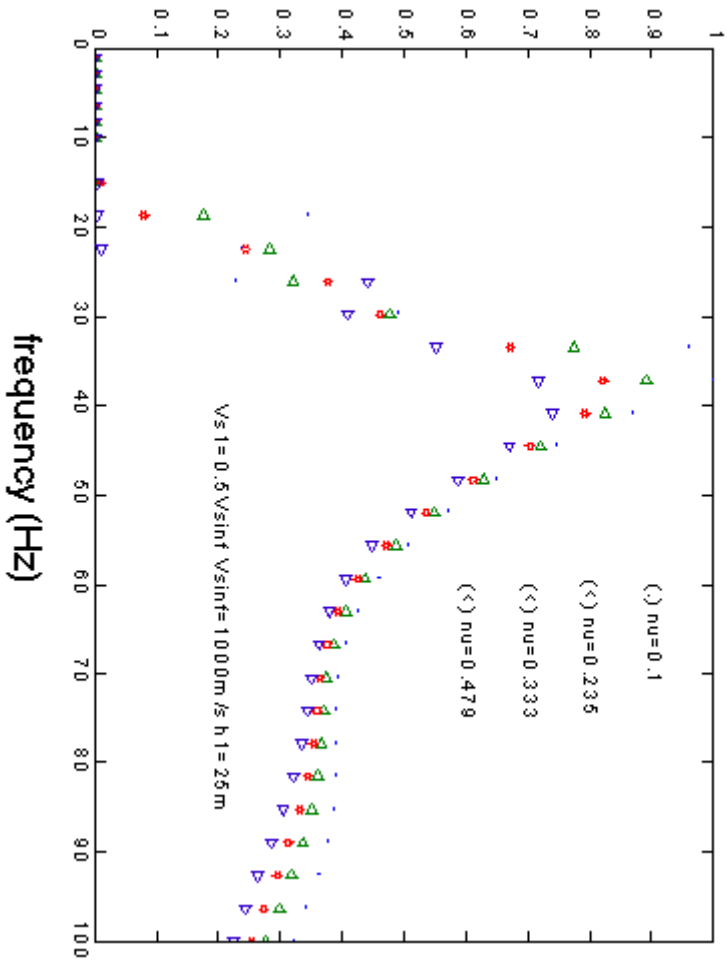

Figure 2.58: Influence of Poisson ratio on the resonant peak of the 3rd mode.

It has also been shown the error associated to each point in the assumption of a Gaussian distribution of the error. As it can be seen the relative error of the dimensionless quantity $\bar{y}$ is always less than 5%, that proves the formula (2.46) to be valid.

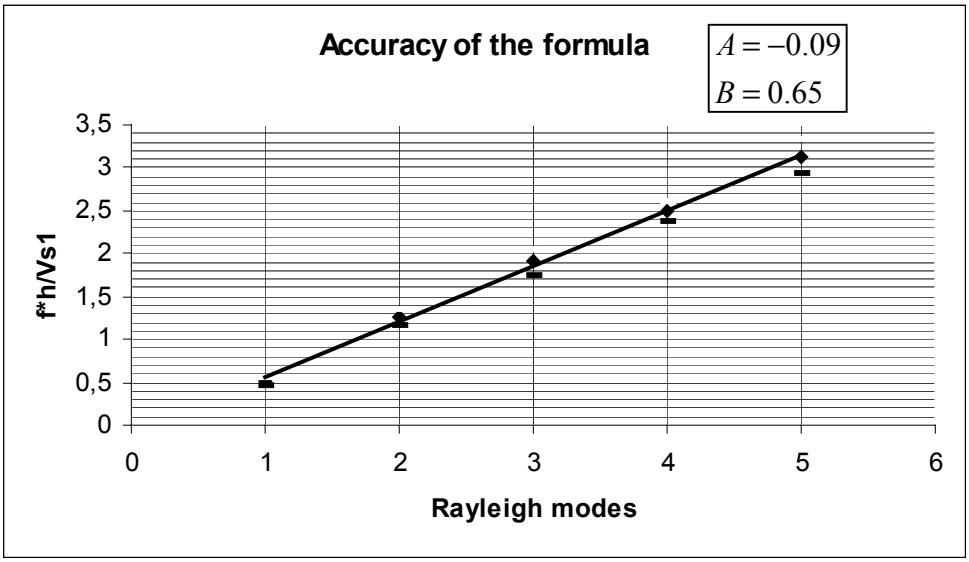

Figure 2.59: Determination of the constants A and B and associated error.

To test the validity of the formula (2.46) consider the example in fig.2.60. The predicted frequencies of resonance of each mode are reported in table 2.10:

	Mode 1	**Mode 2**	**Mode 3**	**Mode 4**	**Mode 5**
Resonant frequency (Hz)	14.9	32.3	49.6	66.9	84.3

Table 2.10: Resonant frequencies for the example in fig.2.60.

The agreement between the predictions of the formula (2.46) and the calculated modal spectra are excellent.

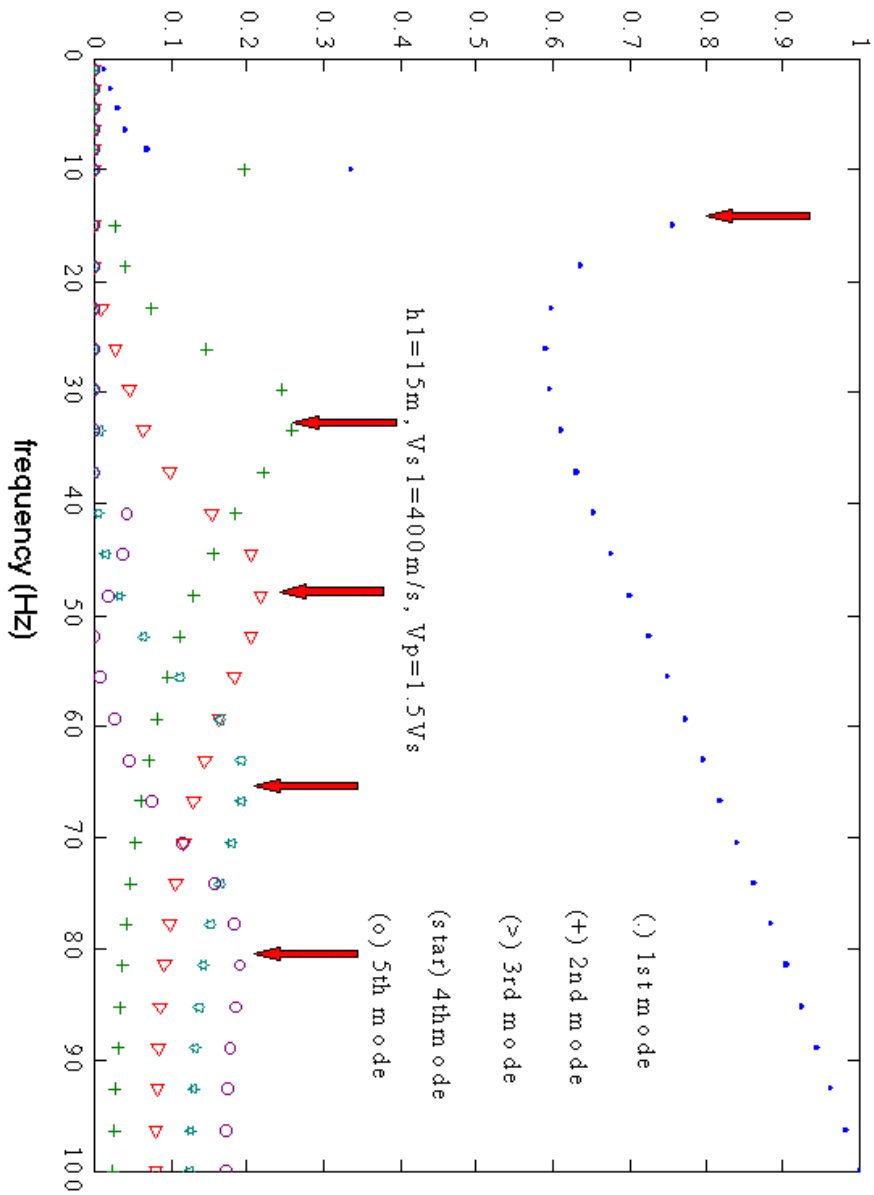

Figure 2.60: Normalized modal spectra of the displacements and frequencies of resonance for travelling Rayleigh waves in a layered system: a single layer over a half-space.

It must be observed that the phenomenon of wave propagation we deal with is represented in a three dimensional space in a bi-dimensional domain, so the system resonance has to be identified by a pair of independent variables, say the frequency and the wave number. When dealing with wave phenomena, between the temporal and the spatial scales a precise relationship exists:

$$c = \frac{\lambda}{T} = \lambda \cdot f = \frac{2\pi \cdot f}{k} \tag{2.48}$$

that links the wave number with the frequency. Hence from (2.46) the resonant wave numbers can be evaluated:

$$k_R(j) = \frac{2\pi \cdot f_R}{c} \cong \frac{2\pi \cdot (A + Bj) \cdot Vs_1}{h_1 \cdot c} \tag{2.49}$$

It is expected that, during the propagation of a disturbance, the frequency and the wave number be not independent, but strictly correlated by the dispersion relation of the system. In Chapter 5 the wave numbers of resonance as well as the frequencies will be shown for the real site Wolfriver.

2.8.1.5 Comparison between Rayleigh and Shear Waves

Eventually an interesting analogy can be established with the so called shear column model (Silvestri and Lanzo, 1999), in which vertically travelling shear waves are assumed in the same system, with a rigid half-space as it is schematically illustrated in fig.2.61:

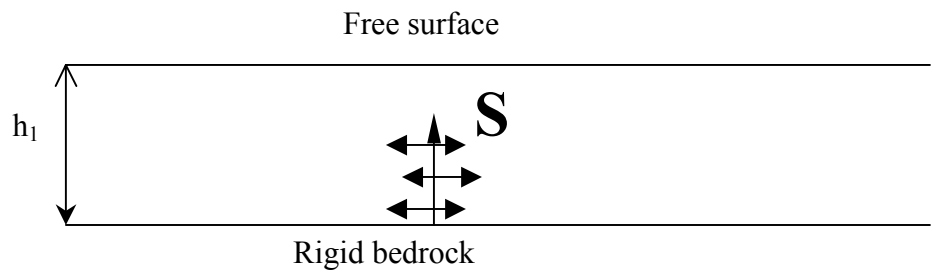

Figure 2.61: Shear column model.

In this case the frequencies of resonance of the system are well-known (see for example Kramer, 1996):

$$f_{shear}(j) = (-0.25 + 0.5j)\frac{Vs_1}{h_1} \tag{2.50}$$

It is evident the formal analogy between the two formulas (2.46) and (2.50), even if it should not be expected, because of their completely different phenomenon. The two cases are in fact concerned about the propagation of two distinct kinds of waves with different components of motion. It can be seen that, for a fixed j^{th} mode of propagation, the resonant frequency for Rayleigh waves is always greater than the resonant frequency for shear waves in the shear column model (see fig.2.62).

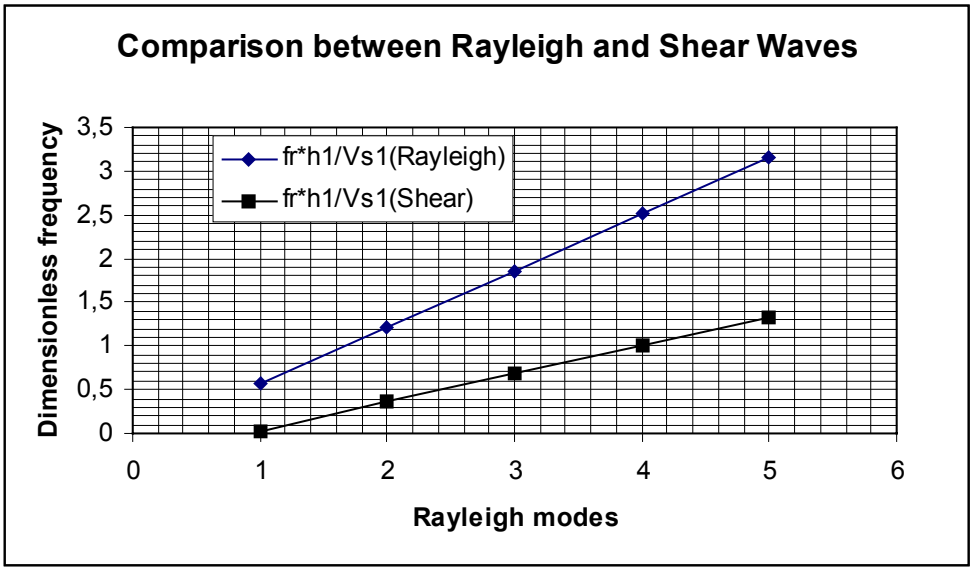

Figure 2.62: Frequencies of resonance for Rayleigh waves and shear column model for a single layer over a half-space.

Chapter 3

Inversion Procedure: Stiffness Profile

Introduction

In Chapter 2 we have defined a new theoretical approach for evaluating the Rayleigh Dispersion relation, that is consistent with the experimental procedure and allows for an insight about the relative importance of all Rayleigh modes in the f-k spectrum. It has been also verified the validity of the new method, by comparing it to other methods, such as standard SASW and Effective phase velocity method by Lai (Lai, 1998).
In this Chapter an *Inversion Algorithm* will be presented, to infer the stiffness profile of both normally and inversely dispersive systems, that accounts for all higher Rayleigh modes.

3.1 The optimization problem

The inversion procedure can be addressed as an optimization problem. The problem falls in the area of non linear curve fitting. The inversion is attempted, by matching the measured *apparent* curve with the theoretical *apparent* curve. The physical parameters, which describe the underlying system, are determined by the curve matching. The aim of the optimization procedure is to select the parameters in such a way, that both functions are matched. The result of the optimization coincides with the result of the general inversion problem.

3.1.1 Mathematical optimization model

The *apparent* measured curve V_{exp} , which describes the dispersion relation for the particular site, is plotted as a function of frequency. V_{exp} is an ordered vector of phase velocities, where the index number corresponds to a certain frequency. In the same manner the theoretical apparent curve V_{theo} is defined. The error for the curve fitting is defined as $e = V_{exp} - V_{theo}$. The *Objective Function* is defined as the sum of the squared errors. Hence the problem is converted into a least square error minimization.
The parameters are classified into two distinct categories: layer thicknesses h and layer stiffnesses, which are described by the shear wave velocities Vs. The physical parameters of the system are subjected to certain limits. The

decision variables of the optimization, the layer thicknesses h_i and the shear wave velocities V_i are subjected to the following constraints:

1) Each layer must be larger than a desired value, otherwise it has no influence on the measured data.
2) The sum of the thickness must be smaller than the maximum depth for which information can be gathered (λ/2).
3) Shear wave velocities must be larger than zero, negative numbers have no physical meaning.

The problem can be classified as a *non linear constrained least square minimization*.

$$\begin{aligned}
&\min \quad \sum_{f=1}^{N}\left(V\exp_f - Vtheo_f(h_i, vs_j)\right)^2 \\
&subjected \quad to \\
&h_i \geq h_{\min} \quad i = 1,2,...M \\
&\sum_{i=1}^{M} h_i \leq z_{\max} \\
&vs_j \geq 0 \quad j = 1,2,...(M+1)
\end{aligned} \tag{3.1}$$

N is the number of frequencies, M is the number of layers. For a problem with M layers M+1 shear wave velocities exist, M shear wave velocities for the M layers plus another shear wave velocity for the half-space.

3.1.2 Optimization approach

The algorithm chosen to solve the optimization problem is the *Penalty Method* as described in (Reklaitis et al, 1990). The problem is converted from constrained minimization problem in an unconstrained series of minimization problems. As penalty term for the constraints, the bracket operator is chosen. The mathematical model (3.1) is transformed to the following problem.

$$\begin{aligned}
P(h_i, vs_j, R) &= \sum_{f=1}^{N}\left(V\exp_f - Vtheo_f(h_i, vs_j)\right)^2 + \\
&+ R\cdot\left[\sum_{i=1}^{M}\left\{(\min(h_i - h_{\min}, 0))^2\right\} + \left(\min\left(z_{\max} - \sum_{i=1}^{M} h_i, 0\right)\right)^2 + \sum_{i=1}^{M+1}\left\{\left(\min\left(vs_j, 0\right)\right)^2\right\}\right]
\end{aligned}$$

(3.2)

where $\min(k,0) = \begin{cases} k & k \le 0 \\ 0 & k \ge 0 \end{cases}$ (3.3).

The R parameter is a penalty factor that combines the *distance* between the experimental and the theoretical responses with the constraints.
The first term of the *Objective Function* represents the *distance* between the experimental and the theoretical system responses. The terms inside the square bracket, which are multiplied by the factor R, represent the penalties associated to the constraints of the initial optimization problem.
The transformed constrained problem is a series of unconstrained non linear optimization problems, which converges to the correct solution for $R \to \infty$. For each iteration with a fixed R the minimization of P is an unconstrained non linear optimization problem. By varying the R parameter, a different importance is given to the *distance* respect to the constraints. Actually, different R parameters could be introduced for each constraint, to specify the several contributions to the *Objective Function*.
The penalty function $P(h_i, vs_j, R)$ is minimized by using a Quasi-Newton algorithm .The particular algorithm used is the Davidon–Fletcher-Powell (DFP) method (Reklaitis et al, 1990, Bras, 2000).

3.1.3 Optimization algorithm

The penalty method for constrained optimization does basically the following four steps:

1) Find x^{t+1} such that $P(x^{t+1}, R^t) \to \min$ with R^t fixed. This step is performed with the Quasi-Newton method (DFP).
2) If $|(x^{t+1} - x^t)| < \varepsilon \to$ terminate , else continue.
3) If x^{t+1} is feasible and not at the boundary terminate, else go (4)
4) $R^{t+1} = dR^t \cdot a$ $(a>1)$, $R^{t+1} = R^t + dR$, and go to (1)

In this case $x = (h_i, vs_j)$.

Step (3) is a monitor to see if the solution is an interior point, of the feasible space or a point which is infeasible or at the boundary of the feasible space. When the solution of the first iteration (x^1) is an interior point regardless of the value of R, it is not necessary to increase R and to solve the problem for the next $P(h_i, Vs_j, R)$ function again. The way the *penalty function* is built, a solution on the border, with a slack variable zero, is only possible if the unconstrained minimum for the original *Objective Function*
$\sum_{f=1}^{N} \left(V\exp_f - Vtheo_f(h_i, vs_j)\right)^2$ is infeasible.
If a minimum is an interior point, its location is independent of R, because the bracket operator ensures that the additive terms of the constraints for

such a point are all zero. If an infeasible solution or a boundary solution is found, the algorithm must continue to increase R .

The unconstrained optimization in step 1 is performed with the following algorithm:

1) Set iter = 0.
2) Calculate $\nabla P(x^{(k)}, R)$
3) If $\left\|\nabla P(x^{(k)}, R)\right\| \le \varepsilon_1$ then terminate, else continue
4) If iter > itermax then terminate, else continue
5) Calculate $s(x^{(k)}) = \nabla P(x^{(k)}, R)^T \cdot A^{(k)} \cdot \nabla P(x^{(k)}, R)$, where $A^{(k)}$ is calculated as

$$A^{(k)} = A^{(k-1)} + \frac{\Delta x^{(k-1)} \Delta x^{(k-1)T}}{\Delta x^{(k-1)T} \Delta g^{(k-1)}} - \frac{A^{(k-1)} \Delta A^{(k-1)} \Delta g^{(k-1)T} A^{(k-1)}}{\Delta g^{(k-1)T} A^{(k-1)} \Delta g^{(k-1)}} \text{ and}$$

$$g^{(k)} = \nabla P(x^{(k)}, R), \ \Delta g^{(k)} = g(x^{(k+1)}) - g(x^{(k)})$$

6) Find $\alpha^{(k)}$ such that $P\left(x^{(k)} + \alpha^{(k)} \cdot s\left(x^{(k)}\right), R\right)$ is minimized (line search).
7) $x^{(k+1)} = x^{(k)} + \alpha^{(k)} s(x^{(k)})$.
8) If ($P(x^{(k+1)},R) < P(x^{(k)},R)$) then continue, else terminate
9) If $\|\Delta x\| \le \varepsilon_2$ then terminate, else continue.
10) k = k+ 1. Got to step 2

The Optimization Algorithm has been implemented by the Author in Matlab, for solving the general problem of site characterization by means of Rayleigh waves.

3.1.4 Numerical gradient

The gradient of the *Objective Function* for this optimization is hard to evaluate symbolically. For this reason it was decided that the gradient is numerically computed. The gradient approximation is based on a forward difference approximation :

$$\left.\frac{\partial f}{\partial x_i}\right|_X = \frac{f(x_1, x_2, ..., x_i + \Delta x, ..) - f(x_1, x_2, ..., x_i, ..)}{\Delta x}$$

where in this case $x = (h_i, vs_j)$ $\quad f = P\left(h_i, vs_j, R\right)$

It must be said that the numerical calculation of the gradient is generally both time expensive and instable. The numerical accuracy depends on the increment Δx, chosen to evaluate the derivatives. In this work the step increment Δx varies within a certain range ($5 \cdot 10^{-3} \div 5$), according to the slope of the *Objective Function* at the current point, in which the *Objective Function* is evaluated. A smaller value of Δx corresponds to a higher absolute value of the components of the gradient.

3.1.5 Line-search function

The DFP algorithm needs a relative exact line-search, so that the Quasi-Newton method converges in a good manner. An exact line-search, which does not relay on gradient information, such as the *golden search method*, on the other hand needs a lot of iterations, which is computationally burdensome. The trade-off here is between achieving a very high convergence of the Quasi-Newton method at the cost of many iterations for the line search or avoiding too many line-search iterations at the cost of a deteriorated overall convergence of the Quasi-Newton method. At first in this project the use of a golden search was implemented, but the computational burden was too high for two reasons. First at the beginning of the iterations, the norm of the direction vector is very large, which indicates a very long direction vector and therefore the golden search had to scan a very long line, to find the minimum. Secondly it was noticed, that the minimum point is never very far away from the starting point of the line-search . From this two facts the following strategy was implemented.
At first we defined the maximum allowable step for each physical parameter in one iteration. This maximum step size can be set by the user, say for the shear wave velocities Vs_{max}=50 m/s and for the thicknesses h_{max}=2.5 m . The line-search $\alpha^{(k)}\, s(x^{(k)})$ is now constricted to α's so that the maximum element for each set of physical parameters never exceeds Vs_{max} or h_{max} respectively.
The second part of the strategy is to find a smaller interval for the golden search method. The interval is now divided into a certain number of subintervals p+1. At the beginning of each subinterval the objective function is evaluated and compared to the value of the objective function at the starting point of the line-search. (Fig. 3.1)

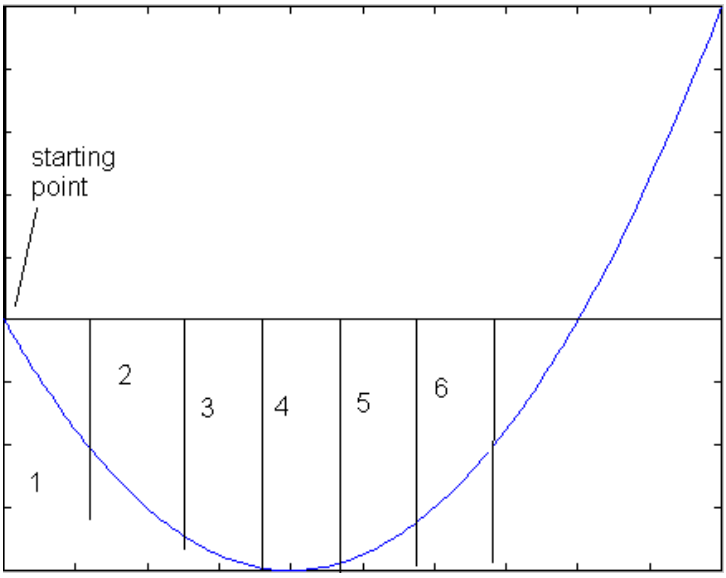

Figure 3.1: Line-search procedure: determination of the subinterval containing the minimum.

As long as the value of the objective function decreases, the starting point of the next subinterval is investigated, as seen in fig. 3.1 from interval 1 to 4. When the objective function value increases, compared to the value of the previous point (form interval 4 to 5), the interval number is stored (m=5). As search interval for the golden section method, the start point of the interval *m* and the start point of the interval *m-2* are used. In the example the interval for the search is the subinterval composed of the sub intervals 3 and 4. In this manner only a fraction of the original global interval (from 1 to *p* in fig.3.1) is searched by the golden search. The assumption for this method is obviously that the function is unimodal. When the evaluation of the first starting point has a higher objective function value than the starting point of the line-search, the first subinterval itself is divided into (p=1) subintervals and the search routine, to establish the search interval for the golden search, is started again on this space. This refinement of the interval is done at maximum 6 times, but the number of times can be modified by the user (see fig. 3.2).

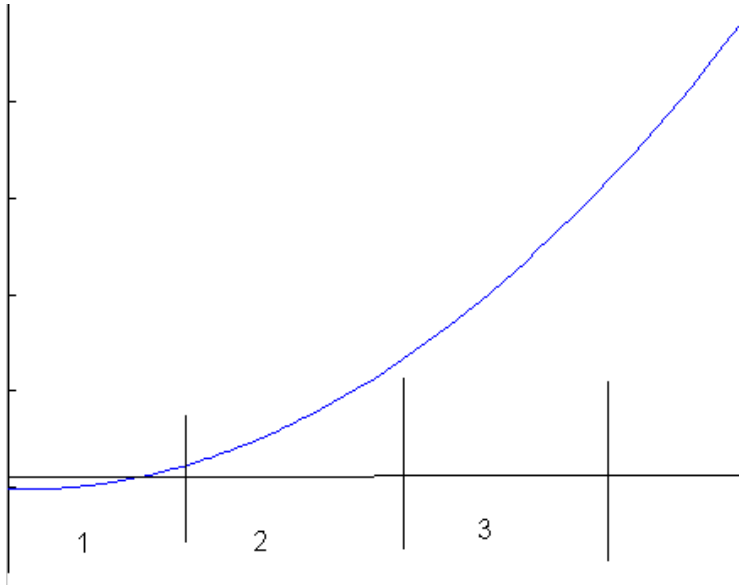

Figure 3.2: Line-search procedure: the current point represents a local minimum.

When the refinement procedure does not find an interval, the golden search is not initialized. The line-search terminates, without delivering a new minimum point in step 6. In this case the Quasi-Newton program stops to do any further iteration and uses the last point as the best result. This happens only when the direction vector and the gradient vector get really small and the algorithm is close to a local minimum.
The algorithm which is described above is outlined below:

1) Calculate $\alpha_1 = Vs_{max} / \max(S_{Vs})$. $\alpha_2 = h_{max} / \max(S_h)$ $\alpha = \min(\alpha_1, \alpha_2)$, where S_{vs} are the elements of the direction vector associated with the shear wave velocities and S_h are the elements associated with the thicknesses. Set ref=1.
2) If $\alpha < 2$ then $\alpha=2$
3)If ref <= 8
Yes : $\alpha_p = \alpha / p$, where p represents the number of subintervals and set n=1.
No : terminate
4) If (n<=p)
Yes : evaluate $P(x^{(0)} + n\, \alpha_p\, s(x^{(0)}))$, where $x^{(0)}$ is the starting point of the line search.
No go to step 6
5) If $P(x^{(0)} + (n-1)\, \alpha_p\, s(x^{(0)})) > P(x^{(0)} + n\, \alpha_p\, s(x^{(0)}))$

Yes : set n=n+1 and got to step 4
No : go to step 6
6) If n=1
Yes : set $\alpha_p=\alpha$, ref=ref+1 and go to step 3
No: go to step 7.
7) Start the golden search to find the local minima.

The golden search also called the *golden section search* is outlined in (Reklaitis et al., 1990). The golden search is used at maximum for 15 iterations to find the minimum. If the golden search does not converge in 15 iterations, the average of the two points, which brackets the minimum is used as an approximation.
This line search has proven to be useful in this optimization project. The general descend property of the Quasi-Newton method holds always true and the line-search is not too burdensome.

3.1.6 Final word on the optimization code

The optimization algorithm presented here is a straightforward implementation of the DFP method as main solver for a penalty approach. The biggest weakness of this program is the line-search function. The line search function was in most cases responsible for the termination of the optimization program. Any further improvements of this code should focus on the line-search function.

3.2 Simulation analysis: Normally dispersive system

Since the computational time to run one forward problem is so long, first an artificial case is studied.

Layer	h(m)	Vp (m/s)	Vs (m/s)	Mass density ρ (Kg/m^3)
1	2	200	100	1800
2	5	400	200	1800
3	7	700	350	1800
Half-space	∞	1200	600	1800

Table 3.1: Characteristics of the artificial case.

In the sequel the mass density ρ and the compression wave velocity V_p will not be repeated, since they will be hold as constant parameters in the sensitivity analysis.

For the considered system (table 3.1) the apparent dispersion curve (fig.3.3) is computed by means of the new method described in Chapter 2. The task now is to solve the inversion problem for a disturbed set of parameters and see if the algorithm converges to the right set of values. Another reason is to gain insight and experience with the *inversion problem*. For example, before doing this step, it was not known if the problem has only one unique minimum or several minima. For all these simulations the maximum assumed depth is 20 m. The system is made of only three layers and therefore it is described by seven variables, i.e. three thicknesses and four shear wave velocities. The test case is kept with such a small number of variables on purpose, so that the overall computational time is not excessively large.

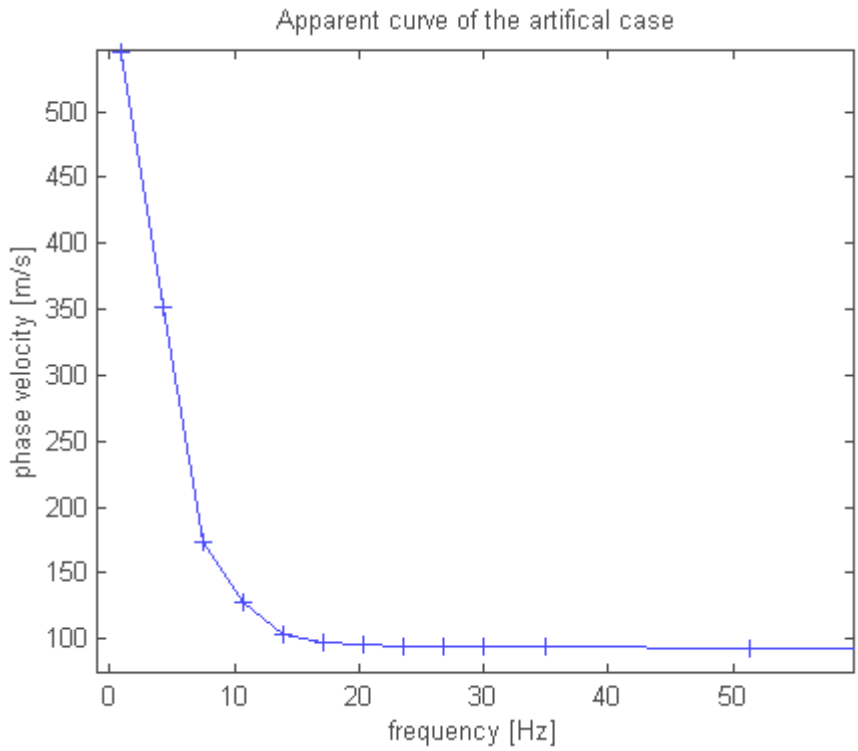

Figure 3.3: Theoretically simulated apparent dispersion curve for the system described in table 3.1.

3.2.1 Solving simultaneously for thicknesses and shear wave velocities.

In the best of all cases, the algorithm could find the correct set of thicknesses and shear wave velocities.

Layer number	Thickness h (m)	Shear wave velocity Vs (m/s)
1	2.3	90
2	4.6	240
3	6.8	330
Half space	-	650

Table 3.2: Perturbed system: both thicknesses and shear wave velocities vary.

The algorithm was initialized with a disturbed set of value. The initial values for this case are given in table 3.2. The initial values are no more than 20% different from the correct values. The problem starts in the neighborhood of the correct solution. The program terminates after 25 iterations, because the line-search function fails to find in the 25th iteration a better minimum. The best set of values in this case are given in table 3.3.

Layer number	**Thickness (h) [m]**	**Shear wave velocity (vs)[m/s]**
1	4.2	100
2	14.7	237
3	2.5	330
Half space	-	611

Table 3.3: Final configuration inverting for both thicknesses and shear wave velocities.

The value of the objective function for each iteration is shown in figure 3.4 . The objective function value decreases from 9.4 10^4 to 48.58. The optimization gives a very good match between the dispersion curves of the inversion process and that one of the forward simulation.

The results are shown in figure 3.5. In figure 3.5 the green circles represent the data of the optimization result, the crosses represent the dispersion curve of the artificial case and the stars represent the dispersion curve of the initial perturbed parameter set. As the figure shows, both curves are very well matched, despite the thicknesses of the profile, at the end of the optimization differ a lot from the true profile. The shear wave velocities of the first layer and the half-space are close to the true values. The shear wave velocities of the second and third layers are barely different from the initial starting configuration. The reason for this behavior is that the shear wave velocity of the first layer is mostly responsible for the asymptotic behavior of the *apparent* dispersion curve, i.e. the values of the phase velocity beyond 35 Hz.

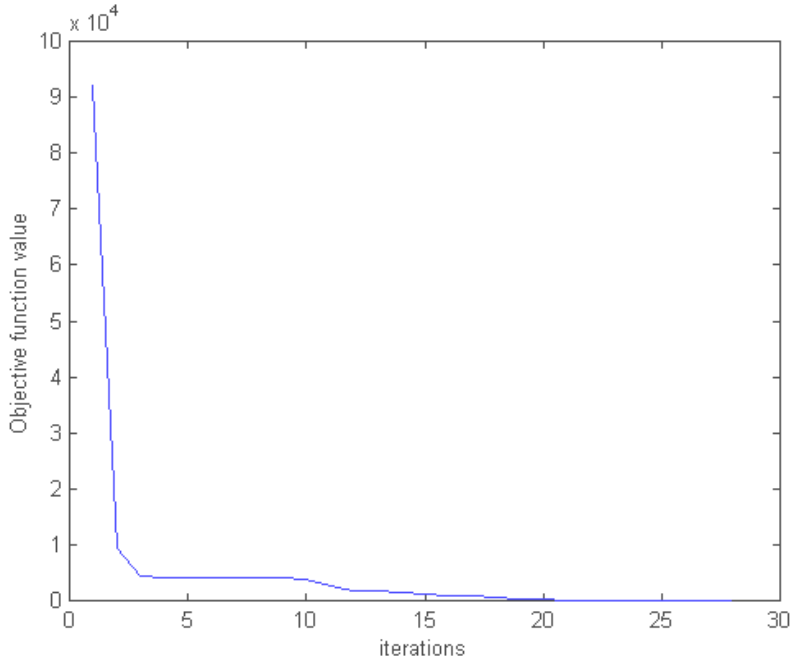

Figures 3.4, 3.5: Objective function for the inversion, starting from the configuration given in table 3.2 and Dispersion curve: initial configuration (blue stars), final configuration (green circles), true profile (plus and continuous line).

The half-space influences mostly the points at the low frequencies, because low frequency waves penetrate into deeper layers. The objective function for the last iteration was not zero, which indicates that the profile is not the true profile, but one which approximates the apparent curve very well. In terms of the optimization problem, this solution corresponds to a local minimum. This fact can be concluded from these data, because the true profile with an objective function value of zero is known. The program converges to a local minimum, with totally different values for the thicknesses and somewhat different values for the shear wave velocities.
Additional factors, which point to the thesis of local minima, are that the objective function value for the last four iterations hardly changes. The norm of the gradient vector is 10^5 at the first iteration and at the last iteration is 77.7. The algorithm terminates, because the line-search function does not find any lower point in the vicinity of the last iteration point. In order to investigate further the behavior of this optimization problem, the program is used with a another starting point.

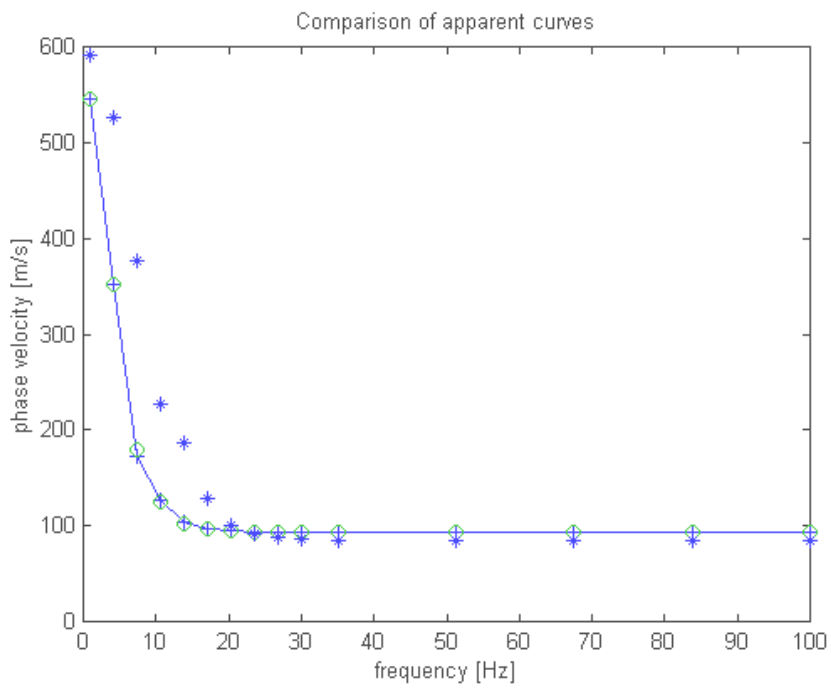

Table 3.4 gives the data for the new starting configuration.

Layer number	Thickness h (m)	Shear wave velocity Vs (m/s)
1	1.2	100
2	2.0	300
3	2.0	400
Half space	-	600

Table 3.4: New perturbed system with both thicknesses and shear wave velocities varied.

The starting configuration has the correct shear wave velocities for the first layer and the half-space, but very distant parameters for all the thicknesses and the shear wave velocities for layers two and three. The reason for this starting point is to see how the thicknesses and the middle layer shear wave velocities change during the inversion process. From the previous optimization and other tests it was observed that the program always converges to the correct shear wave velocities of the first layer and the half-space. Therefore these two parameters are set to their correct values in order

to see the changes in all other parameters. The result of this optimization after 12 iterations is shown in table 3.5.

Layer number	Thickness h (m)	Shear wave velocity Vs (m/s)
1	2.9	100
2	9.8	295
3	2.3	399
Half space	-	600

Table 3.5: Final profile inverted, starting from the initial profile in table 3.4.

The objective function value decreases from $7 \cdot 10^5$ to about 450. The algorithm apparently runs into another local minimum. The two examples presented here and further numerical experiments convinced us, that the problem with both unknown layer thicknesses and unknown shear wave velocities has multiple local minima and it is very hard to find the true global minimum. In this case the global minimum is known a priori and therefore the results can be judged accordingly. In real cases the best match is not known and any solution has to be judged very carefully. Another disturbing fact is that the solutions found in the two presented optimization, are quite far from the true solution, especially for the layer thicknesses information. Only the last and the first shear wave velocities of the profile are correctly found by the inversion.

3.2.2 Sensitivity analysis

From the previous optimizations it was concluded that the incorrect shear wave velocity profile moves the local minimum very far away from its true position. In order to investigate this aspect, the shear wave velocity profile was held constant with small disturbed parameters and the thicknesses of the third layer was held constant at the correct value. The thicknesses of layer 1 and 2 were varied from 1 to 3 m and from 4 to 6 m respectively. The situation is shown in table 3.6.

Layer number	Thickness h (m)	Shear wave velocity Vs (m/s)
1	X	100
2	Y	220
3	7	330
Half space	-	600

Table 3.6: Influence of a slight variation of the shear wave velocity profile on the position of the global minimum.

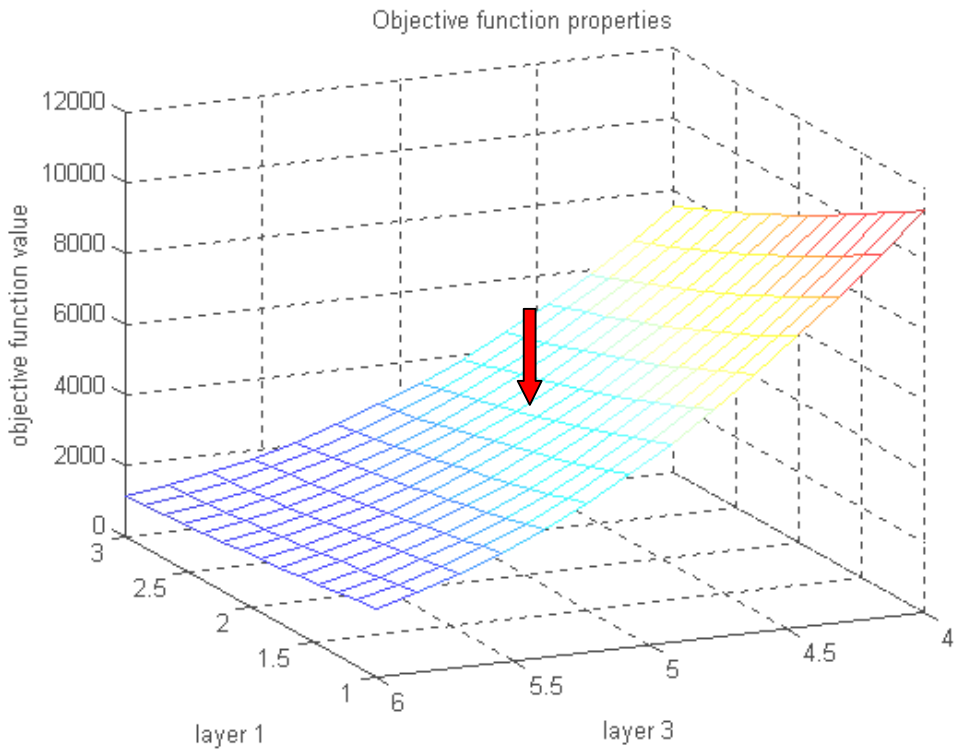

Figure 3.6: Objective function when the shear wave velocity profile is slightly changed from the true configuration.

The objective function is plotted as a 2-D function of X and Y. The plot is shown in figure 3.6. The objective function does not have a local minimum in the vicinity of the true layer profile at 2 and 5m. The plot shows that the objective function surface has probably a minimum for large values of the thickness of layer 2, as demonstrated in the two profiles found in the previous section by the algorithm. From this it can be concluded, that a

small perturbation in the shear wave velocities generates an objective function surface with a minimum very far away from the true value.
If an analogous experiment is done with varied layer thicknesses and fixed shear wave velocities, the result is that the minimum is not at its true position but relatively close to it. Precisely the layer thicknesses are held constant at values slightly different from their true values.

Layer number	**Thickness h (m)**	**Shear wave velocity Vs (m/s)**
1	2.2	100
2	4.8	X
3	7.3	350
Half space	-	Y

Table 3.7: Influence of slight perturbation in the thicknesses of the system.

The shear wave velocity of the half-space ranges from 570 m/s to 630 m/s and the shear wave velocity of the second layer from 170 m/s to 230 m/s. The situation is described in table 3.7. In figure 3.7 the objective function is plotted as a function of X and Y. The figure shows that the minimum of the objective function value is approximately at X=200 m/s and Y=600 m/s, which are the true values of this profile. A plot with finer increments would probably show that the minimum is at slightly different values for X and Y. The objective function value at the minimum is about 125.8. The position of the minimum is on the same position as in the case when the true layer profile is used. Compared to the previous investigation, the problem is less sensitive to changes in thicknesses than in shear wave velocities.

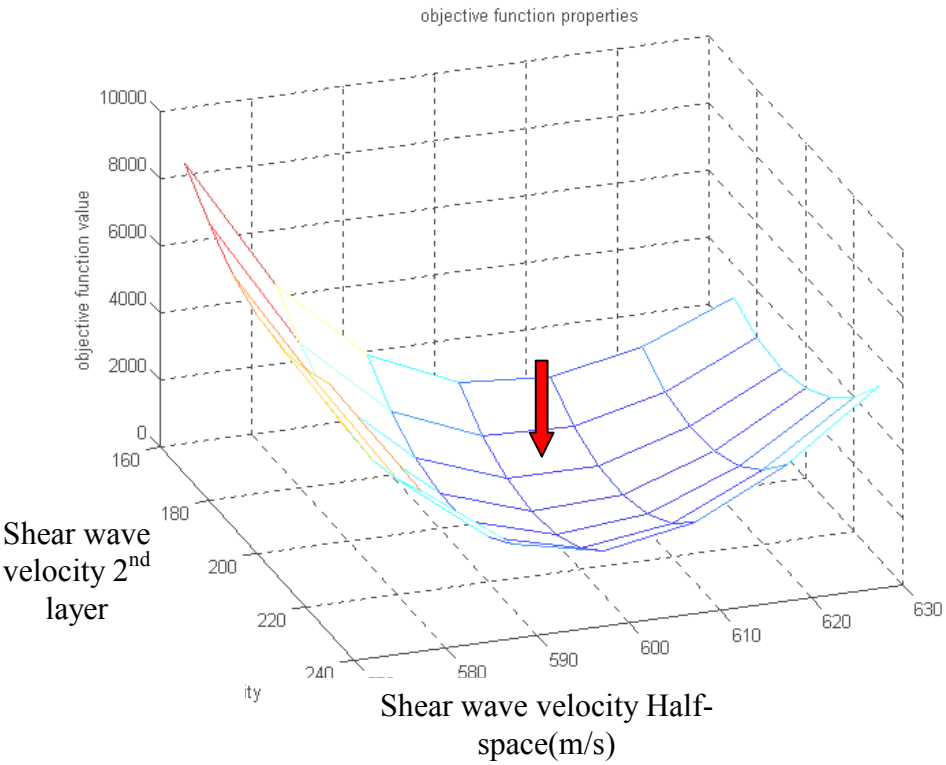

Figure 3.7: Objective function when the thicknesses are slightly perturbed from the true values.

In contrast to the other case a small perturbation in the thicknesses does not generate an objective function surface with a minimum at a very different position, but a minimum very close to the true correct one. The objective function value is not as high for the true minimum position as in figure 3.7, where at the correct position the objective function is around 3000.

Since it has been shown that, for small perturbations of the thicknesses h_i, the position of the best shear wave velocities hardly changes, the question arises what happens if the layer thicknesses profile is seriously different from the actual profile.

To answer this question, the same examination as above is repeated, but this time with a significantly disturbed layer thicknesses profile.

Layer number	Thickness h (m)	Shear wave velocity Vs (m/s)
1	1.2	100
2	6.8	X
3	9.3	350
Half space	-	Y

Table 3.8: New starting configuration with strong perturbations for the thicknesses.

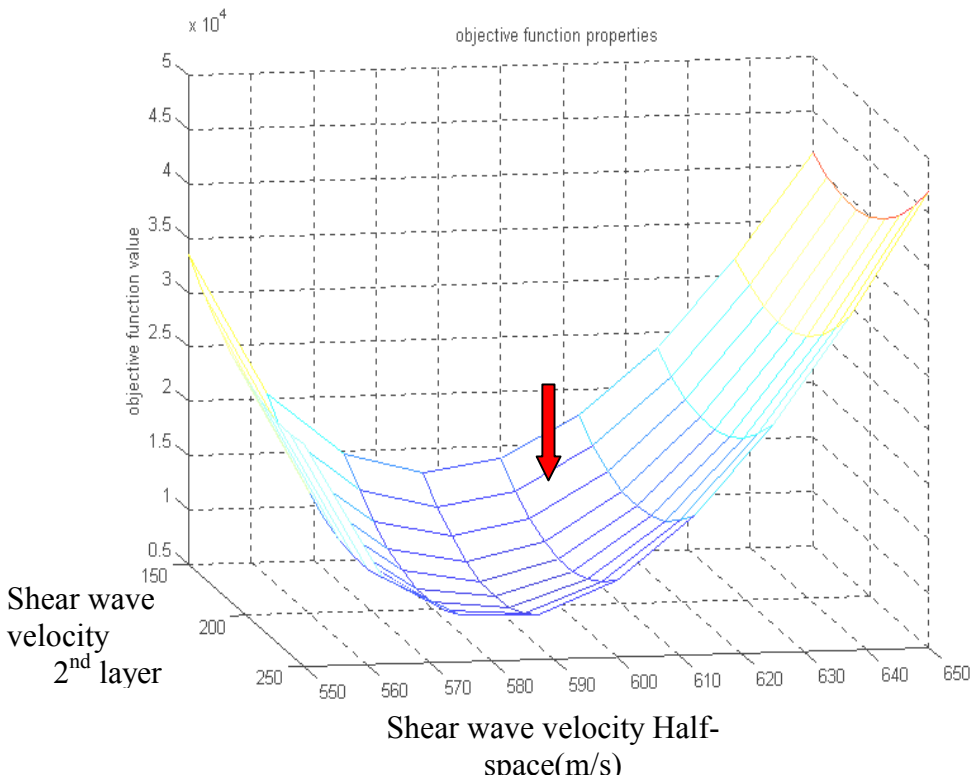

Figure 3.8: Objective function with a strong perturbation of the true values of the thicknesses.
75

The difference between the actual layer thicknesses profile and the true one is between 36% and 55%. The objective function is again plotted as a function of X and Y, as shown in figure 3.8. The minimum is at X=187.5 m/s and Y=612.5 m/s, with an objective function value of $7.28 \cdot 10^3$. The position of the minimum in this case is only 6.5 % and 2.1 % away from the true profile. This is a noteworthy property, because this shows that the

system is very insensitive to the wrong layer thicknesses information. The inversion still converges to a very close shear wave velocity profile.

3.2.3 Solving for layer thicknesses with fixed shear wave velocities

The next numerical evaluation is done with fixed shear wave velocities at their true values.

Layer number	Thickness h (m)	Shear wave velocity Vs (m/s)
1	2.1	100
2	5.3	200
3	6.8	350
Half space	-	600

Table 3.9: Initial point: fixed shear wave velocities and perturbed thicknesses.

The optimization uses only the layer thicknesses as decision variables. As initial guess a perturbed profile as shown in table 3.9 is used.

The program has solved the inversion problem correctly within 17 iterations. The last profile of layer thicknesses is the correct true profile as shown in table 3.10:

Layer number	Thickness h (m)	Shear wave velocity Vs (m/s)
1	2.0	100
2	5.0	220
3	7.0	330
Half space	-	600

Table 3.10: Inverted profile with correct fixed shear wave velocities and varying thicknesses.

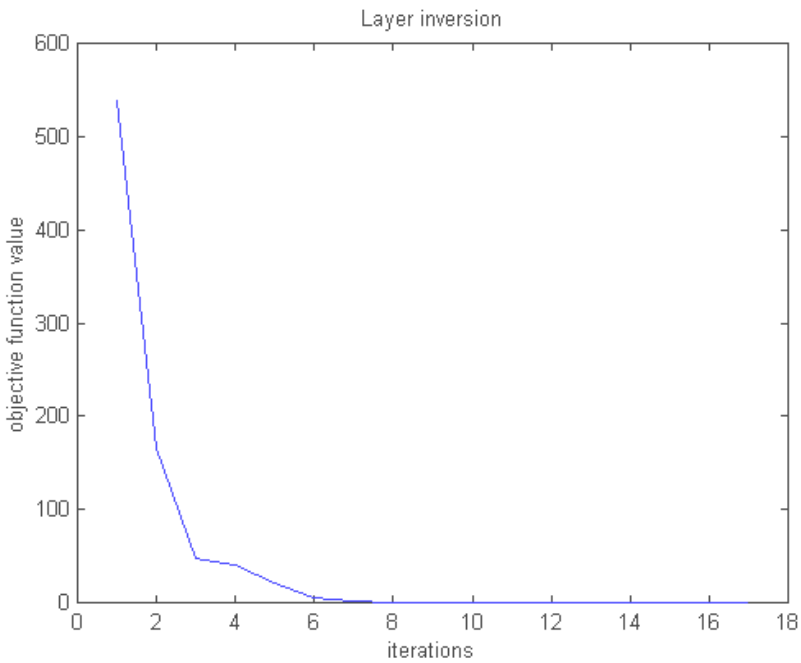

Figure 3.9: Objective function for the inversion with shear wave velocities fixed at their correct values and varying thicknesses.

In figure 3.9 the objective function as a function of the iteration number is shown. The objective function has decreased from 537 to $2 \cdot 10^{-5}$. The program stops after 17 iterations, because the gradient vector is smaller than the defined value of ε_1.

The conclusion from this example and other numerical evaluations is that the objective function in this case has only one minimum and this is at the position of the true layer thicknesses profile.

3.2.4 Solving for shear wave velocities with fixed layer thicknesses

The last investigation for the artificial case is to solve for the shear wave velocities with fixed layer thicknesses. The layer thicknesses are fixed at their true values and the shear wave velocities are disturbed from their true values. The first optimization in this case has the following starting point:

Layer number	Thickness h (m)	Shear wave velocity Vs (m/s)
1	2	140
2	5	210
3	7	330
Half space	-	640

Table 3.11: Inversion with correct fixed thicknesses and shear wave velocities as variables.

The starting point is not too far away from the true shear wave velocity profile. After 21 iterations the program has converged to the correct shear wave velocity profile. The objective function has decreased from $4 \cdot 10^4$ to 0.21. Table 3.12 shows the final result of the optimization for this case. The rate of convergence, measured by the objective function, is very large at the beginning and relatively slow at the end, as figure 3.10 shows.

Layer number	Thickness h (m)	Shear wave velocity Vs (m/s)
1	2	100.0
2	5	199.8
3	7	350.3
Half space	-	600.3

Table 3.12: Inverted profile corresponding to the starting point in table 3.11.

This result shows that for the correct layer thicknesses profile, the shear wave velocity profile converges to its true profile. The question here is if this is a global property (behavior) or a local one, since the initial guess is not very far away from the true solution.

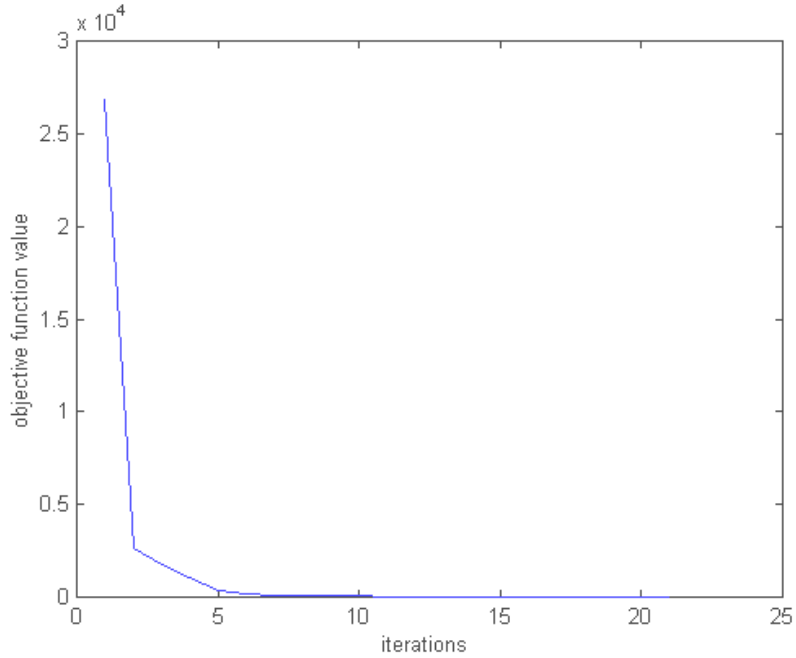

Figure 3.10: Objective function when inverting for only the shear wave velocities.

In order to asses if the above described behavior is valid only locally around the true set of parameters or also true for a more distant starting point, the same case is solved again with another starting point.

Layer number	Thickness h (m)	Shear wave velocity Vs (m/s)
1	2	50
2	5	180
3	7	400
Half space	-	750

Table 3.13: Inversion with strongly perturbed shear wave velocities and fixed thicknesses at their true values.

This starting configuration is quite different from the true one. For the last shear wave velocity the difference is 150 m/s. The objective function value for this starting point is about $4.3 \cdot 10^5$. It has been observed that the Quasi-Newton method for objective function values larger than 10^6 fails to converge. The problem of convergence if the optimum is relative far away is also mentioned in the literature. For this reason, a starting point with an

objective function value lower than 10^6 has been selected. The program for this starting point converges to the correct solution within 20 iterations. Table 3.14 shows the final shear wave velocity profile for this run.

Layer number	Thickness h (m)	Shear wave velocity Vs (m/s)
1	2	99.4
2	5	201.8
3	7	351.0
Half space	-	597.4

Table 3.14: Final profile for the starting profile in table 3.12.

The error of the last iterations is smaller than 0.5 %. The objective function value for iteration 20 is 17.67. The objective function value has decreased within the first 7 iteration down to about 140. Figure 3.11 shows the dispersion curve of the forward simulation as well as the dispersion curve of the profile of the starting point and the dispersion curve after 7 iterations.

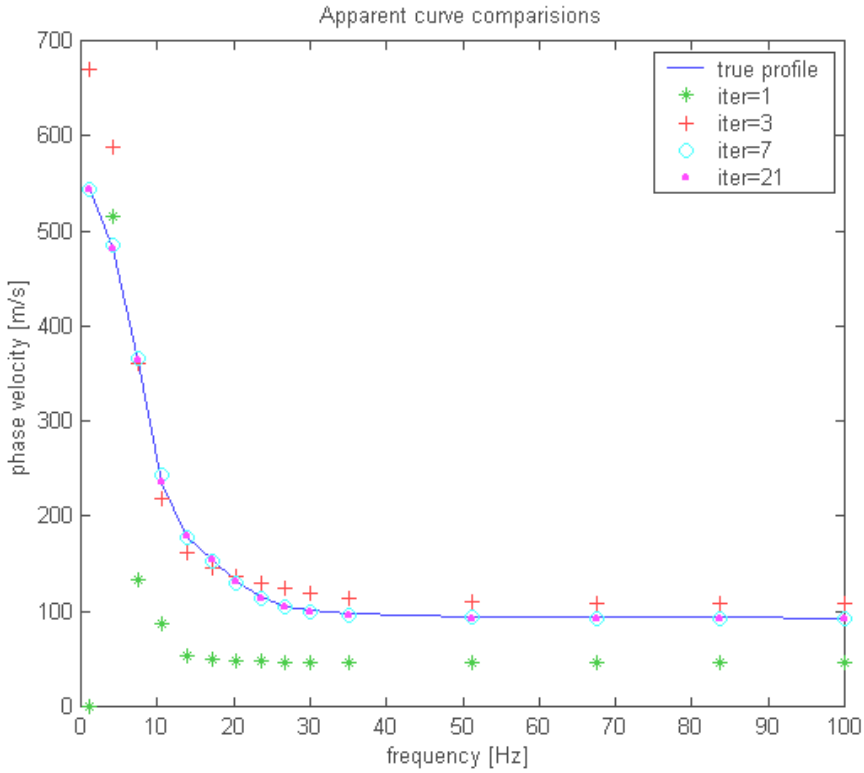

Figure 3.11: dispersion curves: true profile, initial profile (green stars) and final profile (dots).

As the figure above shows, the dispersion curve of the starting point (*) is very far apart from the true dispersion curve (line). After 3 iterations the dispersion curves have become relatively close together (+). At 7 iterations the difference between the dispersion curves can hardly be distinguished. The improvement from iteration 7th to the 21st iteration is hardly recognizable and can only be judged by the value of the objective function.

3.2.5 Conclusions from simulation

The inversion with both perturbed sets of parameters, layer thicknesses and shear wave velocities, has never given the correct true profile. Both described examples and further numerical experiments show strong evidence, that the problem has multiple local minima. Another problem in this situation is that the shear wave velocities of the middle layers have very

little influence on the objective function. The shear wave velocities of the first layer and the half space influence the objective function to a far greater extend than any other parameter in the system. The half space shear wave velocity determines the highest phase velocity of the dispersion curve and the shear wave velocity of the first layer determines the asymptotic behavior of the dispersion curve. These two facts combined and fact that the system is so sensitive to the wrong shear wave velocities, let the program run into local minima very different from the true solution. The later two investigations clearly point to a strategy, to achieve a good inversion result. When either shear wave velocities or layer thicknesses are held constant at their true values, the other set of parameters has converged to its correct profile.

The strategy for a proper inversion process is to fix the thicknesses of the layers and solve for the best possible guess of the shear wave velocities. This approach has two advantages.

First an incorrect guess for the thicknesses information does not cause the program to converge to a complete wrong shear wave velocity profile, but to a profile, which is close to the "true" or best one.

In addition sometimes a guess from other geotechnical site characterization techniques exists and this can be used for a layer profile guess. Additionally from a geotechnical point of view, it is more interesting to invert for the shear wave velocities (layer stiffnesses) rather than the layer thicknesses. This is the same order of magnitude as in the sensitivity plot (figure 3.5). Another fact of the optimization is that all the solutions have converged to an interior point of the domain. In all casees, solving for both thicknesses and shear wave velocities or for one of these, no optimization ever has came close to the boundary of the space. Therefore the penalty method as such is not really used. There is no need for an increase of R, as well as the penalty term does not influence the objective function value. The optimization is the same as for an unconstrained problem. In real cases reported in Chapter 5, with measured data, the same fact has been observed. Despite setting up of the problem as a constrained optimization, the actual problem has turned out to be equivalent to an unconstrained optimization. This is actually good news, since each run of the optimization code takes between 6 and 9 hours

to compute between 15 to 20 iterations. For this reason the problem is less computationally demanding as initially assumed.

3.3 Simulation analysis: Inversely dispersive system

The following example will be considered, in order to show, on one hand, the efficiency of the inversion algorithm for inversely dispersive systems and, on the other hand, to evidence the existence of local minima of the objective function. The characteristics of the system are illustrated in the table 3.15 below:

Layer	h(m)	Vp (m/s)	Vs (m/s)	Mass density ρ (Kg/m^3)
1	5	900	600	1800
2	5	600	400	1800
Half-space	∞	1200	800	1800

Table 3.15: Characteristics of the inversely dispersive system.

The system in table 3.15 can be representative of a profile with either a stiff surface layer or a soft layer trapped between two stiffer ones. As a consequence of the previous sensitivity analysis, the inversion algorithm has been run, inverting for only the shear wave velocities at the correct fixed values of the thicknesses. The starting initial configuration is definitely distant from the true profile. The results are excellent after 6 iterations, with a final profile that is very close to the true profile, as shown in the table 3.16 and fig.3.12.

Starting profile Vs (m/s)	2nd iteration	3rd	4th	5th	Final profile
700	700	652	615	613	612
500	472	434	401	399	399
800	800	798	779	778	778

Table 3.16: Results of the inversion process at all the iterations.

The relative error between the final profile and the true profile is less than 3 % and the match between the final dispersion curve and the true dispersion curve is very good (see fig.3.13). The objective function lowers from a value of $1.02 \cdot 10^5$ to 1200. This example allows us to be aware about the existence of local minima of the objective function. In fact, by plotting the contour plot of the objective function, varying two of the three shear velocities and fixing the other shear wave velocity, it can be seen that other local minima may exist in addition to the global minimum.

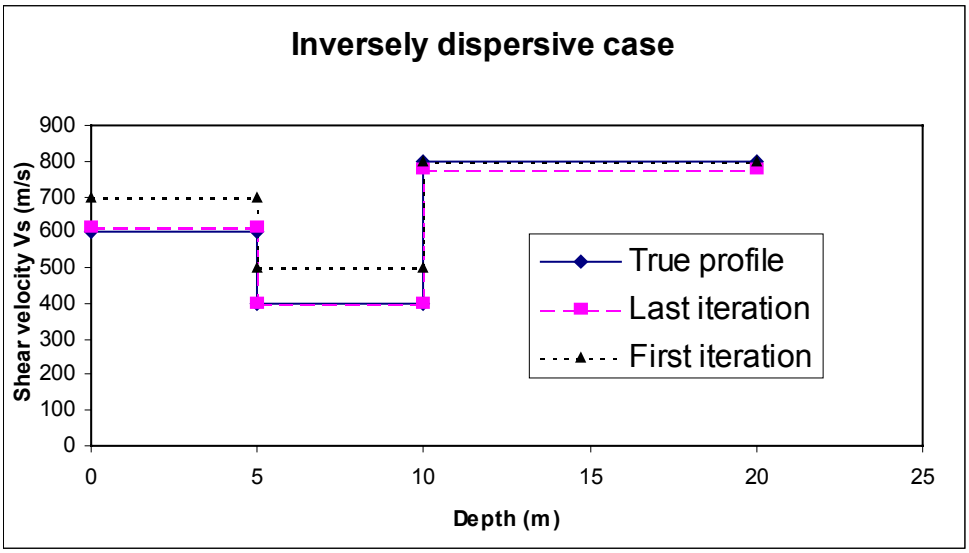

Figure 3.12: Results of the inversion process: initial profile (dash triangles), final profile (dashed squares), true profile (line).

It could happen that a local minimum exists near the global one (see fig.3.14), with no significant change by an engineering point of view. But other local minima generally exist that are quite distant from the global minimum and would lead to erroneous final results (figg.3.14 and 3.15). From this example it can be inferred: first that, if a local search technique is used, then the final profile depends on the starting configuration and secondly that the global minimum is likely to be reached, only combining a global search technique with a local one, if a good starting profile is not available a priori.
Anyway the validity of the optimization algorithm and of the whole inversion method have been checked even in inversely dispersive systems, and they have been successfully applied to real sites as shown in Chapter 5.

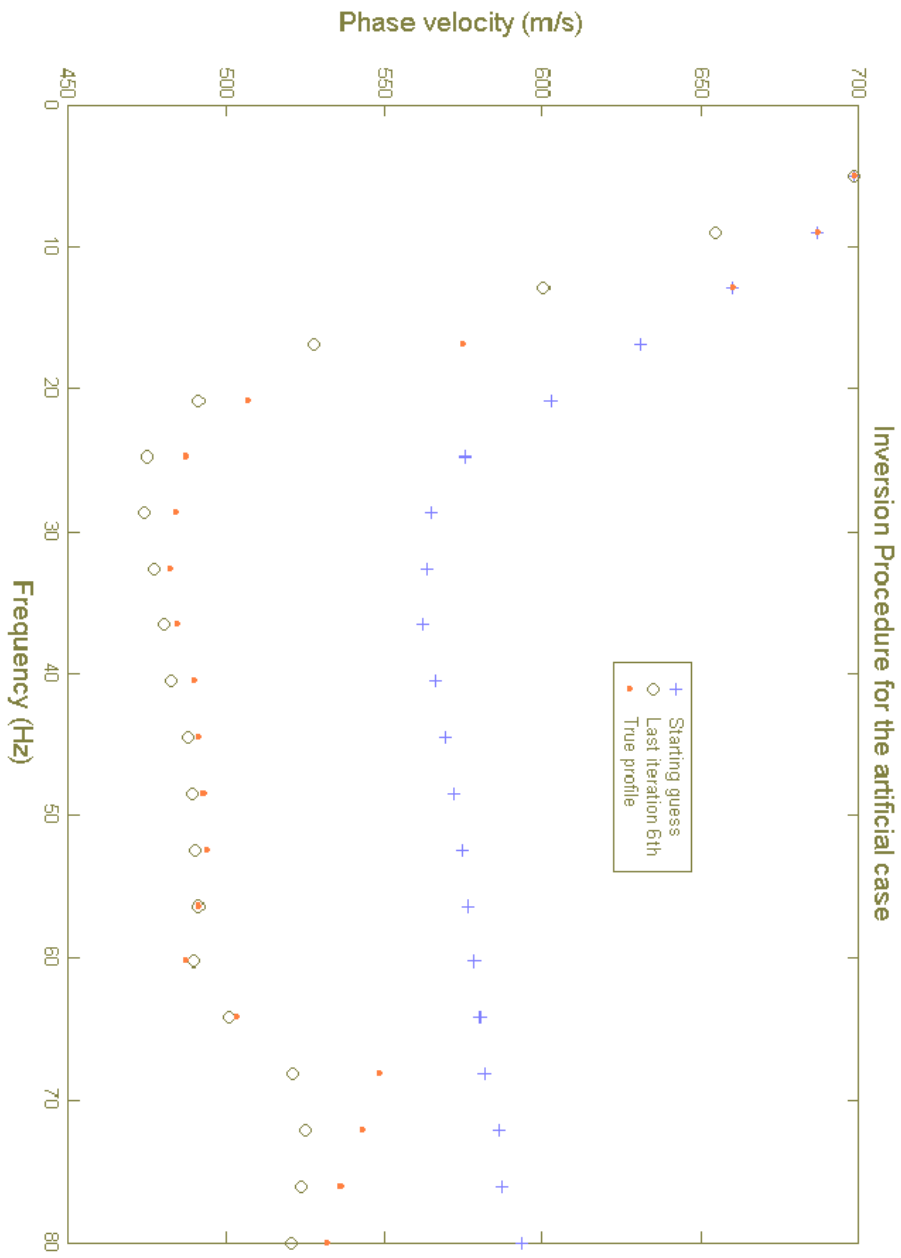

Figure 3.13: Dispersion curves: true profile(red dots), initial profile(blue plus), final profile(green circles).

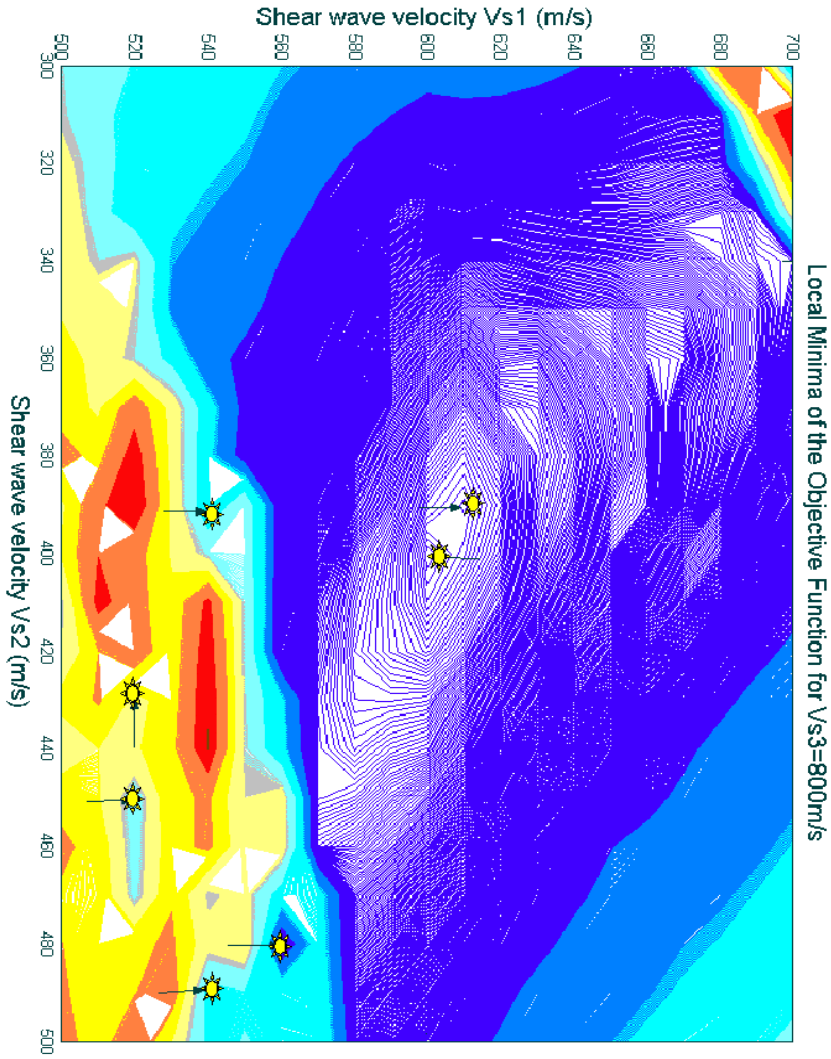

Figure 3.14: Contour plot of the objective function: several local minima exist.

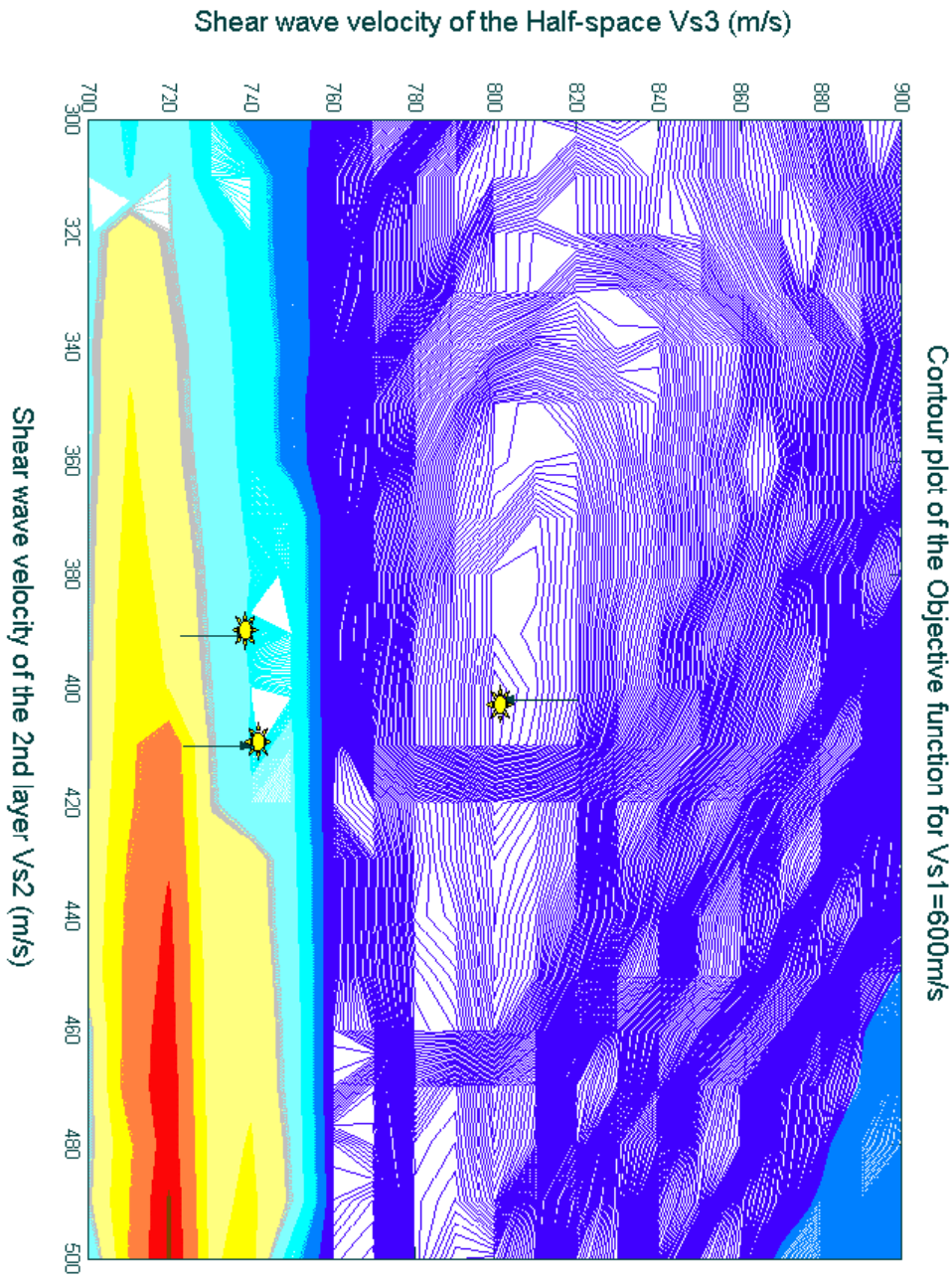

Figure 3.15: Contour plot of the objective function: several local minima exist.

Chapter 4

Inversion Problem: Damping Ratio profile

Introduction

In this Chapter the theory of visco-elasticity will provide us with a powerful model for taking into account the dissipative properties of the soil under investigation. Precisely a Coupled and an Uncoupled procedures can be followed for inverting the dispersion and attenuation relations of the system in order to evaluate the damping ratio profile with depth. A hybrid approach is also proposed, which on one hand relys on a coupled evaluation of the experimental dispersion and attenuation relations and on the other hand is based on an uncoupled simulation of the theoretical dispersion and attenuation relations performed for the inversion process.

4.1 Correspondence Principle of Visco-elasticity

Because of the way the Rayleigh dispersion relation (1.42) in Chapter 1 has been evaluated, it is a complex function with real independent variables, since we deal with real positive frequencies and wave numbers and so are all the mechanical properties. In a more general framework of visco-elastic behaviour of the soil, complex values of the body velocities are used and complex wave numbers are expected as roots of (1.42), in order to justify dissipative viscoelastic phenomena (Lai, 1998, Christensen, 1971). In fact a complex wave number:

$$k^* = k_{\mathrm{Re}} + ik_{\mathrm{Im}} \tag{4.1}$$

gives rise to a wave that propagates with a phase velocity:

$$c = \frac{\omega}{k_{\mathrm{Re}}} \tag{4.2}$$

and decays exponentially along the direction of propagation x with the spatial attenuation coefficient:

$$\alpha = k_{\mathrm{Im}} \tag{4.3}$$

given by the imaginary part of the complex wave number, so that a plane wave can be written as:

$$u(x,t) = A\hat{d}e^{-\alpha x\cdot\hat{p}}e^{ik\mathrm{Re}(ct-x\cdot\hat{p})} \tag{4.4}$$

where $\hat{d}$ and $\hat{p}$ are the unit vectors that indicate the directions of particle motion and propagation of the phase respectively.

Of course (4.4) has a physical sense only for positive values of α, otherwise the perturbation would increase indefinitely with the distance *x*. It is worthy to define the *Attenuation Relation* obtained by representing the attenuation coefficient as a function of the frequency. This *Attenuation* curve is somewhat analogous with the *Dispersion Relation*, except that it is inverted for determining the damping ratio profile as will be explained in the sequel.

Without going deeply into details we will briefly introduce the main concepts beyond the theory of linearly visco-elasticity and its consequences when applied to wave propagation.

A linearly visco-elastic material manifests deformations that are linearly related to the stresses induced by the loads and in addition they depend on the history of the loading process.

This means that inside the material subjected to an instantaneous strain, kept constant in time, a *relaxation* of the instantaneous stress response will occur. On the contrary if an instantaneous stress state, kept constant in time, is created then the *creep* phenomenon will be detected, since the instantaneous strain response will increase asymptotically with time towards a finite value of deformation. In mathematical terms the above explained behavior can be written as (Achenbach, 1999):

$$\tau_{ij} = \delta_{ij}\int_{t_0}^{t}\left[G_B(t-s)-\frac{2}{3}G_S(t-s)\right]d\varepsilon_{kk} + 2\int_{t_0}^{t}\left[G_S(t-s)\right]d\varepsilon_{ij} \tag{4.5}$$

where $G_B(t)$ and $G_S(t)$ are the relaxation functions in bulk and shear respectively.

If we consider a steady-state strain deviator harmonic in time:

$$e_{ij} = e_{ij}^{*}e^{i\omega t} \tag{4.6}$$

then we can assume that it has been generated by a steady-state time harmonic stress deviator:

$$s_{ij} = 2G_S^*(\omega)e_{ij}^* e^{i\omega t} \tag{4.7}$$

where $G^*_S(\omega)$ is a complex modulus depending on the frequency of excitation:

$$G_S^*(\omega) = G_S^{'}(\omega) + iG_S^{''}(\omega) \tag{4.8}$$

By means of the complex modulus above defined it is possible to specify the stress state in (4.5) for the steady-state harmonic case as:

$$\tau_{ij} = e^{i\omega t}\delta_{ij}\left[G_B^*(\omega) - \frac{2}{3}G_S^*(\omega)\right]\varepsilon_{kk}^* + 2\left[G_S^*(\omega)\right]\varepsilon_{ij}^* \tag{4.9}$$

If we substitute (4.4) into (4.9) and together into the equation of motion (1.10) and no body forces are present we get (Achenbach, 1999):

$$[G_S^*(\omega)k^2 - \rho\omega^2]\hat{d} + [G_B^*(\omega) + \frac{1}{3}G_S^*(\omega)]k^2(\hat{p}\cdot\hat{d})\hat{p} = 0 \tag{4.10}$$

From (4.10) two considerations can be made. First in an unbounded visco-elastic region both P and S waves can exist as in the elastic case. Secondly an intrinsic non-linear relationship is manifest between the wavenumber k and the frequency ω, so that visco-elastic waves are both attenuated and dispersive.
For P and S waves the phase velocities given by (4.10) are:

$$V_P^* = \frac{\omega}{k_P^*} = \sqrt{\frac{G_B^*(\omega) + \frac{4}{3}G_S^*(\omega)}{\rho}} \tag{4.11}$$

and

$$V_S^* = \frac{\omega}{k_S^*} = \sqrt{\frac{G_S^*(\omega)}{\rho}} \tag{4.12}$$

As it is known (see for ex. Aki and Richards, 1980) an intimate relation exists between the real and the imaginary parts of the complex moduli appearing in (4.11) or (4.12). It comes out from the *principle of causality* that the real and the imaginary parts of the complex moduli form a pair Hilbert Transforms. As a consequence the attenuation coefficient α and the phase velocity $\frac{\omega}{k_{\mathrm{Re}}}$ in (4.4) are strictly linked and the important statement follows that in visco-elastic media the dissipation of energy is accompanied by *material Dispersion* (Lai, 1998). Hence in layered visco-elastic media at least two types of Dispersion phenomena have to be discerned: the *Geometrical Dispersion* caused by multiple reflections and refractions at the interfaces and the *Material Dispersion* due to the energy losses predicted by the visco-elastic theory inside the material.
At this point the interesting and powerful *principle of correspondence* between elastic and visco-elastic solutions to the dynamic problem will be introduced. It says that the one-sided Laplace transform in time of the visco-elastic solution to a dynamic problem can be obtained from the one-sided Laplace transform in time of the correspondent elastic solution to the same dynamic problem. An essential condition to be respected for the correspondence principle to hold is having time-invariant boundary conditions for the boundary value problem (Christensen, 1971). In fact if we apply the one-sided Laplace transform in time to both (4.5) and (1.6) we obtain (4.13) and (4.14) respectively:

$$\bar{\tau}_{ij} = \delta_{ij}\left[\overline{G}_B(s) - \frac{2}{3}\overline{G}_S(s)\right]\bar{\varepsilon}_{kk} + 2\overline{G}_S(s)\bar{\varepsilon}_{ij} \tag{4.13}$$

$$\bar{\tau}_{ij} = \delta_{ij}\left[B - \frac{2}{3}\mu\right]\bar{\varepsilon}_{kk} + 2\mu\bar{\varepsilon}_{ij} \tag{4.14}$$

By comparing (4.13) and (4.14) it is evident that the visco-elastic solution can be got from the correspondent elastic solution by simply substituting the real moduli with the correspondent complex moduli.
A simple application of the visco-elastic correspondence principle to the S and P wave velocities into an unbounded visco-elastic region leads to the same results reported in (4.11) and (4.12) starting from the knowledge of the corresponding elastic solution.
By means of the visco-elastic correspondence principle it is quite easy to write the displacement field generated by a surface point harmonic source in a visco-elastic layered medium (Lai, 1998). The solution in terms of vertical displacements for the elastic case (2.10) is herein reported:

$$u_{\beta}(x,z,\omega,t) = \sum_{j=1}^{M} \left[A_{\beta}(x,z,\omega) \right]_j \cdot e^{i\left(\omega \cdot t - k_j \cdot x + \varphi_{\beta}\right)} \tag{4.15}$$

or in equivalent form (Lai, 1998):

$$u_{\beta}(x,z,\omega,t) = F_o \cdot S_{\beta}(x,z,\omega) \cdot e^{i\left[\omega t - \psi_{\beta}(x,z,\omega)\right]} \tag{4.16}$$

in which $S(x,z,\omega)$ is the *Rayleigh Geometrical Spreading function*, that together with the $\psi_{\beta}(x,z,\omega)$ in the exponential term considers the combination of all Rayleigh modes when thought as a whole apparent propagating disturbance. The expressions for $S(x,z,\omega)$ and $\psi_{\beta}(x,z,\omega)$ are (Lai, 1998):

$$S_{\beta}(x,z,\omega) = \sqrt{\sum_{ij} \left[A_{\beta}(x,z,\omega)\right]_j \cdot \left[A_{\beta}(x,z,\omega)\right]_j \cdot \cos[r(k_i - k_j)]} \tag{4.17}$$

$$\tan\left(\psi_{\beta}[x,z,\omega]\right) = \frac{\sum_i \left[A_{\beta}(x,z,\omega)\right]_i \cdot sin(k_i \cdot r + \varphi_{\beta})}{\sum_j \left[A_{\beta}(x,z,\omega)\right]_j \cdot \cos(k_j \cdot r + \varphi_{\beta})} \tag{4.18}$$

The solution for the visco-elastic case corresponding to (4.15) and (4.16) are (Lai, 1998):

$$u_{\beta}(x,z,\omega,t) = \sum_{j=1}^{M} \left[A^*_{\beta}(x,z,\omega) \right]_j \cdot e^{i\left(\omega \cdot t - k^*_{j\beta} \cdot x + \varphi_{\beta}\right)} \tag{4.19}$$

and

$$u_{\beta}\left(x,z,\omega,t\right)=F_{o}\cdot S_{\beta}^{*}\left(x,z,\omega\right)\cdot e^{i\left[\omega\cdot t-\psi_{\beta}^{*}(x,z,\omega)\right]} \tag{4.20}$$

that are valid only into subsets of the complex domain where (4.19) and (4.20) are well-defined, single-valued and continuous functions of the independent complex variables.
In (4.19) the complex wave number k_j^* appears that is a complex root of the Rayleigh Dispersion Relation as discussed at the beginning of this section.
In (4.20) it is no longer possible to discern the phase as the simple product between a wave number and the distance, but a complex-valued phase angle is found. Actually it could be defined an *effective* (Lai, 1998) *or* more properly an *apparent* wave number as:

$$\frac{\partial\psi_{\beta}^{*}(x,z,\omega)}{\partial x}=\frac{\omega}{c_{apparent}(x,z,\omega)} \tag{4.21}$$

that is correlated to an *apparent* wavelength:

$$\lambda_{apparent}=\frac{c_{apparent}(x,z,\omega)}{f} \tag{4.22}$$

that represents how the spatial periodicity appears when considering the whole disturbance, made of all the Rayleigh modes.

4.2 Coupled versus Uncoupled Inversion

There are two strategies for determining the *Damping* ratio profile. The first one is the *Coupled Inversion* procedure, that consists of simultaneously inverting the *Dispersion* and the *Attenuation* curves for evaluating at the same time the shear wave velocity and the *Damping* profiles. The second strategy is called *Uncoupled* procedure and allows for the *Damping* ratio determination once the stiffness profile has been separately determined.
In the following both of them will be explained.
The Coupled and Uncoupled strategies have been thought and developed by Prof. Rix and his co-workers (Foti, Lai, Roma, Spang,) at Georgia Institute of Technology of Atlanta in recent years. The Author has been collaborating with them in implementing, improving and applying the two strategies to real sites (Rix et al., 2001b).

The Damping ratio is commonly defined by means of the total energy dissipated and the averaged energy stored in a cycle of harmonic loading, that for a visco-elastic model is proportional to the ratio between the real and imaginary parts of the complex modulus (Lai, 1998):

$$D = \frac{\Delta E_{dissipated}}{8\pi \cdot E_{averaged}} = \frac{\mathrm{Im}(G^*)}{2\,\mathrm{Re}(G^*)} \tag{4.23}$$

A correlation exists between the damping ratio and the so called quality factor Q=1/2D more used in geophysical literature.
The inherent link among the complex wave velocity V^*, the phase velocity V and the attenuation coefficient α can be clearly understood by writing the complex wave velocity using (4.1)÷(4.4):

$$V^* = \frac{\omega}{k^*} = \frac{\omega}{k_{\mathrm{Re}} + i\alpha} = \frac{\omega}{\frac{\omega}{V} + i\alpha} = \frac{1}{\frac{1}{V} + i\frac{\alpha}{\omega}} \tag{4.24}$$

If we consider that the complex wave velocity depends on the damping ratio as (Lai, 1998):

$$V^* = \frac{V(1 - iD)}{(1 + D^2)} \tag{4.25}$$

by comparing (4.24) and (4.25) an important relation comes out among the attenuation coefficient, the phase velocity and the damping ratio:

$$\alpha(\omega) = \frac{\omega}{V(\omega)} \cdot D(\omega) \tag{4.26}$$

This relationship clarifies the reciprocal influence between the dispersion and the attenuation relations.
In principle both the stiffness and the damping ratio are frequency dependent, since they depend on the dispersion and attenuation relations, but frequency independent stiffness and damping ratio profiles are commonly assumed in the frequency range where the earthquake engineering applications are of concern. In practice the stiffness and the damping ratio profiles are supposed to be evaluated at a frequency of

reference and their values at other frequencies are determined by means of a material dispersion relation. For more details the reader is referred to (Lai, 1998).

4.3 Uncoupled Inversion

In the *Uncoupled* procedure the first step consists of inverting the Rayleigh *Dispersion Relation* in order to determine the stiffness profile, neglecting the influence of energy dissipation during the propagation. This assumption does not compromise the results on the inverted stiffness profile, since at the level of strain that is reached in the experiments (less than $10^{-6}\% \div 10^{-3}\%$ depending on the material) the damping ratio is lower than about 5% and the coupling effects between *Material and Geometrical Dispersions* are of less concern (Santamarina and Stokoe, 2001).
Materials that show this kind of behaviour are typically indicated as weakly dissipative media (Lai,1998).
Consider the complex displacements on the free surface for a visco-elastic layered medium (4.20) and make the following assumptions:
1) during propagation only the predominant Rayleigh mode is considered in evaluating the complex phase angle Ψ^*, but all modes are included in calculating the geometrical spreading function $S^*(x,z,\omega)$.
2) for weakly dissipative media substitution of the visco-elastic geometric spreading function $S^*(x,z,\omega)$ with the corresponding elastic one $S(x,z,\omega)$ does not imply appreciable error (Lai, 1998).

The first statement means that the complex phase angle can be substituted by an explicit dependence of the phase upon the distance from the source:

$$\psi^*(x,z,\omega) \cong k^*(z,\omega)\cdot x \tag{4.27}$$

The second hypothesis states that:

$$S^*(x,z,\omega) \cong S(x,z,\omega) \tag{4.28}$$

From the above simplifications the displacements in (4.20) can be rewritten as:

$$u(x,z,\omega,t) = F_o \cdot S(x,z,\omega) \cdot e^{i\left[\omega \cdot t - k^* x\right]} \tag{4.29}$$

This expression is the same as (4.4) if we expand the complex wave number k^* that appears in the exponent. It is worthy to underline that the geometrical spreading function *S(x,z,ω)* is known only if the stiffness and the thickness profiles are known. So in the Uncoupled procedure, once the stiffness and the geometry have been evaluated, only the damping ratio profile remains to be determined.
With regard to this purpose the following relationship among the attenuation curve, the P and S wave velocities and the shear damping ratio D_s profiles will be used (Lai, 1998):

$$\alpha(\omega) = \frac{\omega}{c_R^2}\left\{\sum_i^N \left[V_{p,i} \cdot \left(\frac{\partial c_R}{\partial V_p}\right)_i \cdot k + V_{s,i} \cdot \left(\frac{\partial c_R}{\partial V_s}\right)_i\right] \cdot D_{s,i}\right\} \tag{4.30}$$

in which $\alpha(\omega)$ is the attenuation coefficient, c_R is the Rayleigh phase velocity, V_p and V_s are the body velocities, k is a constant ratio between volumetric and shear damping ratios and D_s is the shear damping ratio. The subindex i refers to the generic layer.
It has been shown (Spang, 1995) that the influence of the value of k on the inverted damping ratio profile is negligible, that is in agreement with the fact that the dispersion relation of Rayleigh waves is relatively insensitive to variations in the V_p profile. Since the value of k ranges between 0 and 1 (Hermann and Mitchell, 1975):

$$0 < k = \frac{D_p}{D_s} < 1 \tag{4.31}$$

a value of k=1 has been chosen for the next analyses.
Formula (4.30) can be expressed in matrix form as:

$$[G] \cdot D_s = \alpha \tag{4.32}$$

where [G]=MxN is a matrix that depends on the partial derivatives of the Rayleigh phase velocity with respect to the body velocities profiles, D_s=Nx1 is the vector of damping ratios, α=Mx1 is the attenuation curve. M is the number of frequencies and N is the number of layers considered.
In the expression (4.32) the knowledge of the Rayleigh dispersion relation and of the body velocities profiles allows for the calculation of the matrix

[G], so that the shear damping ratio profile D_s can be inverted if the attenuation curve α is available.
The inversion can be achieved by means of any proper inversion algorithm, that works well for the particular kind of inversion problem. Rix and his co-workers (Rix et al., 2001) propose a constrained linear inversion algorithm (Constable et al., 1987) that has been used for all the sites investigated and reported in Chapter 5. The strategy of the inversion consists of finding the optimal set of damping ratios, that minimises a multi-objective function, made of two components. The first component is the roughness of the damping ratio profile, defined as (Constable et al., 1987):

$$R = \sum_{i=2}^{N} \left(D_{S,i} - D_{S,i-1} \right)^2 \tag{4.33}$$

This property refers to the smoothness of the inverted profile and it is based on the idea that it is more probable to encounter profiles whose mechanical properties vary gradually rather than profiles with abrupt changes in the characteristics. In the opinion of the Author this idea can be accepted for most of the sites, especially for normally dispersive sites, but there may exist situations in which this strategy causes incorrect results (Hebeler, 2000) and a different algorithm, such as the one proposed in Chapter 3, would be more appropriate.
The second component of the objective function is the *distance* between the experimental and the theoretically inverted shear damping ratio profile in a weighted least-squares sense:

$$\eta = \left\| W\alpha - WGD_s \right\|^2 \tag{4.34}$$

where W=diag{$1/\sigma_1$ $1/\sigma_2$ $1/\sigma_M$} is a diagonal MxM weighting matrix and σ is the standard deviation associated with the uncertainties in the measured experimental attenuation curve. In the sequel it will be shown how to evaluate the variance σ^2 by means of the *coherence* associated to the measured signals. It is required that the distance defined by the Euclidean norm in (4.34) be smaller than an arbitrarily assigned value η^*.
The multi-objective function is given by the sum:

$$Objective = R + \mu \cdot (\eta - \eta^*) \tag{4.35}$$

where the *smoothing parameter* μ has the important role of giving a different weight to the first and second components of the objective

function. By varying the smoothing parameter inside a certain range a regularisation of the objective function is reached with a smoothing effect on the ripples. This effect makes it possible to overcome the intrinsic limitations of a local search technique when dealing with an objective function, which is characterised by the presence of quite close local minima in the space of the variables. As a consequence the probability of finding a global optimum increases.
For the purpose of solving the above explained optimisation problem and finding the optimum of the objective function (4.35) the method of Lagrange multipliers can be adopted (Rix et al., 2001):

$$D_{Soptimum} = [\frac{1}{\mu}\partial^T\partial + (WG)^T WG]^{-1}(WG)^T W\alpha \tag{4.36}$$

where μ is the Lagrangean multiplier that can be chosen arbitrarily among all the possible solutions which assure a positive value of the damping ratios of each layer. The symbol ∂ denotes a matrix NxN given by:

$$\partial = \begin{bmatrix} 0 & \dots & & \dots & 0 \\ -1 & 1 & 0 & \dots & 0 \\ 0 & -1 & 1 & \dots & 0 \\ 0 & \dots & -1 & 1 & 0 \\ 0 & \dots & 0 & -1 & 1 \end{bmatrix} \tag{4.37}$$

In the opinion of the Author the subjectivity in choosing the parameter μ, that is the most reliable damping ratio profile, on one side offers the advantage of the direct judgement of an expert operator but on the other hand inevitably causes an uncertainty in the final solution. In order to overcome the embarrassment in the choice, the value of the parameter μ could be taken, that ensures both positive damping ratios and minimum misfit error. This criterion does not always guarantee the most physically reasonable profile as it will be shown in Chapter 5.
The only ingredient that is needed for using formula (4.30) is the experimental attenuation curve α(ω).
The experimental determination of the attenuation curve is conceptually easy to understand, but the actual handling of the measured data needs particular attention, since the final inverted damping ratio profile is significantly influenced by the experimental attenuation curve.
If only the experimental attenuation curve is required the procedure consists of comparing the absolute values of the experimental and the theoretical Transfer Functions of the system by means of a regression analysis.

If both the attenuation and dispersion curves are needed then the Transfer Functions as complex quantities are considered instead of their absolute values.
The absolute value of the experimental vertical displacement on the free surface of the system is given by:

$$\left|u(x,\omega)_{\exp erimental}\right| = \frac{\left|acc(x,\omega)\right|}{\omega^2 \cdot C(\omega)} = \frac{\left|vel(x,\omega)\right|}{\omega \cdot C(\omega)} \tag{4.38}$$

in which C(ω) is the calibration factor of the receivers (see Chapter 5 for more details).
The spectrum of either accelerations or velocities in (4.38) can be determined from the measured particle accelerations or velocities respectively at a finite number of stations on the free surface of the layered half-space.
The experimental Transfer function can be obtained from the displacements (4.38) and the measured input by means of :

$$\left|Tr(x,\omega)_{\exp erimental}\right| = \frac{\left|u(x,\omega)_{\exp erimental}\right|}{InputForce} \tag{4.39}$$

In the formula (4.38) the same hypothesis as in section (2.6) has been assumed about the stationariness of the travelling perturbance. Such an assumption may be unrealistic for the whole signal, but it represents a good approximation nearby the maximum point of the envelope of the signal, where the main energy of the perturbation is located.
The absolute value of the theoretical Transfer Function can be obtained from the theoretically predicted displacements (4.29) in an analogous manner as in the (4.39) :

$$\left|Tr(x,\omega)_{theoretical}\right| = \frac{\left|u(x,\omega,t)_{theoretical}\right|}{InputForce} = \frac{\left|F_o \cdot S(x,z,\omega) \cdot e^{i\left[\omega \cdot t - k^* x\right]}\right|}{F_o \cdot e^{i\omega \cdot t}} \tag{4.40a}$$

$$\left|Tr(x,\omega)_{theoretical}\right| = \left|S(x,z,\omega) \cdot e^{-ik^* x}\right| = \left|S(x,z,\omega) \cdot e^{-i\left(\frac{\omega}{V_R} + i\alpha_R\right)x}\right| \tag{4.40b}$$

$$\left|Tr(x,\omega)_{theoretical}\right| = \left|S(x,z,\omega)\right| \cdot e^{\alpha x} \tag{4.40c}$$

By comparing (4.40c) and (4.39) at each frequency it is possible to determine the attenuation coefficient $\alpha(\omega)$ that best matches the theoretical and the experimental Transfer Functions. This task is accomplished by means of the Levenberg Marquardt non-linear inversion algorithm (Press et al., 1992, Rix et al., 2001b).
As an example we anticipate the results obtained at the site Mud A (USA), whose characteristics will be further explained in Chapter 5. We only say that it is located on an artificially made island on the Mississippi river and it is mainly constituted by silty sands.
As a first step it is necessary to explain how the standard deviations that appear in the weighting matrix W in formula (4.34) can be calculated.
The standard deviation σ associated to any measured data is correlated to the relative error ε and the averaged quantity $|w|$ that has been measured by means of:

$$\sigma = \varepsilon \cdot |\, w_{averaged} \,| \tag{4.41}$$

In this case as measured quantity $|w|$ the vertical displacements have been considered.
The relative error can be evaluated by using the *coherence* γ^2 (see fig.4.1) just defined in Chapter 2 (2.?):

$$\varepsilon = \left| \frac{\sqrt{1-\gamma^4}}{\gamma^2 \cdot \sqrt{2N}} \right| \tag{4.42}$$

where N is the number of the averaged measurements.

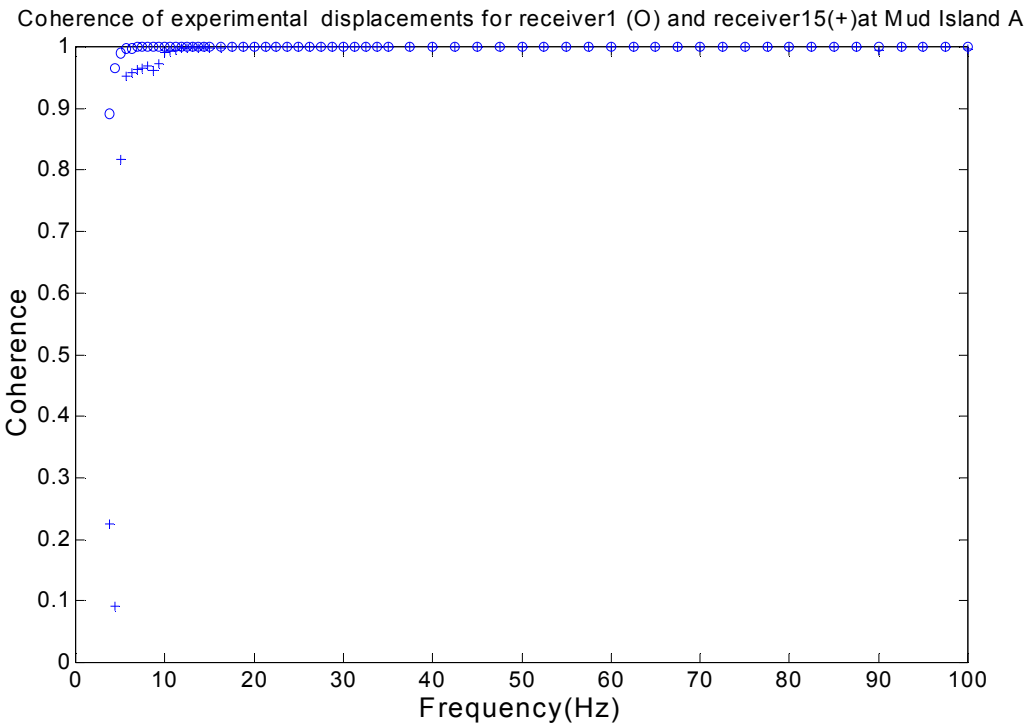

Figure 4.1: Coherence of the experimental displacements measured at the receivers 1st (circles) and 15th (plus). A good quality of the measured data can be observed above 10 Hz, where the coherence is equal to 1.

It must be underlined that it is easy to demonstrate that the coherence associated to the measurements is the same for both the displacements and the accelerations.
The *variance* associated to any measured data is defined as the square of the standard deviation σ, so the variance for the vertical displacements is given by:

$$\mathrm{var}[|\, w(\omega)\,|] = \sigma^2[|\, w(\omega)\,|] \tag{4.43}$$

If the assumption is made of a Gauss distribution of the experimental measurements, that are assumed independent events, only two quantities are needed to describe the uncertainties associated to the measured data: the expected value w_{averaged} and the standard deviation σ. If also the attenuation coefficient at each frequency is determined by means of a non-linear least-square algorithm such as Levenberg Marquardt, then the uncertainty in

estimating the attenuation coefficient α can be approximately calculated using (Lai, 1998, Menke, 1989):

$$\mathrm{var}(\alpha) \approx \left[\left(J_\alpha^T J_\alpha\right)^{-1} J_\alpha^T\right] \mathrm{cov}\left[|w(\omega)|\right] \left[\left(J_\alpha^T J_\alpha\right)^{-1} J_\alpha^T\right]^T \tag{4.44}$$

in which the covariance matrix cov[|w(ω)|]=n x n is diagonal with the non-zero elements equal to the variances of |w(ω)| given by (4.43) because of the hypothesis of uncorrelated measured data (Lai,1998).
The term J_α is a n x 1 vector whose components are given by (Lai,1998):

$$\left(J_\alpha\right)_k = \left[J_\alpha(\omega)\right]_k = \frac{\partial \,|\, w(x_k,\omega) \,|}{\partial \alpha} = -x_k \cdot |\, w(x_k,\omega) \,| \tag{4.45}$$

where k=1÷n indicates the generic receiver and n is the total number of receivers.
By using (4.43) and (4.44) it is possible to calculate the terms of the weighting matrix W in (4.34).
In fig.4.2 the comparison between the experimental (circles) and the theoretical (dots) absolute value of the vertical displacements is illustrated at the frequencies between 15Hz and 21.25Hz. It is interesting to notice the oscillating behavior of both the responses due to the superposition of all the Rayleigh modes. This aspect assumes relevance when dealing with inversely dispersive sites, especially at frequencies greater than the cut-off frequency of the second mode of Rayleigh. In fact below the cut-off frequency of the second mode of Rayleigh only the fundamental mode exists and the Geometrical Spreading Rayleigh function $S(x,z,\omega)$ reduces to a constant factor proportional to 1/√x that governs the geometrical attenuation law of the Rayleigh waves through a homogeneous half-space.

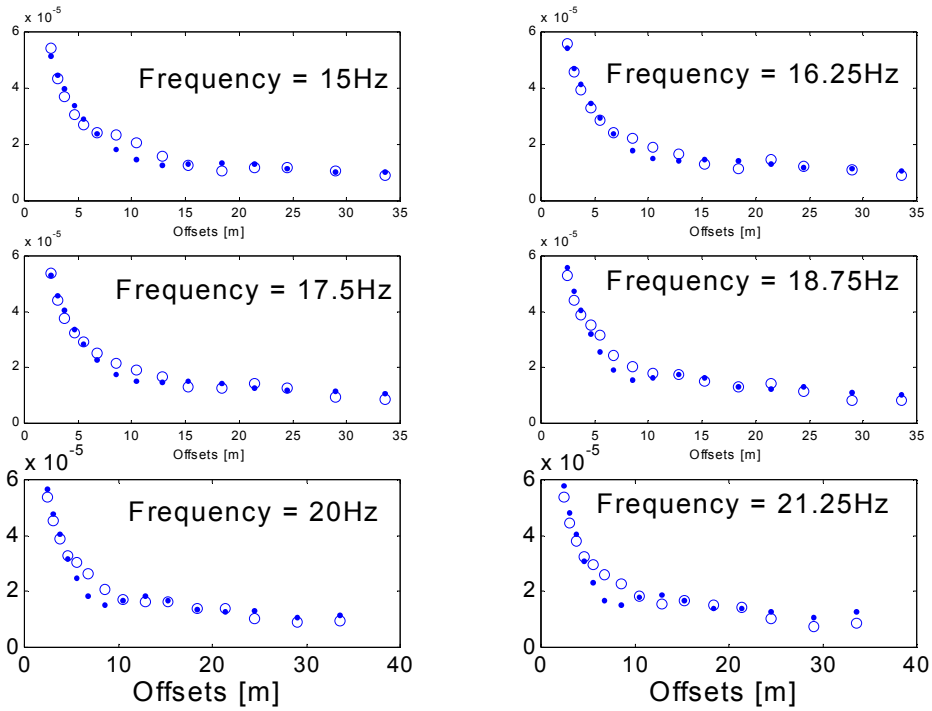

Figure 4.2: Experimental (circles) and the theoretical (dots) absolute value of the vertical displacements at Mud A site.

The simplified attenuation law 1/√r is equivalent to using only one mode of Rayleigh, that is the fundamental mode (Foti, 2000, Rix et al., 2000). It has got some limitations in simulating the oscillating behaviour of the spatial wave train made of all the Rayleigh modes. In fig.4.3 the influence of considering the simplified geometrical attenuation law 1/√r instead of the Geometrical Spreading Rayleigh function $S(r,z,\omega)$, calculated using all the Rayleigh modes (fig.4.4), is visible in terms of the attenuation curve. It can be observed that, if the contribution of higher modes of Rayleigh is ignored, the *Attenuation* curve mainly decreases with frequency, instead of increasing, as it is expected according to the formula (4.26). In making this consideration we are assuming a shear damping ratio evaluated at a frequency of reference and it is also supposed that the influence of the phase velocity V(ω) consists in any oscillations of the Attenuation curve localised at some frequencies.

In the Author's opinion the significant oscillation presented by the *Attenuation* curve in fig.4.4 around the frequency of 80Hs is not correlatable to the *Dispersion Relation*, since V(ω) is almost constant at high frequencies (fig.5.36). A possible cause that seems reasonable is represented by the near

field effects that disturb the data acquired at the receivers close to the source, where the wave components at high frequency are mainly detected. In fact the higher the frequency of the wave, the higher the number of oscillations into a fixed space, the more rapid the attenuation with distance. This means that the receivers located in the far field detect high frequency components of motion that are more affected by noise, because their intensity has just been considerably attenuated.

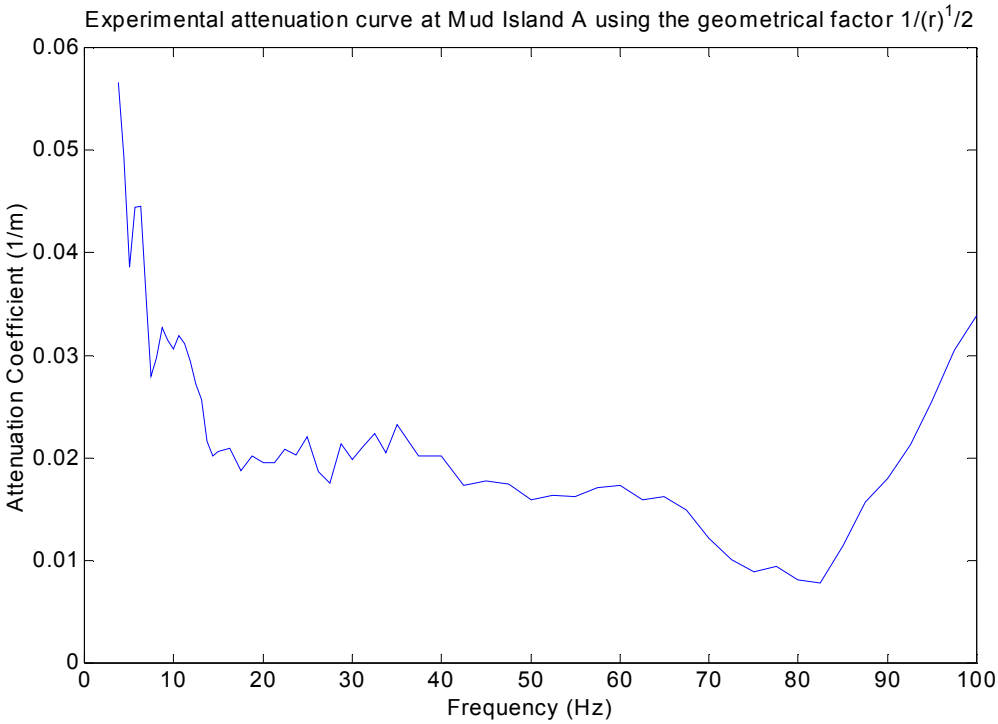

Figure 4.3: Experimental Attenuation curve at site Mud A using a simplified geometrical attenuation law $1/\sqrt{r}$.

For the *Attenuation* curve at the site Mud A site the proper choice has been made of excluding the frequencies higher than 70 Hz, to be used for the inversion of the final *Damping* ratio profile (fig.4.5).
The obtained *Damping* ratio profile is reliable, since for sands, values below 2% are expected at very small deformations and a decreasing trend is observed, due to the increasing stress state with depth, which causes an increment of the stiffness, provided the material is the same.

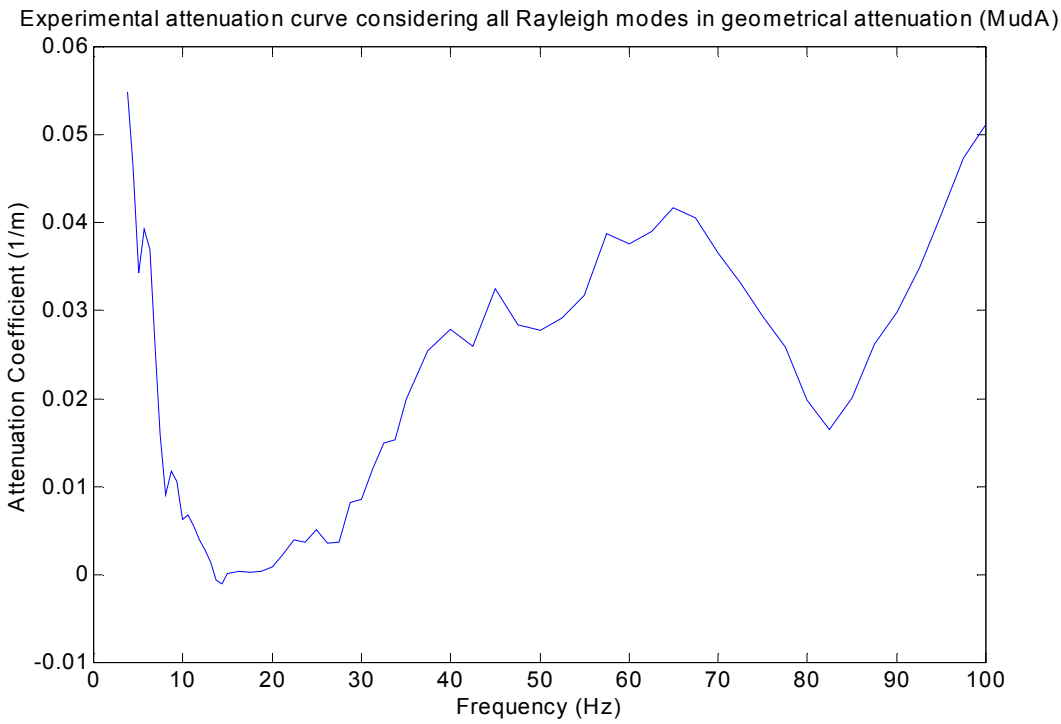

Figure 4.4: Experimental *Attenuation* curve at site Mud A when *the Geometrical Spreading Rayleigh* function $S(x,z,\omega)$ is calculated using all the Rayleigh modes.

It can be said that the Uncoupled procedure represents a valid alternative to the *Coupled* procedure when the stiffness profile and the stratigrafy of the site are available and a preliminary *Damping* ratio profile is desired before proceeding with a theoretically more refined *Coupled* Inversion.

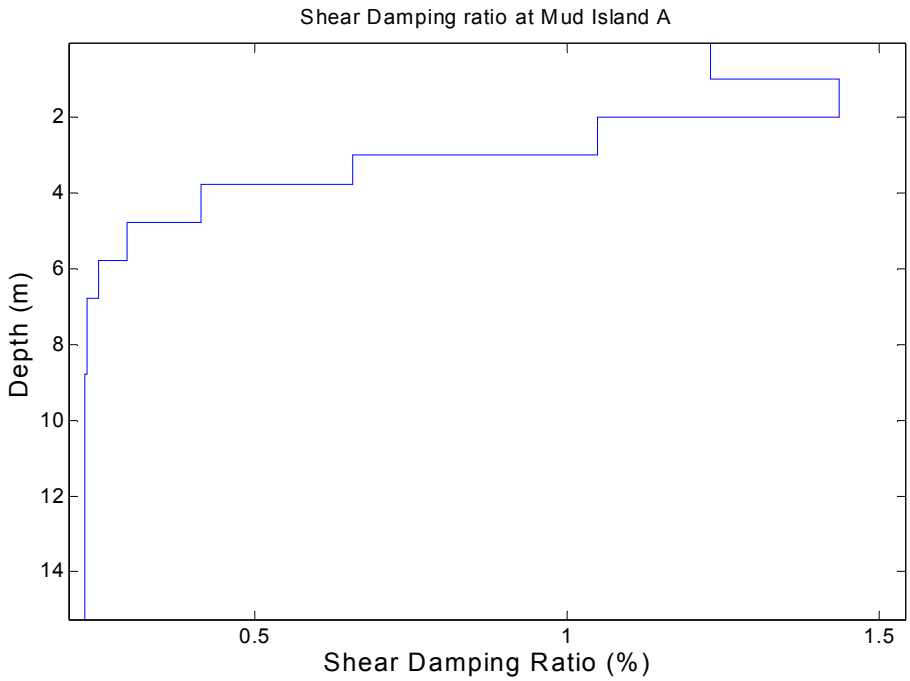

Figure 4.5: Inverted *Damping* ratio profile at site Mud A (USA).

4.4 Coupled Inversion

The *Coupled Inversion* of *Dispersion* and *Attenuation* curves is possible by means of the complex wave velocities as defined in (4.11) and (4.12) and the application of the elastic-viscoelastic correspondence principle to the Rayleigh eigenproblem. In fact if the complex Rayleigh wavenumbers are found the theoretical complex phase velocity specified in (4.24) can be calculated and successively compared to the experimental complex phase velocity. In this way a basis is available for an optimisation algorithm that varies the initial geometrical and mechanical parameters of the model until a properly built objective function is minimised.

The main differences with respect to the Uncoupled Inversion concern the idea of measuring and theoretically evaluating together the *Attenuation* and *Dispersion Relations*. As just anticipated in section 4.3 the comparison between the experimental and the theoretical responses of the system is made by using the *Displacement Transfer Function* .

In order to measure both the attenuation coefficient and the phase velocity of Rayleigh waves a procedure analogous to the one used for the *Uncoupled*

Inversion can be used, except that the experimental complex wave number is determined as it appears in (4.29), instead of the attenuation coefficient α only. The advantage of this technique is the consistency guaranteed by adopting the same array of receivers for measuring the attenuation and the dispersion. The regression analysis used to obtained the experimental apparent wave numbers is the same as in the Uncoupled procedure i.e. the *Levenberg Marquardt* algorithm with the difference that the distance between the theoretical and the experimental *Transfer Functions* must be defined in a complex plane. If the distance at each frequency is calculated as:

$$dis\tan ce(\omega) = \sqrt{\left[Tr(x,\omega)_{\exp} - S(x,\omega)\cdot e^{-ik^*(\omega)x}\right]\cdot conj\left[Tr(x,\omega)_{\exp} - S(x,\omega)\cdot e^{-ik^*(\omega)x}\right]} \tag{4.46}$$

then the objective function to be minimised is given by the summation of the square distances at all the n_f frequencies of interest (Rix et al., 2001):

$$Objective = \sum_{j=1}^{n_f}[dis\tan ce_j(\omega)]^2 \tag{4.47}$$

Once the experimental complex wave number k^* has been found at each frequency it is a straightforward task to calculate the experimental Dispersion and *Attenuation* curves by means of:

$$k^*(\omega) = \frac{\omega}{V(\omega)} + i\alpha(\omega) \tag{4.48}$$

In fact it comes out that:

$$V(\omega) = \frac{\omega}{\mathrm{Re}[\mathrm{k}^*(\omega)]} \tag{4.49}$$

$$\alpha(\omega) = \mathrm{Im}[k^*(\omega)] \tag{4.50}$$

It should be highlighted that the evaluated experimental wave number has to be intended as an *apparent* result, that is as it appears by measuring the travelling perturbation with an assigned configuration of receivers. The term *apparent* assumes the same meaning as it has been given in the previous

Chapters 2 and 3 and it refers to the interaction between the system response and the array of receivers.
As an example of the Coupled determination of the experimental Dispersion (fig.4.6)and Attenuation (fig.4.7) relations(Rix et al., 2001), consider the Mud B site, that is located nearby the previously mentioned Mud A site and whose characteristics are described in details in the next Chapter 5.

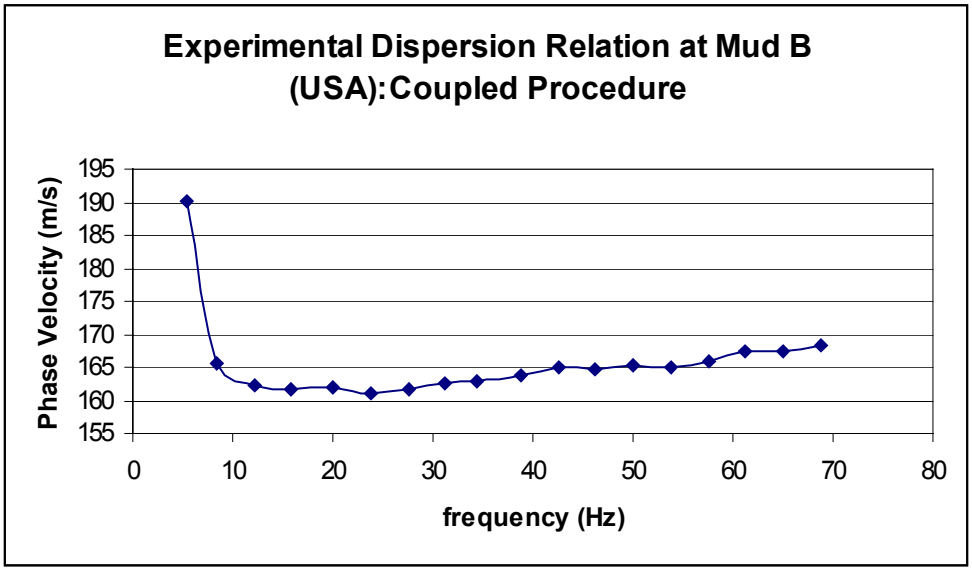

Figure 4.6: Experimental Dispersion Relation at Mud B site (USA) by means of the Coupled procedure of measurement.

As can be seen in fig.4.7 at about 75Hz there exists a relatively great valley of the Attenuation curve, as already observed in fig.4.4 for site Mud A. As already said it is believed that this behaviour be unfaithful for the reasons that have already been explained above. Hence for the Coupled Inversion Procedure the frequencies higher than 70Hz have been excluded and the resulting Attenuation curve shown in fig.4.8 has been used.
Once the experimental response of the system has been evaluated the next step consists of theoretically reproducing the same system response in order to compare them in the framework of an Inversion procedure.

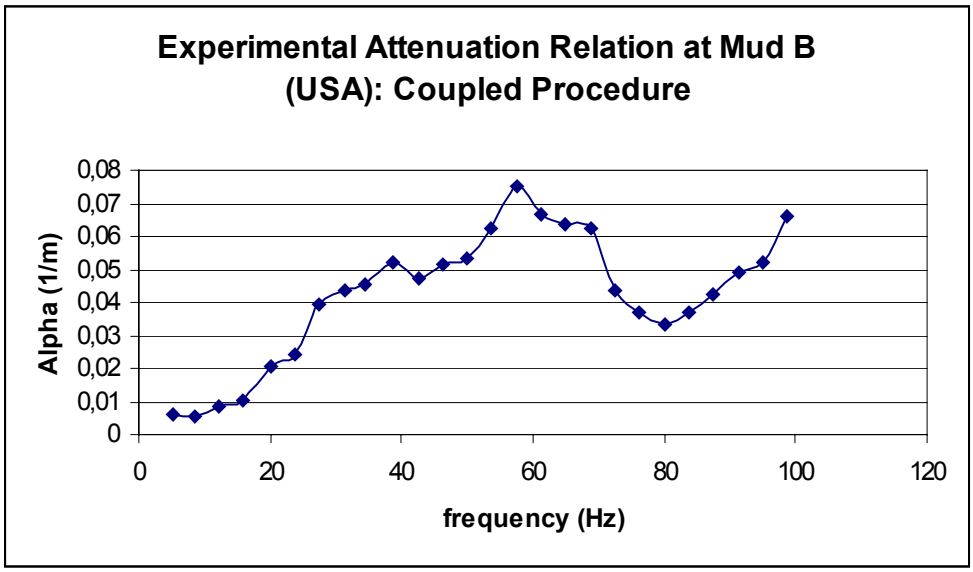

Figure 4.7: Experimental Attenuation Relation at Mud B site (USA) by means of the Coupled procedure of measurement (frequencies higher than 70 Hz included).

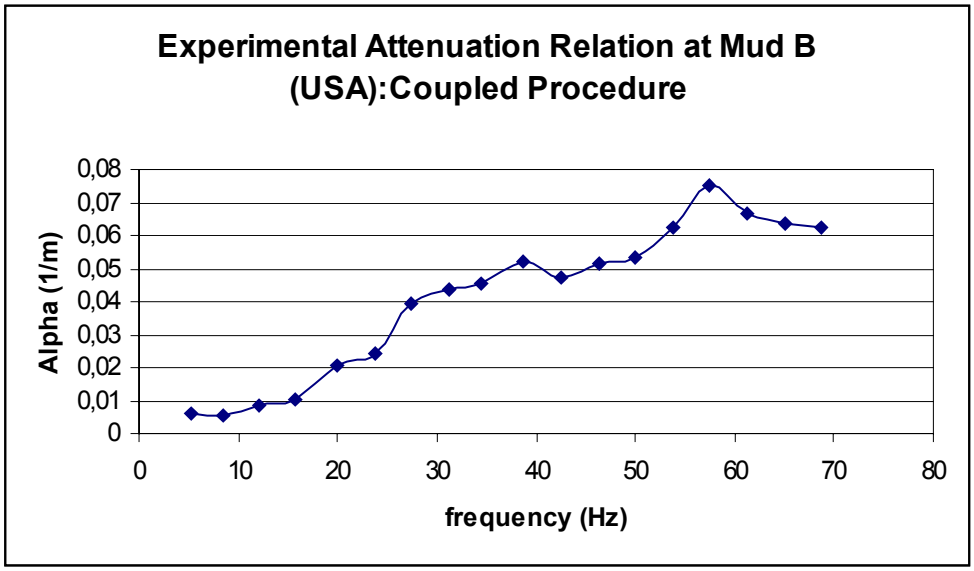

Figure 4.8: Experimental Attenuation Relation at Mud B site (USA) by means of the Coupled procedure of measurement: (frequencies higher than 70 Hz excluded).

The strategy of the optimisation algorithm is the same as for the Uncoupled Inversion, that is the roughness of the stiffness and damping ratio profiles is minimised together with the distance between the experimental and the theoretical responses of the system. Of course all the elastic variables are substituted by the corresponding complex quantities, so that equation (4.36) becomes (Rix et al., 2001):

$$V^*_{Soptimum} = (\frac{1}{\mu}\partial^T\partial + [W^*(J^*_S)_{V^*_{S0}}]^H \cdot [W^*(J^*_S)_{V^*_{S0}}])^{-1}[W^*(J^*_S)_{V^*_{S0}}]^H W^* d^*_0$$

(4.51)

where the superindex H represents the Hermitian operator,

$(J^*_S)_{V^*_{S0}}$ is the n_f x n_L (n_f and n_L are the numbers of frequencies and layers respectively) Jacobian matrix whose elements are the complex partial derivatives:

$$(J^*_S)_{jk} = \left[\frac{\partial(V^*_R)_j}{\partial(V^*_S)_k}\right]_{V^*_{S0}} \qquad (j=1,\ldots, n_f\,;\ k=1,\ldots, n_L) \qquad (4.52)$$

in which V^*_R is the vector of the n_f theoretically predicted Rayleigh complex phase velocities, V^*_{S0} is the current configuration of the system parameters. Also:

$$d^*_0 = (J^*_S)_{V^*_{S0}} \cdot V^*_S = (J^*_S)_{V^*_{S0}} \cdot V^*_{S0} + (\cdot\overline{V}^*_R - V^*_{R0}) \qquad (4.53)$$

where $\overline{V}^*_R$ is the vector of the n_f experimental Rayleigh complex phase velocities and V^*_{R0} is the n_f x 1 vector of the theoretical Rayleigh complex phase velocities corresponding to the current set of parameters V^*_{S0}. Formula (4.53) comes out from a first order approximation of the non-linear relationship:

$$V^*_R(\omega) = V^*_R[V^*_S(\omega)] \qquad (4.54)$$

between the complex Rayleigh phase velocity and the complex shear wave velocity around the current set of parameters V_{S0}^*

$$V_R^*(V_S^* \rightarrow V_{S0}^*) = V_R^*(V_{S0}^*) + (J_S^*)_{V_{S0}^*} \cdot [V_S^* - V_{S0}^*] \tag{4.55}$$

so that the optimisation algorithm belongs to a local-search technique. The last observation does not necessarily imply that the final inverted profiles be close to the starting profiles but only that the final configuration depends on the initial guess of the system parameters. As already explained in Chapter 3 a local-search techniques based on gradient of the objective function information are likely to find a local minimum in the space of the independent variables, but there are no certainties whether the found maximum is the optimum in absolute terms.
Actually the best strategy for the Inversion procedure would be adopting a global-search technique for pinpointing a limited set of possible candidates to be used as initial guess for a local-search technique. Successively a good criterion for discerning the desired optimum is taking the lowest value of the objective function among those given at the several local minima found by means of the local-search algorithm.
Once the complex shear wave velocity profile V^*_S has been inverted the corresponding real shear wave velocity and damping ratio profiles can be easily determined by means of (4.12):

$$V_S = \frac{\omega}{\mathrm{Re}\left[(k_S^*)^2\right]} = \frac{[\mathrm{Re}(V_S^*)]^2 + [\mathrm{Im}(V_S^*)]^2}{\mathrm{Re}(V_S^*)} \tag{4.56a}$$

$$D_S = \frac{\mathrm{Im}\left[(V_S^*)^2\right]}{2\,\mathrm{Re}\left[(V_S^*)^2\right]} = \frac{\mathrm{Re}(V_S^*) \cdot \mathrm{Im}(V_S^*)}{[\mathrm{Re}(V_S^*)]^2 - [\mathrm{Im}(V_S^*)]^2} \tag{4.56b}$$

For the above mentioned site Mud B the final shear wave (fig.4.9a) and damping ratio (fig.4.9b) profiles are reported below (Rix et al., 2001).

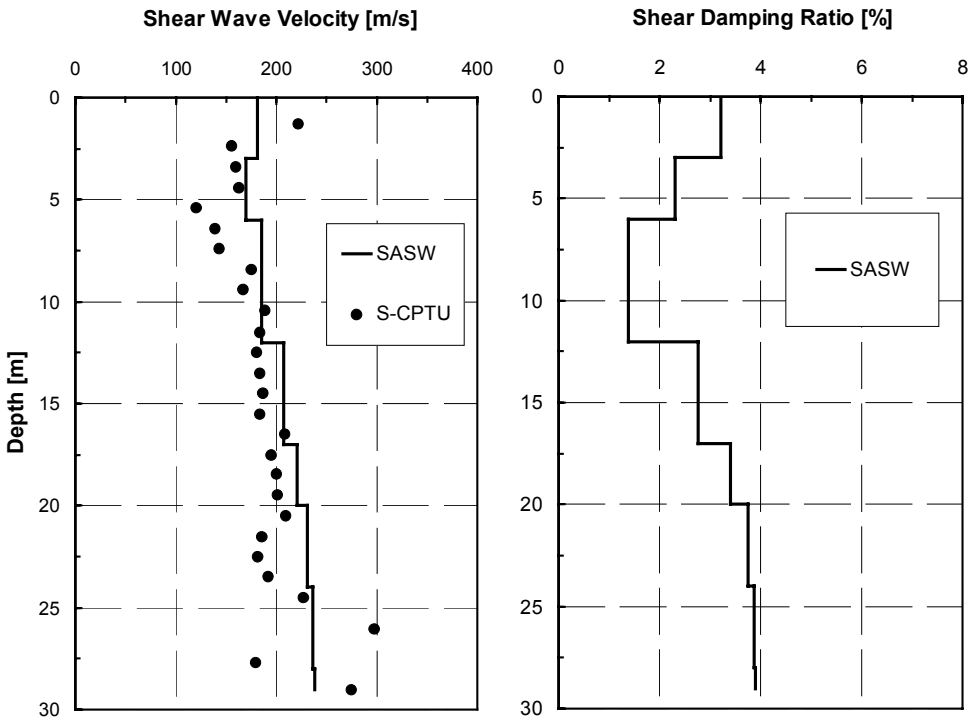

Figure 4.9a, b: Shear Wave Velocity and Shear Damping Ratio Profiles Obtained Using the CoupledInversion Algorithm at Mud B site , Memphis, TN (USA)

As can be observed in fig.4.9a the agreement between the SASW method (bold line) and the seismic cone penetration test (dots) is excellent and the *Damping* ratio profile is reasonable.
In the next Chapter 5 an interesting comparison will be shown between the Uncoupled and the Coupled Inversion procedures with reference to the site Mud B.
In concluding this Chapter it can be said that the Coupled Inversion is more rigorous and formally more elegant than the Uncoupled Inversion. Also the Coupled procedure offers an intrinsic correlation between the real and the imaginary parts of the complex-valued shear wave velocity V^*_S, because they satisfy the Riemann-Cauchy conditions, provided that the Rayleigh complex phase velocity $V^*_R(V^*_S)$ be an analytic single-valued function in its complex domain. This intrinsic property constitutes an additional internal constraint in the Inversion procedure, which mitigates the ill-posedness of the Rayleigh Inverse Problem (Lai, 1998).
Nevertheless the Uncoupled Procedure has proved to be a complementary technique whose results will be shown to be in very good agreement with

the Coupled Procedure (Chapter 5). The last consideration enables one to asses s that the level of deformations reached in the dynamical tests, performed in our work, are so small that the dissipative mechanisms of the material do not influence significantly the system response in terms of the Rayleigh Dispersion Relation. This means that the material and the geometrical dispersions of Rayleigh waves can approximately be considered as two independent phenomena and their coupling can be neglected, without any relevant error in the above specified level of strains.

Chapter 5

Experimental Results: Real Cases

Introduction

In the sequel a detailed description of the equipment used for the experimental tests will be given and the most significant results about real sites will be presented and commented.
As just anticipated in the previous Chapters the determination of the soil properties at a site relies on the theoretical simulation of an experiment in situ. As a consequence it becomes a key point having clear information about the experimental test and the instrumentation used for the purpose.
First of all it is worth remembering that the basic idea for studying the system response consists of perturbing it on a point on the free surface and then of measuring the induced vibrations at a finite number of locations on the free surface.
So in the following a first section will discuss the different types of sources that have been adopted for the experiments and another section will focus on the kinds of equipment used for acquiring the travelling perturbation.
A series of real sites will follow which have been successfully inverted by means of the procedures explained in the previous Chapters.

5.1 Impulsive and Harmonic Point Sources

In Chapter 2 we referred to both an impulsive and a harmonic vertical point source and two different procedures have been explained, which allow for the evaluation of the same system response in terms of the apparent geometrical dispersion curve of Rayleigh waves (see Appendix A).
The impulsive source may be represented by either a hammer shot or a heavy weight left dropped from a certain height.
The hammer has a mass of 6Kg and it is used to generate high frequency waves, that are useful for investigating the upper side of the site.
As heavy weight a mass of 80÷130Kg has been dropped from a height of about 3m by means of the system illustrated in fig.5.1.
The total amount of energy that is put inside the system is about:

$$E_{tot} = mgh = 130Kg \cdot 9.81m/s^2 \cdot 3m = 3826J$$

and it is possible to excite low frequencies down to around 5Hz ÷10Hz to get information about the deeper layers of the site.

Figure 5.1: Device for lifting the weight drop at a height of 3m.

In case impulsive sources other than those reported above are used in the experiments they will be specified.
The harmonic point source is an electro-mechanical vibratory shaker (Model 400 Electro-Seis^{R} Shaker by APS Dynamics, Inc.), whose picture is illustrated in fig.5.2.

Figure 5.2: Electro-mechanical vibratory shaker (Model 400 Electro-Seis[R] Shaker by APS Dynamics, Inc.)

The maximum stroke for the oscillations of the shaker mass is 6.25 inches and the shaker mass of 30.6 Kg allows the generation of forces from 445 N to 60 N in the frequency range of 1-200 Hz.

The frequency input of the shaker as it has been measured by the accelerometer mounted on the top of the framework at Houston site (USA) is reported in fig.5.3.

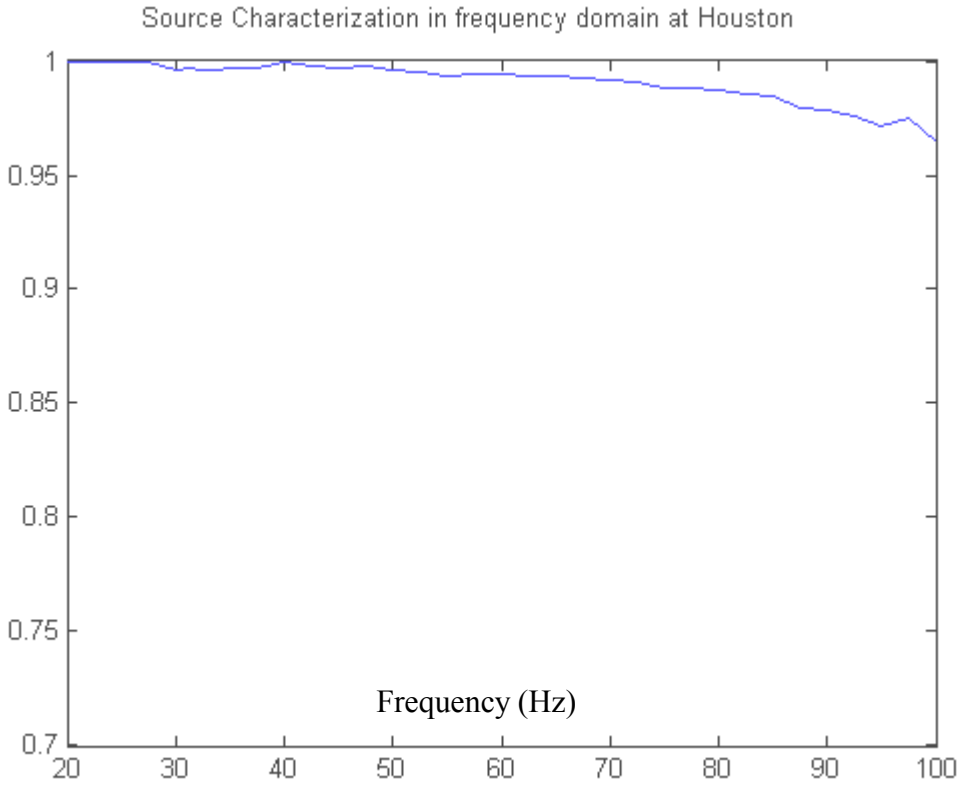

Figure 5.3: Normalized PSD of the harmonic source input at Houston.

The Power Spectral Density of the acceleration has been measured on the top of the source by means of a source-mounted Wilcoxon Research Model 728T High Sensitivity, Low-Noise accelerometer.
As can observed from fig.5.3 the input given by the harmonic source is sufficiently the same at different frequencies. Hence with this source it is possible to input the same energy level at different frequencies, so that the site response can be investigated in the frequency range of interest.

5.2 Acquisition Instrumentation

The main tools needed for the experiments are:
1) a seismograph or digital analyzer for gathering the soil response

2) the receivers, which can be either geophones or accelerometers, depending whether the particle velocities or accelerations are measured.
There have been two different series of campaigns: the first one in USA, the second one in Italy. In USA the experimental data have been collected by means of Wilcoxon Research 731A Ultra-Quiet, Ultra Low Frequency seismic accelerometers and a 16-channel Hewlett Packard VXI-based digital signal analyzer. In Italy the seismograph ABEM model Terraloc MK6 (see fig.5.4) and the geophones Sensor model SM-6/U-B vertical transducers (see fig.5.5) with a natural frequency of 4.5Hz and a damping factor of 0.6 have been used.

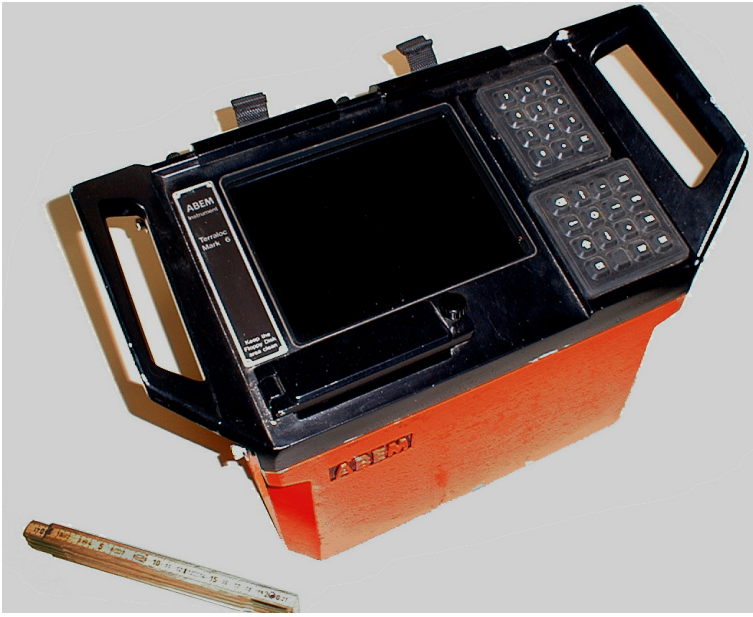

Figure 5.4: Seismograph ABEM model Terraloc MK6.

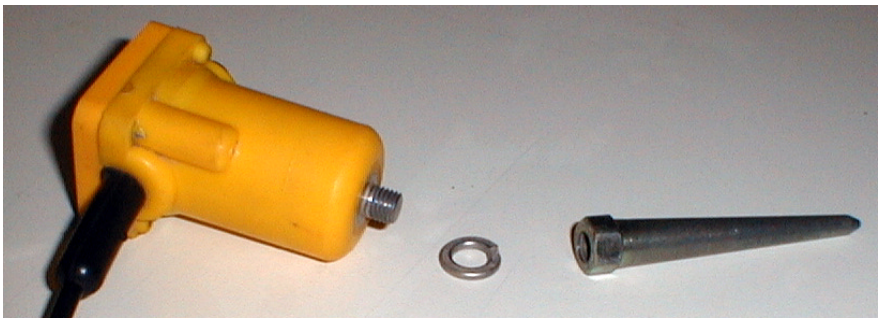

Figure 5.5: geophones Sensor model SM-6/U-B vertical transducers.

5.3 Sites Investigated

In the following some of the investigated real sites will be described and their characterization by means of the inversion procedures explained in the previous Chapters will be shown in terms of the thicknesses and either shear wave velocity or shear damping ratio.
A summary list of the sites is reported in table 5.1. The experimental measurements of either the particle velocities or the particle accelerations at the sites: Houston Leeve Park, S16, Wolf River, Mud A, Mud B and at Verzuolo have been gently provided by Prof. Rix and Hebeler and Dr. Foti respectively.

Site	Country	Dispersion	Inversion
Houston	USA	Normal	Vs
S16	USA	Normal	Vs
Wolf River	USA	Inverse	Vs
Verzuolo	Italy	Inverse	Vs
Pisa Tower	Italy	Inverse	Vs
Mud A	USA	Normal	Vs-Ds
Mud B	USA	Normal	Vs-Ds

Table 5.1 : List of real sites that have been inverted.

5.3.1 Houston Levee Park

The site is located in Germantown, Tennessee (USA) not so far away from the Mississippi River (Hebeler, 2001).
The experimental test has been performed, by using a vertical harmonic shaker, operating in the range of frequency of interest, that is between 5-100 Hz divided into 57 points with a sampling frequency equal to 0.6250Hz. In order to evaluate the experimental dispersion curve, the vertical component has been considered and the procedure explained in Chapter 2 has been followed, so the experimental data are shown in fig. 5.6. It can be seen that the behavior of the experimental phase velocity is quite smooth and resembles the typical tendency of normally dispersive sites, in which the stiffness increases with depth. For the inversion

procedure, not all the calculated points of the experimental curve have been used, but only 15 frequencies have been selected.

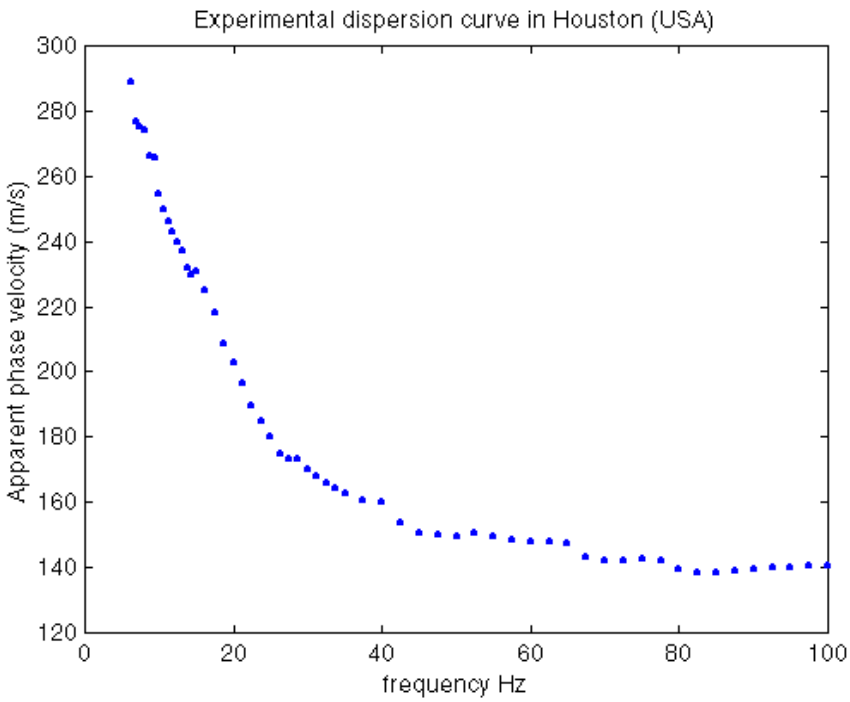

Figure 5.6: Experimental dispersion curve in Houston (USA)

This operation does not influence so much the accuracy of the inversion process, since it has been proved (Yuan and Nazarian, 1993) that, increasing the number of points beyond approximately (0.5 - 1.0)·D, where D is the number of the unknowns, only increases the computational cost of the inversion, without adding information to the dispersive characteristic of the medium.

For the inversion process the thicknesses were kept constant and the shear wave velocities were used as decision variables of the optimization. Also the mass density ρ and the P-wave velocities were fixed, since previous studies have demonstrated that these parameters influence the phase velocity less than 5% (Nazarian, 1984). For the P-wave velocities in the unsaturated layers a value equal to 1.5 times the S-wave velocities

has been assumed, that means a constant Poisson ratio of about 0.2. The following table summarizes the assumed parameters for the starting guess X_{01} for the optimization routine.

Layer	H	Vs	ν	ρ
	(m)	(m/s)	Poisson	(kg/m3)
1	2	140	0.2	1900
2	2	200	0.48	1900
3	2	210	0.48	1900
4	2	280	0.48	1900
5	3	300	0.48	1900
6	3	325	0.48	1900
7	3	330	0.48	1900
Half-space	∞	365	0.48	1900

Table 5.2: Initial configuration X_{01} for the Inversion.

After 25 iterations the final profile, that corresponds to the "optimal" solution is reported in the table 5.3.

Layer	h	Vs	Vp	ρ
	(m)	(m/s)	(m/s)	(kg/m3)
1	2	152	280	1900
2	2	226	400	1900
3	2	233	420	1900
4	2	288	560	1900
5	3	300	600	1900
6	3	320	650	1900
7	3	325	660	1900
Half-space	∞	353	730	1900

Table 5.3: Final configuration after the Inversion.

In fig. 5.7 both the experimental, the starting guess X_{01} and the "optimal" dispersion curves are illustrated. As it is evident, the starting guess is good enough, in fact the general trend of the experimental curve is quite similar. It must be observed that the final solution matches almost perfectly the experimental data.

In fig.5.8 it is also possible to visualize the variation of the objective function during the several iterations. As a confirmation of the fast convergence of the algorithm, just after the first 5 iterations the objective function decreases from about 4800 to 210, decreasing only to 137.6 in the successive 20 iterations.

Below are tabled the values of the objective function P and its gradient N for all the 8 variables for the initial guess X_{01} and for the last iterations.

Variables	N(initial guess)	N(optimum)
1	-405	0
2	-122	0
3	-54.9	-1.0
4	-13.9	-0.7
5	-8.6	0
6	-3.4	0
7	-1.7	0.03
8	-3.8	-0.3
Objective function value	4.80E+03	137.6

Table 5.4: Gradient of the Objective Function for the initial and the inverted configurations.

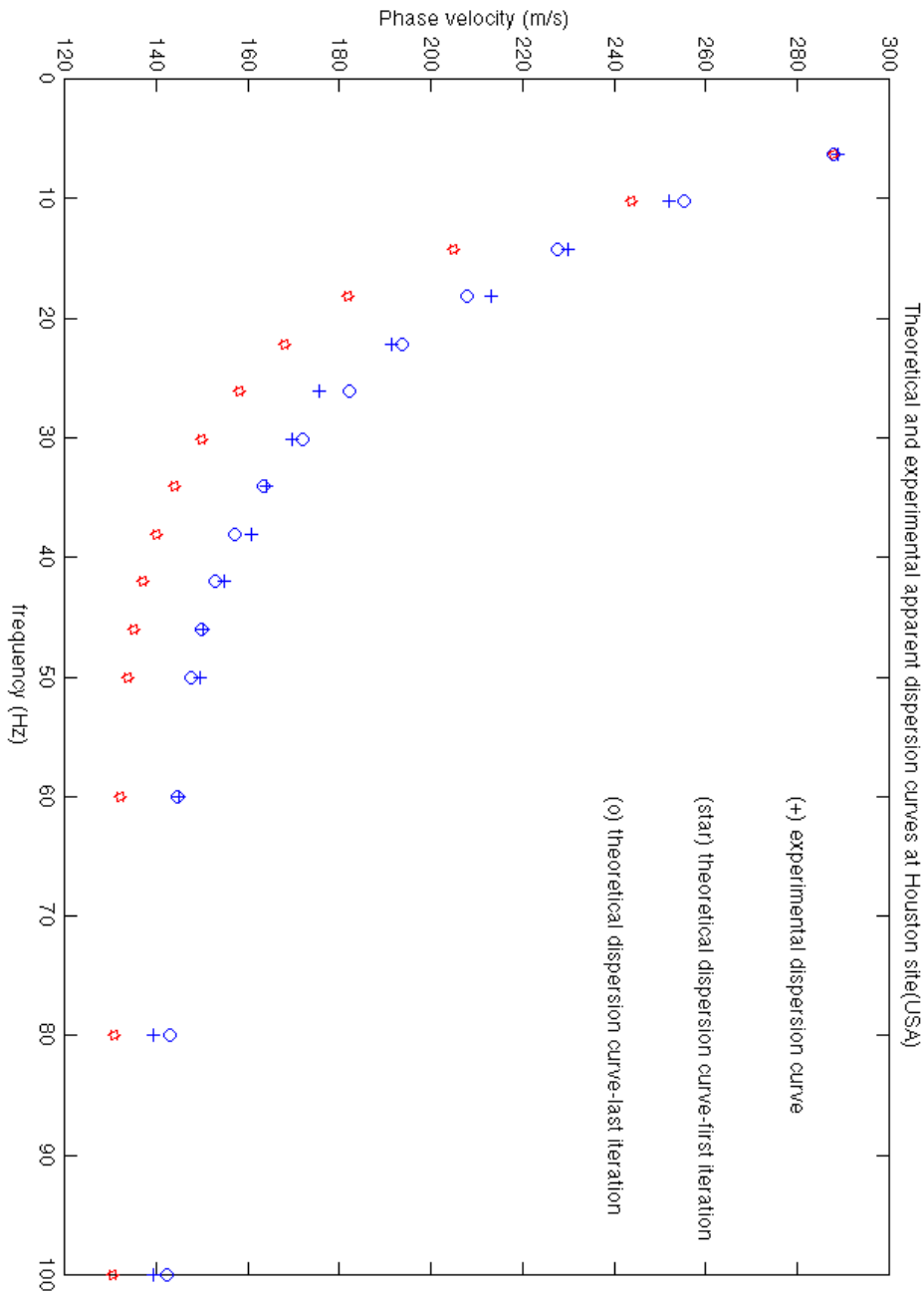

Figure 5.7: Experimental, initial guess X_{01} and "optimal" inverted dispersion curves .

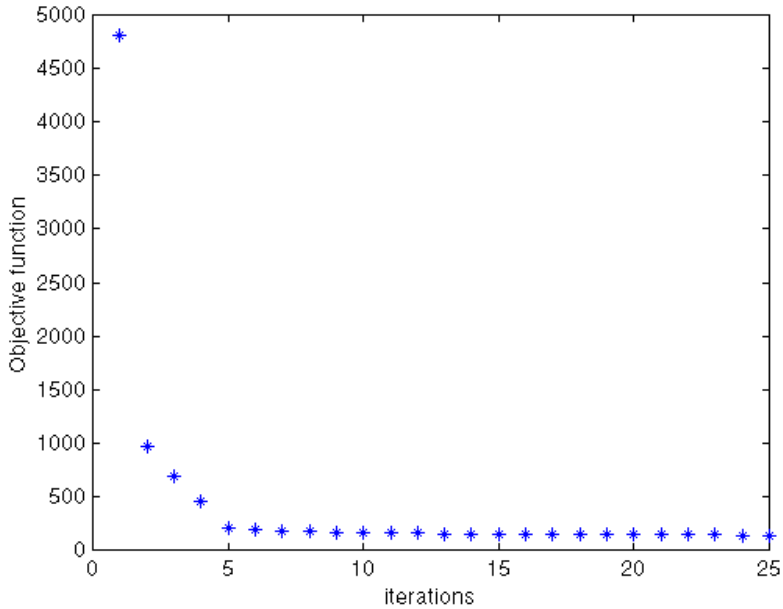

Figure 5.8: Reduction of the Objective Function with the number of iterations for initial guess X_{01}.

The low values of the components of the gradient represent a necessary condition for the optimality and, considering the decreasing trend, it can be said that the final configuration is not a maximum. In order to check if the final solution is a minimum rather than a saddle point, another initial guess has been considered, characterized this time by a dispersion curve above the experimental data, as visible in fig.5.9.
In the fig.5.9 the final iteration for the different initial guess X_{02} is also shown. Below in table 5.5 analogous considerations about the gradient of the objective function have been made as for the previous guess.

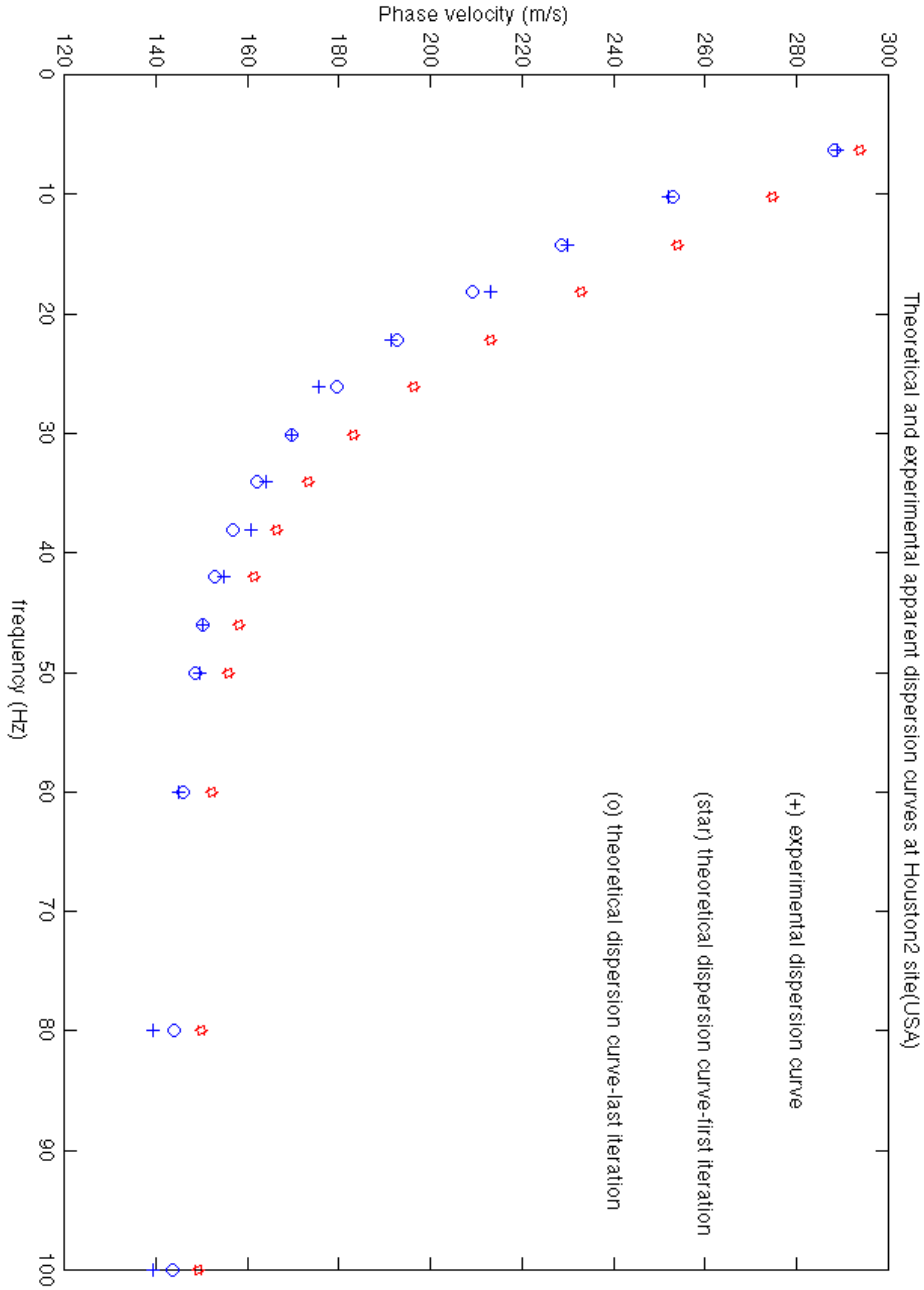

Figure 5.9: Experimental, initial guess X_{02} and "optimal" inverted dispersion curves .

Variables	N(initial guess)	N(optimum)
1	261	4.6
2	101	-1.5
3	45	-1.5
4	24.9	-1.0
5	19.8	-0.4
6	10.3	0.07
7	5.7	0.05
8	17.6	-2.0
Objective function value	3.1152e+003	101.8

Table 5.5: Gradient of the Objective Function for the initial and the inverted configurations.

In this second case the inversion process ended after 17 iterations and the trend of the objective functions is compared in the fig. 5.10 .
The following three considerations sum it all up:
1) the two objective functions converge to about the same value and they also present the same tendency, in fact they both decrease in the first 5 iterations
2) the convergence to the experimental curve has been obtained starting with both a curve above and below it and
3) it is reasonable to think of the found solution as a global optimum.

It is also interesting to observe in figures 5.11 and 5.12, the reduction of the relative error between the initial (stars) and the final curves (crosses) with respect to the experimental curve at all the frequencies for both cases X_{01} and X_{02}.
Even with this second starting configuration the variation of the velocities between the guess and the final solution is not relevant (see table 5.6)
Eventually we can say that the final configurations starting with two distinct initial guesses are very close to each other and the greatest differences concern the S-wave velocities of the intermediate layers.

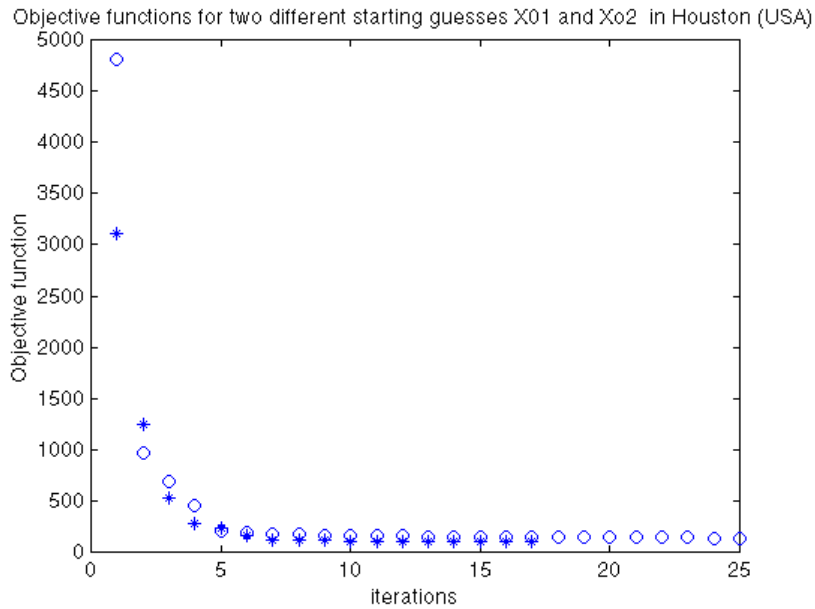

Figure 5.10: Comparison between objective functions for two different starting points X_{01} and X_{02}

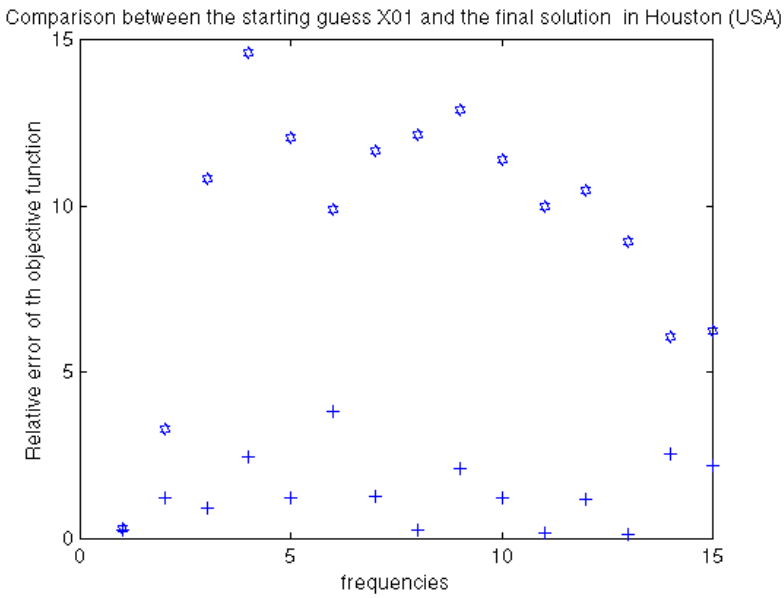

Figure 11: Relative distance between experimental and theoretical system responses at different frequencies for the initial (X_{01}) and inverted configurations.

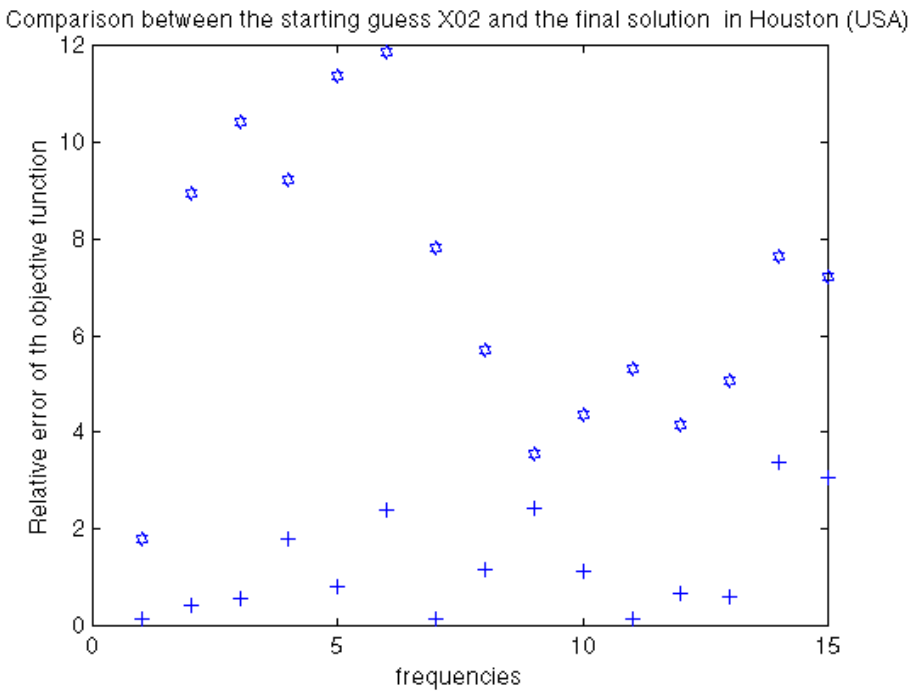

Figure 5.12: Relative distance between experimental and theoretical system responses at different frequencies for the initial (X_{02}) and inverted configurations.

Layer	Vs (m/s) Initial(X01)	Vs (m/s) Final(X01)	Vs (m/s) Initial(X02)	Vs (m/s) Final(X02)	Vs (m/s) Averaged
1	140	152	160	153	153
2	200	226	230	214	220
3	210	233	280	252	243
4	280	288	305	284	286
5	300	300	325	289	293
6	325	320	335	311	316
7	330	325	340	329	327
∞	365	353	345	357	355

Table 5.6: Comparison between the inverted profiles at Houston Leeve Park starting from two different initial configurations.

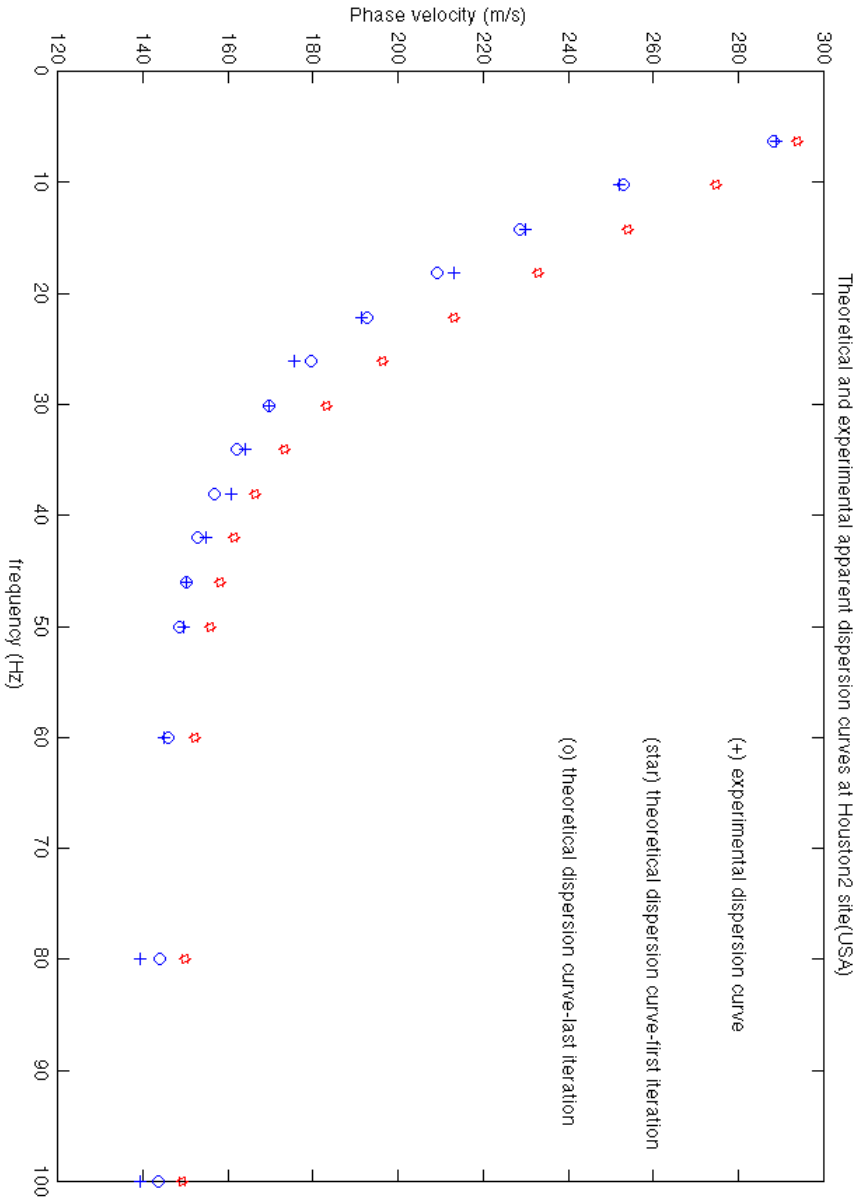

Figure 5.13: Comparison among the initial guess X_{01}, the final and the complete experimental dispersion curves.

This enables us to conclude that the apparent phase velocity is mostly influenced by the velocities of the layers that are located at great depth or at the surface of the half-space, whereas it is less sensitive to the variation of the velocities of the intermediate layers.
In fig. 5.14 how good the match of the complete experimental data is, even using a reduced number of points for the inversion process.
Finally we can show in fig.5.15 a comparison between the results obtained herein and those by Hebeler (Hebeler, 2001), who used the same experimental data, but a different inversion algorithm (Rix and Lai, 1998).
It can be observed that, beside some little discordance for the intermediate layers, the agreement is excellent and the two profiles present the same trend.

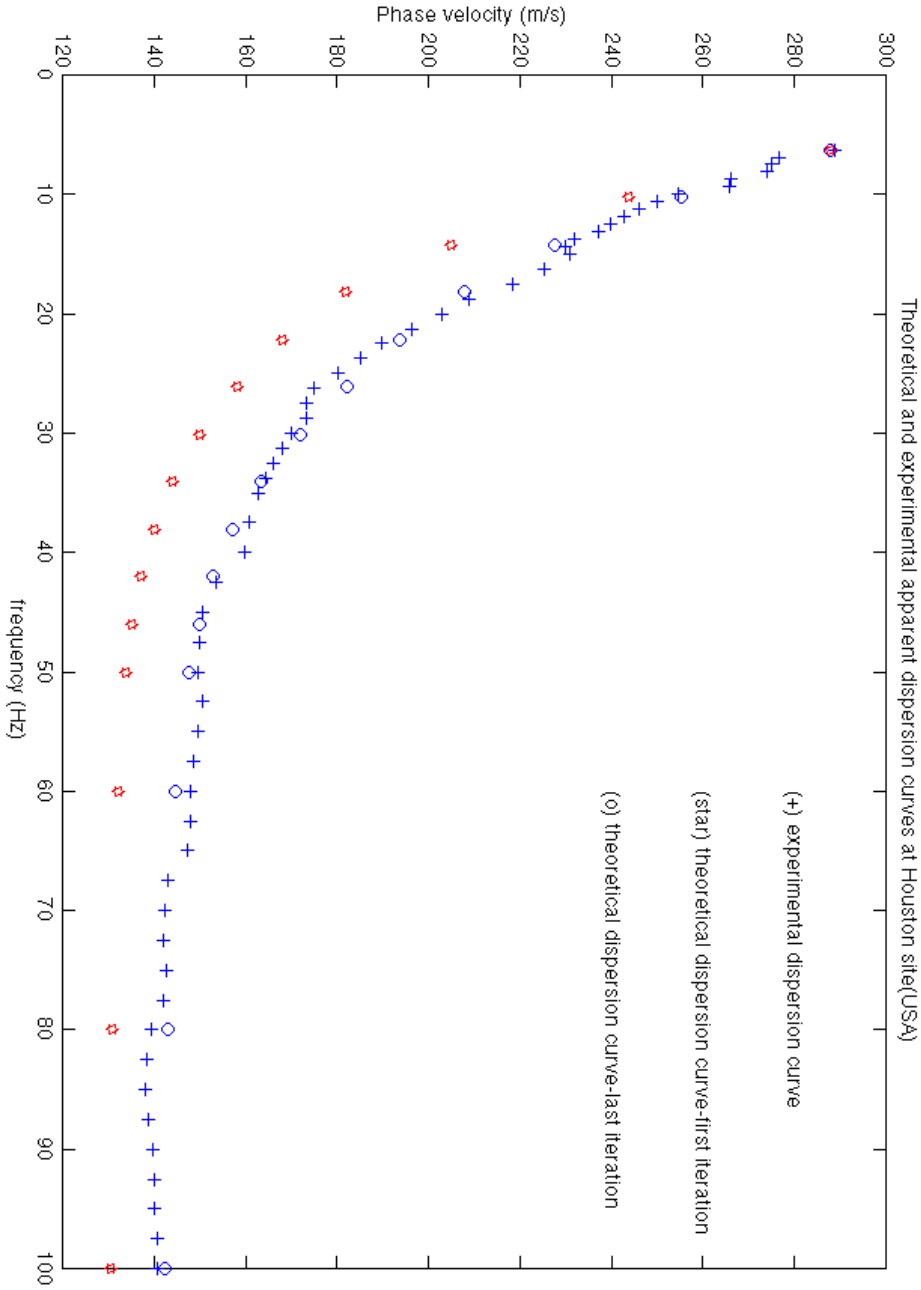

Figure 5.14: Comparison among the initial guess X_{01}, the final and the complete experimental dispersion curves.

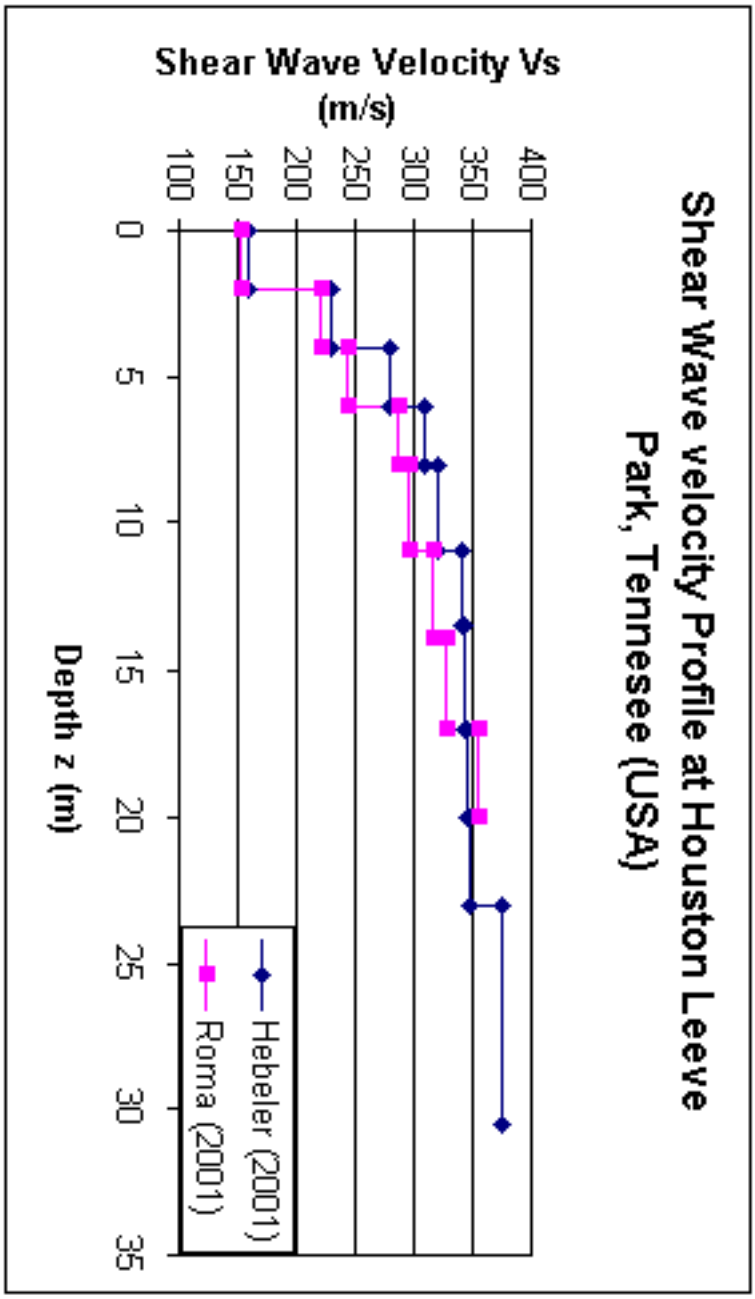

Figure 5.15: Comparison of the results with the analysis by Hebeler (Hebeler, 2001).

5.3.2 Street 16

This site, called S16, is located within the Shelby County, Tennessee, near the Memphis metropolitan area, where Dr. Ron Street of the University of Kentucky has investigated several other sites by seismic refraction methods (Street, 1999).
The experimental testing parameters consist of an array geometry of 16 accelerometers (zero means that the first accelerometer is mounted on the top of the source), given by the following positions vector expressed in meters:

x=[0 2.6667 3.3333 4.0000 5.0000 6.0000 7.3333 9.3333 11.3333 14.0000 16.6667 20.0000 23.3333 26.6667 31.6667 36.6667].

The frequency range is between 3.75 Hz and 100 Hz, with a varying spacing of $\Delta f = 0.625$ between 3.75 Hz –15 Hz , $\Delta f = 1.25$ Hz between 16.25Hz and 355 Hz and $\Delta f = 2.5$ Hz between 37.5 Hz and 100 Hz. The experimental dispersion curve (see fig.5.16) for Rayleigh waves has been gently provided by Prof. Rix and Hebeler (Hebeler, 2001) and it has been calculated by means of the procedure explained in Chapter 2 for harmonic source.
In fig.5.16 the dots represent the complete experimental dispersion curve, instead the circles represent the experimental points properly chosen for the inversion process. As can be observed, the data above 90 Hz have been discarded, since they have been judged not reliable and they do not add any important information about the stratigraphy.
The starting configuration for the shear wave velocities has been chosen by considering the trend of the experimental dispersion curve. In fact it makes someone think of a normally dispersive site, because the experimental phase velocity never increases considerably with frequency.
In table 5.5 both the initial and the finally inverted shear wave velocity profiles are reported (see fig.5.17) (Roma et al., 2002). After 11 iterations the objective function has decreased from 7000 to 800, proving the successful inversion (see fig.5.18).

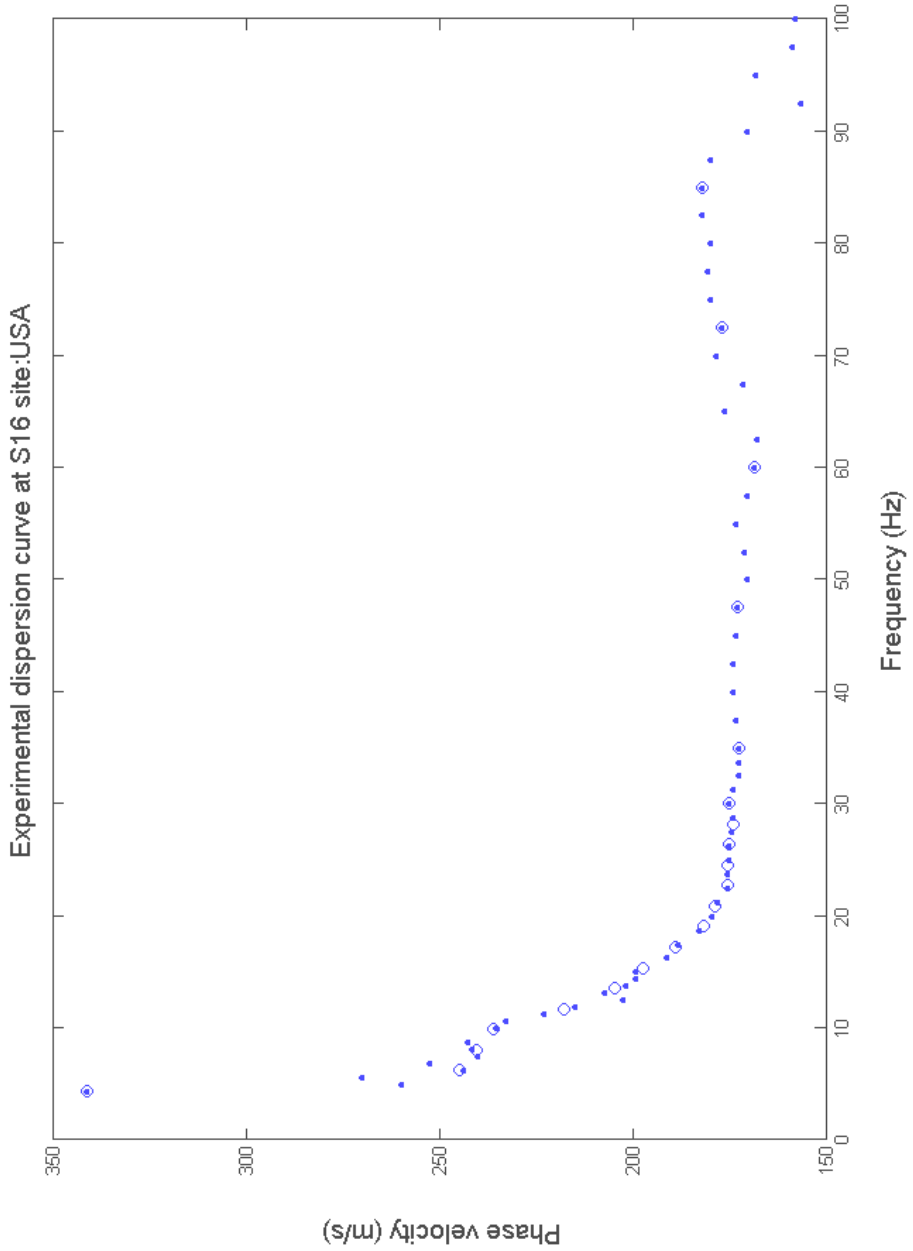

Figure 5.16: Experimental dispersion curve for Rayleigh waves at S16 site.

Layer	ρ(Kg/m^3)	h (m)	ν	Vs (m/s)	Vs (m/s)	Gs (MPa)
			Poisson	Initial	Final	Final
1	1900	3.5	0.2	180	188	67
2	1900	3	0.48	200	244	113
3	1900	5	0.48	250	279	148
4	1900	3.5	0.48	300	279	148
5	1900	5.5	0.48	400	377	270
6	1900	9.5	0.48	500	482	441
7	1900	7.7	0.48	600	596	675
Half-space	1900	∞	0.48	800	796	1204

Table 5.5: Results of the Inversion process at S16 site (USA).

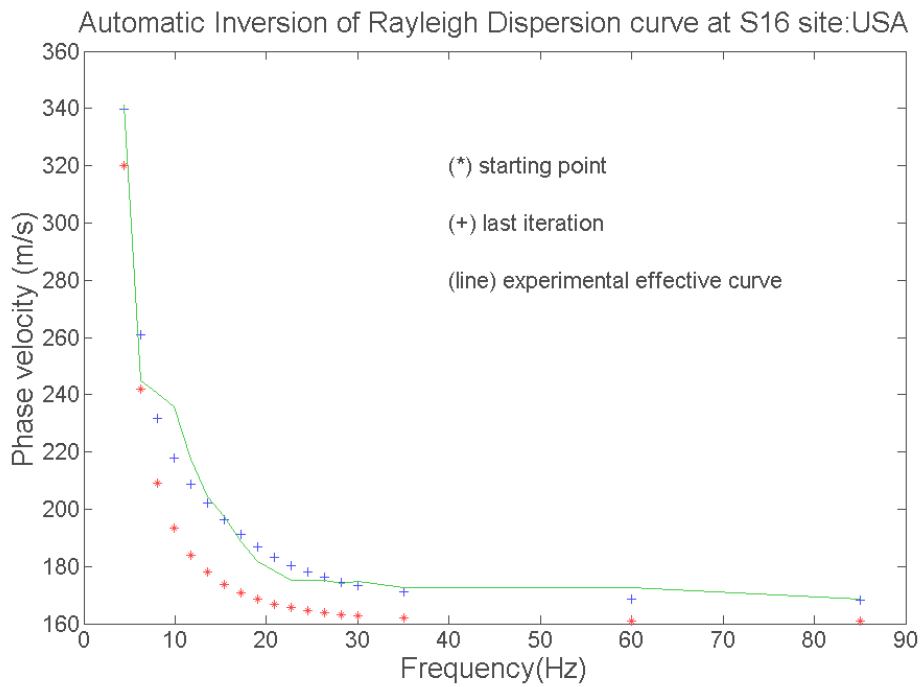

Figure 5.17: Experimental dispersion curve (green bold line), starting (red stars) and final (blue crosses) theoretical dispersion curves at S16 site.

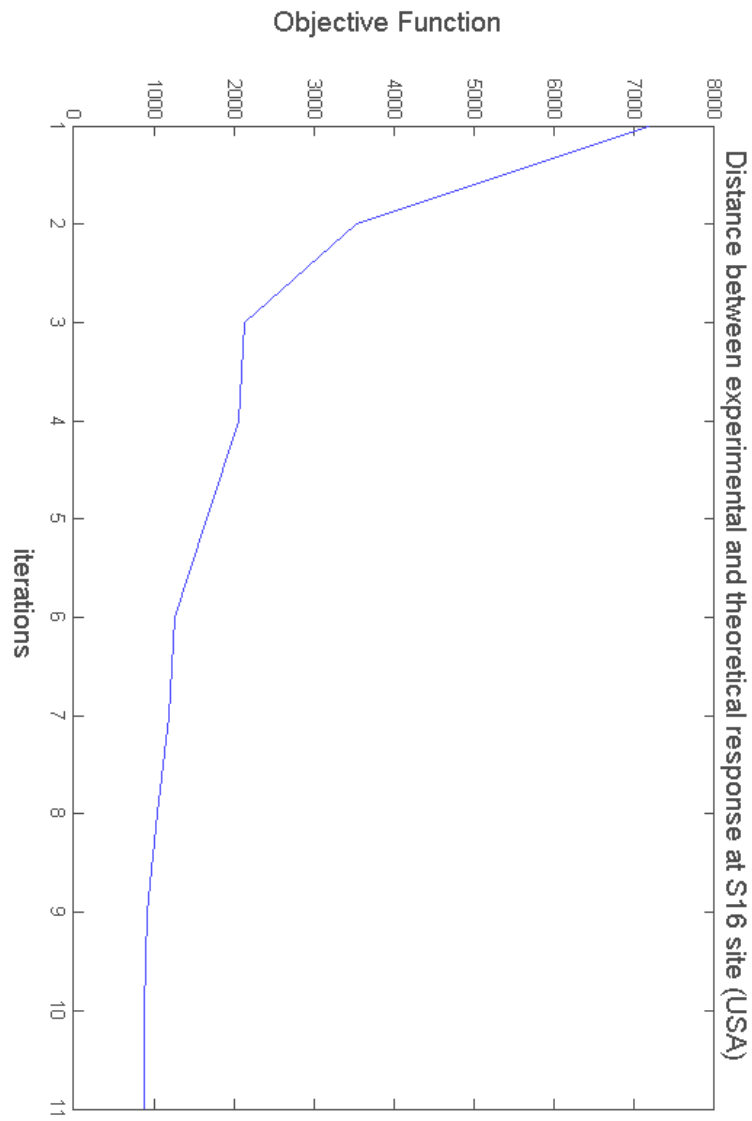

Figure 5.18: Objective Function reduction during the Inversion process at S16 site.

For this site alternative investigations and analyses are available. Precisely in fig.5.19 the interpretations of the seismic refraction results (blue line with triangles) by Prof. Street (Street, 1999) and the inversion of Multichannel SASW (black line with rhombus) by Hebeler (Hebeler, 2001) are plotted together with the final profile, obtained by the author. It should be underlined that the identifications of the sites by Hebeler, based on Multichannel SASW, are performed by means of a inversion algorithm, which is different from that one used in this thesis. The following fundamental differences in the procedures exist:

1) The algorithm used by Hebeler (Lai and Rix, 1998) makes use of the effective phase velocity concept as system response. The effective phase velocity depends on distance from the source and a spatially averaged value is assumed for the system response. Instead the inversion procedure used in this thesis uses the apparent phase velocity, which is the result of a 1D Fourier transformation of the wave field from the frequency-space domain to the frequency-wave number domain.
2) The algorithm used by Hebeler (Lai and Rix, 1998) states the inversion problem differently from the algorithm presented in this thesis. The two non-linear constrained optimization problems are mathematically different, as well as the optimization algorithms, that are used for solving the mathematical inverse problem. In this thesis the penalty method associated with the Davidon-Fletchell-Powell method is used. In the algorithm used by Hebeler is based on a paper by (Constable et al 1987).

From the fig.5.19 a perfect agreement among the several results can be noticed down to a depth of about 8m. Below the depth of 8m the seismic refraction results differs from the profiles obtained by Hebeler and the author.

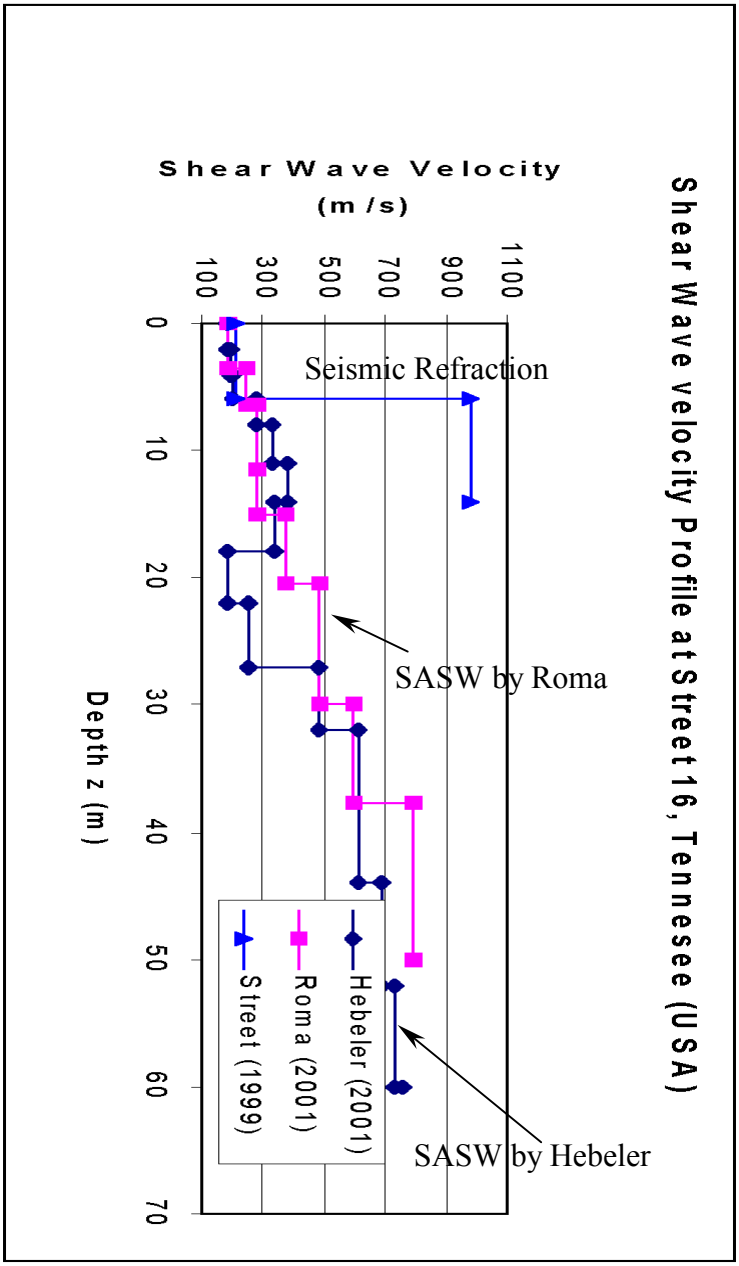

Figure 5.19: Comparison among different analyses and investigations at S16 site.

5.3.3 Wolf River

The Wolf River site is located near the Shelby Farms park, approximately 30 m north from the Wolf River. The frequency subintervals for the experiment are the same adopted at S16 site and so is the configuration of the receivers. The experimental dispersion curve (dots) shows an inversely dispersive trend, as it can be observed in fig.5.20, where the theoretical dispersion curve (circles) corresponding to the last iteration is also illustrated. The table 5.6 and fig. 5.21 and fig.5.22 summarize the results of the inversion process:

Layer	ρ(Kg/m^3)	h (m)	ν	Vs (m/s)	Vs (m/s)	Gs (MPa)
			Poisson	Initial	Final	Final
1	1900	3.5	0.2	180	188	67
2	1900	3	0.48	200	244	113
3	1900	5	0.48	250	279	148
4	1900	3.5	0.48	300	279	148
5	1900	5.5	0.48	400	377	270
6	1900	9.5	0.48	500	482	441
7	1900	7.7	0.48	600	596	675
Half-space	1900	∞	0.48	800	796	1204

Table 5.6: Results of the Inversion process at Wolf River site (USA).

In fig.5.22 the results of the Seismic Cone Penetration Test (CPTU) (Schneider, 1999) are plotted together with the profile identified by means of the algorithm, which has been developed in this thesis. The two profiles show a good agreement, especially in the upper side of the ground.

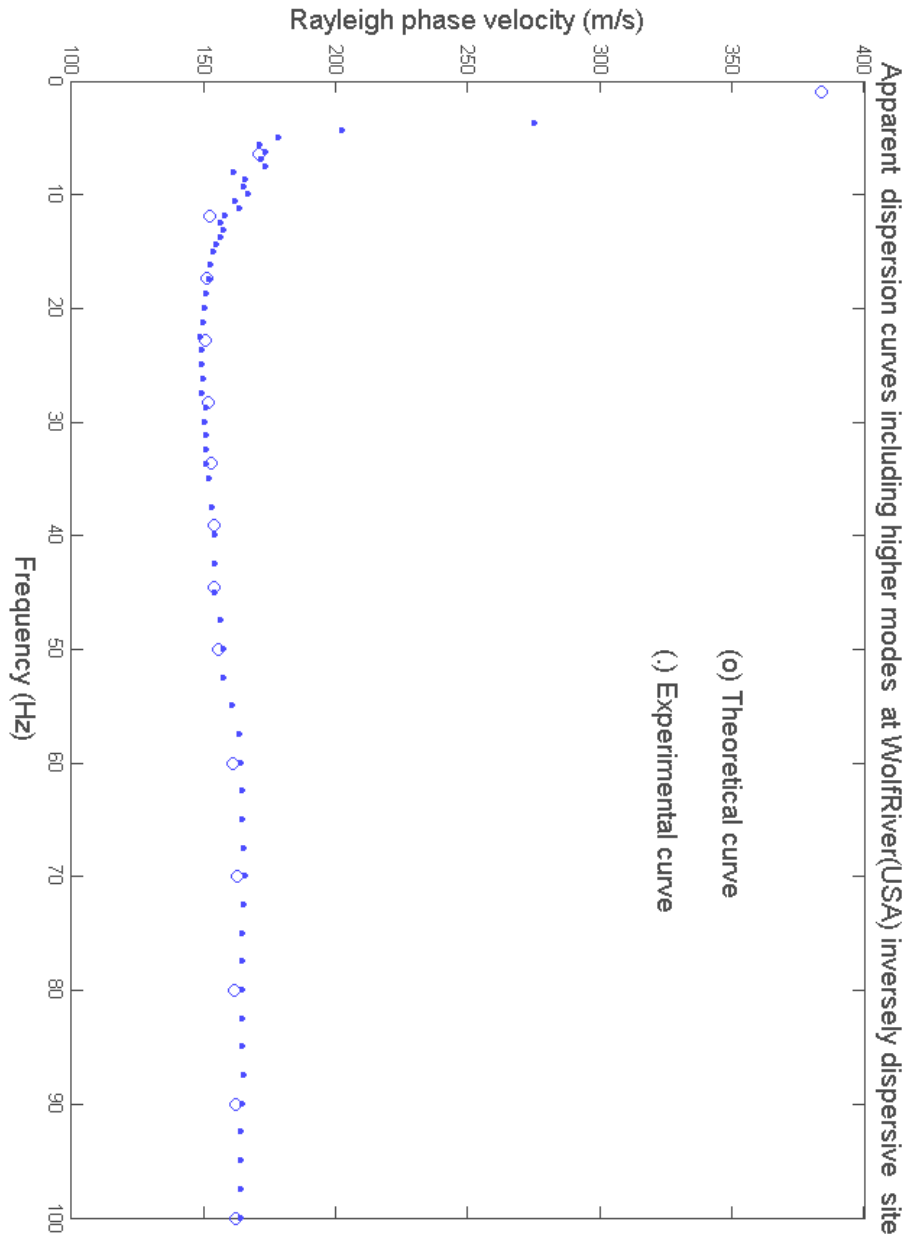

Figure 5.20: Experimental and theoretical responses at Wolf River site (USA).

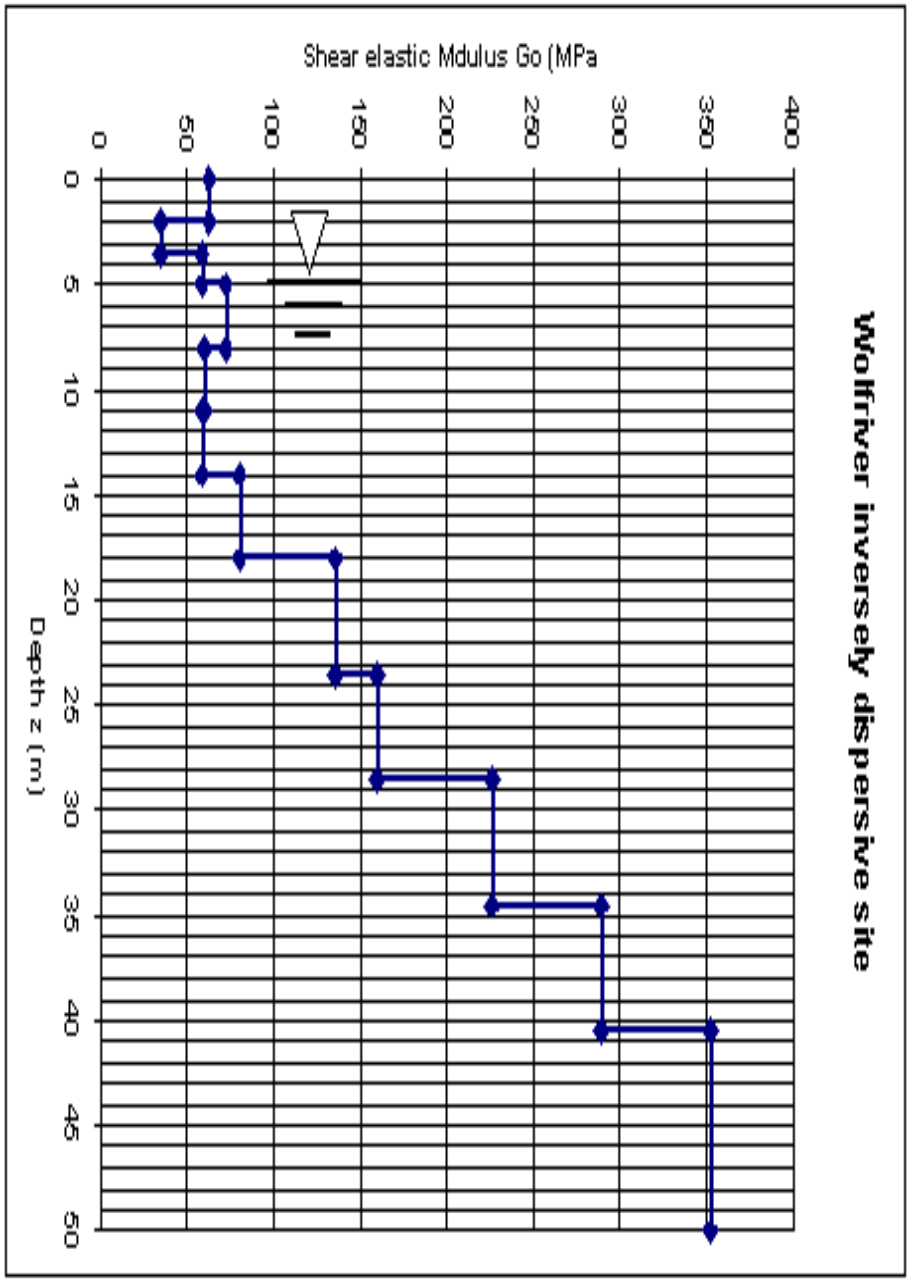

Figure 5.21: Inverted shear Modulus profile at Wolf River site (USA).

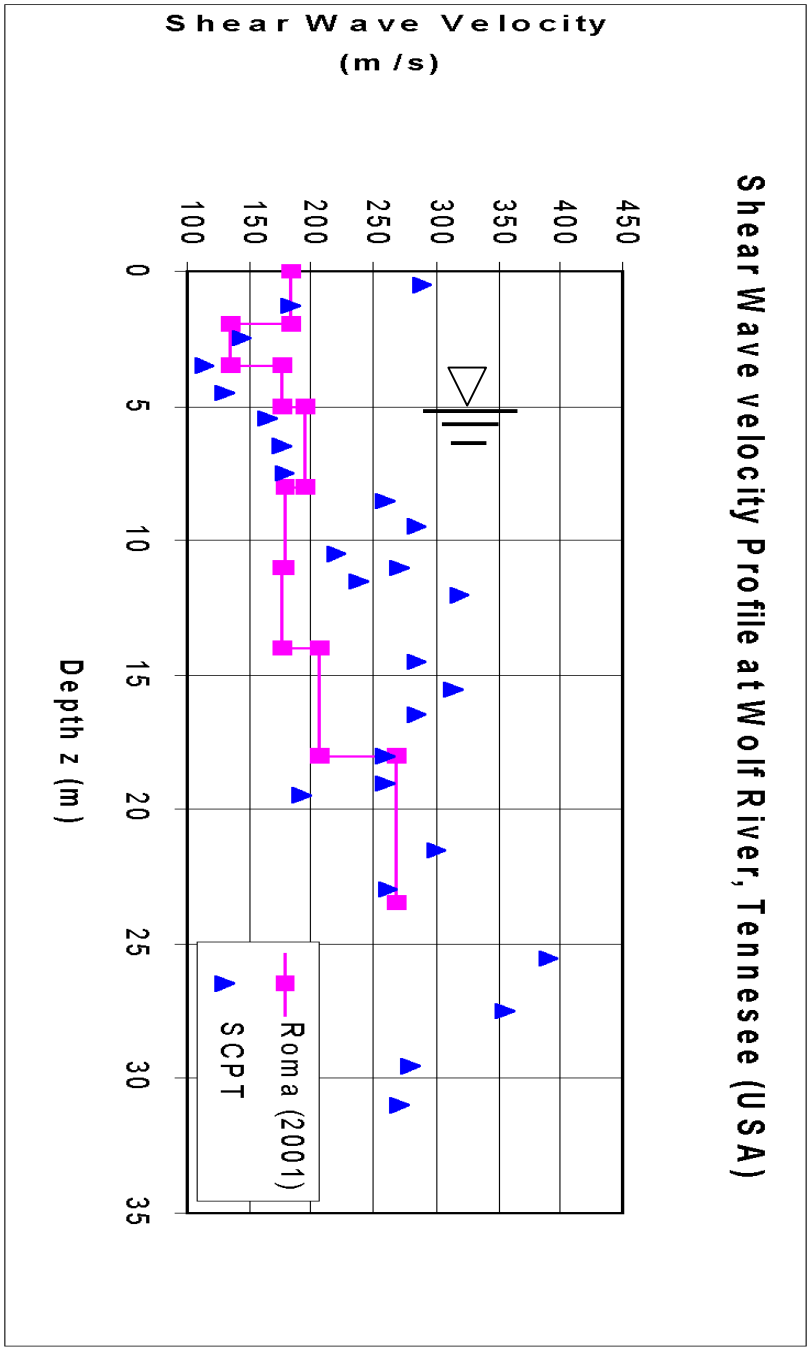

Figure 5.22: Inverted shear wave velocity profile at Wolf River site (USA).

Since this site is inversely dispersive it is interesting to make some considerations about the relative importance of the Rayleigh modes.
In fig.5.23 the experimental and theoretical dispersion curves are represented in the f-k domain. As it can be revealed by fig.5.24 the global response of the system (either experimental or theoretical) coincides with the fundamental Rayleigh mode up to a frequency of about 55 Hz (or equivalently until a wave number of about 2.4 rad/m) and then transits towards the 2nd mode of Rayleigh. The same observation can be made looking at the Rayleigh Dispersion Relation in terms of phase velocity in fig.5.25 on the frequency axe and in fig.5.26 on the wave number axe.
As it has been explained in Chapter 2 a very clear way for understanding the transition of predominance from the fundamental mode towards the higher modes of Rayleigh is given by the normalized spectra of the modal energy or displacements (see fig.5.27 and fig.5.28).

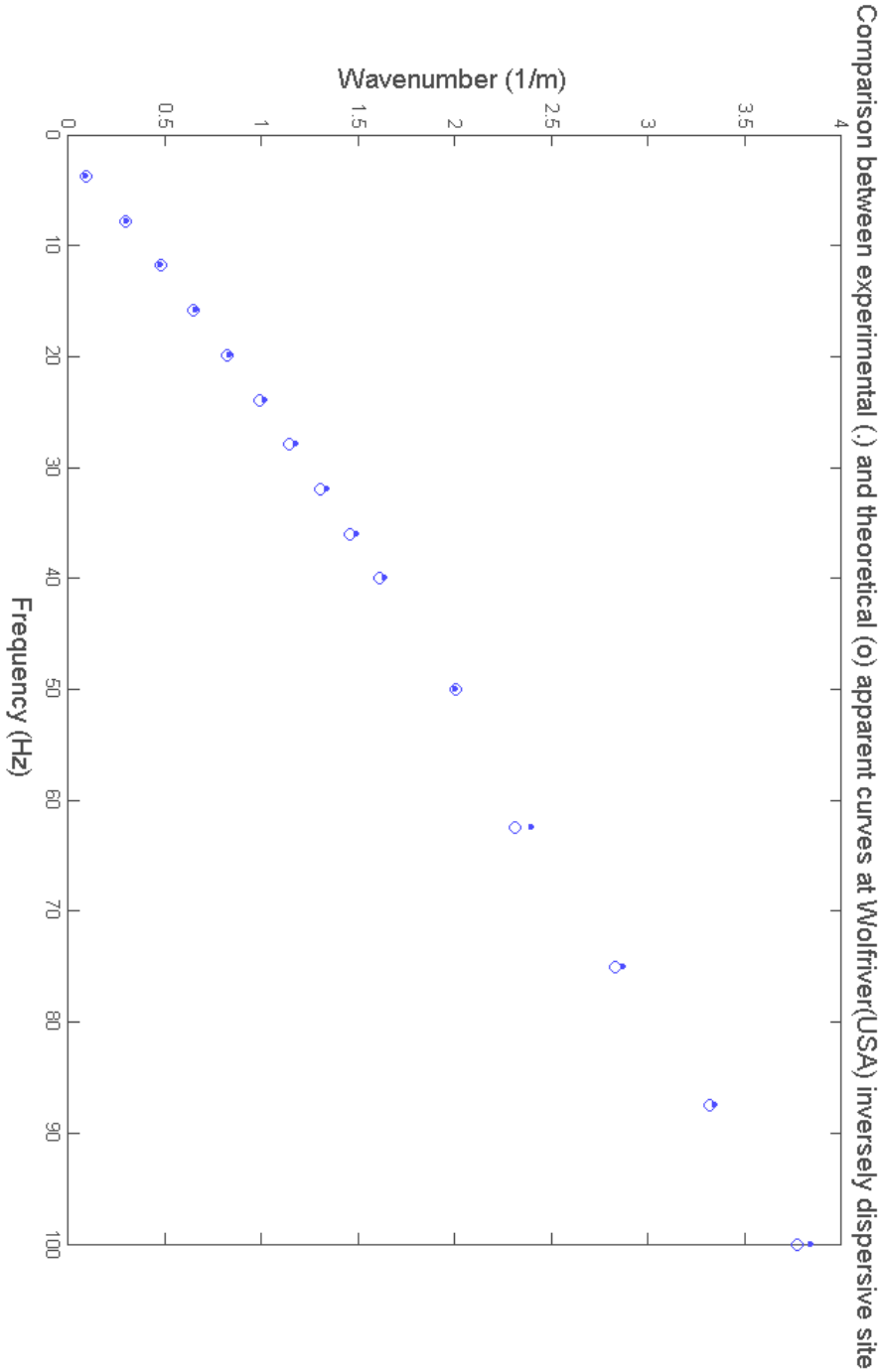

Figure 5.23: Experimental (dots) and theoretical (circles) responses at Wolf River site.

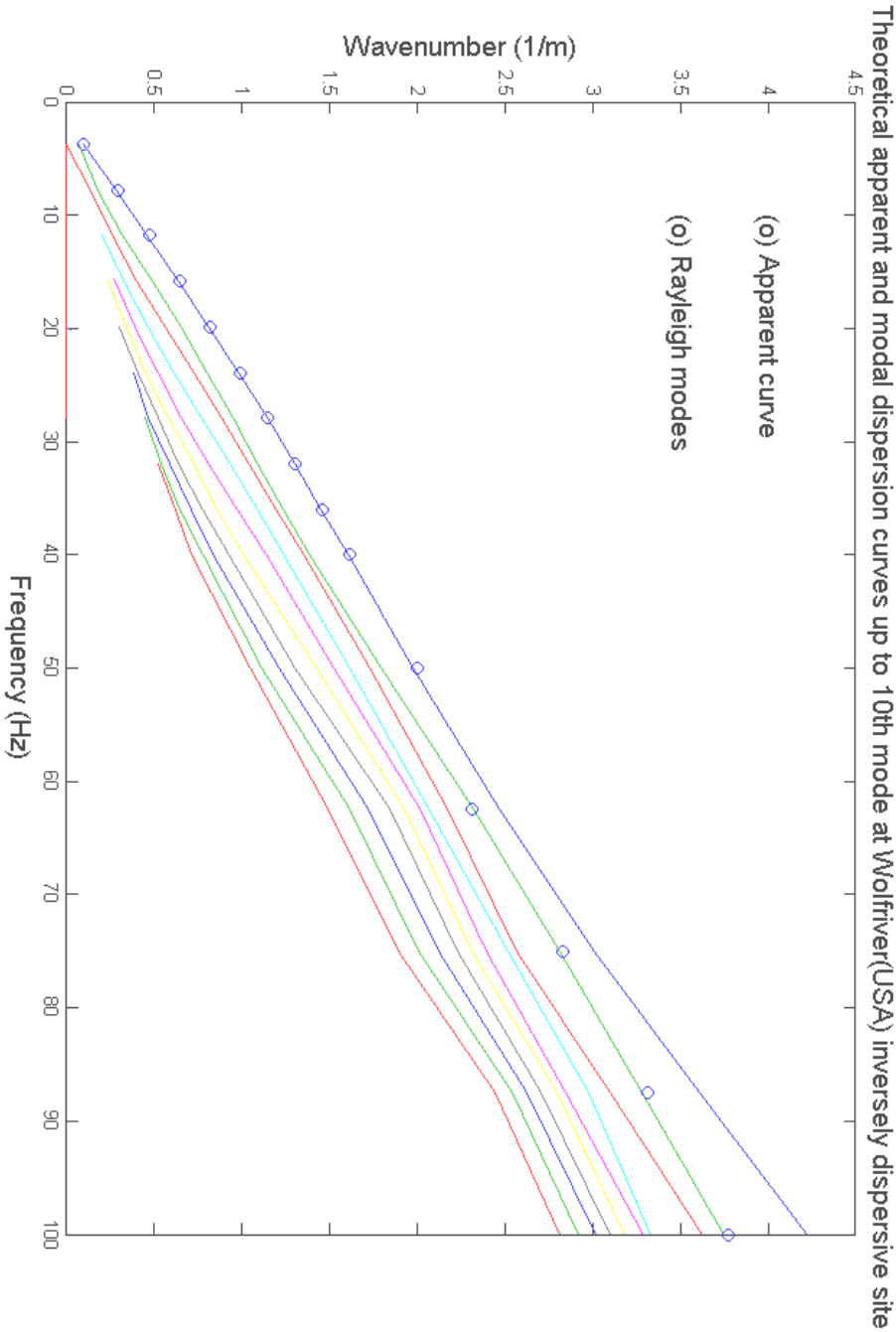

Figure 5.24: Experimental dispersion curve (dots) and theoretical Rayleigh modes at Wolf River site.

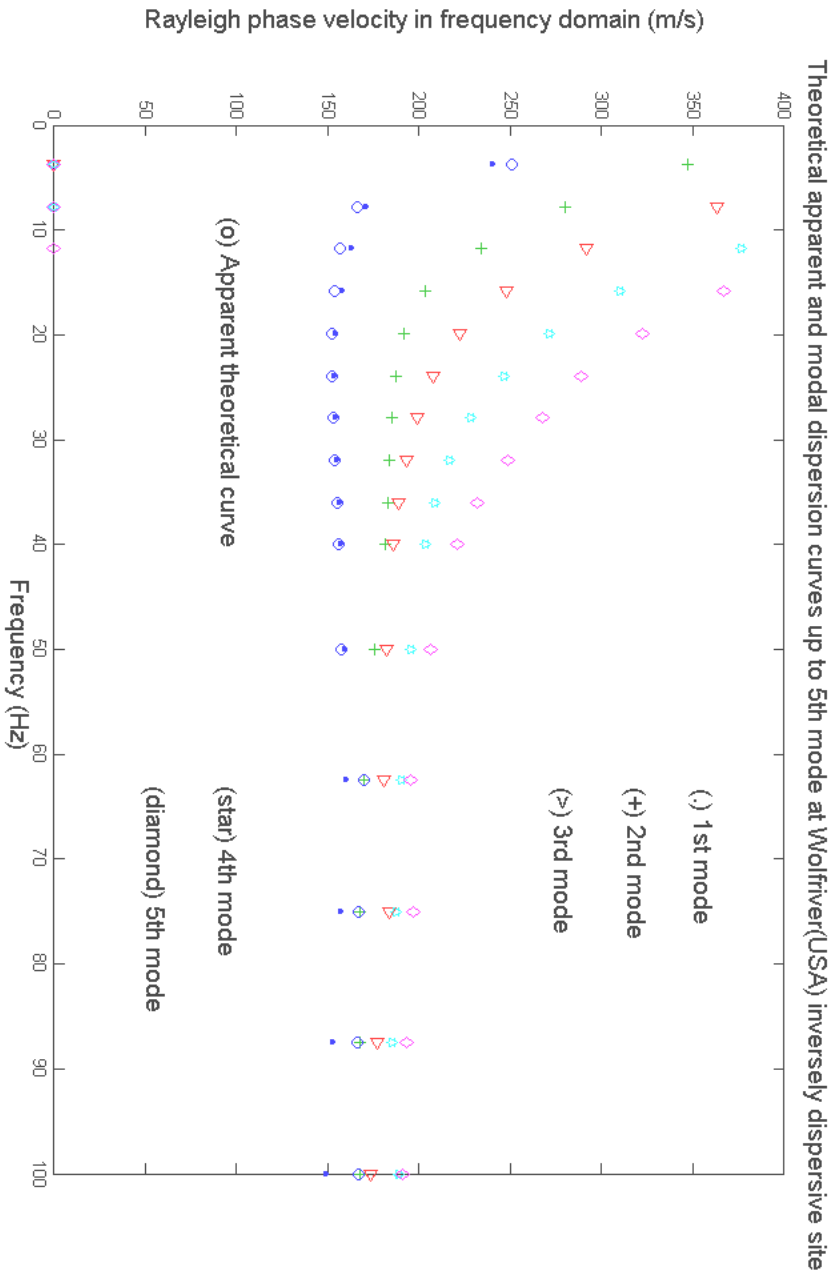

Figure 5.25: Global response (circles) and theoretical Rayleigh modes at Wolf River site.

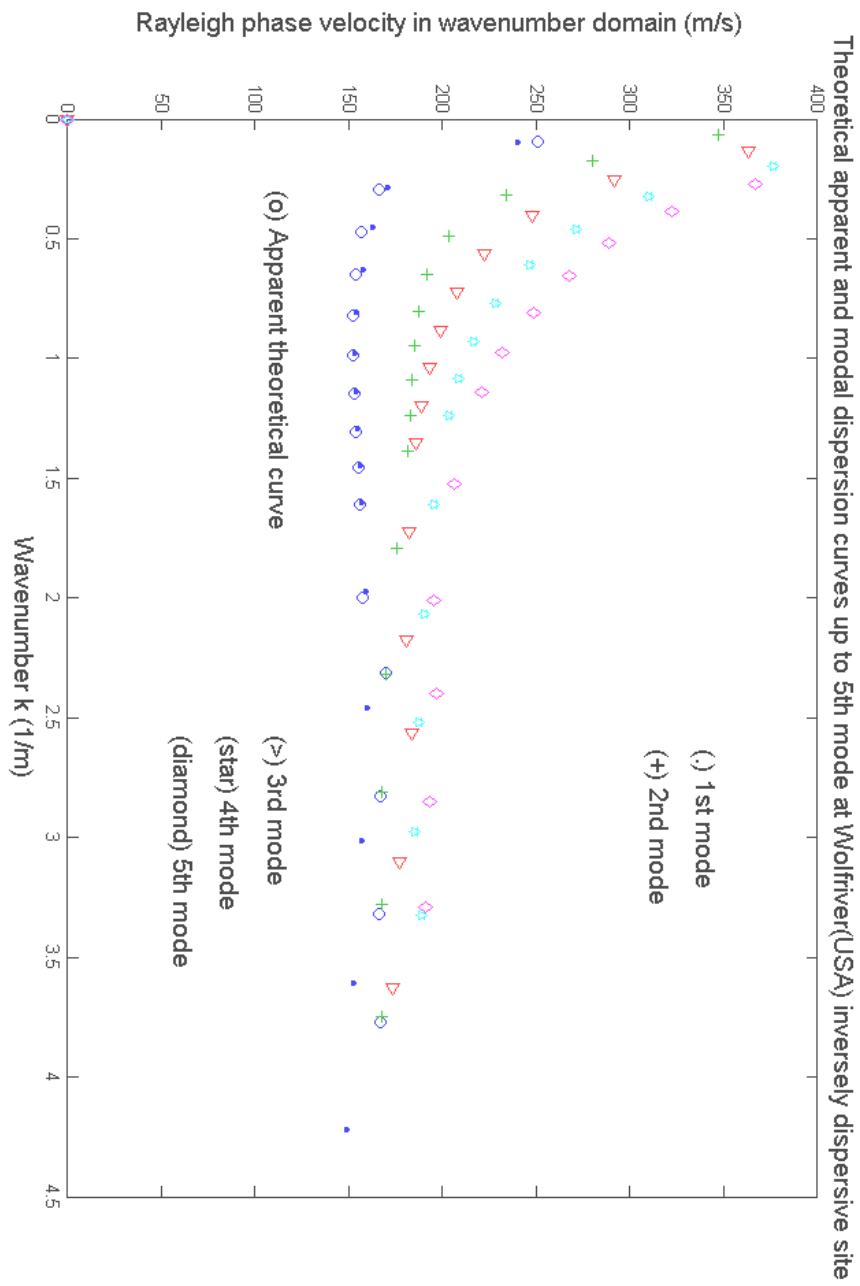

Figure 5.26: Global response (circles) and theoretical Rayleigh modes at Wolf River site.

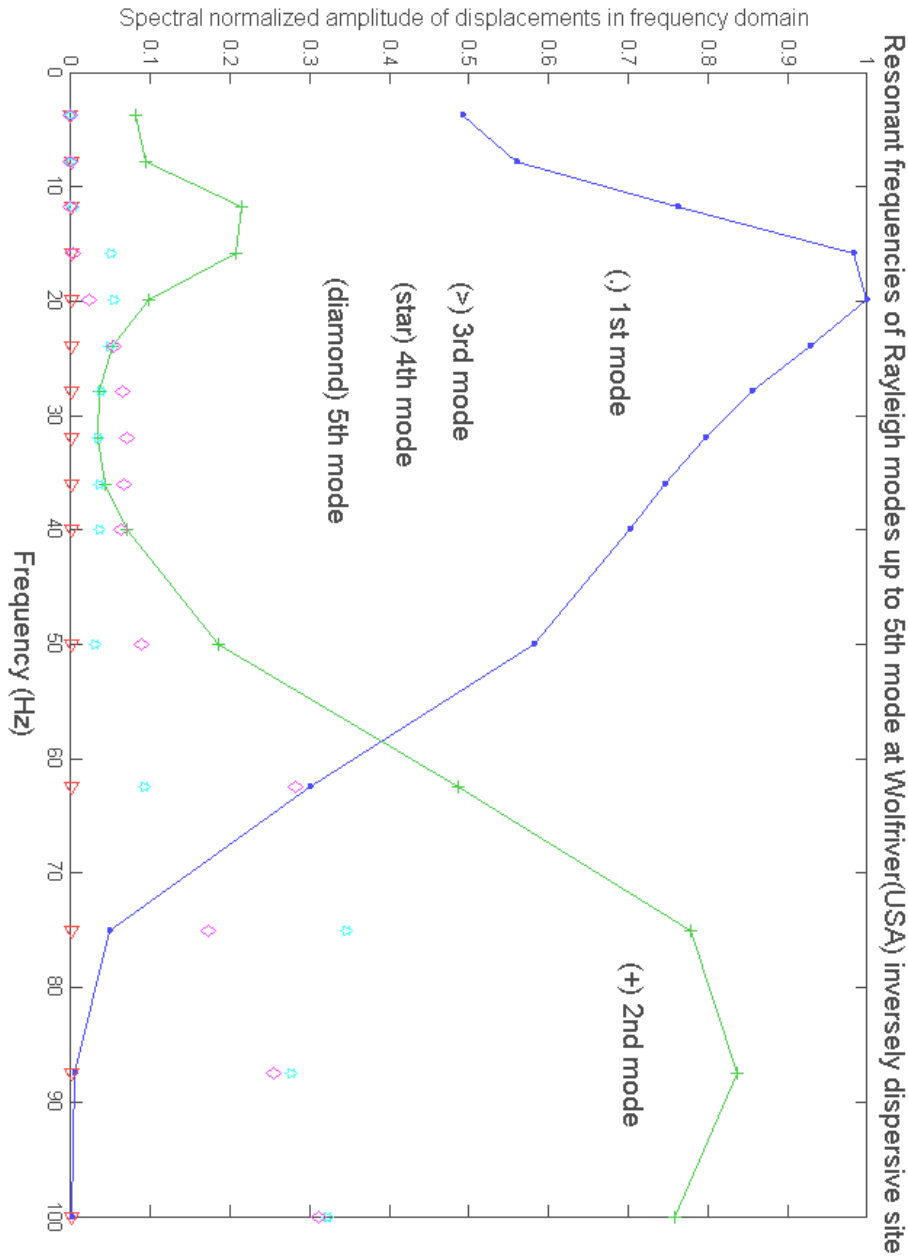

Figure 5.27: Relative importance of Rayleigh modes as a function of the frequency of excitation.

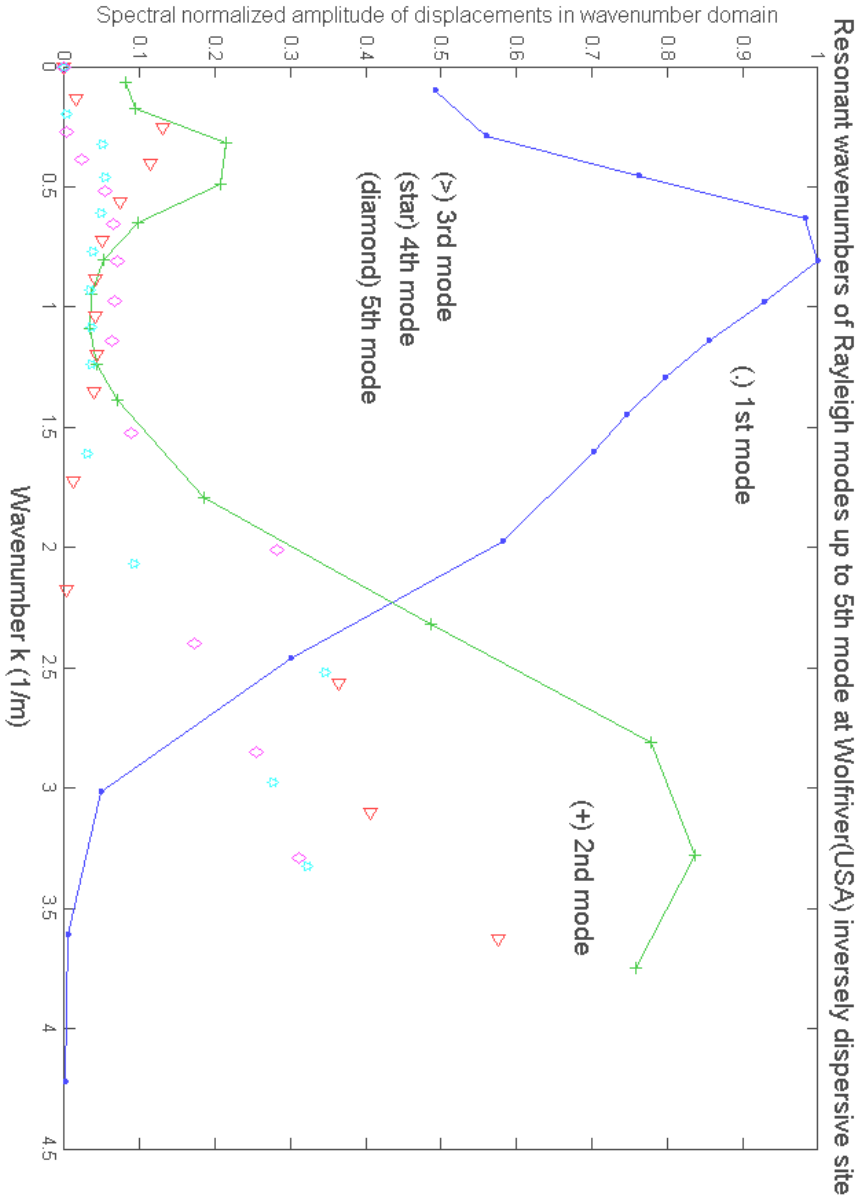

Figure 5.28: Relative importance of Rayleigh modes as a function of the wave number of excitation.

5.3.4 Verzuolo

Verzuolo (CN, Italy) site is located in the north-west of Italy and the geotechnical characterization serves the planning and the construction of a cogeneration plant, acting in combined cycle of approximately 120 MW for the production of electrical energy and steam. The plant, constructed by Fiat Engineering SPA, in association with General Electric-Nuovo Pignone on the premises of the Burgo paper-mill, consists of two General Electric MS 6001 B turbines, a Nuovo Pignone EHNK 50/90 steam turbine and two steam generators operating on two levels of pressure.
Specifically the Author has worked on the dynamic design of the foundations of the thermo-electric power plant, during the 2000 for Ingegneria Geotecnica firm in Turin (Italy).

Layer	ρ(Kg/m^3)	h (m)	ν	Vs (m/s)	Vs (m/s)	Gs (MPa)
			Poisson	Initial	Final	Final
1	1900	3.5	0.2	180	188	67
2	1900	3	0.48	200	244	113
3	1900	5	0.48	250	279	148
4	1900	3.5	0.48	300	279	148
5	1900	5.5	0.48	400	377	270
6	1900	9.5	0.48	500	482	441
7	1900	7.7	0.48	600	596	675
Half-space	1900	∞	0.48	800	796	1204

Table 5.6: Results of the Inversion process at Verzuolo site (Italy).

For this site the impulsive source illustrated in fig.5.1 has been adopted and the seismograph ABEM Terraloc MK6 with 24 vertical geophones SENSOR model SM-6/U-B (natural frequency 4.5 Hz) already described in the previous sections of this Chapter. As a consequence the experimental dispersion curve in fig.5.29 has been calculated by means of the spectrum of the measured velocities as has been explained in Chapter 2.
The experimental dispersion curve and the theoretical simulation at the last iteration are reported in fig.5.30, whereas the inverted profile is described in table 5.6 above and graphically represented in fig. 5.33.

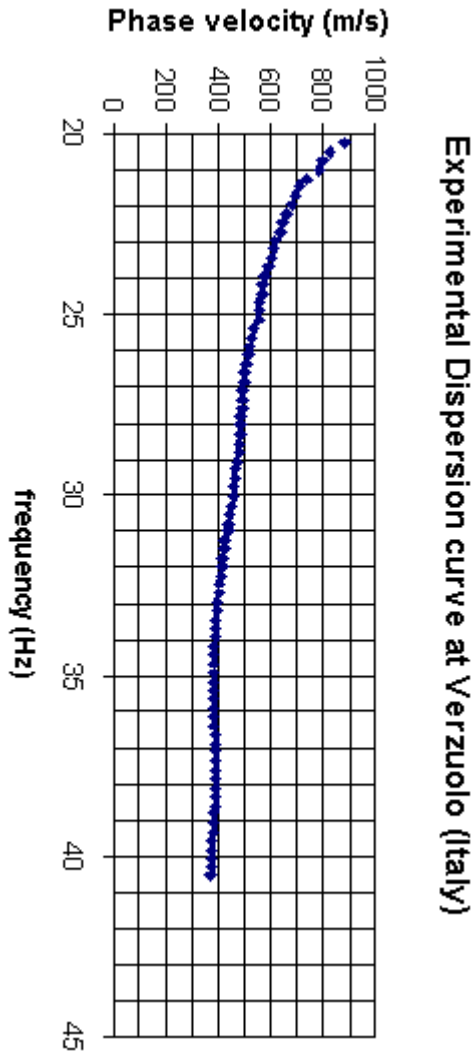

Figure 5.29: Experimental dispersion curve at Verzuolo site (Italy).

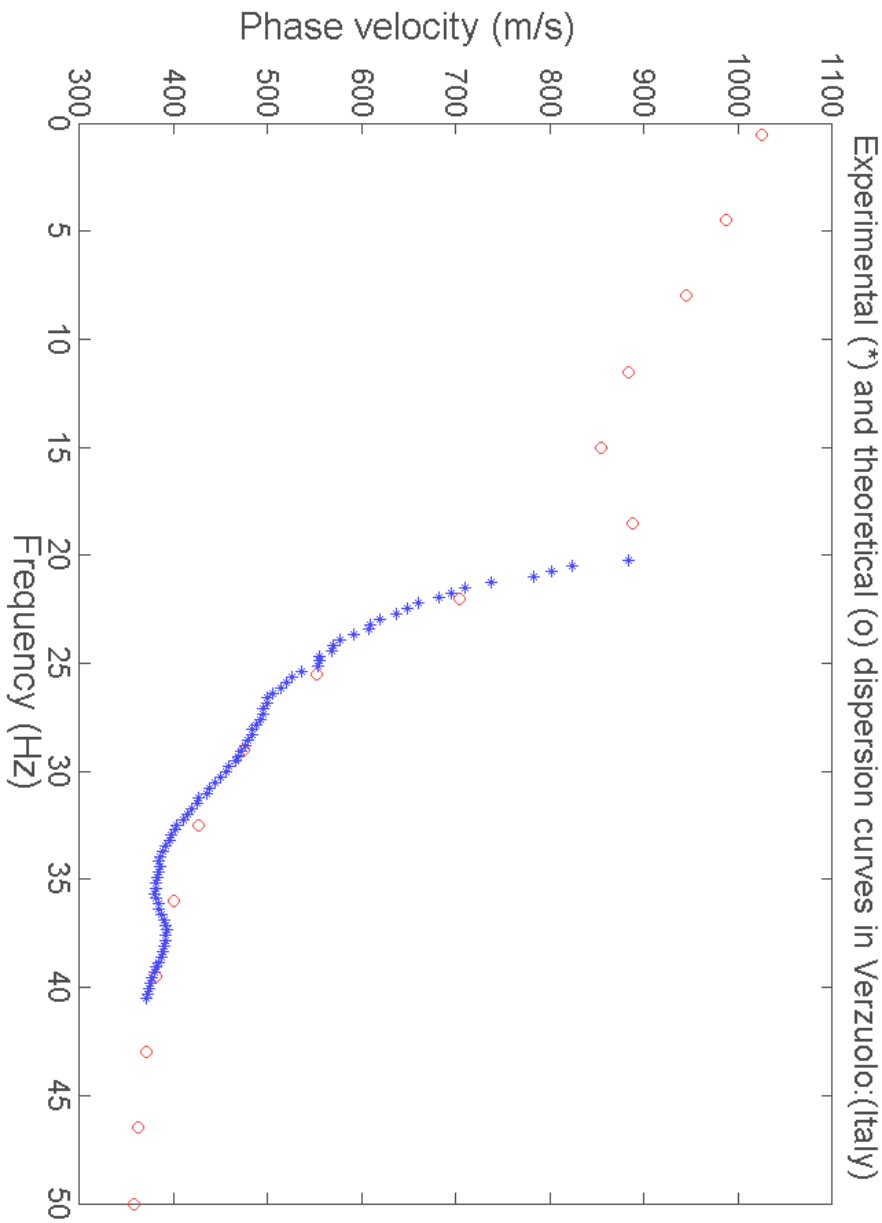

Figure 5.30: Inversion results at Verzuolo site (Italy): experimental (crosses) and theoretical (circles) system responses.

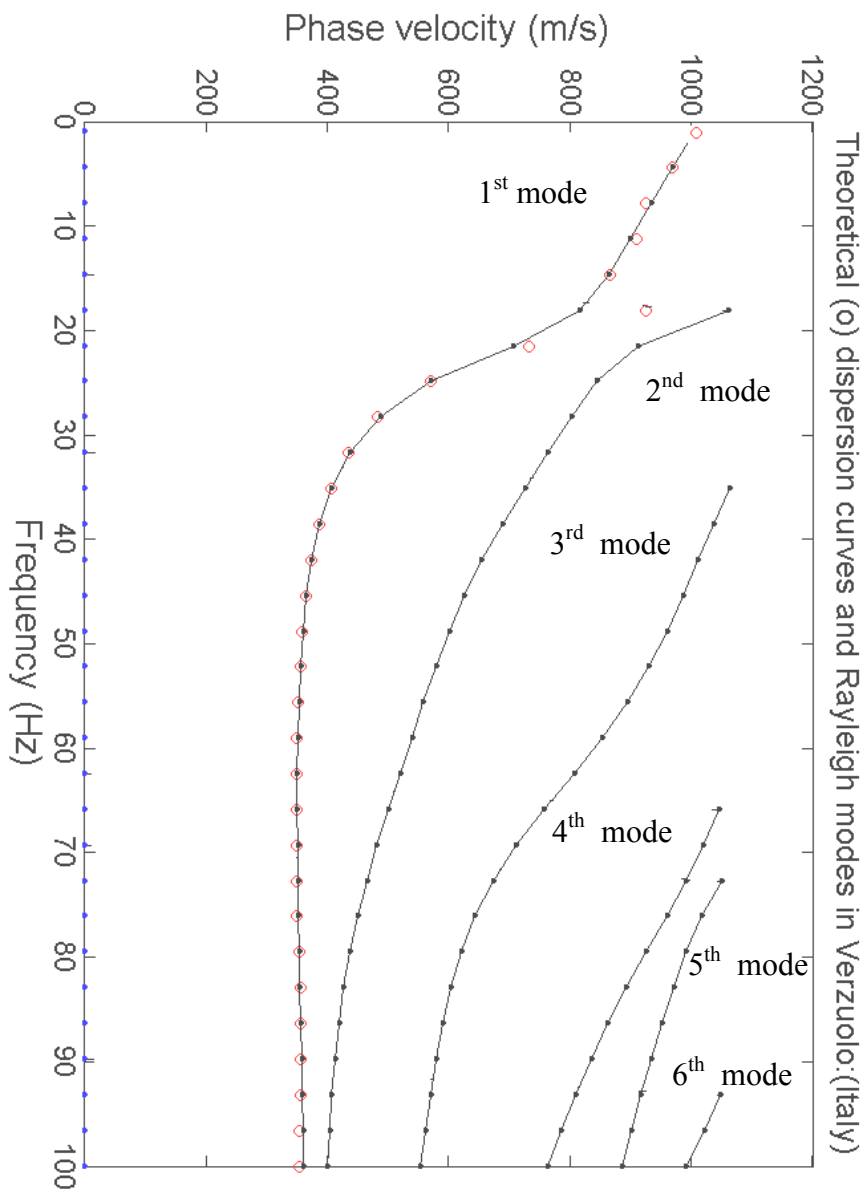

Figure 5.31: Rayleigh modes (solid lines) and theoretical apparent dispersion curve (circles) at Verzuolo site (Italy).

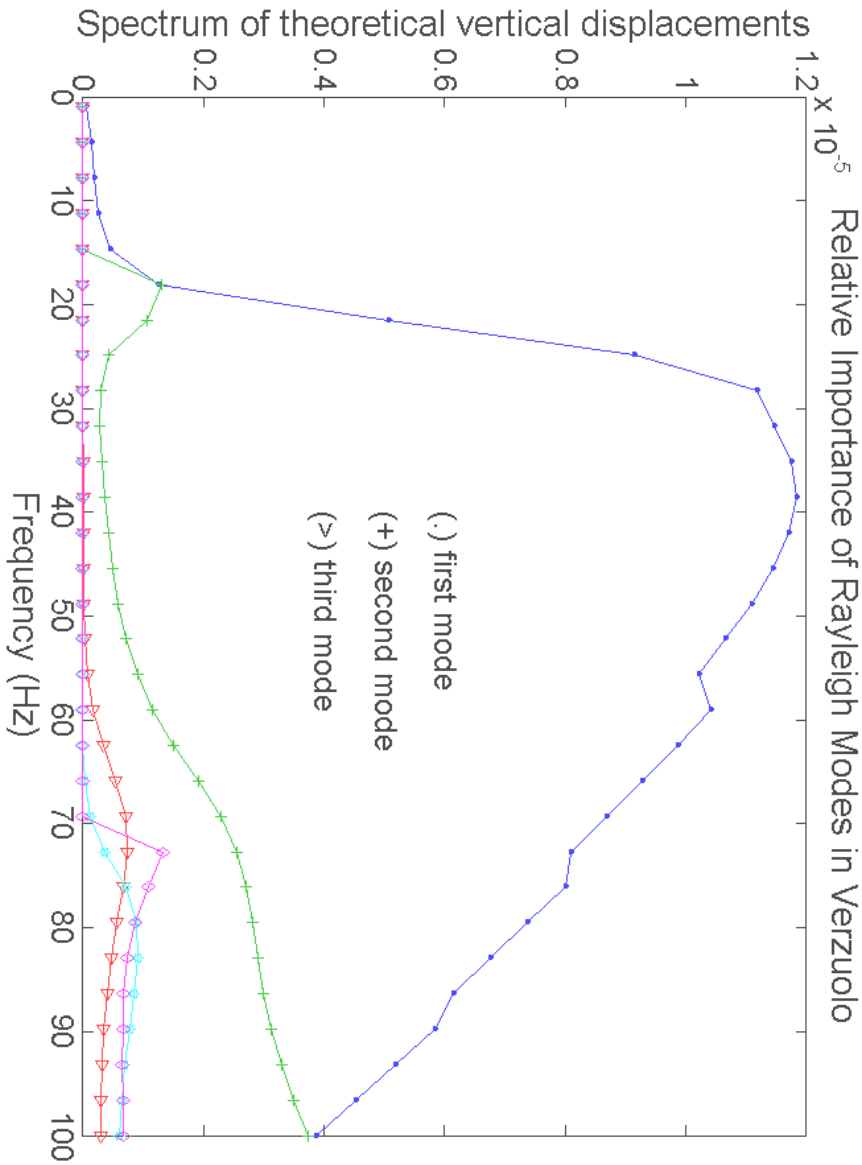

Figure 5.32: Spectrum of displacements theoretically simulated with the inverted profile at Verzuolo site (Italy).

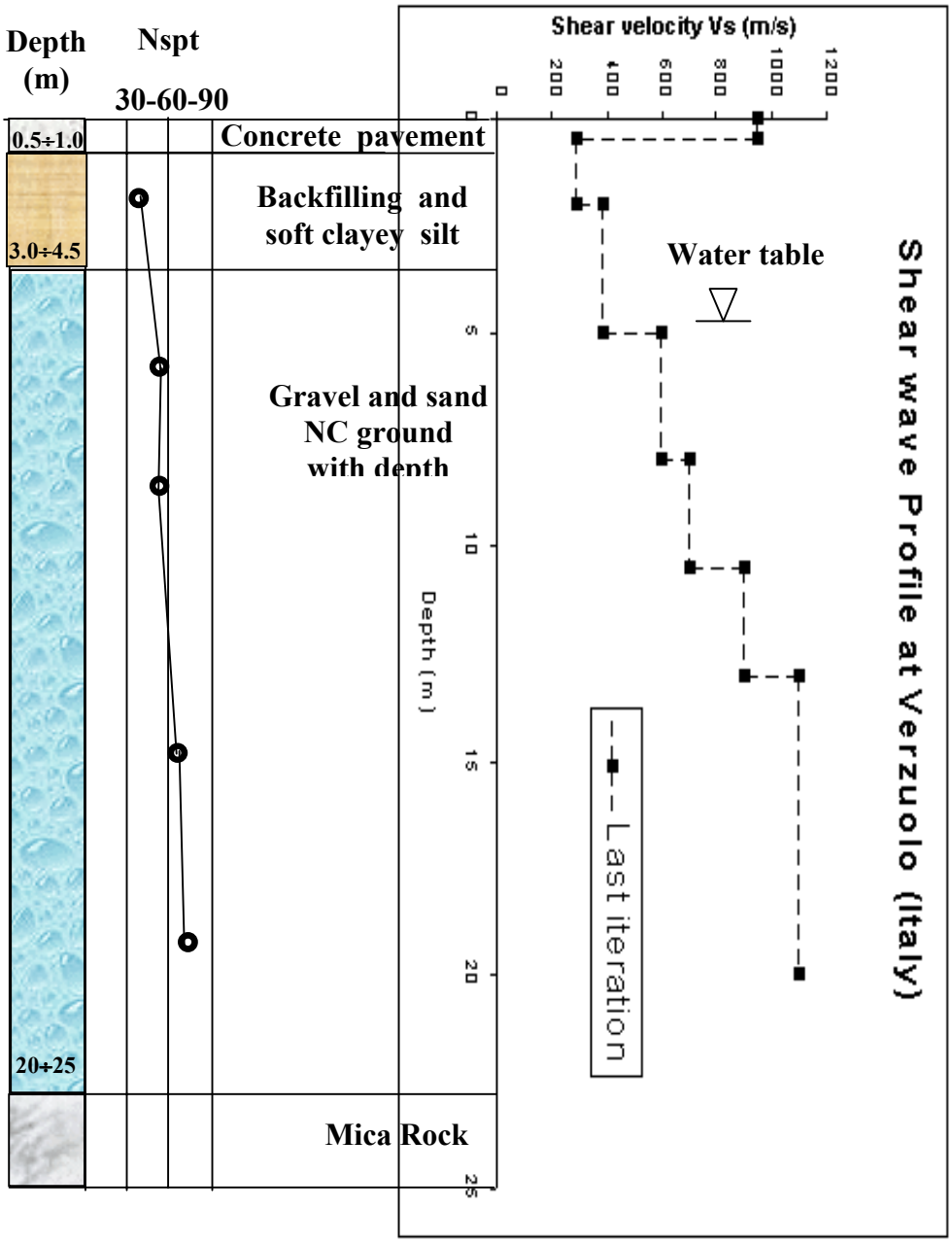

Figure 5.33: Inverted profile at Verzuolo site (Italy) with prediction of the water table position.

In fig.5.33 the results of a drilling survey with in situ Standard Penetration Tests (SPT) have been reported on the left side of the inverted shear wave velocity profile. Precisely 8 drillings have been performed down to a maximum depth of 30m and the averaged geotechnical characterization is summarized in the same fig.5.33.
As can be observed the water table position has been represented in the same fig. 5.33. In this site the water table position was not known a priori, so several positions for the water table have been tried until a satisfactory agreement has been achieved between the experimental and the theoretical dispersion curves. It should be said that in normally dispersive systems Nazarian et al. (1984) have shown how the influence of the Poisson ratio is less than 5% on the dispersion curve. From the several theoretical simulations performed at Verzuolo it has been observed that the optimal minimum of the objective function can be reached only if the water table depth is around 5m. By positioning the water table at different depths, the global system response in terms of dispersion curve completely coincides with the fundamental mode of Rayleigh at all the frequencies. Instead, if the water table depth is set at z=5m, at a frequency of about 20Hz the predominance passes from the first mode to the second mode and then the fundamental mode becomes again the most important (see fig.5.31). This kind of behavior can again be clearly observed looking at the modal spectra of the displacements in fig.5.32. From the same fig.5.32 other precious information are available for a dynamical soil-structure interaction and vibrations transmitted to other surroundings around the turbo-gas machine. In fact the frequency of resonance of the site at f=40Hz can be recognized for the fundamental mode of Rayleigh. This frequency is distant enough from the two frequencies of excitation at which the superstructure works, i.e. 50Hz and 86Hz, so that the induced vibrations on the surface are below the prescribed targets. In a very simplified analysis the layered half-space can be assumed to be a semi-infinite half-space with the following characteristics:

ν	ρ (Kg/m^3)	G_S (Mpa)	D_S (%)
0.35	1900	600	<5%

Table 5.7: Characteristics of the equivalent Half-space used in the simplified analysis for a preliminary design of the base foundation of the vibrating machine.

The choice of a Poisson ratio ν=0.35 is justified by the need of averaging the values ν=0.2 and ν=0.45 corresponding to the unsaturated and saturated layers.

The geometrical characteristics of the rectangular foundation are reported in table 5.8 below, instead the external forces acting on the mass centroid of the base foundation are summarized in table 5.9.

Base Foundation	
Width (m)	B=4
Length (m)	L=21.7
Height (m)	H=1.8
Depth of the base (m)	h=1.8
Total mass (Kg)	M=66900
Centroid from the top of the foundation (m)	Z_G=0.243

Table 5.8: Geometrical Characteristics of the base foundation.

External Loads on the Base Foundation respect to the centroid	
Horizontal Forces (KN)	450
Vertical Forces (KN)	886
Bending Moment (KN·m)	109.5

Table 5.9: Resulting external loads on the Base Foundation for the preliminary design.

From the above data about the soil (predominantly gravel), the base foundation and the external loads, the natural frequencies of the system made of base foundation and superstructure have been calculated by means of the formulas suggested by Prakash and Puri (1988). It comes out that the natural vertical and horizontal frequencies are about $f_{vertical}$=19Hz and $f_{horizontal}$=31.8Hz respectively and the maximum displacement corresponds to the vertical displacement equal to $4 \cdot 10^{-5}$m as can be seen in fig.5.34, where the amplitude of the vertical displacement has been plotted as a function of the circular frequency of excitation. In fig. 5.35 and fig. 5.35 similar plots for the amplitudes of the horizontal and rotational displacements are reported as a function of the circular frequency of excitation. Of course a deeper analysis is needed for a rigorous evaluation of the vibrations induced on the surroundings, i.e. buildings, other operating machines, that takes into account the layered nature of the site and the higher degrees of freedom of the machine.

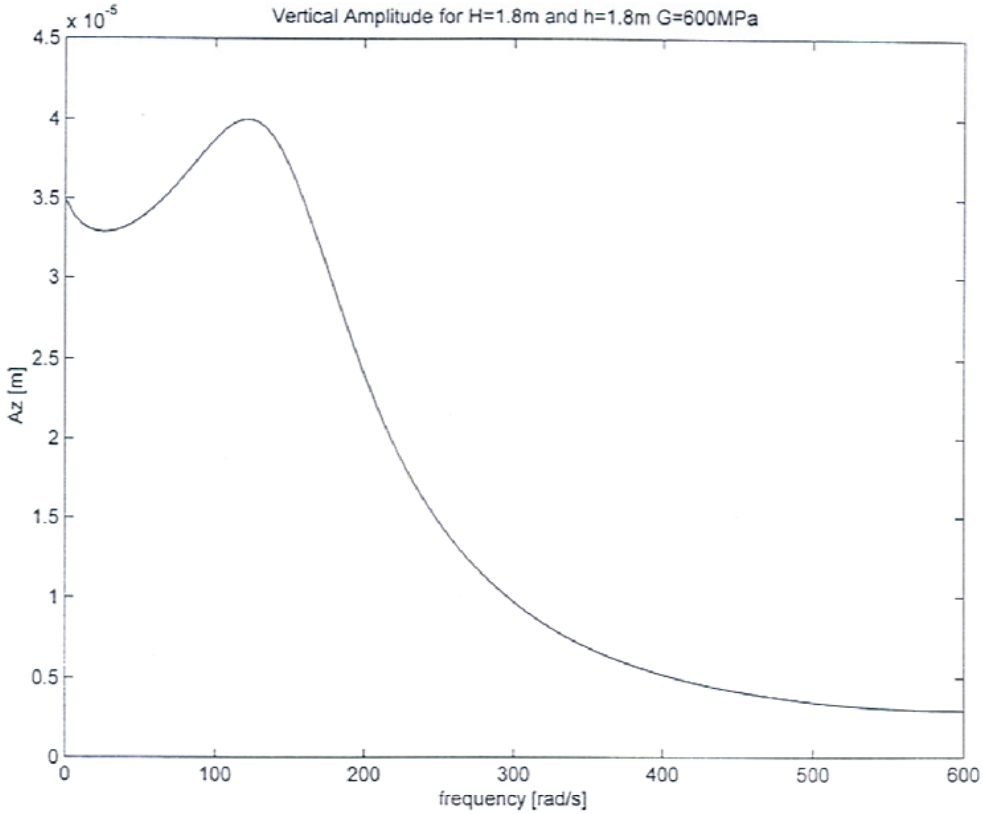

Figure 5.34: Vertical amplitude of the base foundation for a harmonic vertical source of constant intensity equal to 886kN at Verzuolo site (Italy).

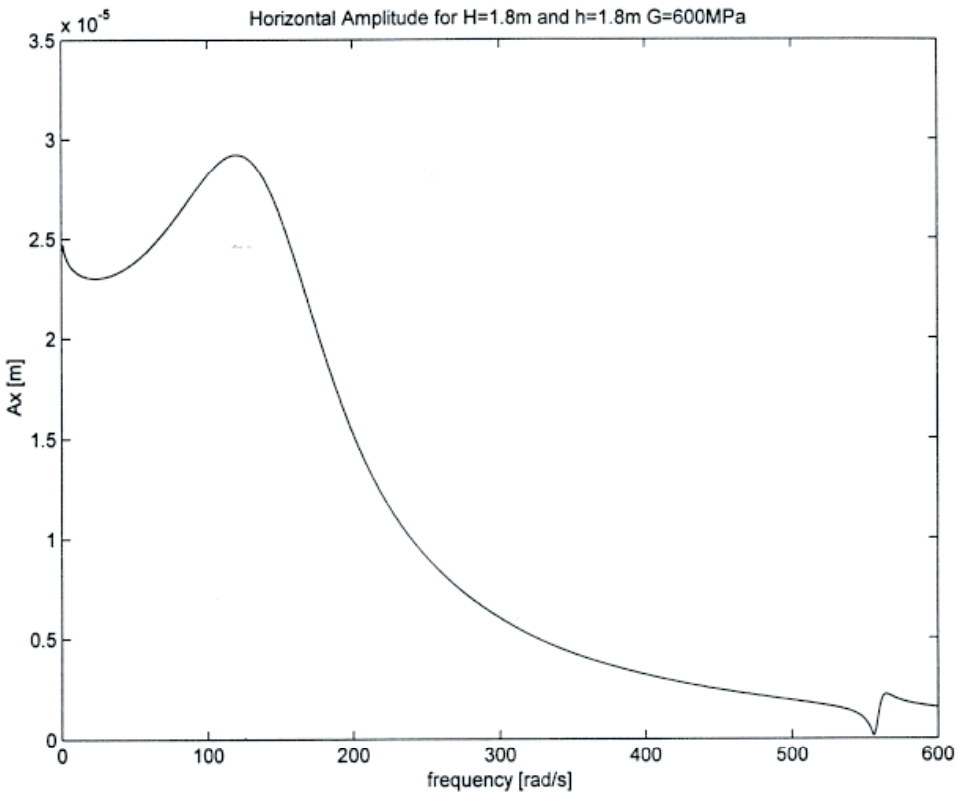

Figure 5.35: Horizontal amplitude of the base foundation for both a harmonic horizontal source of constant intensity equal to 450 kN and a harmonic bending moment of constant intensity equal to 109.5 kNm at Verzuolo site (Italy).

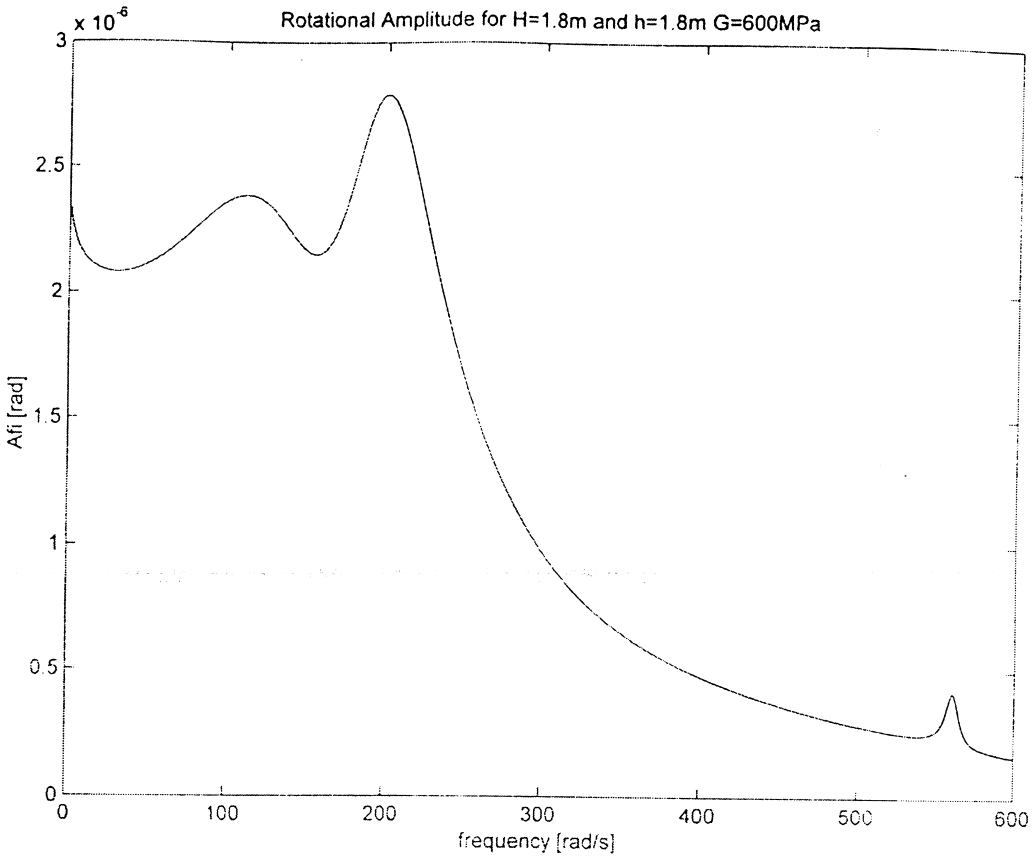

Figure 5.36: Rotational amplitude of the base foundation for both a harmonic horizontal source of constant intensity equal to 450 kN and a harmonic bending moment of constant intensity equal to 109.5 kNm at Verzuolo site (Italy).

5.3.5 The Tower of Pisa

In the summer of 2001 an experimental campaign of investigations was conducted in Pisa around the Leaning Tower with the double aim of checking innovative techniques such as SASW in a well known site on one hand and on the other hand for getting additional information on the Square of Miracles (see fig.5.37).

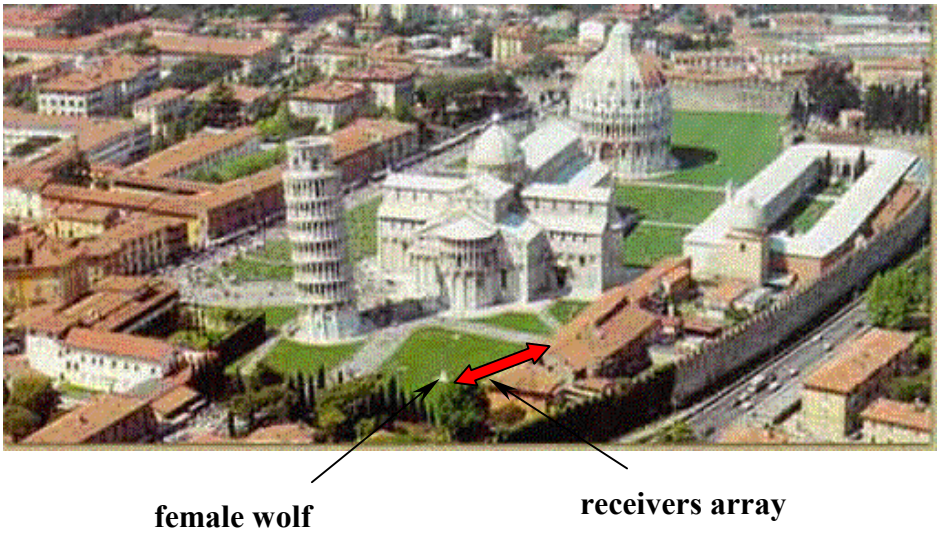

Figure 5.37: Square of Miracles and location of the array of receivers for Multichannel SASW at Tower of Pisa site.

The array of the 24 geophones was set about 40m away from the Tower in the direction opposite to the side the Tower is inclined. Precisely on a grass field near the statue of the female wolf as illustrated in fig.5.37 and fig.5.38. The configuration of receivers used at the Tower of Pisa site consists of 24 geophones placed 1.5m from each other from the 1st receiver to the 8th receiver and 3.0m from the 8th receiver to the 24th receiver, covering a total extension of 58.5m. The source was 1.5m distant from the 1st receiver. As already anticipated in Chapter 2 by using the harmonic source it has been possible to obtain an experimental dispersion curve even at low frequencies. In fig.5.39 both the experimental and the theoretically inverted dispersion curves are shown.

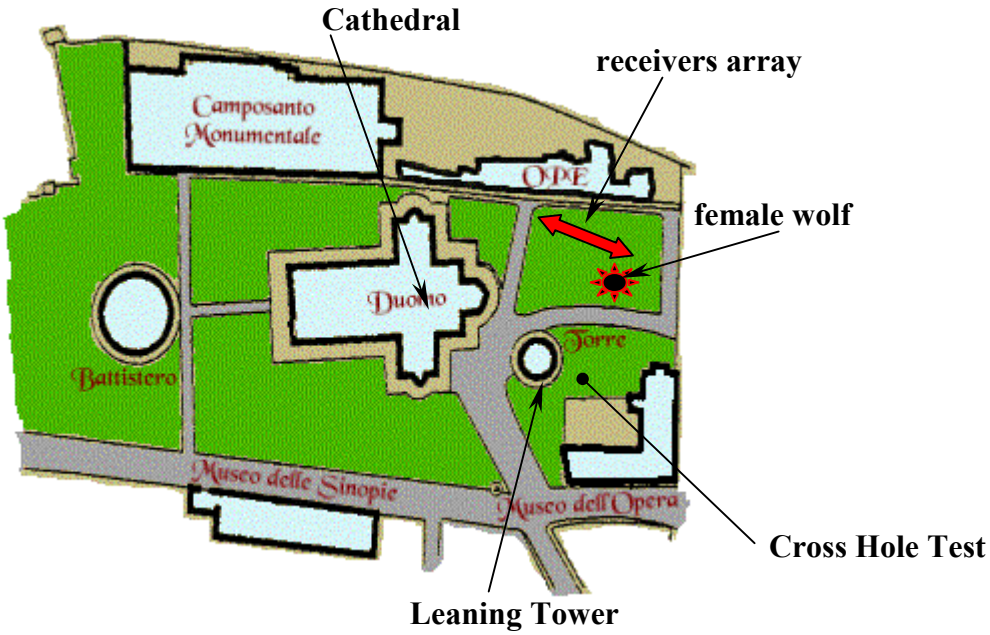

Figure 5.38: Square of Miracles and location of the array of receivers at the Tower of Pisa site.

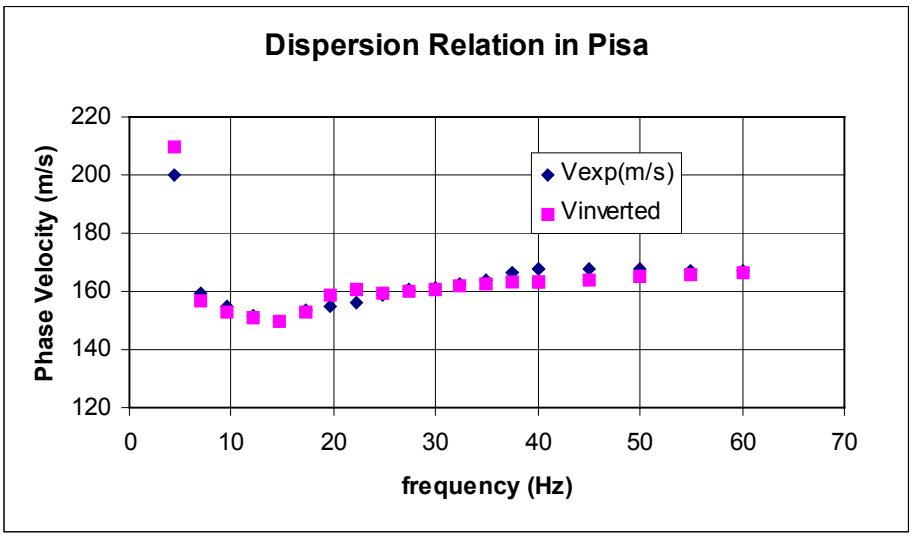

Figure 5.39: Experimental and theoretical (last iteration) dispersion curves at the Tower of Pisa site.

As can be recognized the agreement between the experimental and the theoretical system responses is excellent and the inverted shear wave velocity profile together with the other soil properties are summarized in table 5.10.

Layer	ρ(Kg/m^3)	h (m)	ν	Vs (m/s)	Gs (MPa)
			Poisson	Final	Final
1	1800	1.5	0.2	190.0	65.0
2	1800	1.5	0.2	170.0	52.0
3	1800	3.0	0.48	175.0	55.1
4	1800	2.5	0.48	150.0	40.5
5	1800	3.0	0.48	140.0	35.3
6	1800	5.0	0.48	200.0	72.0
7	1800	5.0	0.48	250.0	112.5
Half-space	1800	∞	0.48	300.0	162.0

Table 5.10: Results of the Inversion process at Pisa Tower (Italy).

The graphical representation of the inverted shear wave velocity profile is reported in fig.5.40, together with the vertically polarized shear wave velovity profile from Cross Hole (CH) test (Lo presti et al, 2002). A good agreement can be observed between the results from CH and the Multichannel SASW method based on Rayleigh waves. Except from the upper 3m of the profile the trend is the same. One possible reason for which the shear wave velocities from CH test and from Multichannel SASW are different in the upper 3m could be the fact that they have not been performed exactly on the same location (see fig.5.38) and the upper layers are represented by man made ground, characterized by horizontally spatial mechanical variability. On the left side of the fig. 5.40 a simplified description of the stratigraphy is illustrated (Lo Presti et al., 2002).

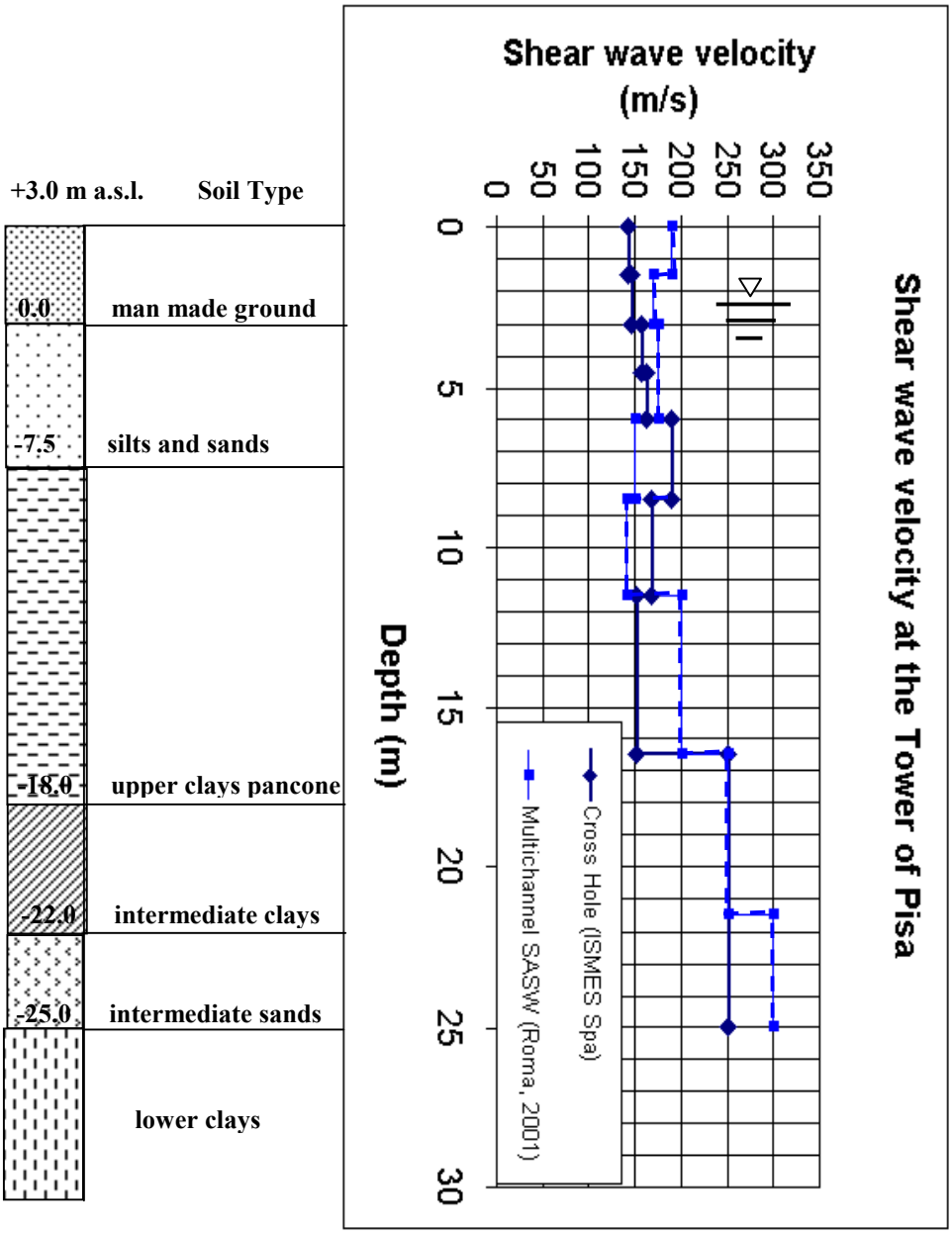

Figure 5.40: Inverted shear wave velocity profile at the Tower of Pisa site: Multichannel SASW (Roma, 2001) versus Cross Hole (ISMES Spa).

5.3.6 Mud A and Mud B

These two sites are on an artificial island of the Mississippi River in Memphis (USA, Tennesee) mainly made of loose sedimentary layers of sand and silt. For these sites 16 accelerometers, covering a total length of about 34m, and the harmonic source have been used in a range of frequency between 3.75-hz and 100Hz. The experimental dispersion curve (circles) together with the theoretical Rayleigh modes corresponding to the finally inverted profile are represented in fig.5.41 for Mud A. As can been observed the experimental global response of the system coincides with the fundamental mode of Rayleigh as usually happens when dealing with essentially normally dispersive site. In fact the finally inverted profile is tabled in table 5.11.

Layer	ρ(Kg/m^3)	h (m)	ν	Vs (m/s)	Gs (MPa)
			Poisson	Final	Final
1	1800	1	0.2	146	38
2	1800	1.0	0.2	154	42
3	1800	1	0.2	162	47
4	1800	0.8	0.2	165	49
5	1800	1	0.2	175	55
6	1800	1.0	0.48	145	37
7	1800	1	0.48	160	46
8	1800	2.0	0.48	165	49
9	1800	3.2	0.48	161	46
10	1800	2.0	0.48	175	55
11	1800	3	0.48	182	59
12	1800	3	0.48	198	70
13	1800	4	0.48	225	91
14	1800	4.0	0.48	250	112
Half-space	1800	∞	0.48	390	273

Table 5.11: Results of the Inversion process at Mud A (USA).

In fig.5.42 and fig.5.43 the shear wave velocity and the shear tangential modulus at very small deformations for Mud A site are plotted.

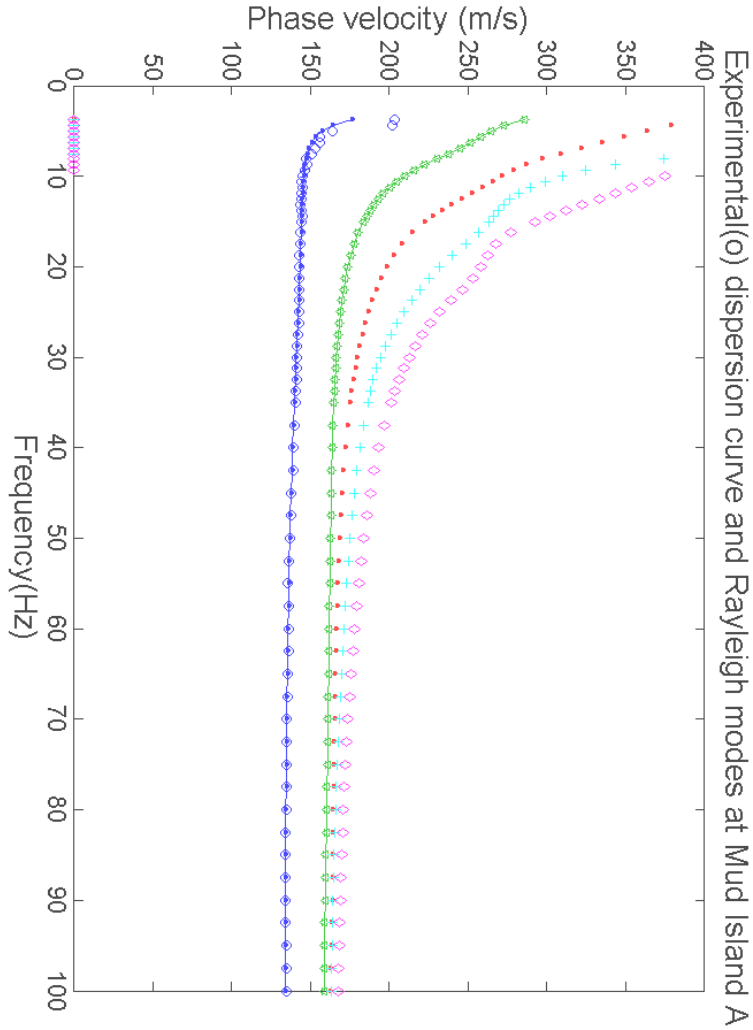

Figure 5.41: Experimental dispersion curve (circles) and theoretical Rayleigh modes at Mud A site.

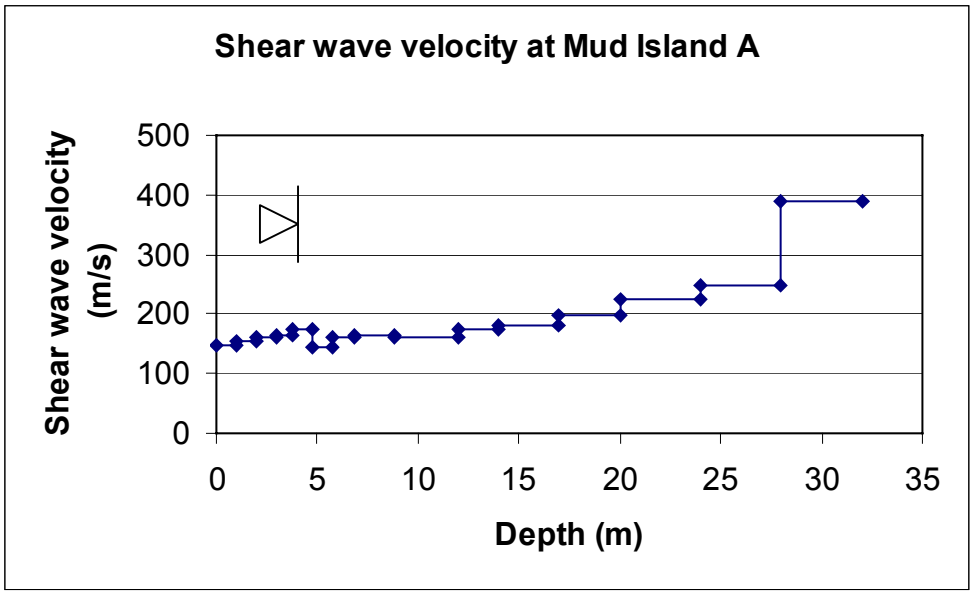

Figure 5.42: Inverted shear wave velocity profile at Mud A site.

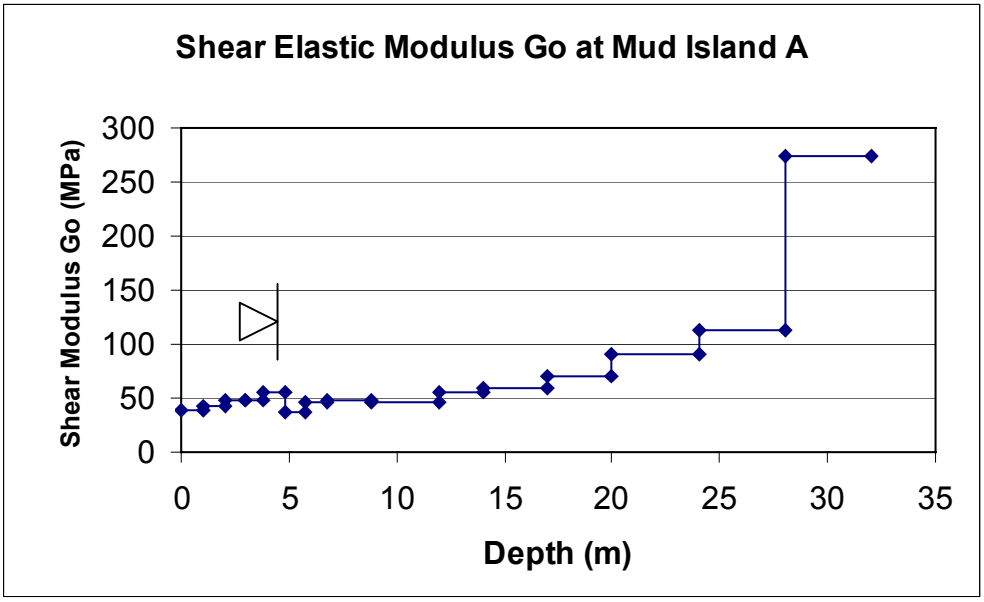

Figure 5.43: Inverted shear Modulus profile at Mud A site.

For completeness the shear damping ratio profile already shown in Chapter 4 in fig.4.5 is here reported in fig.5.44.

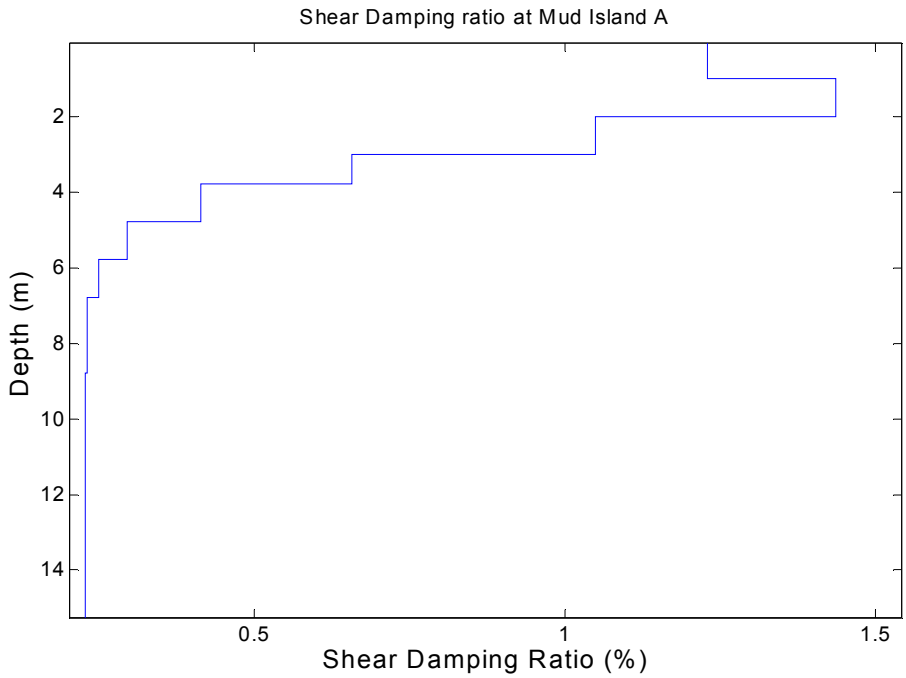

Figure 5.44: Inverted Damping Ratio profile at site Mud A (USA).

For Mud B site fig.5.45 illustrates the experimental dispersion curve (circles) and the theoretical Rayleigh modes obtained with the finally inverted profile (see table 5.12). As for Mud A the experimental dispersion curve coincides with the fundamental mode of Rayleigh, in fact the site is essentially normally dispersive.

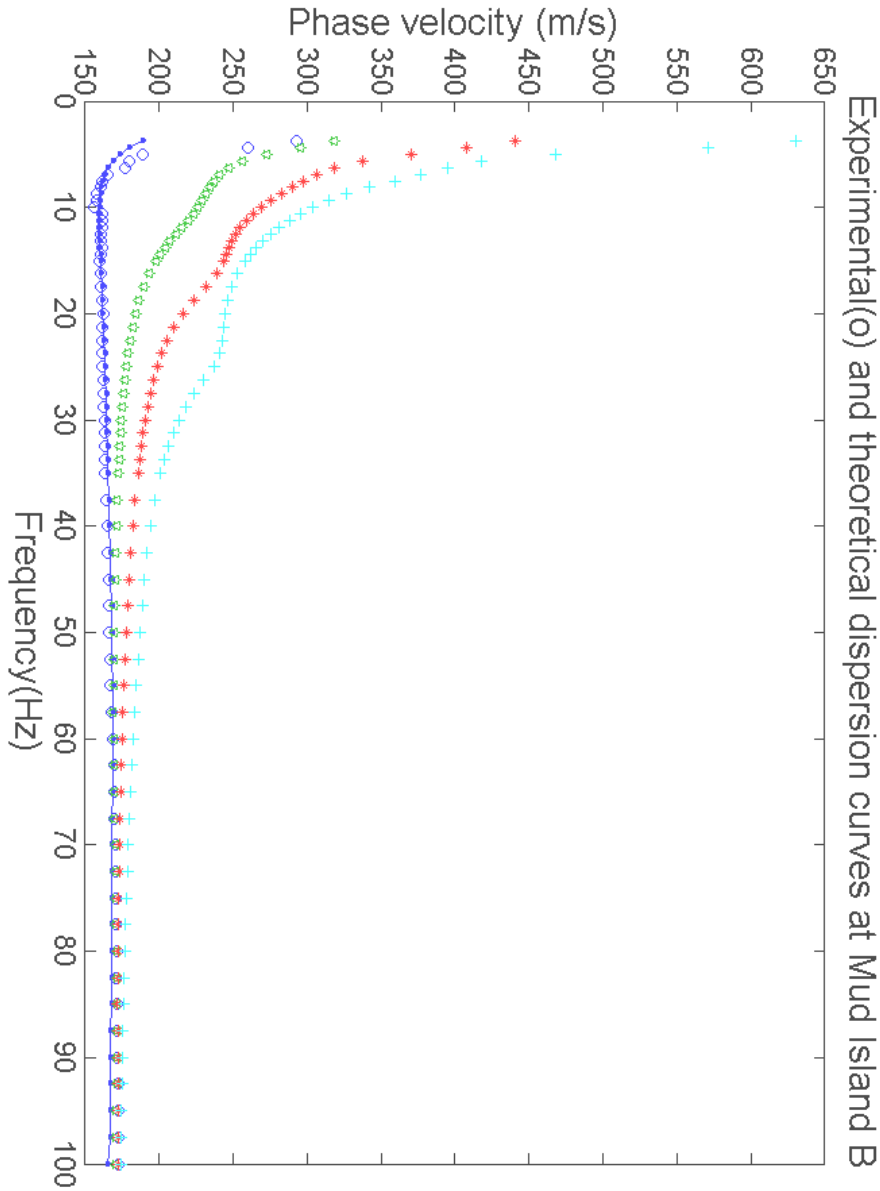

Figure 5.45: Experimental dispersion curve (circles) and theoretical Rayleigh modes at Mud B site.

Layer	ρ(Kg/m^3)	h (m)	ν	Vs (m/s)	Gs (MPa)
			Poisson	Final	Final
1	1800	1.5	0.2	195	68
2	1800	1.5	0.2	180	58
3	1800	2.5	0.2	170	52
4	1800	2.5	0.2	170	52
5	1800	5	0.48	165	49
6	1800	6	0.48	190	64
7	1800	7	0.48	280	141
8	1800	10.0	0.48	225	91
Half-space	1800	∞	0.48	665	796

Table 5.12: Results of the Inversion process at Mud B (USA).

For Mud B site an interesting comparison between the uncoupled and the coupled procedure will follow. In Chapter 4 the results of the coupled procedure have been shown, now the results of the uncoupled inversion will be commented.
By means of the inverted shear wave velocity profile the theoretically simulated and the experimental vertical displacements have been compared (see for example fig.5.46) at several frequencies in order to evaluate the attenuation curve in fig.5.47.
By comparing the experimental attenuation curves (see fig.5.48) obtained with the Coupled and the Uncoupled procedures at least two aspects are visible. The first one is that the attenuation curve obtained with the uncoupled procedure (red points) is always below the attenuation curve obtained with the coupled procedure (blue points), even if the order of magnitude is the same. The second feature is that the coupled inversion allows for a more extended attenuation curve towards the low frequencies. In this regard the coupled procedure should be preferred to the uncoupled inversion.
The final inverted shear damping ratio profile at Mud B site following the uncoupled procedure is represented in fig.5.49.

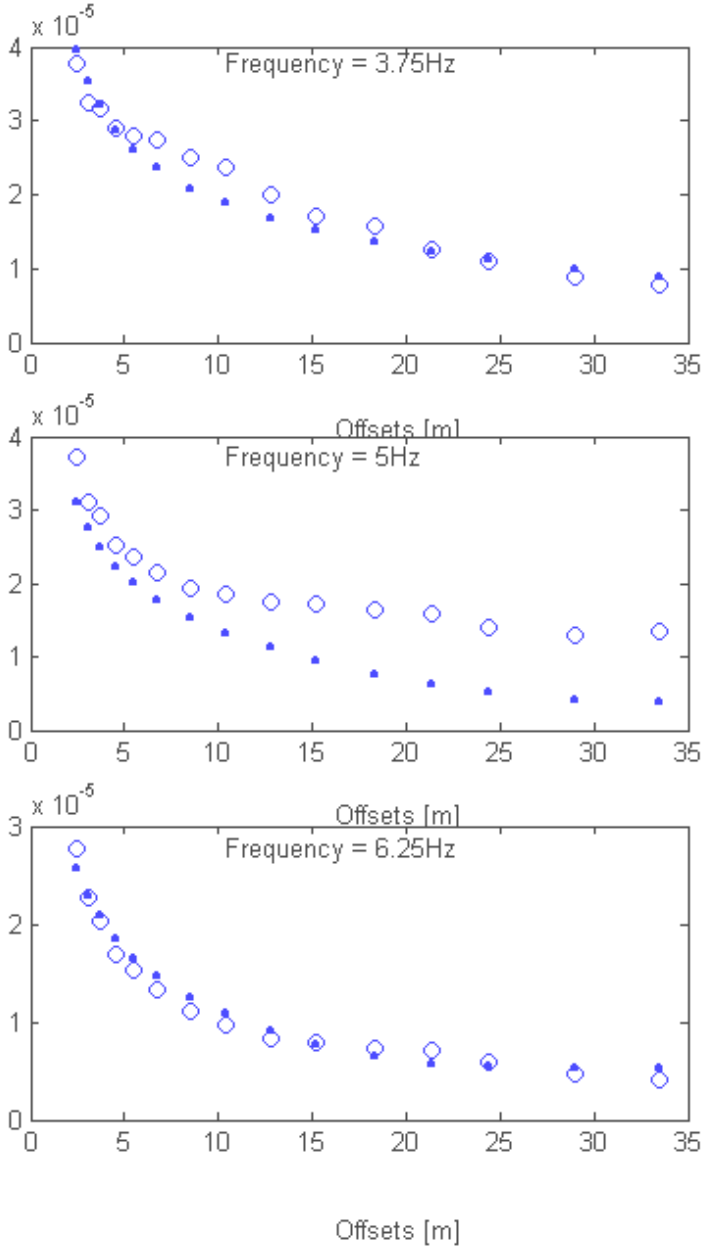

Figure 5.46: Experimental (circles) and theoretical displacements at Mud B site. Amplitude in [m].

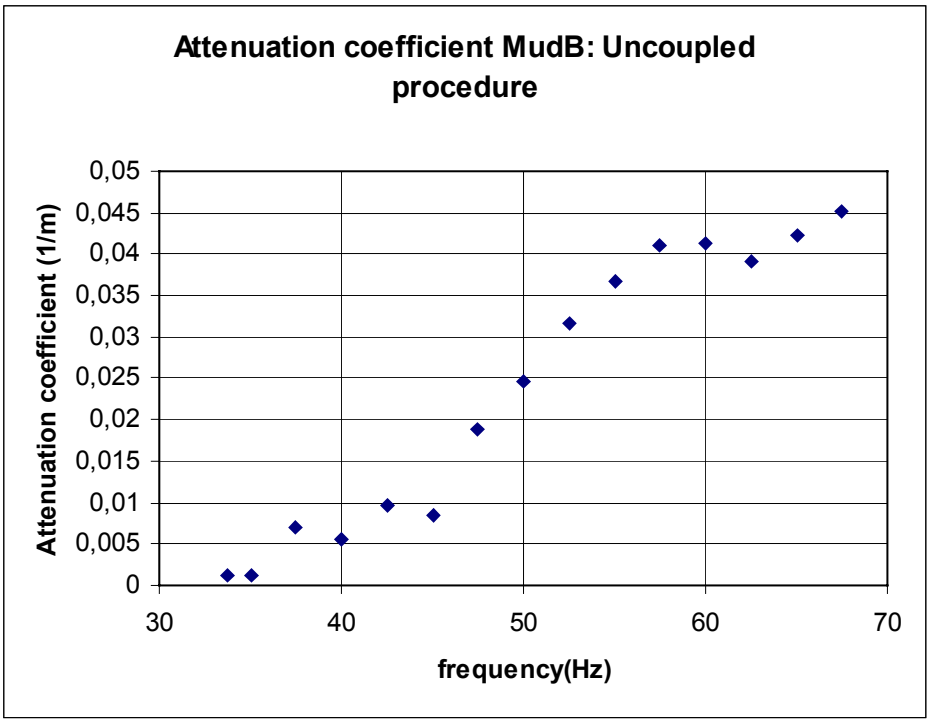

Figure 5.47: Experimental attenuation curve at Mud B site following the uncoupled inversion.

A comparison between the coupled and the uncoupled procedure says that the results are of the same order of magnitude and in very good agreement but there are still some differences for some layers as is summarized in table 5.13.

Layer	h (m)	Ds (%)	Ds (%)
		Coupled	Uncoupled
1	1.5	3	1.5
2	1.5	2.2	1.3
3	2.5	1.4	1.4
4	2.5	2.8	1.8
5	5	3.3	3.3
6	6	3.8	3.5
7	7	3.9	3.5
8	10.0	4	3.5
Half-space	∞	4	3.5

Table 5.13: Coupled versus uncoupled inversions for determining the shear damping ratio profile at Mud B.

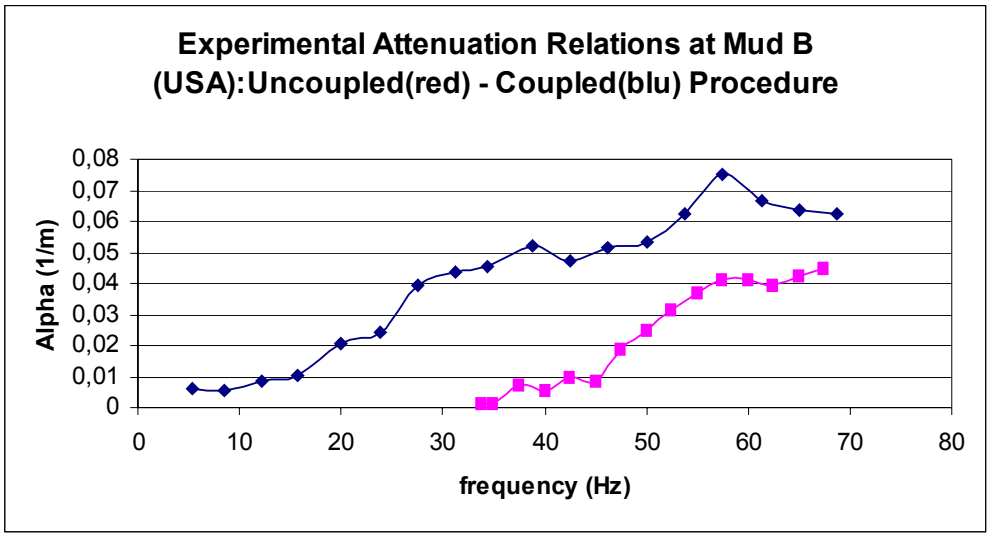

Figure 5.48: Experimental attenuation curves at Mud B site following the uncoupled (red points below) and the coupled (blue points up) inversions.

Since the experimental attenuation curves obtained by means of the coupled and the uncoupled procedures shows quite different magnitude a hybrid approach has been followed between the coupled and the uncoupled procedures. The experimental attenuation curve from the coupled regression analysis of the experimental measurements has been combined with the shear wave velocity profile obtained with the uncoupled inversion and the uncoupled procedure has been performed using these two independent data.
The final shear damping ratio profile is tabled in table 5.14 together with the pure coupled and the pure uncoupled procedures. The results are not so distant from the previous ones and they appear to follow the same trend. Also the order of magnitude is the same. Finally the experimental and the theoretical attenuation curves are compared in fig.5.50 and the agreement is really satisfactory.

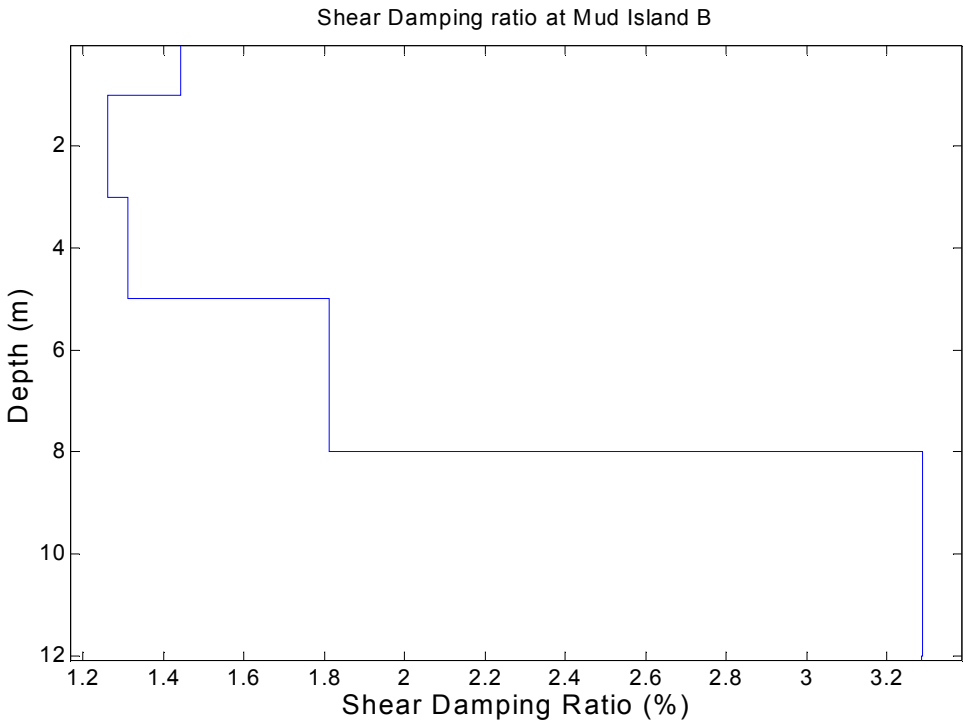

Figure 5.49: Shear damping ratio profile at Mud B site following the uncoupled procedure.

Layer	h (m)	Ds (%)	Ds (%)	Ds (%)
		Coupled	Hybrid	Uncoupled
1	1.5	3	3.4	1.5
2	1.5	2.2	3	1.3
3	2.5	1.4	2.5	1.4
4	2.5	2.8	3.8	1.8
5	5	3.3	3.8	3.3
6	6	3.8	3.8	3.5
7	7	3.9	3.8	3.5
8	10.0	4	3.8	3.5
Half-space	∞	4	3.8	3.5

Table 5.14: Coupled, uncoupled and hybrid approaches for determining the shear damping ratio profile at Mud B.

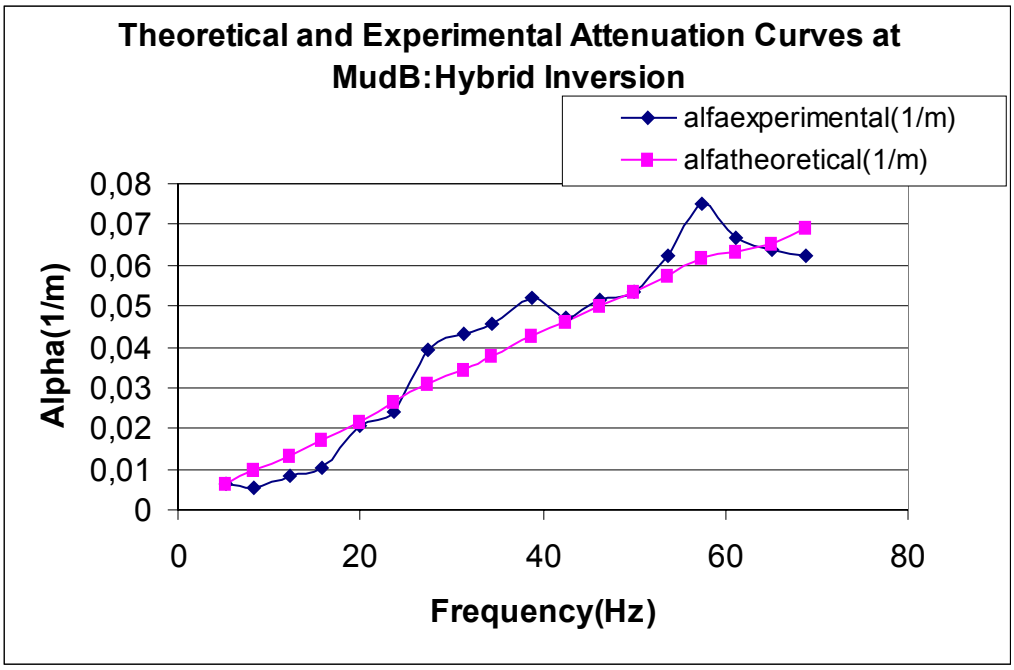

Figure 5.50: Experimental (Coupled regression) and theoretical (Uncoupled inversion) attenuation curves in the Hybrid approach at Mud B site.

By comparing the comparison the results obtained by means of the coupled, the uncoupled and the hybrid approaches for determining the shear damping ratio profile it can be said that the corresponding profiles follow the same trend with depth, they always keep below 5% so the values for D_S appear reasonable. This means that the uncoupled inversion also represents a valid

alternative to the coupled procedure which in principle is more rigorous, but at the same time more expensive in terms of computational efforts and time. In the opinion of the Author further investigations are necessary for supporting the inversion procedures proposed hereafter and improvements and new ideas are to be hoped for, to determine the shear damping ratio profile via the SASW technique.

5.3.7 Final Considerations on the Experimental Investigations

From all the real sites that have been investigated some aspects can be underlined. First of all it has been proved that the uncoupled inversion technique for the shear wave velocity and thickness profiles, that relies on the DFP optimization algorithm, gives excellent results and very few doubts are left on the determination of the stiffness profile.
Secondly the main role assumed by the experimental data must be stressed. In fact a reliable and accurate experimental system response is the fundamental basis for a correct soil characterization. This is true especially in non-invasive surface waves analysis for ill-posed inverse problems such as the Rayleigh Inversion problem.
The damping ratio determination needs further investigations and efforts, even if the results achieved hereafter are definitely encouraging. In this regard it has been shown how important it is to consider the higher modes of Rayleigh in the evaluation of the experimental attenuation curve. In fact a simplified attenuation law such as $1/\sqrt{r}$ is commonly adopted (Foti, 2000), but it causes unsatisfactory results, when dealing with inversely dispersive systems (see fig.4.3 and fig.4.4).

Conclusions and Recommendations

The use of surface waves for soil characterization represents at the same time a challenging and an attractive tool. This research has had as main goal the development of a pragmatic means for determining the shear wave velocity Vs, the shear damping ratio Ds and the thickness h profiles.

The work has been aimed at understanding in which manner the higher Rayleigh modes superimpose during propagation and how they can be used for soil characterization. The attention is especially towards inversely dispersive media, in which the stiffness profile does not gradually increase with depth, but softer layers are trapped between stiffer ones or vice versa stiffer layers are between softer ones.

On one side it has been clarified how the higher modes combine together in different zones of the frequency-wave number (f-k) spectrum, to give a unique apparent dispersion curve, as found in experimental tests. On the other hand the importance of the configuration of receivers in both experiments and theoretical simulations has been stressed. As a consequence the dispersion curve obtained from the field test and the one obtained from simulation must be considered "*apparent*" responses of the system coupled with the receivers array. In fact the "*apparent*" dispersion curve of Rayleigh waves is the result of what can be either measured or simulated by adopting that particular configuration of receivers rather than another one. Hence the need for using the same configuration of receivers in the experiments and in the theoretical simulations assumes fundamental relevance.

It has been observed that the spectrum of the vertical displacements of each Rayleigh mode, when represented in the f-k domain independently from the other modes, shows at least one main peak for which the system response is maximized. It is worthy to note that the position of these modal peaks in the f-k domain individuates the frequencies and the wave numbers of resonance of the system for travelling Rayleigh waves and it has also been shown that they do not depend on the receivers array. This means that they represent an intrinsic characteristic of the system itself.

Specifically for a single layer over an infinite half-space a sensitivity analysis has allowed for a simple formula to be established among the frequencies of resonance of the system for Rayleigh waves and the geometrical and mechanical properties of the system. The utility of such a formula comes out in all those engineering applications when

surface vibrations generated by Rayleigh waves are concerned (for example see Verzuolo site in Chapter 5). In fact in a mono-dimensional simplified model it is commonly assumed that vertically travelling shear waves are responsible for vibrations induced by earthquakes, but daily experience makes us aware that thousands of kilometers away from the epicenter the main damages are caused by Rayleigh waves in conjunction with local site amplification effects.
Once the relative importance of Rayleigh modes has been comprehended, a convenient procedure has been proposed for taking into account all the Rayleigh modes in the theoretical simulation of the experimental test. The procedure is based on three main points:
1) an analytic expression for the far field response due to only Rayleigh waves is used.
2) The experimental test is theoretically simulated except that only 1D Fourier transformation from frequency-space to frequency-wave number is applied instead of a 2D Fourier transformation from time-space to frequency-wave number domain.
3) If a vertical point source is used on the free surface of the layered half-space either the experimental or the theoretical dispersion curve does not depend on the energy content of the source. The energy content of the source allows for the dispersion curve to be evidenced into a certain range of frequency rather than another interval.
Point 3) is an important result that has been theoretically demonstrated and experimentally verified. Thanks to this achievement the procedure mentioned in point 2) has been implemented with a lot of time saving.
After a theoretical method, coherent with the experiment in situ has been assured, the next step consists of the inversion process.
In this thesis both the uncoupled and the coupled techniques have been adopted for determining the stiffness and the damping ratio profiles at a site. Particularly for the uncoupled evaluation of the stiffness profile a quasi-Newton constrained optimization algorithm (DFP) has been implemented. At first both the thickness and the shear wave velocities have been considered as independent variables in the uncoupled inversion process, but it has been discovered that the contemporary inversion of the thickness and the shear wave velocities may give unrealistic results. Instead the independent inversion of either the shear wave velocity or the thickness gives very satisfactory results, especially for normally dispersive sites. For inversely dispersive media the existence of local minima of the objective function, defined as the "*distance*" between the theoretical and the experimental responses, makes the inversion process more difficult and gives rise to the problem of non-uniqueness. The non-uniqueness can be mitigated by adding a priori information and by adopting the

same procedures in situ and in the simulation. If a local search technique is used the only manner for overcoming the problem of the local minima consists of starting from different initial configurations which seem to be "good" candidates and then taking as final inverted profile that one for which the objective function reaches the absolute minimum.

There are no theoretical criteria for being sure whether the found minimum is absolute or not. In fact even if the domain of the independent variable is convex, no information is available about the objective function, that remains a sort of obscure box.

The shear damping ratio Ds can be determined by either an uncoupled or a coupled procedure. Moreover a hybrid approach has been proposed. In all cases the results that have been obtained are in good agreement each other, but in the Author's opinion there is still much room about this issue. It has been shown how relevant the use of all the Rayleigh modes is in the Geometric Rayleigh Spreading function and how limiting it is to use a too simplified and inadequate attenuation law of $1/\sqrt{r}$. Another aspect that deserves a comment is the use of either an impulsive or a harmonic source. Of course the harmonic source is necessary for evaluating the Transfer Function of the system and hence for determining the Damping profile according to the currently used procedure. Also the harmonic source offers the advantages of getting a better signal to noise ratio even at low frequencies. Nevertheless the impulsive source allows for a transient picture of the travelling disturbance in the time-space domain. In this domain it is possible to have a clear image of the dispersion phenomenon and a direct measurement of the group velocity of the whole perturbance could be attempted. With regard to this a well established concept is that the group velocity coincides with the velocity of the energy associated to the whole disturbance.

Even if the mathematical idealization of the physical reality predicts the existence of independent Rayleigh modes, each of them travelling at their own phase and group velocities, the perturbance spreads away in the time-space domain as a whole signal, made of different components superimposed together. To this complicated perturbation it is possible to associate a certain energy, that travels at a speed that depends on time and space. In the case of a time impulsive source an analytic expression for the effective or apparent group velocity has been formulated.

This quantity has not only got a precise meaning but it may also reveal either an additional or more sensitive system response to the unknown parameters.

The choice of using either the accelerometers or the geo-phones for detecting the disturbance depends on the characteristics of the receivers and the reliability associated to them at different frequencies. It has also been proved that under certain conditions it is completely equivalent to use the spectrum of either the energy or the displacements as well as the velocities or the accelerations in evaluating the Rayleigh dispersion curve.

One subject needs some considerations. Is it correct to consider the travelling disturbance as a complicate signal where all the modes are combined and hence assuming only an apparent or effective dispersion curve? Should it be more appropriate trying to experimentally discern the different components of motion such as the Rayleigh modes? The answer is not unique but it depends on the purpose. If a sufficient space is available for the experimental investigations, then the dispersion phenomenon can take place and the higher modes can be experimentally taken apart from each other. Notice that when an impulsive source is used for exciting a layered system on the free surface, at each frequency more than one Rayleigh mode is excited at the same time. As a consequence each Rayleigh mode has got different wave numbers that correspond to different frequencies and travel at different speeds. So a wave packet in front of the whole wave train and another wave packet at the back could in principle contain different components of the same Rayleigh mode. Again in order to clarify how it is possible to experimentally separate the Rayleigh modes, the spectrum of each independent mode says that the response of each mode is more or less intense at different frequencies. Hence for a given Rayleigh mode a significant amount of energy is associated only to some wave numbers, the other wave numbers that travel with different group velocities transfer a negligible amount of energy, so that their contribution to the wave field can be ignored.

Instead if the space available in situ is not sufficient for the separation of the different Rayleigh modes, then a greater number of receivers could help a lot but the way to be followed consists of considering all the components of motion as a whole complicate perturbation. With this regard concepts such as apparent or effective phase or group velocities assume relevance.

Recommendations for Future Research

There are many features that still need further investigation. About the stiffness profile it can be said that satisfactory results have been achieved by many researchers but very few of them consider the higher Rayleigh modes in the inversion procedure. When dealing with inversely dispersive profiles it becomes mandatory to make use of all Rayleigh modes.
About the optimization algorithm to be used for the inversion problem, in the Author's opinion the "*best*" algorithm in an absolute sense does not exist. Each optimization algorithm may work well or not depending on the particular problem to be solved. Only a certain experience on several real cases can permit a continuous improvement of the optimization algorithm.
About the damping ratio profile Ds the use of all Rayleigh modes seems necessary for reliable results. Both the coupled and the uncoupled procedures have shown to be promising and other applications to real sites are needed. In particular a proper strategy would be to compare the results from SASW method and from other techniques on a simple site, as homogeneous as possible with depth or at least normally dispersive, that be well known and documented by means of alternative investigations.
In this research the dispersion and the attenuation curves have been adopted as system response, because of the great amount of available experimental data and because of the knowledge accumulated in past years by several researchers.
In the Author's conviction in the framework of a coupled procedure a more appropriate quantity to be chosen as system response is the f-k spectrum of either displacements or energy. This choice is justified by the fact that both dispersion and attenuation curves are quantities derived from the spectrum, that is directly calculated from the measurements.

Another aspect is the importance of the experimental response. It is a matter of fact that the better the experimental response, the more successful the inversion. In this work an attempt has been made to extract more than one dispersion curve from the measured data. In some cases it has been possible to define two experimental apparent dispersion curves. The use of two curves instead of only one could definitely help reduce the non-uniqueness problem.
Until now one limiting hypothesis for the model used for the forward simulation of the experiments has been the horizontal layering of the medium. If the possibility of an inclination of any layer is admitted,

the mathematical problem of the wave propagation becomes more complicate and the possible combinations for the geometry increase considerably. Nevertheless there are two situations that at least deserve to be analyzed. The first geometry I is that one in which all the layers are parallel and inclined at the same angle with respect to the verticality (see fig.C.1). The only difference respect to the horizontal layering is the inclination of the gravity. Since the gravity is a static force and is not considered in the equations of motion, for this geometry the same solutions as for the horizontally layered half-space can be adopted, provided that the source be applied perpendicularly to the surface. The second geometry II consists of a set of parallel layers except the surface one, that is inclined with respect to the others. There are two sub-cases, i.e. IIa the top layer is horizontal and the other ones are inclined (see fig.C.2) or IIb the top layer is the only one inclined and the other ones are horizontal (see fig.C.3). Anyway if the gravity is neglected in the equations of motions they are completely equivalent.
The first consideration on this geometry concerns the loss of the radial symmetry with respect to the horizontal layering. Hence in the experimental tests it is necessary to detect the perturbation on both sides of the source. By intuition it could be said that a disturbance propagates towards the surface on the side of the source where the interfaces of the layers reach the surface (left side in fig.C.2, right side in fig.C.3), instead on the other side another disturbance travels away from the free surface. As a consequence one should expect a greater intensity of the perturbation on one side of the source with respect to the other side.

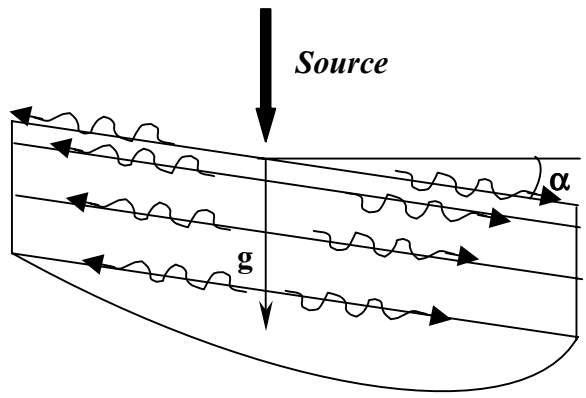

Figure C.1: Layering I: all layers parallel and inclined at α.

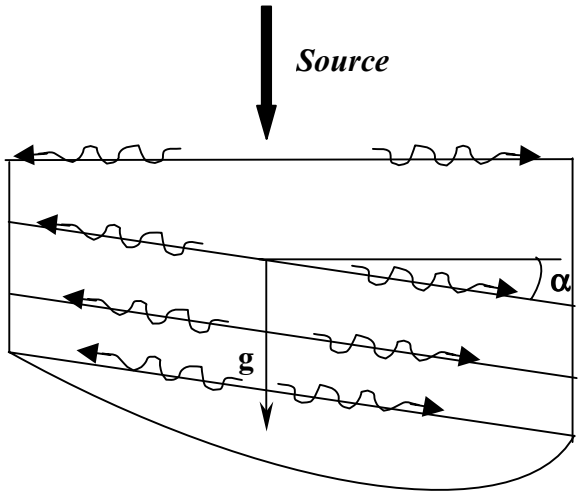

Figure C.2: Layering IIa: surface layer horizontal and all deeper layers parallel and inclined at α.

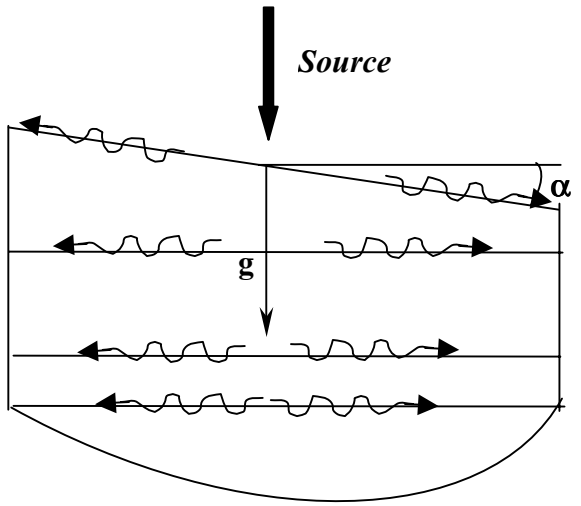

Figure C.3: Layering IIb: surface layer inclined at α and all deeper layers parallel and horizontal.

A last recommendation is about the potential use of the frequencies and the wave numbers of resonance for determining the damping ratio profile. In correspondence of a frequency of resonance for the jth mode the other modes have less importance, so the mistake in considering only the jth mode in the inversion process is mitigated. The Author would like to underline the utility of finding explicit relationship among the geometrical and mechanical properties of the system and the frequencies and the wave numbers of resonance. In fact, once the site has been characterized, the knowledge of the conditions of resonance of the site is necessary for many engineering applications, when dealing with surface waves. In this research only one layer over a half-space has been studied and investigations on a layered half-space with two layers over an infinite half-space are being analyzed by the Author. Investigations on systems with additional layers would be auspicious.

In the aim of a soil characterization by means of non invasive techniques a winning strategy consists of using different methods, which should be seen as complementary rather than alternative. So several methods can be borrowed from geophysics, such as seismic reflection and refraction. Also information from SH and Love waves can be very useful for the purpose.

In conclusion the Author manifests his encouragement in investing time in the analysis of surface waves for soil characterization. The efforts are not only justified by a pragmatic goal, i.e. the soil characterization, but by the nobler stimulus of learning from what mater nature shows us.

Vita

Vitantonio Roma was born in Brindisi, on the heel of Italy , the 10th November 1973. After attending the High Secondary School Liceo Scientifico "Enrico Fermi" in Brindisi at the age of 18 he moved to Turin, where he attended the Civil Engineering courses at the Technical University of Turin (Politecnico di Torino). In the academic year 1997-1998 he was student assistant to the courses "Tecnica delle Costruzioni" (Design of the Structures) and "Progetto di Ponti" (Design of Bridges). In May 1998 he graduated cum laude as a Civil Structural Engineer with a thesis on passive seismic isolation of structures, whose title was: "Attenuazione della Risposta sismica di Strutture su pali" (Attenuation of the Seismic Response of Structures founded on piles). He was awarded for the best Structural Engineering thesis of the year by the Association "Ex Allievi del Politecnico di Torino". During the period from August 1998 until June 1999 he served the Navy at the Genova Port, working as civil engineer at the State Property Office.

In November 1998 he started his PhD programme under the guidance of Professor Renato Lancellotta in the Structural and Geotechnical Engineering Department at the Technical University of Turin (Politecnico di Torino). During the period from November 1999 until August 2000 he has worked first for a Structural Engineering firm and then for a Geotechnical Engineering firm (Ingegneria Geotecnica srl) in Turin and in June 2000 he became member of the Civil Engineers Association of Brindisi.

In August 2000 he left Turin for Atlanta, where he worked as a research visiting PhD student under the guidance of Professor Glenn Rix at the Civil and Environmental Engineering Department of the Georgia

Institute of Technology. After 10 months he came back to Italy to complete his PhD research on soil characterization using Rayleigh waves propagation in layered media.

In November 2001 he has joined the Geodata Spa company as a structural and geotechnical engineer, working in the field of underground structures, subways, foundation engineering, soil-structure dynamical interaction.

He is currently involved in a couple of research projects in the field of the seismic local amplification effects and soil-structure dynamical interaction at the Technical University of Turin (Politecnico di Torino).

At the moment he is member of:

1) Soil Mechanics and Foundation Engineering Research Group of the Structural and Geotechnical Engineering Department at the Technical University of Turin (Politecnico di Torino)
2) Dynamical Research Group of the Structural and Geotechnical Engineering Department at the Technical University of Turin (Politecnico di Torino)
3) Italian Geotechnical Association (AGI)
4) International Society for Soil Mechanics and Geotechnical Engineering (ISSMGE)
5) International Society of Rock Mechanics (ISRM)
6) Geotechnical Commitee of Brindisi

Current contact information:

Vitantonio Roma,

Geodata Spa
C.so Duca degli Abruzzi 48/E, 10129
Torino(Italia)
e-mail:vitanton@ciaoweb.it or
vro@geodata.it
Tel. +39 0115810611 or +39 3474411919
Fax. +39 011597440

Or

Dipartimento di Ingegneria Strutturale e Geotecnica
Politecnico di Torino
C.so Duca degli Abruzzi 24, 10100
Torino (Italia)